Development of a patient-specific unicompartmental knee replacement

by

Johan van der Merwe

Dissertation presented for the degree of Doctor of Philosophy in the Faculty of Engineering at Stellenbosch University

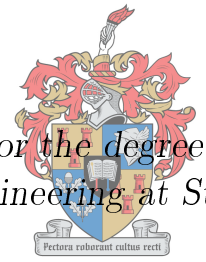

UNIVERSITEIT
iYUNIVESITHI
STELLENBOSCH
UNIVERSITY

Promoter: Dr. D.J. Van den Heever

March 2018

Declaration

By submitting this dissertation electronically, I declare that the entirety of the work contained therein is my own, original work, that I am the sole author thereof (save to the extent explicitly otherwise stated), that reproduction and publication thereof by Stellenbosch University will not infringe any third party rights and that I have not previously in its entirety or in part submitted it for obtaining any qualification.

Date: ..... March 2018 .....

UNIVERSITEIT·STELLENBOSCH·UNIVERSITY
jou kennisvennoot • your knowledge partner

Plagiaatverklaring / Plagiarism *Declaration*

1 Plagiaat is die oorneem en gebruik van die idees, materiaal en ander intellektuele eiendom van ander persone asof dit jou eie werk is.
Plagiarism is the use of ideas, material and other intellectual property of another's work and to present is as my own.

2 Ek erken dat die pleeg van plagiaat 'n strafbare oortreding is aangesien dit 'n vorm van diefstal is.
I agree that plagiarism is a punishable offence because it constitutes theft.

3 Ek verstaan ook dat direkte vertalings plagiaat is.
I also understand that direct translations are plagiarism.

4 Dienooreenkomstig is alle aanhalings en bydraes vanuit enige bron (ingesluit die internet) volledig verwys (erken). Ek erken dat die woordelikse aanhaal van teks sonder aanhalingstekens (selfs al word die bron volledig erken) plagiaat is.
Accordingly all quotations and contributions from any source whatsoever (including the internet) have been cited fully. I understand that the reproduction of text without quotation marks (even when the source is cited) is plagiarism.

5 Ek verklaar dat die werk in hierdie skryfstuk vervat, behalwe waar anders aangedui, my eie oorspronklike werk is en dat ek dit nie vantevore in die geheel of gedeeltelik ingehandig het vir bepunting in hierdie module/werkstuk of 'n ander module/werkstuk nie.
I declare that the work contained in this assignment, except where otherwise stated, is my original work and that I have not previously (in its entirety or in part) submitted it for grading in this module/assignment or another module/assignment.

14774607 **Studentenommer / *Student number***	**Handtekening / *Signature***
J van der Merwe **Voorletters en van / *Initials and surname***	23 November 2017 **Datum / *Date***

Abstract

Development of a patient-specific unicompartmental knee replacement

J. van der Merwe

Dissertation: PhD

March 2018

Patient-specific Unicompartmental Knee Replacements (UKRs) could potentially restore an Osteoarthritic (OA) knee closer to its pre-pathological state than off-the-shelf products. Nevertheless, the current state-of-the-art is still heavily reliant on a technician's interpretation and skill in order to reproduce healthy geometries. This dissertation therefore focused on developing a reliable, semi-automated approach to implant design. Inter-patient variability and inter- and intra-observer agreement and reliability was studied for a set of landmarks defined on the distal femur and proximal tibia. This provided necessary input to downstream processes. The variation in a populations' knees was captured by Statistical Shape Models (SSMs), and the subsequent use of a Graphical User Interface (GUI) was investigated to incorporate local constraints as part of sparse SSM estimation. These estimates formed the base of the implants' femoral components, and together with matching metal-backed, motion-guided tibial components were created using automated B-spline parametrisations. Sixteen unseen knees were used as test candidates and it was found that the resulting condyle estimations were sufficiently accurate, while the generated implant components matched normal knee anatomy. Both the GUI-based estimation and the automated design process showed good repeatability. The implant design presented here is ready for pre-clinical testing and evaluation.

Uittreksel

Ontwikkeling van 'n patientspesifieke unikompartementele knie vervanging

J. van der Merwe

Proefskrif: PhD

Maart 2018

Pasiëntspesifieke Unikomaptementele Knie Vervangings (UKVs) kan moontlik 'n Osteoartritiese (OA) knie nader aan sy voorpatologiese toestand herstel as van-die-rak produkte. Nietemin, die huidige stand-van-die-kuns is steeds sterk afhanklik van die tegnikus se interpretasie en vaardigheid om gesonde geometrieë na te maak. Hierdie proefskrif het dus gefokus op die ontwikkeling van 'n betroubare, semi-automoatiese benadering tot implantaat ontwerp. Inter-pasiënt veranderlikheid en inter- en intra-waarnemer ooreenkoms en betroubaarheid is bestudeer vir 'n stel landmerke wat op die distale femur en proximale tibia gedefinieer is. Dit het die nodige insette vir afstroomprosesse verskaf. Die variasie in 'n populasie se knieë is gevang deur Statistiese Vormmodelle (SVs), en die daaropvolgende gebruik van 'n Grafiese Gebruikerskoppelvlak (GGK) is ondersoek om lokale beperkinge in te sluit as deel van 'n yl SV-skatting. Hierdie skattings het die basis van die implantate se femorale komponente gevorm, en is geskep met behulp van geoutomatiseerde B-spline parametrisasies tesaam met die ooreenstemmende metaalgesteunde, bewegingsgeleide tibiale komponente. Sestien versteekte knieë is as toetskandidate gebruik en daar is bevind dat die resulterende kondiele-skattings akkuraat genoeg was terwyl die gegenereerde implantaat-komponente ooreenstem met normale knie anatomie. Beide die GGK-gebaseerde skattings en die outomatiese ontwerpproses het goeie herhaalbaarheid getoon. Die implantaat ontwerp wat ons hier aanbied is gereed vir voor-kliniese toetsing en evaluering.

Acknowledgements

I would like to thank the Medical Research Council for funding this work. Specifically Tony Bunn and Giovanni Milandri, for their management support.

My sincerest appreciation to the late Prof. C. Scheffer, for making it all possible and providing valuable advice, guidance and mentorship.

Of course, thank you also Dr. Dawie van den Heever, for filling those big shoes and the wholehearted support as both colleague and promoter.

Dr. P. Erasmus, for always making time, for your invaluable guidance and honest interest in my work.

To my friends at BERG, thank you for sharing all the ups and downs of academic life, and thank you for all those cups of coffee.

My parents, Cobus and Carin, my heartfelt gratitude for the start you've given me in life. I wouldn't be here today if it weren't for your support.

And finally, last but certainly not the least, my wife Leigh. You were there for me through thick and thin, thank you so much for your patience and unconditional love and support.

Dedications

To Him Whose mercies are new every morning

Table of contents

List of figures

List of tables

Nomenclature

Abbreviations

2D	Two Dimensional
3D	Three Dimensional
ACL	Anterior Cruciate Ligament
ANOVA	Analysis of Variance
AP	Antero-Posterior
B-splines	Basis splines
BERG	Biomedical Engineering Research Group
CAD	Computer Assisted Design
CAM	Computer Assisted Manufacturing
CC	Cranio-Caudal
CoCr	Cobalt-Chrome
CPD	Coherent Point Drift
CT	Computed Tomography
DESS	Dual Echo Steady State
DOF	Degrees of Freedom
EM	Expectation Maximisation
FA	Face Array
FE	Flexion-Extension
FEA	Finite Element Analysis
FFC	Flexion Facet Center

GCA	Geometric Center Axis
GDP	Gross Domestic Product
GMM	Gaussian Mixture Model
GPA	Generalised Procrustes Analyses
GUI	Graphical User Interface
HTO	High Tibial Osteotomy
ICC	Intra-class correlation coefficient
ICP	Iterative Closest Point
IE	Internal-External
LCL	Lateral Collateral Ligament
MCL	Medial Collateral Ligament
MIS	Minimally Invasive Surgery
ML	Medio-Lateral
MRI	Magnetic Resonance Imaging
OA	Osteoarthritis
OAI	Osteoarthritis Initiative
P	Point
PA	Point Array
PCA	Principle Component Analysis
PDM	Point Distribution Model
PEA	Posterior Epicondylar Axis
RMSD	Root Mean Square Distance
ROI	Region of Interest
SEA	Surgical Epicondylar Axis
SOM	Self Organising Map
SSA	Statistical Shape Analysis
SSM	Statistical Shape Model

STL	Stereolithography
SVD	Singular Value Decomposition
TKA	Total Knee Arthroplasty
TKR	Total Knee Replacement
UHMWPE	Ultra-High-Molecular-Weight Polyethylene
UKA	Unicompartmental Knee Arthroplasty
UKR	Unicompartmental Knee Replacement

Annotations

c	Triangle corner
$c.n$	Next corner
$c.o$	Opposite corner
$c.o.n$	Next corner to $c.o$
$c.o.p$	Previous corner to $c.o$
$c.p$	Previous corner
$c.t$	Triangle index of corner
fAC	femoral Anterior Condyle
fAPLd	femoral Antero-Posterior Lateral distance
fAPMd	femoral Antero-Posterior Medial distance
fAr	femoral Anterior radius
fAS	femoral Articular Surface
fCS	femoral Cartilage Surface
fFS	femoral Full Shape
fGc	femoral Geometric center
fINA	femoral Intercondylar Notch Apex
fLDP	femoral Lateral Distal Point
fLE	femoral Lateral Epicondyle
fLPC	femoral Lateral Posterior Condyle

fLPCc	femoral Lateral Posterior Condyle center
fLPP	femoral Lateral Posterior Point
fLr	femoral Lateral radius
fLTP	femoral Lateral Trochlea Peak
fLTS	femoral Lateral Terminal Sulcus
fMDP	femoral Medial Distal Point
fME	femoral Medial Epicondyle
fMLAa	femoral Medio-Lateral Anterior angle
fMLDa	femoral Medio-Lateral Distal angle
fMLPa	femoral Medio-Lateral Posterior angle
fMPC	femoral Medial Posterior Condyle
fMPCc	femoral Medial Posterior Condyle center
fMPP	femoral Medial Posterior Point
fMr	femoral Medial radius
fMS	femoral Medial Sulcus
fMTP	femoral Medial Trochlea Peak
fMTS	femoral Medial Terminal Sulcus
fTEd	femoral Trans Epicondylar distance
fTG	femoral Trochlear Groove
fTGc	femoral Trochlear Groove center
tAPd	tibial Antero-Posterior distance
tAS	tibial Articular Surface
tAT	tibial Anterior Tubercle
tFS	tibial Full Shape
tGc	tibial Geometric center
tGCd	tibial Geometric Centre distance
tLC	tibial Lateral Condyle

tLCc	tibial Lateral Condyle center
tLCR	tibial Lateral Cortical Rim
tLPa	tibial Lateral Posterior angle
tLPP	tibial Lateral Posterior Point
tLr	tibial Lateral radius
tLS	tibial Lateral Spine
tLTP	tibial Lateral Transverse Point
tLVa	tibial Lateral Varus angle
tMC	tibial Medial Condyle
tMCc	tibial Medial Condyle center
tMCR	tibial Medial Cortical Rim
tMCRc	tibial Lateral Cortical Rim center
tMCRc	tibial Medial Cortical Rim center
tMLd	tibial Medio-Lateral distance
tMPa	tibial Medial Posterior angle
tMPP	tibial Medial Posterior Point
tMr	tibial Medial radius
tMS	tibial Medial Spine
tMTP	tibial Medial Transverse Point
tMVa	tibial Medial Varus angle
tSC	tibial Spine Center

Symbols

$\mathbf{a}$	Triangle area array	[mm^2]
A	Mesh area	[mm^2]
$\mathbf{b}$	Parameter vector	[u.l.]
$\mathbf{C}$	Covariance matrix	[mm^2]
$\mathbf{c}$	Triangle aspect ratio	[u.l.]

$\mathbf{C}_i$	Inner covariance matrix	[mm^2]
$\mathbf{C}_p$	Posterior covariance matrix	[mm^2]
$\mathbf{D}$	Discrete difference matrix	[u.l.]
d	Number of dimensions	[u.l.]
$\tilde{\mathbf{E}}$	Blended penalty matrix	[u.l.]
$\mathbf{E}$	Penalty matrix	[u.l.]
$\mathbf{e}$	Edge vector	[mm]
E	Energy function	[u.l.]
$\mathbf{F}$	Low pass filter transfer function	[u.l.]
$\mathbf{f}$	Face connectivity array	[u.l.]
f_c	Corresponding point set scale factor	[u.l.]
f_d	Ratio between motion smoothing and data fitting	[u.l.]
f_k	Gaussian kernel width	[mm]
f_n	Expected noise factor	[u.l.]
f_n	Negative scale factor	[u.l.]
f_p	Positive scale factor	[u.l.]
f_r	Sampling density factor	[u.l.]
f_s	Scale factor	[u.l.]
f_t	Target point set scale factor	[u.l.]
$\mathbf{f}_u$	Updated face array	[u.l.]
f_{pd}	Poisson disk sampling factor	[u.l.]
$\mathbf{G}$	Gaussian kernel	[u.l.]
$\mathbf{H}$	Hessian matrix	[u.l.]
H	Mean curvature	[u.l.]
$\mathbf{h}_v$	Per vertex importance function	[u.l.]
$\mathbf{h}_{mc}$	Per sample importance function	[u.l.]
$\mathbf{I}$	Identity matrix	[u.l.]

ICC	Intra-class correlation coefficient	[u.l.]
ICC_o	Inter-observer reliability	[u.l.]
ICC_w	Intra-observer reliability	[u.l.]
$\mathbf{k}$	Gaussian curvature array	[u.l.]
K	Gaussian curvature	[u.l.]
k_1	Minimum principle curvature	[u.l.]
k_2	Maximum principle curvature	[u.l.]
$\mathbf{k}_u$	Knot vector	[u.l.]
k_{pb}	Pass band frequency	[u.l.]
$\mathbf{L}$	Linear map	[u.l.]
$\mathbf{l}$	Region of interest vertex labels	[u.l.]
$l_{1,2,3}$	Triangle side lengths	[mm]
$\mathbf{M}$	Blended basis function matrix	[u.l.]
$\mathbf{N}$	Basis function matrix	[u.l.]
$\mathbf{n}$	Normal vector	[mm]
$\mathbf{n}_d$	Direction vector	[mm]
n_F	Number of smoothing iterations	[u.l.]
n_f	Number of faces	[u.l.]
n_k	Number of retained eigenvectors	[u.l.]
n_m	Number of randomly generated model instances	[u.l.]
n_q	Number of data points	[u.l.]
$\mathbf{N}_R$	Residual\Noise matrix	[mm]
n_r	Number of reference points	[u.l.]
n_s	Number of model shapes	[u.l.]
n_t	Number of target points	[u.l.]
n_v	Number of vertices	[u.l.]
n_{ku}	Number of knots in the u direction	[u.l.]

n_{kv}	Number of knots in the v direction	[u.l.]
n_{mc}	Number of Monte Carlo samples	[u.l.]
n_{pd}	Number of desired Poisson disk samples	[u.l.]
n_{Pu}	Number of control points in the u direction	[u.l.]
n_{Pv}	Number of control points in the v direction	[u.l.]
n_P	Number of control points	[u.l.]
n_{Qu}	Number of data points in the u direction	[u.l.]
n_{Qv}	Number of data points in the v direction	[u.l.]
n_{v_j}	Number of vertices in neighbourhood	[u.l.]
$\mathbf{O}$	Circulant matrix	[u.l.]
$\mathbf{o}$	Corner table opposing indices	[u.l.]
$\mathbf{P}$	Control polygon/net	[mm]
p_u	B-spline degree in the u direction	[u.l.]
p_v	B-spline degree in the v direction	[u.l.]
$\hat{\mathbf{q}}$	Adjusted point set	[mm]
$\mathbf{Q}$	Grid of data points	[mm]
$\mathbf{q}$	Data point array	[mm]
$\mathbf{R}$	Rotation matrix	[u.l.]
$\mathbf{r}$	Radii array	[mm]
r	Radius	[mm]
r_c	Correlation coefficient	[u.l.]
$\mathbf{t}$	Translation array	[mm]
t	Projection offset	[u.l.]
$\mathbf{U}$	Eigenvector matrix	[mm]
$\mathbf{u}_e$	Eigenvectors	[mm]
$\mathbf{U}_p$	Posterior eigenvector matrix	[mm]
$\mathbf{u}_u$	B-spline parameter vector	[u.l.]

$\bar{\mathbf{v}}$	Arithmetic mean of point set	[mm]
$\grave{\mathbf{v}}$	Mapped vertex coordinate	[mm]
$\tilde{\mathbf{v}}$	Penalised and adjusted point set	[mm]
$\mathbf{V}$	Right singular unitary matrix	[mm]
$\mathbf{v}$	Vertex array	[mm]
$\mathbf{v}_a$	Aligned point set	[mm]
$\mathbf{v}_c$	Corresponding point set	[mm]
$\mathbf{v}_f$	Faired point set	[mm]
$\mathbf{v}_m$	Procrustes mean point set	[mm]
$\mathbf{v}_o$	Ray origin	[mm]
$\mathbf{v}_p$	Projected point set	[mm]
$\mathbf{v}_r$	Reference point set	[mm]
$\mathbf{v}_t$	Target point set	[mm]
$\mathbf{v}_u$	Updated point array	[mm]
$\mathbf{v}_{mc}$	Monte Carlo samples	[mm]
$\mathbf{v}_{pd}$	Poisson disk samples	[mm]
$\mathbf{W}$	Weight matrix	[u.l.]
$\mathbf{w}$	Corner table vertex indices	[u.l.]
$\bar{\mathbf{x}}$	Concatenated Procrustes mean point set	[mm]
$\bar{\mathbf{x}}_p$	Concatenated posterior Procrustes mean point set	[mm]
$\tilde{\mathbf{x}}$	Approximated point set	[mm]
$\mathbf{x}$	Concatenated point set	[mm]
$\mathbf{y}$	Input data	[mm]
$\Delta\mathbf{X}$	Centred training matrix	[mm]
η	Regularisation term	[u.l.]
$\mathbf{\Lambda}$	Eigenvalue matrix	[u.l.]
λ_e	Eigenvalues	[u.l.]

$\mathbf{\Lambda}_i$	Posterior eigenvalue matrix	[u.l.]
$\mathbf{\Sigma}$	Singular value matrix	[u.l.]
σ_b	Inter-subject standard deviation	[mm]
σ_E	Standard error of the estimate	[mm]
σ_M	Standard error of the mean	[mm]
σ_o	Inter-observer standard deviation	[mm]
σ_w	Intra-observer standard deviation	[mm]
σ_G	Standard error of generality	[mm]
σ_S	Standard error of specificity	[mm]
τ_c	Aspect ratio degradation tolerance	[u.l.]
τ_d	Dihedral angle change tolerance	[°]
χ^2	Chi-squared distribution	[u.l.]
ψ	Displacement function	[mm]

1. Introduction

1.1 Background

Osteoarthritis (OA) is a group of diseases that results in the deterioration of synovial joints, and is typically characterized by pain and reduced joint functionality (Garstang and Stitik, 2006; Martin and Buckwalter, 2002). The total cost of treatment thereof has been estimated at between 1 to 2.5% of first-world countries' Gross Domestic Product (GDP) (March and Bachmeier, 1997). In particular, OA of the hip and knee has been ranked as the 11$^{\text{th}}$ highest contributor to global disability, with OA of the knee having the greater global age standardised prevalence of the two, estimated at 3.8% (Cross *et al.*, 2014). Therefore, much effort is being expended in the study of the knee in order to improve diagnosis, treatment and prevention of OA (Buckwalter *et al.*, 2004; Peterfy *et al.*, 2008; Eckstein *et al.*, 2014). Indeed, the concepts upon which modern knee arthroplasty is based may be traced back as far as Thermostocles Gluck's lectures in Berlin during 1890 (Callaghan, 2003). The ensuing decades have seen knee replacement surgery develop extensively, and it has become a common method used for treating joint degradation. During 2004 nearly half a million primary knee arthroplasties were performed in the United States alone (Riddle *et al.*, 2008), with projections exceeding three million procedures by 2030 (Kurtz *et al.*, 2007).

1.2 Motivation

Despite their prevalence, knee implants have some shortcomings that stem primarily from discrepancies between their standardised geometries and those of the patients' joints (Demange *et al.*, 2015; Fitz *et al.*, 2013; Van den Heever *et al.*, 2012*b*). Complications include soft tissue impingement, subsidence, implant loosening and increased likelihood of post-operative joint pain (Chau *et al.*, 2009; Fitzpatrick *et al.*, 2008; Mahoney and Kinsey, 2010). For localised OA, Unicompartmental Knee Arthroplasty (UKA) is preferred over Total Knee Arthroplasty (TKA) where the entire joint is replaced as UKA may result in faster recovery rates and improved post operative joint kinematics (Newman *et al.*, 1998; Patil *et al.*, 2005). However, since UKA is essentially a partial

resurfacing of only the diseased portion of the joint, it naturally requires much greater compatibility with the remaining structures of the patient's knee, which is only undermined by the aforementioned issues.

It has been suggested that patient-specific implants may be able to address these problems (Fitz, 2009; Van den Heever, 2011), especially considering that recent advances in additive manufacturing technologies continue to make customised solutions more cost effective (Harrysson and Cormier, 2006). A method for designing such an implant has previously been developed and patented by Stellenbosch University's Biomedical Engineering Research Group (BERG). Basis splines (B-splines) were used in order to investigate the Antero-Posterior (AP) curvature of the distal femoral condyles (Kosel *et al.*, 2010). Several different methods of parameterising said curvature presented in literature were subsequently compared, and B-splines were indeed found to be the most accurate (Van den Heever *et al.*, 2011*b*). Self Organising Maps (SOMs) were then used to estimate non-pathological measurements and geometry of diseased joints (Van Schalkwyk, 2010; Van den Heever, 2011), as part of a method to select the femoral component for TKA (Van den Heever *et al.*, 2011*a*), and to investigate gender and race differences in distal femoral morphology (Van den Heever *et al.*, 2012*a*). Finally, a SOM algorithm was also used to estimate B-spline parameters describing healthy cartilage geometry as part of the design methodology for a patient-specific Unicompartmental Knee Replacement (UKR) (Scheffer *et al.*, 2010; Van den Heever *et al.*, 2012*b*). The validity of the method has been demonstrated by the work of Van den Heever (2011), although with the following limitations:

- The parametrised Region of Interest (ROI) is greatly depended on manual user input, resulting in variability of the design procedure.
- The healthy shape estimates were limited to localised planar sections, disregarding features apparent only in three dimensions.

1.3 Aim and objectives

The aim of the current work was therefore to create a *repeatable* method for designing a patient-specific implant that adequately reproduces an individual's healthy knee *surfaces* in order to facilitate natural post-operative joint kinematics. In particular, our objectives were to:

- investigate and model healthy knee joint geometry,
- develop reliable surface-based estimations of pre-defined pathological geometries, and
- standardise and automate the implant design process.

1.4 Overview

A brief introduction to the knee and UKRs is given in Chapter 2. This is followed by a detailed investigation of the knee's local landmark variation in Chapter 3, while Chapter 4 focuses on capturing its global shape variation via Statistical Shape Modelling (SSM). Chapter 5 uses these models in order to estimate predefined, healthy ROIs that relate to the pathological geometries replaced during UKA. Chapter 6 describes a semi-automated implant design approach based on B-spline parametrisations, and Chapter 7 ends off with final remarks.

The work contained in the Appendices are not crucial to the understanding of the main contributions of this dissertation, but nevertheless discuss important theory and algorithms upon which it is based. Appendix A presents an overview of Statistical Shape Analysis (SSA), which is used throughout Chapters 3 to 5. Appendix B presents various mesh handling algorithms derived from current best practices in literature, and culminates in a direct mesh re-sampling algorithm which plays a crucial role during shape model pre-processing. Finally, Appendix C discusses the B-spline parametrisation methods which form the cornerstone of the semi-automated design process.

1.5 Conclusions

To conclude, the method developed combines a number of concepts from the current state-of-the art into a novel UKR design that is *patient-specific*, *anatomically accurate*, reproduces *normal knee motion* and is ultimately *repeatable*. Additional original contributions, apart from the design in Chapter 6, includes:

- a report on the most suitable landmarks to use in conjunction with scan-based reconstructions of the knee (Chapter 3),
- a study on the shape variation specific to knee ROIs replaced during UKA (Chapter 4),
- an evaluation of knee SSMs at the hand of local morphological measurements (Chapter 4), and
- an investigation on the repeatability of posterior/constrained statistical shape estimation (Chapter 5).

The topic was suggested and promoted by the late Prof. C. Scheffer, the previous head of BERG. Dr. D. van den Heever, who developed the initial prototype, initially acted as co-supervisor and eventually as promoter. Dr. P. Erasmus, one of the leading knee specialists in South Africa, acted as consultant and appeared as co-author on the papers resulting from the research. Funding was obtained from the Medical Research Council of South Africa for the duration of the study.

2. The knee

2.1 Functional anatomy

As per Palastanga *et al.* (2006), the knee is the largest and one of the most complex joints in the human body, a synovial bicondylar hinge joint with tibiofemoral and patellofemoral articulation. It is made up of the femur, tibia, fibula and patella. Stability is provided by the collateral and cruciate ligaments, as well as the muscles crossing the joint. Menisci, or semilunar cartilages, are attached to the periphery of the tibia's condyles. The menisci's functions include increasing the congruence of the tibiofemoral joint, weight-bearing and load transfer, shock absorbance and lubrication. The articulating surfaces of the femur, tibia and patella are covered with hyaline cartilage, providing a smooth surface which facilitates movement as well as providing limited elasticity for offset and shock absorbance. The entire joint is encased in a synovial membrane, which secretes a fluid that supplies nourishment and acts as lubricant. Figure 2.1 illustrates the anatomy of the knee.

2.2 Anatomic references

A number of definitions and anatomic references used throughout this work are listed in Table 2.1 and illustrated in Figure 2.2. Note that these definitions are not absolute or measurable, but merely descriptive.

2.3 Articular surfaces

The articulating surface of the femur is subdivided into three compartments, namely the medial and lateral condyles, and the trochlear groove (Palastanga *et al.*, 2006). The condyles of the femur rest on those of the tibia, while the trochlear groove opposes the articulating surface of the patella. The junction of the patellar and tibial cartilage is defined by a faint sulcus on each side. Laterally, this sulcus is almost transverse, while its medial counterpart is oblique and begins more anteriorly. The shapes of the condyles in a Medio-Lateral (ML) direction are convex, and generally matches the concavity of the opposing tibial condyles. In the sagittal plane, the radii and centres of the

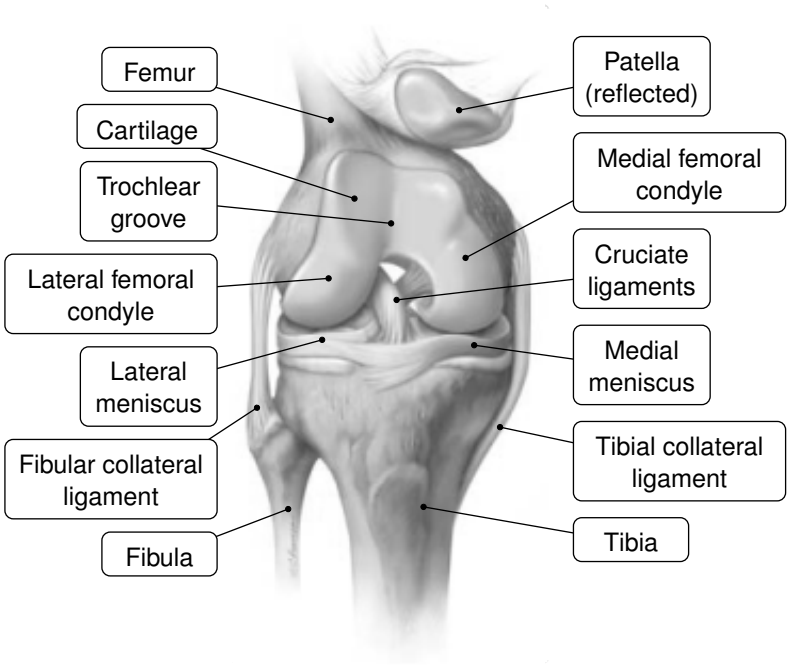

Figure 2.1: Anatomy of the knee (Illustration: 2001 Christy Krames)

Table 2.1: Anatomic reference terms

	Term	Definition
Planes	Coronal	Vertical plane dividing the body into front and back
	Sagittal	Vertical plane dividing the body into left and right
	Transverse	Horizontal plane dividing the body into upper and lower
Translations	Anterior	Forwards
	Posterior	Backwards
	Medial	Toward the middle or inside
	Lateral	Toward the outside, left or right
	Superior	Above
	Inferior	Below
	Proximal	Towards the beginning or torso
	Distal	Further from the beginning or torso
Rotations	Abduction	Motion away from mid-line of body
	Adduction	Motion towards mid-line of body
	Flexion	Motion decreasing joint angle
	Extension	Motion increasing joint angle
	Internal	Inward rotation
	External	Outward rotation
	Varus	Inward turning of bone (bow-legged)
	Valgus	Outward turning of bone (knock-kneed)

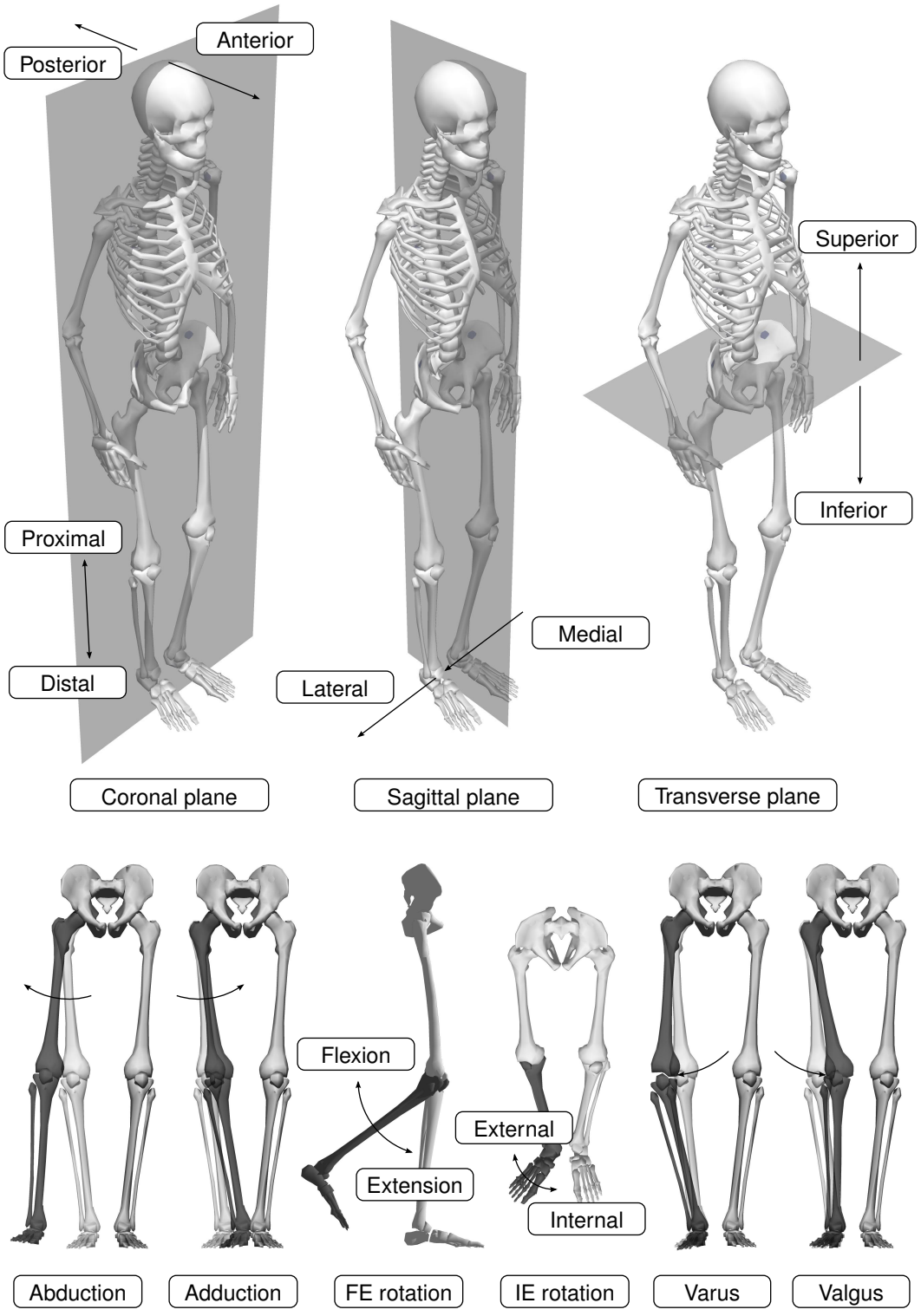

Figure 2.2: Anatomic references of the human body (Illustration: J. v.d. Merwe)

condyle curvatures vary. Furthermore, each condyle becomes flatter anteriorly, and each have different curvature radii. Finally, the trochlear groove is well-marked, with the lateral area it delimits larger and more prominent than the medial. The trochlear groove terminates at the intercondylar notch.

The cartilage on the tibial condyles are separated by the intercondylar eminence and posterior and anterior triangular regions. The entire articulating surface is inclined postero-inferiorly 3-5° with respect to the transverse plane. The medial condyle is the larger and is slightly concave, while the lateral side is concave coronally, but convex in the sagittal plane.

2.4 Tibiofemoral joint motion

Movement of the knee occurs in all six Degrees of Freedom (DOF). Due to this complexity it is classified as a modified hinge joint, as opposed to a pure one (Palastanga *et al.*, 2006). There are two separate articulations taking place during movement of the knee. The first is that between the femur and tibia, which varies the length of the lower limb. Movement of the femoral condyles with respect to those of the tibia is a combination of rolling and gliding. The second is the articulation between the femur and the patella, in which the patella acts as a bearing surface and a lever for the quadriceps tendon (Krevolin, 2003).

The primary motion of the knee is considered to be the Flexion-Extension (FE) of the tibiofemoral joint. In general, the FE axis of rotation as well as the contact areas between the femoral and tibial condyles move anteriorly during extension, and posteriorly during flexion, relative to the tibia. This may be ascribed to the constantly changing radii of the respective condyles interacting with the cruciate ligaments akin to a four-bar linkage (Palastanga *et al.*, 2006; Smith *et al.*, 2003). Still, the FE arc may be divided into three sections, as shown in Figure 2.3. These are classified according to their modes of articulation, namely the active functional, passive and terminal extension arcs.

The active functional arc, extending between 10°/20° and 110°/120°, is so named because it is entirely under active muscle control, and is most used during everyday activities (Freeman, 2001). During FE within the active arc the medial femoral condyle's motion is small compared to that of the lateral condyle, resulting in Internal-External (IE) rotation of the femur relative to the tibia (Freeman *et al.*, 2005). Apart from the interaction between motion of the pelvis and the hip as well as the angle between the lower limb's mechanical and anatomic axes, when considering the knee in particular we may ascribe IE rotation to the following mechanisms (Palastanga *et al.*, 2006):

- The medial femoral condyle rests within its concave counterpart on the tibia, while the lateral tibial condyle is convex, allowing the lateral

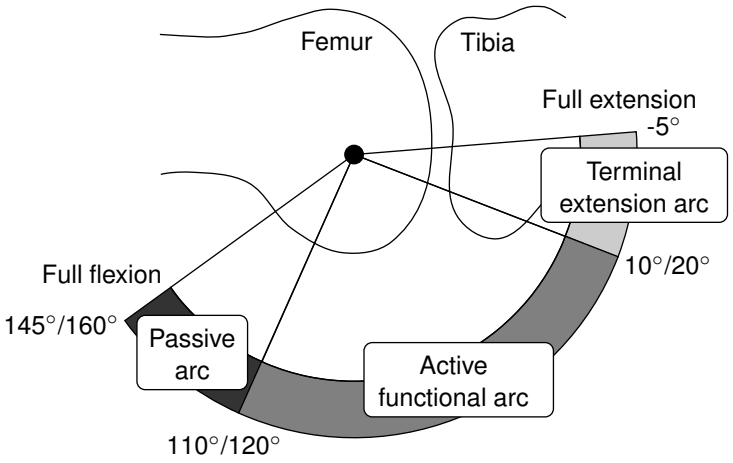

Figure 2.3: Knee FE arc, sagittal view (Adapted from Freeman (2001))

femoral condyle to glide over its surface.

- The medial femoral condyle rests against the medial tubercle, while the lateral side is less constrained in this manner.
- The fixation and direction of the collateral ligaments causes the Lateral Collateral Ligament (LCL) to become stretched sooner than the Medial Collateral Ligament (MCL).

The region between -5° at hyperextension and 10°/20° is known as the terminal extension arc. The medial femoral condyle continues to remain relatively antero-posteriorly static, though contact between it and the tibia moves anteriorly on the femur via pure gliding as the knee is extended (Freeman, 2001). Laterally, the femoral condyle rolls in an anterior direction, thereby continuing the internal rotation of the femur relative to the tibia (Freeman *et al.*, 2005). Here the rotation is due to the Anterior Cruciate Ligament (ACL) becoming stretched (Palastanga *et al.*, 2006). As the knee approaches terminal extension, the tension in the ligaments increase until it eventually locks, known as screw home (Smith, 1956). In this position no accessory movement is possible, and maximum contact between the condyles of the tibia and femur exists. The knee is now in its most stable position. Conversely, during the initial stages of flexion from the fully extended position, external rotation of the femur is affected by the action of the popliteus, flexors gracilis, sartorius and semitendinosus (Palastanga *et al.*, 2006).

Within the passive arc, ranging from 110°/120° to 145°/160°, continued flexion may only occur under external stimulus (Freeman, 2001). This happens during actions such as kneeling and squatting, to the extent that the posterior soft muscles allow. At extreme flexion angles lift-off may be experienced by the medial femoral condyle, while the lateral femoral condyle becomes posteriorly subluxed (Nakagawa *et al.*, 2000). Relative rotation of the femur with respect to the tibia during passive flexion depends on the type of activity performed.

Finally, it should be noted that the menisci also move and deform during FE. As the knee flexes, both lateral and medial menisci move posteriorly, with the lateral translating further than the medial. The lateral meniscus is also subject to greater distortion. Their movement is due to the passive action of the femoral condyles, as well as various fibres and ligaments (Palastanga *et al.*, 2006).

2.5 Osteoarthritis and arthroplasty

One of the most common causes of arthritis is degeneration of the joint cartilage and underlying bone, a condition known as Osteoarthritis (OA). While OA is not necessarily an inevitable consequence of aging, there is a strong association. Aging cartilage undergoes fraying, softening, loss of matrix tensile strength and stiffness - all factors contributing to the risk of OA (Martin and Buckwalter, 2002). Post-traumatic OA, on the other hand, is progressive joint degradation following physical injury, affecting young, middle-aged, as well as elderly patients (Buckwalter and Brown, 2004). All of these diseases are characterised by joint pain and loss of function, and treatment depends on relevant patient selection criteria. High Tibial Osteotomy (HTO), Unicompartmental Knee Arthroplasty (UKA) and Total Knee Arthroplasty (TKA) are discussed below.

HTO is a surgical procedure during which the proximal tibia is partially sectioned and repositioned in order to change the joint's alignment, usually indicated for younger, more active patients. However, while HTO may restore a greater post-operative range of motion, UKA exhibits faster recovery rates, better functional results, lower revision rates, fewer complications and less post-operative pain (Santoso and Wu, 2017; ZhenWu Cao *et al.*, 2017). Furthermore, revision to TKA is less demanding from UKA than it is from HTO (Dettoni *et al.*, 2010; Lim *et al.*, 2017).

During UKA the articular surfaces of a single femoral and corresponding tibial condyle are replaced, as shown in Figure 2.4. Its popularity has increased in recent years in part due to its suitability to the mini-incision technique (Laskin, 2001). In conjunction with this, additional benefits that UKA has over TKA is the preservation of bone, less soft tissue damage, faster recovery, improved range of motion and lower cost (Callahan *et al.*, 1995; Newman *et al.*, 1998; Price *et al.*, 2001; Shakespeare and Jeffcote, 2003). Despite these advantages, patient selection criteria for UKA is particularly strict, resulting in a relatively small number of procedures performed (Stern *et al.*, 1993; Riddle *et al.*, 2008). As per Kozinn and Scott (1989) these criteria include:

- Arthritis isolated to a single compartment
- Low required levels of post-operative activity
- Weight below 82 kg

- Over 60 years of age
- Minimal pain experienced during rest
- More than 90° of flexion
- Less than 15° of angular deformity
- Absence of inflammatory arhtropathy
- Intact cruciate ligaments

However, it is worth noting that there is some controversy regarding stringent adherence to criteria such as age, obesity and activity level based on recent evidence (Hamilton *et al.*, 2017; Jones *et al.*, 2017; Palumbo and Scott, 2014).

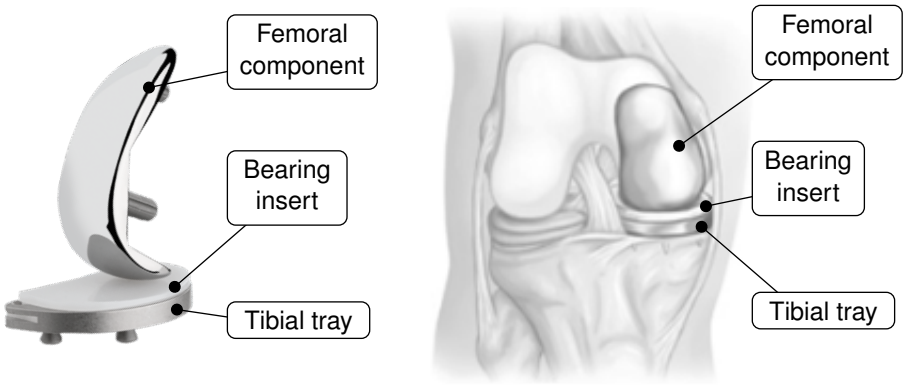

(a) Zimmer High-Flex Knee System (Photo: Zimmer, Inc (2014))

(b) *In-vivo* (Illustration: American Academy of Orthopaedic Surgeons (1995))

Figure 2.4: Unicompartmental knee implant

TKA is a procedure in which all three compartments of the knee are replaced. As shown in Figure 2.5, these are the medial and lateral condyles of the distal femur and proximal tibia, as well as the trochlear groove and patellar cartilage. Either one, or both cruciate ligaments may be resected, depending on the design of the implant. Mancuso *et al.* (1996) lists severe non-localised pain, osteo- or rheumatoid arthritis and joint instability as indications for TKA. As mentioned previously, TKA is performed much more often than UKA, in apparent contradiction to the precedence UKA receives within younger patients. This is due to the fact that implants are more likely to fail within the lifetime of a younger patient (Weale *et al.*, 2001). Finally, revision of primary UKA to TKA is preferable to primary TKA revision (Saldanha *et al.*, 2007).

Other variations on the theme of knee arthroplasty are also available, allowing the surgeon to tailor the treatment to the specific needs of the patient. An example is bi-unicompartmental knee arthroplasy, in which two UKRs are used to replace the articulating surfaces of both the medial and lateral tibiofemoral compartments. Bicompartmental knee implants, on the other hand, replace

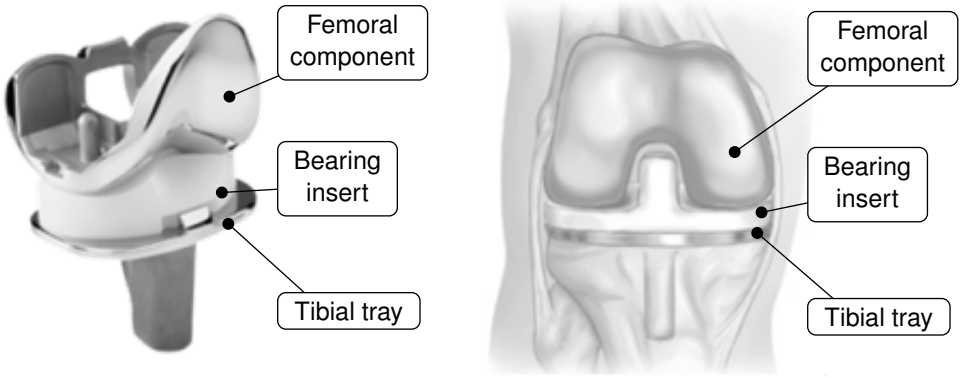

(a) Zimmer LPS Flex Mobile Knee (Photo: Zimmer, Inc (2014))

(b) *In-vivo* (Illustration: American Academy of Orthopaedic Surgeons (1995))

Figure 2.5: Total knee implant

either the medial or lateral tibiofemoral condyle, as well as the cartilage associated with the patellofemoral joint. The potential advantages are the same as for UKA when compared to TKA, though without the limitation of replacing just one compartment (Jemmett and Roy, 2016; Sabatini *et al.*, 2016).

2.6 UKR design

Figure 2.6 shows a stylised representation of a contemporary UKR. Such designs are for the most part based on a universal 'template', which consist of a femoral component articulating against a tibial one. Variations in design typically do not occur on this macro-concept scale, but rather within the respective features. The primary features are the articular surfaces, bone-implant interfaces, mobility and method of fixation.

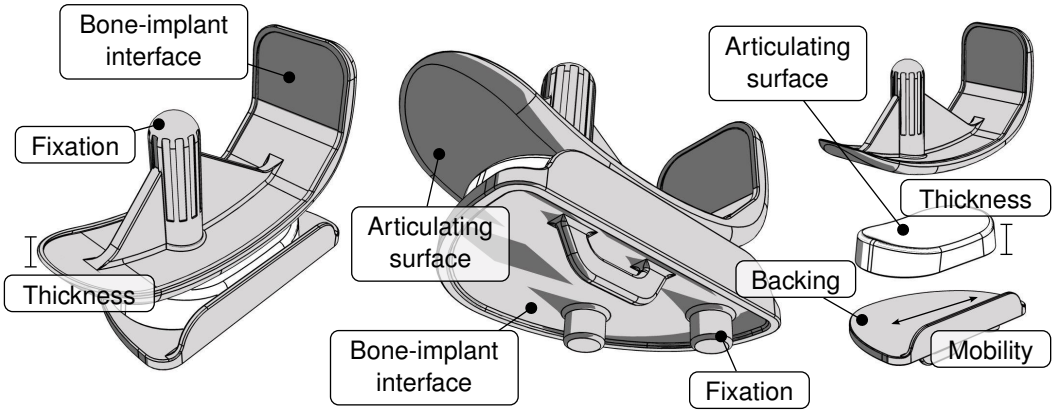

Figure 2.6: UKR design features (Illustration: J. v.d. Merwe)

2.6.1 Alignment

The objective during UKA is to restore a patient's pre-pathological joint alignment and intra-articular spacing (Scuderi and Tria, 2009). Since the disease is unilateral, the correction must also be unilateral. It is important to preserve the original biomechanical relationships between the geometries and ligaments. Assuming that the ligaments have not contracted during the progression of the disease, this may generally be achieved by replacing it with an implant with dimensions and shape that again tension the ligaments.

2.6.2 Anatomical design methodology

Indeed, the anatomical design methodology rests on the premise that the biomechanics of the knee are affected by the joint's geometry (Amiri, 2008; Eckhoff *et al.*, 2005; Van den Heever, 2011). Implant design should therefore attempt to emulate such anatomical geometries of the articulating surfaces in order to properly restore normal alignment and motion to the joint (Nuno *et al.*, 2001; Van den Heever, 2011; Zoghi *et al.*, 1992). The basic movement pattern may be summarised as flexion of the femur about some transverse axis coupled with synchronous tibial rotation about a medially displaced vertical axis (Walker *et al.*, 2009). Morphologically, this is facilitated by the high congruence, and hence stability, of the medial compartment, while the geometry of the lateral tibiofemoral condyles allows for greater AP translation (Amiri, 2008). Since a partial knee replacement procedure inherently requires that the restored geometry be biomechanically compatible with the remaining structures, a focus emphasised in patient-specific applications, an anatomical design methodology is adopted here.

2.6.3 Femoral component

Parametrisations of the distal femur's articulating surfaces may be classified as either planar or surface-based. Planar parametrisations consider the femoral geometry in a single plane only, typically the sagittal. On the other hand, surface-based approximations consider topological variations in all three dimensions. These parametrisations may be subdivided further into geometric primitive or free-form categories. The geometric primitive category typically fits arcs, spheres, etc. to the distal femur, while free-form representation employ mathematical functions to describe the articulating geometry.

Geometric primitive planar parametrisations in literature include fitting circles or circular arcs (Cobb *et al.*, 2008; Hollister *et al.*, 1993; Iwaki *et al.*, 2000; Martelli and Pinskerova, 2002), ellipses (Biščević *et al.*, 2005), involutes of a circle and Archimedean and logarithmic spirals (Rehder, 1983). Free-form parametrisations include polynomials (Van den Heever, 2011) and B-spline curves (Kosel *et al.*, 2010; Van den Heever *et al.*, 2012*a*).

Surface-based geometric primitives such as spheres (Amiri, 2008; Iranpour *et al.*, 2010; Kurosawa *et al.*, 1985; Zoghi *et al.*, 1992) and cylinders (Eckhoff *et al.*, 2005; Koo *et al.*, 2005; Miranda *et al.*, 2010) are often used to represent the posterior portions of the condyles. Walker (1988) and Zoghi *et al.* (1992) extended this methodology to the distal portions of the femur, concluding respectively that these surfaces could be approximated by sections of oblique cones with their bases parallel to the sagittal plane, and partial toroids. Zoghi *et al.* (1992) also fitted a cylinder to the anterior lateral condyle.

Diathrodal joint surfaces parametrised by free-form mathematical formulations include many studies implementing a global bivariate polynomial approximation (Ateshian *et al.*, 1992; Hirokawa *et al.*, 2004; Van Ruijven *et al.*, 1999; Wismans *et al.*, 1980). This method has the advantages of simplicity and higher order continuity (Van Ruijven *et al.*, 1999). Least squares B-spline fitting (Ateshian *et al.*, 1993) has the additional advantage of being both flexible and manageable, especially as implemented in computer assisted design applications (Hirokawa *et al.*, 2004). B-splines, however, require gridded, ordered datapoints for fitting (Ateshian *et al.*, 1993; Piegl and Tiller, 1997). Since many digitization methods of physical entities result in random scattered point clouds, significant preparation is usually required before using B-splines to create the relevant models. Coons (1967) developed a method for bicubic B-spline patch interpolation oft encountered in literature (Ateshian *et al.*, 1991; Hefzy and Yang, 1993; Scherrer and Hillberry, 1979). Though forcing the parametrisation to pass through each digitized point, this method not only has the normal B-spline dataset restrictions, but is additionally limited to first order continuity across the patch boundaries. Second order continuity is a requirement for curvature analysis so that higher order surface derivatives can be computed (Ateshian *et al.*, 1992).

While a major limitation of Two Dimensional (2D) methods is that variations in surface geometry are not adequately represented (Zoghi *et al.*, 1992), they typically result in fewer parameters when compared to their surface-based counterparts. Furthermore, geometric primitives sacrifice versatility and accuracy for simplicity when measured against free-form implementations. Finally, it should be mentioned that fitting via approximation, as opposed to interpolation, yields smoother results. This characteristic is desirable when filtering noise from data, but may result in poorer fidelity when the surface being modelled includes sharp edged or undulating features.

The particular type of parametrisation therefore depends on the application, and category combinations are also possible. An example of such a combination is the Total Knee Replacement (TKR) designed by Amiri (2008). In this case, the medial condyle was approximated by a sphere. The lateral compartment was sectioned by ML planes, along a simplified FE profile. Each of these sections were then parametrised by fitting circular arcs. Finally, B-splines were fitted to the sectioned profiles in order to develop the complete implant geometry.

2.6.4 Tibial component

Tibial components generally consist of either a single, all-polyethylene bearing surface, or a metal-backed insert as shown in Figures 2.6 and 2.7. Early Finite Element Analyses (FEA) have shown that metal-backed components distribute loads more evenly across the bone-implant interface (Bartel *et al.*, 1982; Lewis *et al.*, 1982; Murase *et al.*, 1983). They are also modular, facilitating the surgical procedure and bearing exchange (Hutt *et al.*, 2015). However, their disadvantages include increased cost as well as backside wear between the insert and the metal tray (Cheng *et al.*, 2011). While there is some controversy regarding the clinical outcomes of metal-backed versus all-polyethylene tibial components in TKA (Gudnason *et al.*, 2014; Voss *et al.*, 2016), the latest research suggests that all-polyethylene designs have a higher risk of early failure in UKA through tibial collapse and aseptic loosening, likely due to greater localised stresses (Hutt *et al.*, 2015; Koh *et al.*, 2017*a*).

Metal-backed components are able to accommodate either mobile or fixed bearing inserts. Mobile inserts, such as the Oxford Knee (Biomet UK Limited, Swindon, UK) shown in Figure 2.7(a) have full congruence between the articulating surfaces of the femoral component and insert. Due to the femoral component being spherical, this supports rotation about all three axes, while the flat metal tray accommodates relative AP and ML translation. The theoretical advantages of a mobile over a fixed UKR bearing design are that it results in more natural joint motion and reduced wear, although comparisons in literature do not indicate clear differences in clinical outcomes (Ko *et al.*, 2015; Murphy *et al.*, 2015; Peersman *et al.*, 2015). Normal mobile inserts are also prone to dislocation in the lateral condyle due to large translations compared to the medial (Pandit *et al.*, 2010).

(a) Oxford Partial Knee (Photo: Biomet (2017))

(b) Zimmer High-Flex Knee System (Photo: Zimmer, Inc (2014))

Figure 2.7: Fixed and mobile tibial components

In contrast to mobile designs, full articulation occurs solely between the insert and femoral component of fixed bearings, shown in Figure 2.7(b). Fixed bearing inserts' articulating surfaces are either flat or have varying degrees of congruence. In the latter case, these surfaces are made to accommodate those of the accompanying femoral components in order to minimise polyethelene wear and mimic natural biomechanical joint behaviour (Steklov *et al.*, 2010). A number of TKR designs make use of guided femoral motion to generate matching insert surfaces (Amiri, 2008; Koh *et al.*, 2017*b*; Pejhan *et al.*, 2016; Walker, 1988, 2014), though there does not appear to be any such UKR examples in literature.

2.7 Patient-specific UKRs

Most implant articulating surfaces are based on generic profiles intended to fit the largest population possible (Van den Heever, 2011). Symmetric implant types even disregard the anatomic differences between the medial and lateral condyles in the favour of a simplified design (Demange *et al.*, 2015; Slamin and Parsley, 2012). However, UKRs with patient-specific articulating surfaces have the potential to restore the anatomical surface, and thus the joint kinematics, to a state closer to normal than conventional designs (Fitz, 2009; Van den Heever, 2011). Literature reports relatively few cases of customisation of the articular surfaces. Often, patient-specific designs focus on better sizing, fit and preservation of bone-stock at the bone-implant interface, while the articulating surface remains generic (Lin *et al.*, 2005; Sathasivam *et al.*, 1999). Presented here is a summary of patient-specific UKR designs with customised articular surfaces. The first is that of Van den Heever (2011), who's work is the basis for this study. Second is the iUni® (Conformis, Massachusetts, USA), one of the first commercially available fully customised UKR implants.

Van den Heever (2011) fitted 2D B-spline curves to 60 healthy patients' distal femoral cartilage. For both the medial and lateral condyles, sagittal and transverse sections were parametrised. The cartilage was segmented from Magnetic Resonance Imaging (MRI) scans using Mimics (Materialise, Leuven, Belgium) software. In an additional software package, 3-Matic (Materialise, Leuven, Belgium), the sagittal plane was positioned at the most distal point on the relevant condyle, perpendicular to the Surgical Epicondylar Axis (SEA). The transverse plane, orthogonal to the mechanical axis, was placed to intersect the same point. The mechanical axis was estimated from the axial plane in the scans, while the SEA was approximated by rotating the Posterior Epicondylar Axis (PEA) by 3° as shown in Figure 2.8(a). By performing sagittal and transverse sections on each condyle, four sets of datapoints were obtained. After sorting, cubic B-spline curves with 10 basis functions were fitted to each. The parametrisations for all specimens, in addition to reference measurements not affected by pathology for each knee, were stored in a database used to

train the SOM.

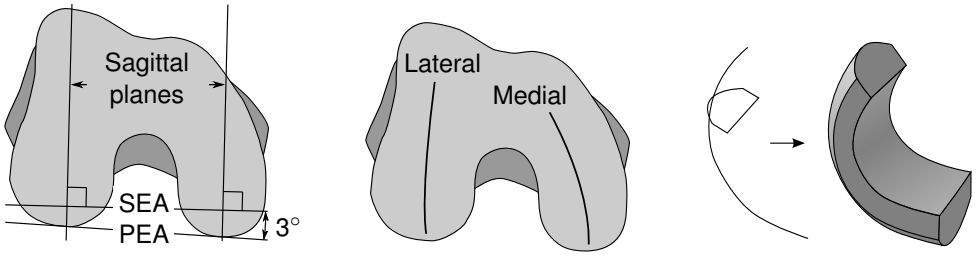

(a) Epicondylar axes (b) Condyle curvature (c) Curve loft

Figure 2.8: SOM UKR
(Illustration: Adapted from Van den Heever (2011))

When presented with a pathological knee, MRI scans are acquired, and segmented as previously. Reference measurements similar to those in the database are performed, and used as input to the SOM. During training, hidden relationships between the measurements and non-pathological parametrisations are established, allowing the estimation of a pathological knee's original cartilage geometry. For each condyle, the sagittal and transverse profiles are thus estimated. In order to account for the curvature of the condyles when viewing the distal femur in a transverse plane as per Figure 2.8(b), three points were placed centrally on the relevant condyle. A polynomial was fitted to these points, and the sagittal estimate warped in the mediolateral direction to fit the polynomial. Afterwards, the transverse profile was lofted together with the warped sagittal curve in order to obtain the patient-specific surface as illustrated in Figure 2.8(c). Finally, the tibial component was a mobile bearing design. The metal-backed tray follows the cortical rim curvature of simulated cuts performed on the proximal tibia. The insert's articular surface was designed to be fully congruent at zero degrees flexion through a binary subtraction procedure. All of the operations were performed in the Computer Assisted Design (CAD) software package Autodesk Inventor (San Rafael, California, USA).

The iUni®'s articulating surface is defined by the geometry of the patient's bone, offset by a predetermined distance based on average cartilage thickness (Steines and Zhuravlev, 2012). Partial Computed Tomography (CT) scans of the hip, knee and femur were obtained, and proprietary software derived the surface data of the bone (Steklov *et al.*, 2010). The mechanical axis was defined through the femoral head and the centre of the talus (Fitz, 2009). Before design commences, the knee is realigned virtually to a neutral biomechanical axis, resulting in the correction designed into the implant.

As per Steines and Zhuravlev (2012) and illustrated in Figure 2.9, an automated design procedure starts by requesting the user to place sketch points centrally on the patient's segmented condyle. A local cubic spline curve is

constructed segment by segment, as the points are placed. Once the centerline has been defined, a 2D contour is projected orthogonally onto the condyle from a predetermined view orientation. Said view is orientated axially so that the most distal point on the condyle is towards the user. The contour itself, which defines the outline of the implant, is made up of predefined elements such as points, straight lines and arcs. Constraints allow for automated generation of these elements, though user modification thereof is possible. The articulating surface is then determined by sweeping an arc of fixed radius along the central curvature at a predetermined offset. The radius of the arc is determined by measuring the patient's coronal curvature at several locations on the central curve, and using these measurements to derive a mean curvature. The arc's angle is defined heuristically, and all parameters are adjusted to maintain a minimum implant thickness value of three millimetres. This arc also forms the basis of the matched, concave articular surface of the metal-backed, fixed bearing. The tibial component's profile again follows simulated cuts on the cortical rim of the proximal tibia in order to maximise coverage (Steklov *et al.*, 2010).

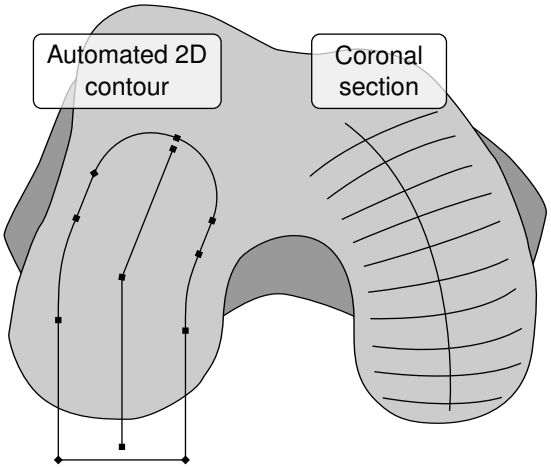

Figure 2.9: Automated Conformis iUni® design (Illustration: Adapted from Steines and Zhuravlev (2012))

A major distinction in the parametrisation by Van den Heever (2011) is that it is based on healthy cartilage geometry. The SOM estimation method therefore has the advantage of bypassing the effect of pathological changes in the articulating surfaces such as cartilage degradation and the presence of osteophytes. This parametrisation is however derived from localised planar sections, disregarding surface variations. The iUni®, on the other hand, takes into account the geometry of the entire surface, albeit by fitting a geometric primitive to averaged coronal sections of the pathological bone surface. This method is also semi-automatic, potentially reducing the design lead time and user variation.

2.8 Conclusions

The knee is both large and complex, and also one of the joints most susceptible to OA. Joint arthroplasty is a common treatment that replaces the affected geometries in order to restore function and alleviate pain. Compared to TKR, UKR only resurfaces the condyle affected, and could potentially result in improved post-operative biomechanics. UKRs share a number of common features and mostly vary within their secondary design aspects. Nevertheless, the majority are off-the-shelf products, and do not fit well on individuals. Patient-specific implants have been developed in order to overcome this limitation, though they are subject to a technician's interpretation and skill regarding healthy condyle shape and position.

3. Morphology

3.1 Introduction

Magnetic Resonance Imaging (MRI) has come to play an important role in the study of the knee (Eckstein *et al.*, 2014). It is the modality of choice for investigating articular cartilage (Braun and Gold, 2012; Choi and Gold, 2011), and additionally, it may be used to accurately reconstruct the osseous geometries (Van den Broeck *et al.*, 2014). Indeed, bone models are important for defining joint coordinate systems, regions of interest, and identifying morphological features (Grood and Suntay, 1983; Van der Merwe *et al.*, 2013; Victor *et al.*, 2009*a*). Furthermore, these models are often usefully represented as surface meshes derived from the segmented MRI data. Examples in literature include quantitative analyses (Bowes *et al.*, 2015; Bredbenner *et al.*, 2010) and anatomical models of the knee (DeFrate *et al.*, 2004; Pena *et al.*, 2006; Yue *et al.*, 2011), as well as design and evaluation of patient-specific instrumentation and implants (Frye *et al.*, 2015; Howell *et al.*, 2008; Van den Heever *et al.*, 2012*b*).

Such digital measurement, modelling, Computer Assisted Design (CAD) or other in-silico applications must invariably be related back to the intra-operative situation via homologous, surgically relevant and accessible landmarks (Victor *et al.*, 2009*a*). Landmarks are also required to set up the aforementioned coordinate systems, delineate regions of interest and locate morphological features. There appears, however, to be a sparsity of information regarding which landmarks are most appropriate for use upon Three Dimensional (3D) meshes of the knee, especially for those derived from MRI data. In particular, it is the variability between specimens as well as the reliability and agreement within and among the observers who define those landmarks that must be considered, as any uncertainties are liable to affect subsequent measurements and procedures (Della Croce *et al.*, 1999; Kedgley *et al.*, 2015).

Most landmark centred studies that rely on 3D surface meshes investigate the variation of morphology between specimens (Cobb *et al.*, 2008; Cho *et al.*, 2015; Puthumanapully *et al.*, 2014; Van Haver *et al.*, 2014; Victor *et al.*, 2009*b*). Observer agreement or reliability for the landmarks themselves, if reported, is generally only done so in support of the precision of the specific method or principle rater and is secondary to the main research questions or objectives.

Few authors seem to explicitly investigate surface mesh landmarks for both inter- and intra- observer agreement and reliability. Esfandiarpour *et al.* (2009) did so for 18 femur models derived from MRI scans, but only for the medial and lateral epicondyles. And Victor *et al.* (2009*a*) studied a full set of landmarks defined on Computed Tomography (CT) reconstructions of both the femur and the tibia, although their sample size was limited to six knees. To the best of our knowledge, this is the extent of literature on the matter.

So the question remains: which landmarks should be preferred when using MRI-derived surface meshes of the knee? We attempt to answer this by investigating the inter- and intra- observer agreement and reliability, as well as inter-specimen variability, for a larger set of landmarks defined on 3D surface meshes reconstructed from twenty MRI scans. Furthermore, since any coordinate system of the knee is based on landmarks which themselves vary, we propose to use Generalised Procrustes Analyses (GPA) for alignment purposes instead. This has the advantage of avoiding accumulation or coupling of variation during subsequent analyses, an issue which appears to be largely ignored in clinical studies that investigate knee morphology. Finally, we discuss the results and attempt to provide a guideline for selecting landmarks most suited to in-silico applications.

3.2 Methods

3.2.1 Terminology

In order to maintain clarity and consistency, we adopt here the terminology discussed by Bartlett and Frost (2008).

Subjects refer to the sample of femur and tibia meshes from the population that make up our dataset, and is used interchangeably with 'targets' and 'specimens'.

Observers or raters, are the expert volunteers who performed the measurements on the dataset.

Observations are the measurements that the observers took in the form of landmark coordinates identified on the targets.

Agreement quantifies the closeness of multiple measurements made on the same targets, and has the same unit as the measurements themselves. For instance, if multiple observers were to perform measurements on the same dataset, their measurements may differ systematically due to observer bias. Agreement is often reported in terms of standard deviation.

Reliability is the relationship between the true variability we see between targets and measurement errors arising from e.g. multiple observers or

observations. This is in contrast to agreement, which does not depend on population variability. Reliability may be given as the Intra-class correlation coefficient (ICC):

$$ICC = \frac{\sigma_b^2}{\sigma_b^2 + \sigma_w^2} \tag{3.1}$$

Here σ_b is the between-target or inter-specimen standard deviation, while σ_w is the within-target standard deviation due to measurement error. High reliability (values close to one) means that the measurement error is small in comparison to the population variability, and vice versa. In other words, it is (or isn't) possible to discriminate between different subjects given the error prone measurements.

Repeatability in our case refers to the intra-observer variability, i.e. the variability in measurements performed on the same subject by the same observer.

Reproducibility is the inter-observer variability, or variability in measurements performed on the same subject by different observers.

3.2.2 Data

The Faculty of Health Sciences (Stellenbosch University, South Africa) approved the collection of twenty (eight male and 12 female) subjects' right knee (distal femur and proximal tibia) MRI scans, ranging in age from 16 to 57 with a mean of 30.9 years. Inclusion criteria specified that subjects be skeletally mature with no identifiable osseous and cartilaginous pathology. Scan slice thickness along the transverse axis of the knee was 1.5 mm, with a resolution of 512×512 pixels in the sagittal plane. Pixel size was between 0.38 to 0.47 mm with an average of 0.4 mm.

Each scan's distal femur and proximal tibia was segmented in the sagittal plane by an expert using Mimics software. First, initial thresholds were applied in order to isolate the geometries, depending on the gray values. Then the threshold results from every second slice was manually cleaned, with masks interpolated between these edited slices. The masks were cleaned by closing all remaining holes via a multi-slice morphology operation followed by a single smoothing iteration. From the results, 3D models of the osseous geometries were constructed. These models underwent a wrapping operation, and was smoothed once more while compensating for shrinkage in order to further remove small artefacts due to segmentation. Mesh triangles were reduced in order to decrease the mesh size before the resulting meshes were validated against the original scans. Finally, Stereolithography (STL) files that contain the data as face-vertex surface meshes were exported.

3.2.3 Observations

A Matlab (MathWorks, Massachusetts, USA) program with a simple Graphical User Interface (GUI) was created to place landmarks directly on the triangulated surface meshes. Figure 3.1 shows the GUI mid-observation. The program presented the meshes to the observers in random order and random orientation so as to prevent memorisation. Once a mesh was shown, the observers were free to align it so that they may best identify the landmarks, which were also requested in random order for each new mesh. Observers were allowed to redo landmarks until they were satisfied. The observation data was recorded relative to the native orientation of the respective meshes as segmented from the tomographic scan data. Landmarks were classified as one of three types:

Point (P): The three dimensional Cartesian coordinates of where a ray along the observer's direction of view and located on the program's cursor intersects the appropriate mesh face.

Point Array (PA): A list containing a predetermined number of points, each individual point as defined previously.

Face Array (FA): A list of all mesh faces that lie at least partially within a sphere with a user specified radius and centred around intersection points as defined previously. Instances of the sphere were repeatedly defined as the observer dragged the cursor along the mesh's surface to 'paint' a portion of it.

The landmarks used here were primarily derived from similar studies in literature (Esfandiarpour *et al.*, 2009; Victor *et al.*, 2009*a*; Victor, 2009; Cobb *et al.*, 2008), as well as discussions with the collaborating orthopaedic surgeon. Figure 3.2 and Table 3.1 describe the full set of landmarks defined on the distal femur, while Figure 3.3 and Table 3.2 does so for the proximal tibia. Observers were provided with similar tables and figures describing the anatomic landmarks, for reference. Alternatively, computed landmarks are those that were calculated afterwards from point or face arrays, and therefore only indirectly identified by the observers.

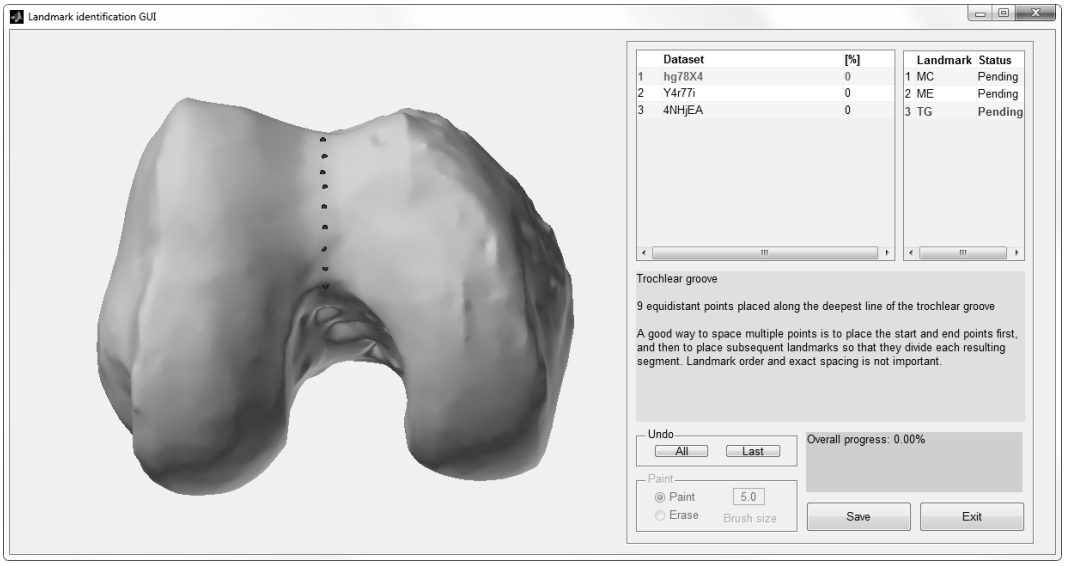

Figure 3.1: Landmark identification GUI (Illustration: J. v.d. Merwe)

Table 3.1: Femoral landmarks

ID	Landmark	Description	Type
		Anatomic landmarks	
fME	Medial epicondyle	Most prominent bony protrusion over the medial condyle	P
fMS	Medial sulcus	Indentation on the medial condyle's bone surface	P
fLE	Lateral epicondyle	Most prominent bony protrusion over the lateral condyle	P
fMTP	Medial trochlea peak	The most anterior point of the medial trochlear ridge	P
fLTP	Lateral trochlea peak	The most anterior point of the lateral trochlear ridge	P
fINA	Intercondylar notch apex	The most anterior and distal termination of the intercondylar notch	P
fTG	Trochlear groove	9 equidistant points placed along the deepest line of the trochlear groove	PA
fMTS	Medial terminal sulcus	Medial end of the medial condyle's groove	P
fLTS	Lateral terminal sulcus	Lateral end of the lateral condyle's groove	P
fMPP	Medial posterior point	Most posterior point on the medial condyle	P
fLPP	Lateral posterior point	Most posterior point on the lateral condyle	P
fMDP	Medial distal point	Most distal point on the medial condyle	P
fLDP	Lateral distal point	Most distal point on the lateral condyle	P
fMPC	Medial posterior condyle	The spherical part of the medial condyle's posterior articular surface	FA
fLPC	Lateral posterior condyle	The spherical part of the lateral condyle's posterior articular surface	FA
		Computed landmarks	
fTGc	Trochlear groove center	Center of a circle fitted to the trochlear groove point array (fTG)	P
fMPCc	Medial posterior condyle center	Center of a sphere fitted to the medial posterior condyle face array's vertices (fMPC)	P
fLPCc	Lateral posterior condyle center	Center of a sphere fitted to the lateral posterior condyle face array's vertices (fLPC)	P

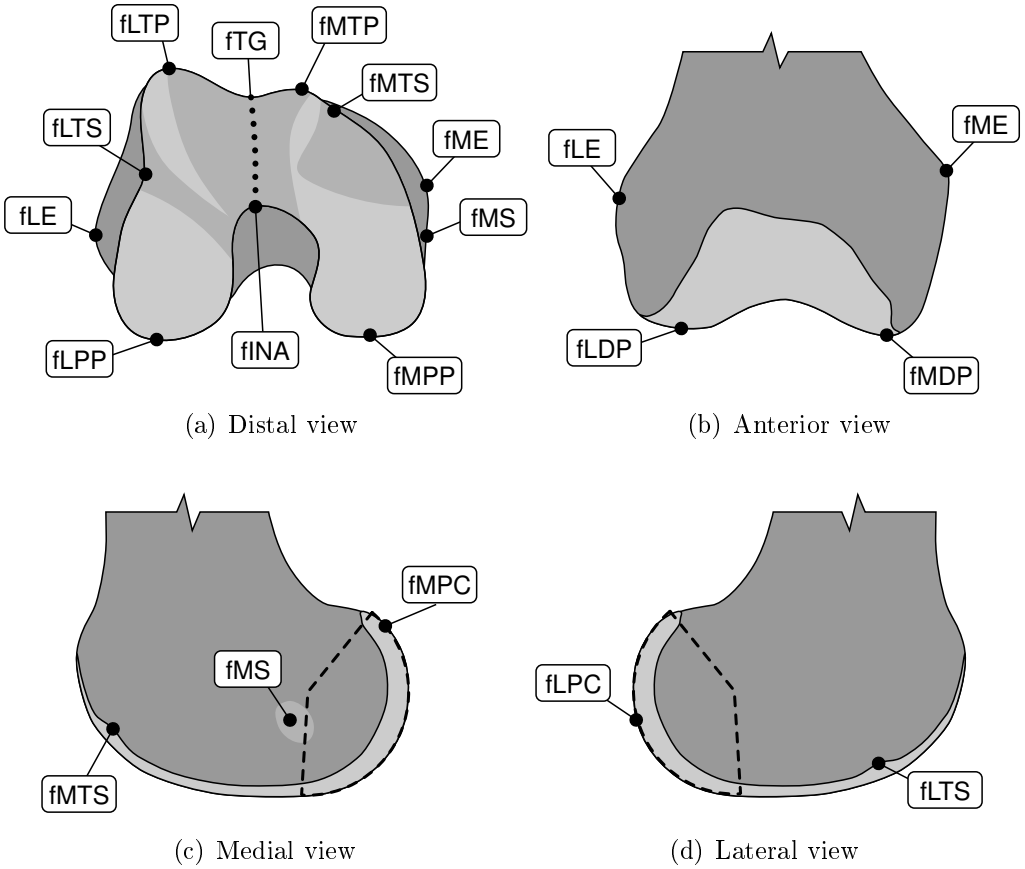

(a) Distal view (b) Anterior view

(c) Medial view (d) Lateral view

Figure 3.2: Femoral landmarks (Illustration: J. v.d. Merwe)

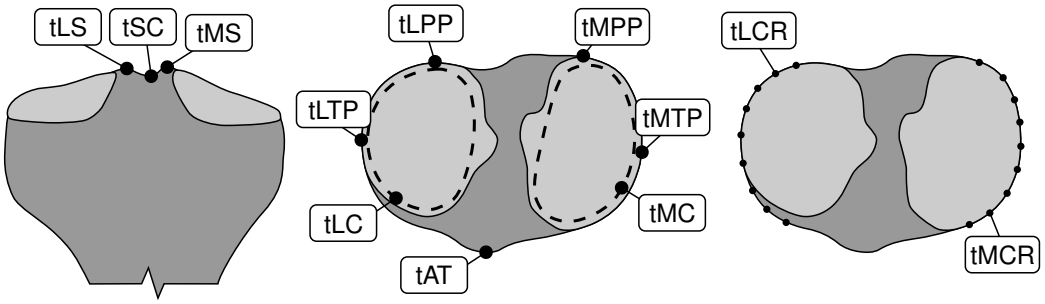

(a) Anterior view (b) Proximal view (c) Proximal view

Figure 3.3: Tibial landmarks (Illustration: J. v.d. Merwe)

To better convey the spatial arrangement of the landmarks, wire-frames were defined separately for the anatomic and computed landmarks as shown in Figure 3.4. In the case of the femur's computed landmarks, the triangular frame is defined on the trochlear groove's and medial and lateral condyle's centers (fTGc, fMPCc and fLPCc), while two lines are defined separately between

Table 3.2: Tibial landmarks

Anatomic landmarks			
ID	**Landmark**	**Description**	**Type**
tMCR	Medial cortical rim	9 equidistant points placed along the medial half of the medial plateau's cortical rim	PA
tLCR	Lateral cortical rim	9 equidistant points placed along the lateral half of the lateral plateau's cortical rim	PA
tMC	Medial condyle	The articular surface of the medial plateau	FA
tLC	Lateral condyle	The articular surface of the lateral plateau	FA
tMS	Medial spine	Most proximal point on the medial spine	P
tLS	Lateral spine	Most proximal point on the lateral spine	P
tSC	Spine center	Center point of the saddle region between the spines	P
tMTP	Medial transverse point	Most medial point on the medial cortical rim	P
tLTP	Lateral transverse point	Most lateral point on the lateral cortical rim	P
tMPP	Medial posterior point	Most posterior point on the medial cortical rim	P
tLPP	Lateral posterior point	Most posterior point on the lateral cortical rim	P
tAT	Anterior tubercle	Most prominent point on the tibial tubercle	P
Computed landmarks			
tMCRc	Medial cortical rim center	Center of a circle fitted to the medial cortical rim point array (tMCR)	P
tLCRc	Lateral cortical rim center	Center of a circle fitted to the lateral cortical rim point array (tLCR)	P
tMCc	Medial condyle center	Geometric mean of the medial posterior condyle face array's vertices (tMC)	P
tLCc	Lateral condyle center	Geometric mean of the lateral posterior condyle face array's vertices (tLC)	P

the tibia's cortical rim centres (tMCRc, tLCRc) and condyle centres (tMCc, tLCc).

3.2.4 Alignment

Prior to analysis, one observer identified the femoral and tibial anatomical landmarks once, on all n_s (twenty) datasets. The computed landmarks were calculated and included subsequently, replacing their respective point or face arrays (PA or FA) as part of the observation. This formed a set of n_s observations $\mathbf{v}_c$ each containing a homologous list of landmark coordinates. GPA, often used in anthropometric studies (Cavaignac *et al.*, 2016; Harmon, 2007; Nicholson and Harvati, 2006), was performed in an attempt to remove variation among specimens that was solely due to pose (rotation and translation). Given all $\mathbf{v}_c$, GPA essentially solves the least squares ordinary Procrustes problem in an iterative, pair-wise fashion, resulting in n_s point sets $\mathbf{v}_a$ aligned to the Procrustes mean $\mathbf{v}_m$ (Rohlf and Slice, 1990). This mean observation then serves as the reference for subsequent analyses investigating local and global landmark variation about it. For more details on the GPA method used, please refer to Appendix A.2.

The Procrustes mean shapes $\mathbf{v}_m$ for both the femur and tibia was transformed to a coordinate system similar to that of Grood and Suntay (1983) as shown in Figure 3.5. The femur's Medio-Lateral (ML) or x-axis was defined parallel to a line connecting the centres of the spheres fitted to its poste-

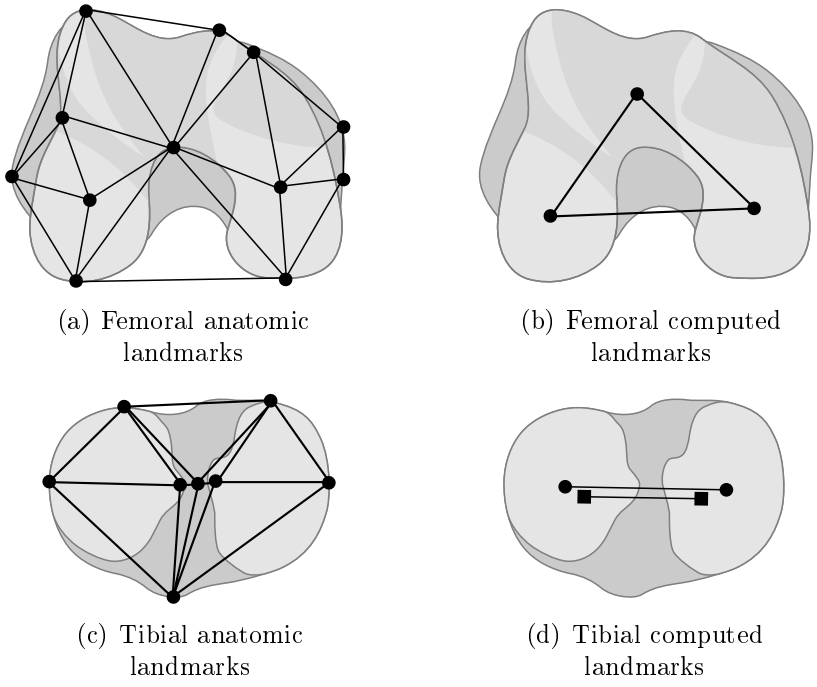

(a) Femoral anatomic landmarks

(b) Femoral computed landmarks

(c) Tibial anatomic landmarks

(d) Tibial computed landmarks

Figure 3.4: Wireframe models, viewed axially (Illustration: J. v.d. Merwe)

rior condyles (Kurosawa *et al.*, 1985), with lateral taken as positive for right knees. The coronal plane was defined parallel to both this line and the femur's anatomical axis, containing the x-axis and its orthogonal, the Cranio-Caudal (CC) or z-axis with positive defined cranially. Following the right-hand rule, the Antero-Posterior (AP) or y-axis is taken as orthogonal to both the x and z axes, the anterior direction being positive. These axes pass through the origin on the femoral Intercondylar Notch Apex (fINA).

The tibia's origin was at the tibial Spine Centre (tSC), with the z-axis parallel to its anatomic axis and positive in the cranial direction. The coronal plane was set parallel to the CC axis as well as a line passing through tMCc and tLCc, respectively. Once again, the x-axis was contained within the coronal plane, orthogonal to the z-axis and pointing laterally, while the y-axis was orthogonal to the coronal plane and positive in the anterior direction.

Note, however, that in the case of the femur and tibias' mean observations, the anatomic axes were not available as part of the homologous point sets. Instead, these axes were estimated separately for each individual mesh, with the relevant mean unit vector only computed after GPA alignment. This was achieved by extracting the principle direction of a single sheet hyperboloid fitted to the vertices above the cross-sectional area with 60% of the widest section (Andrews and Séquin, 2014). This particular quadric approaches cones or cylinders if the shaft geometry is closer to those boundary conditions, but generally assumes an elliptical cross section horisontally and a hyperbolic one vertically. Furthermore, after the translation and rotation required to trans-

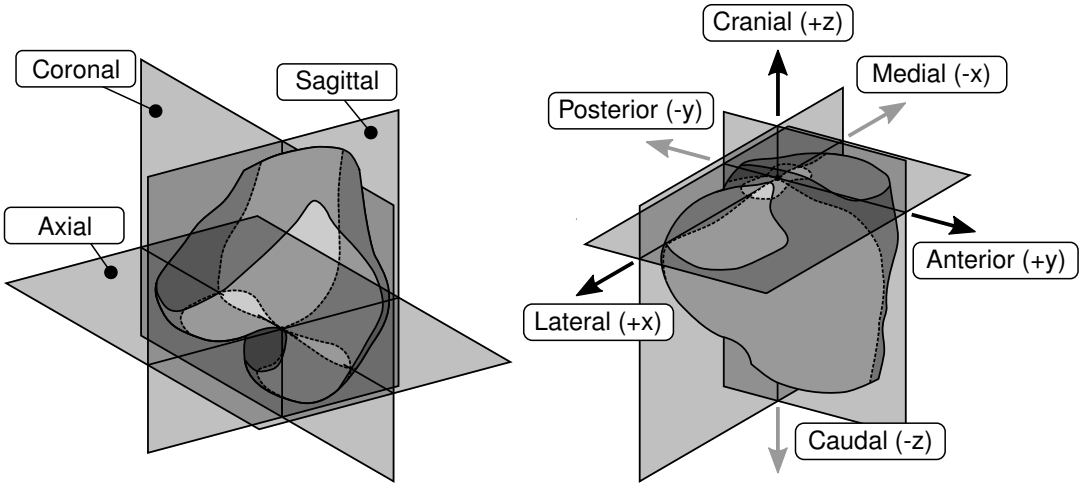

(a) Distal femur showing the coordinate planes

(b) Proximal tibia showing the axes

Figure 3.5: Coordinate systems of the knee (Illustration: J. v.d. Merwe)

form the mean observations into their coordinate frames were determined, the exact same transformation was applied to the individual observations as well. This maintained the landmarks' variability about the Procrustes means, while enabling qualitative description thereof in terms of standard anatomic reference frames.

3.2.5 Analysis

In order to investigate the inter-specimen variability, Principle Component Analysis (PCA) was used to determine the principle directions and magnitudes of variation within the aligned observations. PCA entails performing a linear transformation to align an uncorrelated orthogonal basis set of vectors to successive directions of greatest variance found in the data. These $min(n_s - 1, n_r d)$ modes of variation are represented in magnitude and direction by their eigenvalues λ_e and eigenvectors $\mathbf{u}_e$, respectively. We repeated this for each local landmark cluster such that $n_r = 1$, as well as the global set of observations with $n_r = 15$ and $n_r = 12$ for the femur and tibia, respectively, centred about the Procrustes means.

In the case of each individual landmark grouping, the PCA resulted in $d = 3$ principle directions along which the variation occurs in 3D space. Assuming normal distributions about the Procrustes mean landmarks we also computed the 95% confidence levels along each eigenvector for three degree of freedom χ^2 distributions. However, in order to investigate the global shape variation, since both the femur and tibia observations had $n_s - 1 = 19$ non-degenerate modes of variation, the coordinates of the eigenvectors could not be plotted in 3D space. Instead, we superimposed the first few most important modes on

the mean shape, scaled to $\pm 3\sqrt{\lambda_e}$ of their respective eigenvalues or variances λ_e along the eigenvectors $\mathbf{u}_e$ (Cootes *et al.*, 2004). For more detail on PCA, please refer to Appendix A.3.

The repeatability and reproducibility of a random sample of observers was estimated by having three observers each repeat three sets of observations on a subset of eight femurs and tibias. The observers were skilled biomedical engineers familiar with knees and knee implants. Each observer received instruction on how to perform measurements in the GUI along with documentation similar to Figures 3.2 and 3.3 and Tables 3.1 and 3.2, with no additional training. The transformations required to subsequently align each of the observed femoral and tibial targets to their anatomic coordinate systems were carried over from the alignment procedure of before. A two-way random effects Analysis of Variance (ANOVA) model was fitted to the measurements in order to obtain the inter-subject, inter-observer and intra-observer standard deviations, σ_b, σ_o and σ_w respectively (Bartlett and Frost, 2008). These serve as measures of agreement. Note that in some cases we may obtain negative estimates of variance from the ANOVA, which is impossible. It is standard practice then to accept this as evidence of zero variance. Finally, inter-observer reliability is defined as:

$$ICC_o = \frac{\sigma_b^2}{\sigma_b^2 + \sigma_o^2 + \sigma_w^2} \tag{3.2}$$

And intra-observer reliability by:

$$ICC_w = \frac{\sigma_b^2 + \sigma_o^2}{\sigma_b^2 + \sigma_o^2 + \sigma_w^2} \tag{3.3}$$

3.3 Results

The landmark scatter about the Procrustes mean femur and tibia is shown in Figure 3.6. Note that the femur is viewed distally, while the tibia is shown proximally. Confidence ellipses based on the 95% χ^2 distribution are given along the principle axes of variation for each landmark cluster. The anatomic axes are useful for describing variation in terms of established frames of reference, i.e. anterior, medial, etc., while the principle axes illustrate the directions in which the variation may be concentrated, if at all. The computed landmarks are offset posteriorly for the purposes of illustration. The standard deviation of the Euclidean distances between the mean and the observations is shown as an interpolated surface function on the wireframes. Based on this standard devation as well as the size of the landmarks' confidence ellipses, it is clear that the landmarks which exhibit the least inter-specimen variation are the trochlear groove center (fTGc), the medial posterior condyle center (fMPCc),

the lateral posterior condyle center (fLPCc) as well as the intercondylar notch apex (fINA). The remaining landmarks all show greater variation, and the medial terminal sulcus (fMTS) the most. Similarly for the tibia, the spine center (tSC), medial spine (tMS) and lateral spine (tLS) shows least variation. The anterior tubercle (tAT) along with the landmarks defined on the cortex rim of the tibia varies most.

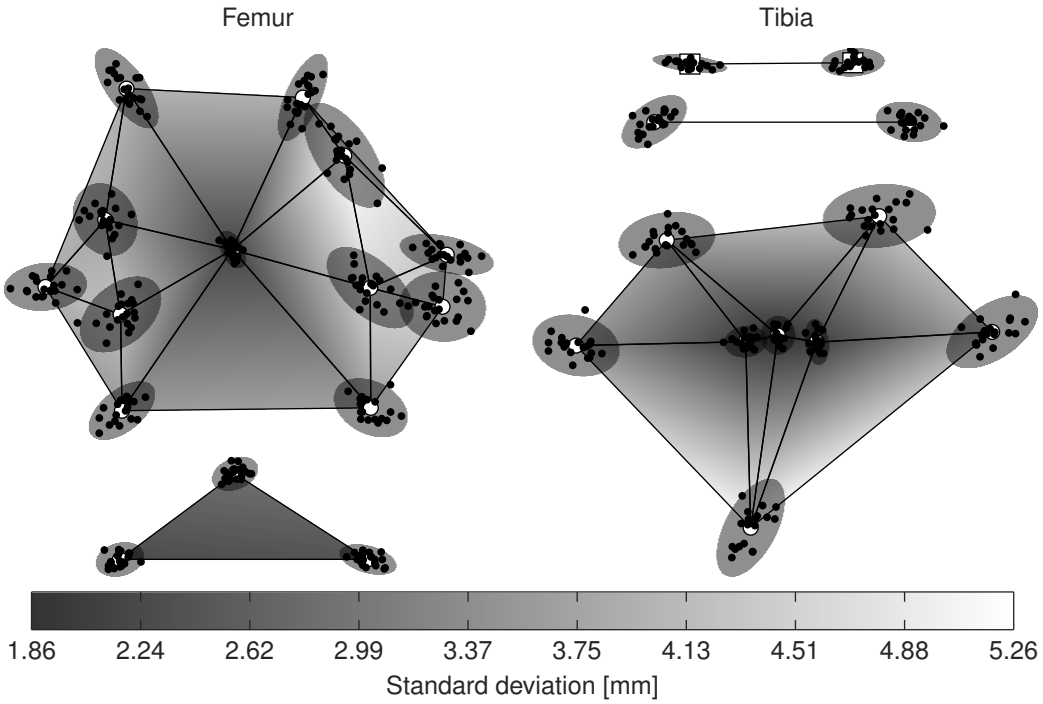

Figure 3.6: Inter-specimen landmark scatter (Illustration: J. v.d. Merwe)

From Figure 3.7, it can be seen that the contribution of the femur and tibia's first and largest mode of inter-specimen global variation is close to 50%. This is primarily related to scale, as illustrated by Figure 3.8. Here the wireframes indicate the $\pm 3\sqrt{\lambda_e}$ limits of each mode offset from the mean, while the colors mapped to the mean shapes are based on the Euclidean distances between these limits. For clarity, the distances between the modes of the tibia's computed landmarks are further emphasized by marker size. It appears that the first mode mostly affects the landmarks around the outside of the shapes rather than the more central ones. The second mode of the femur describes AP elongation, though the greatest effect can be seen in the position of the fMTS. In the case of the tibia a similar adjustment of the AP size is apparent, although this is limited to the tAT and landmarks on its medial condyle. The third mode seems to affect joint width, and is slightly rotated about the long axis of the tibia when compared to the femur. Regardless of which of the

first three modes are adjusted, the femoral medial and lateral condyle centers (fMCc and fLCc) as well as the tibial condyle rim centers (tMCRc and tLCRc) remain relatively stable.

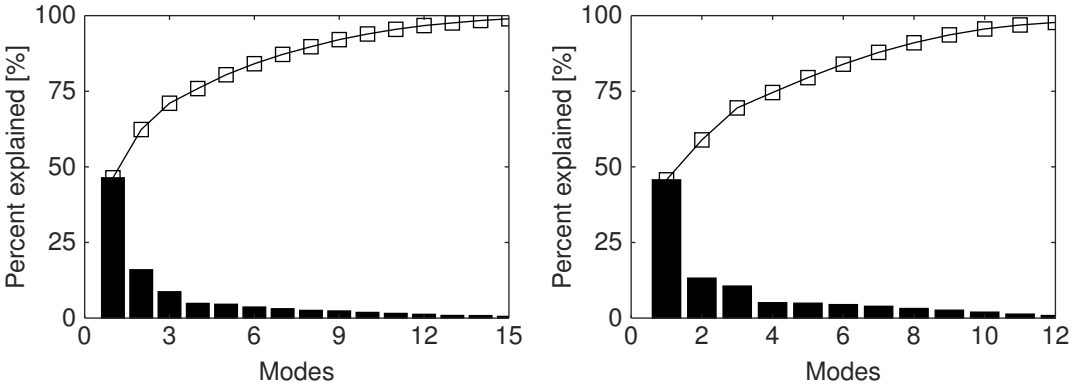

(a) Femur (b) Tibia

Figure 3.7: Inter-specimen Pareto chart (Illustration: J. v.d. Merwe)

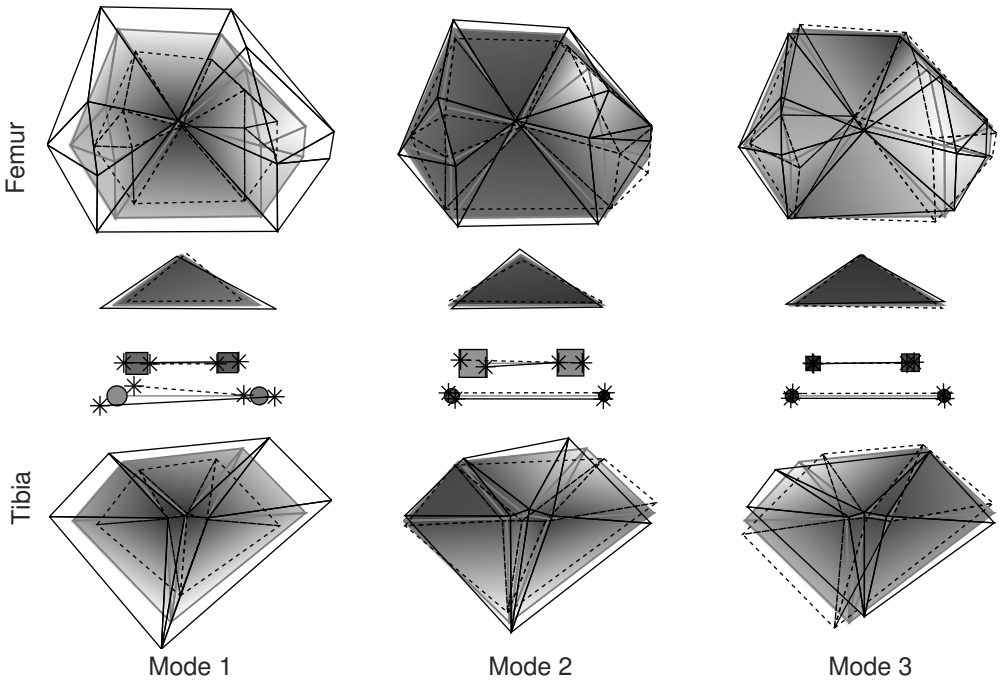

Figure 3.8: Global inter-specimen variation (Illustration: J. v.d. Merwe)

Table 3.3 lists the inter-specimen variation as well as the inter and intra-observer agreement and reliability along each of the axis directions and Eu-

clidean distances $\|\mathbb{R}^3\|$ from the mean. Note that the reliability measures were only computed from these distances. The inter-specimen deviation quantifies the results from Figure 3.6. In the case of the femur, inter-observer agreement for the computed landmarks range between 0 and 1.17 mm, while that for the medial epicondyle (fME) in the CC direction and fMTS in the AP direction are greatest at 5.1 and 4.03 mm respectively. The fMCc and fLCc have excellent inter-observer reliabilities of 0.97 and 0.96, though that of the fTGc is only 0.58. Similarly, while the fINA has very low inter-observer deviation, it also has poor reliability, and is likely due to its comparatively large variance. This trend of the computed femoral landmarks and the fINA continues for intra-observer agreement and reliability. However, the least repeatable observations are not the fMTS and fME, but instead the lateral distal point (fLDP) in the Medio-Lateral direction at 5.69 mm.

Table 3.3: Landmark variation

	Inter-specimen σ [mm]				**Inter-observer** σ_o [mm], ICC_o					**Intra-observer** σ_w [mm], ICC_w				
ID	ML	AP	CC	$\|\mathbb{R}^3\|$	ML	AP	CC	$\|\mathbb{R}^3\|$	r	ML	AP	CC	$\|\mathbb{R}^3\|$	r
fME	3.39	1.49	2.11	4.26	0.18	2.20	5.10	1.91	0.58	0.36	1.80	2.17	0.99	0.91
fMS	3.14	2.54	2.10	4.55	0.34	2.55	1.44	0.00	0.90	0.42	3.28	2.62	0.92	0.90
fLE	3.01	1.74	1.91	3.96	0.28	0.67	2.21	0.87	0.79	0.47	1.05	2.64	1.23	0.86
fMTP	1.81	3.14	1.50	3.92	0.00	0.00	0.52	0.18	0.98	0.70	0.15	1.14	0.39	0.98
fLTP	2.31	2.90	1.53	4.01	0.00	0.05	1.26	0.54	0.94	0.51	0.18	1.09	0.52	0.97
fINA	1.00	1.36	1.42	2.20	0.03	0.18	0.00	0.20	0.50	0.60	0.85	0.71	0.65	0.54
fMTS	2.93	3.78	2.15	5.24	3.12	4.03	2.70	0.75	0.76	1.77	2.41	1.70	0.88	0.86
fLTS	2.35	2.63	1.42	3.80	0.25	1.10	0.00	0.00	0.90	0.64	1.51	0.60	0.67	0.90
fMPP	2.67	2.14	1.37	3.68	0.48	0.01	0.53	0.38	0.85	1.17	0.10	1.14	0.75	0.88
fLPP	2.40	2.12	1.61	3.59	1.26	0.12	0.53	0.87	0.86	1.03	0.10	1.32	0.62	0.95
fMDP	3.14	2.94	1.65	4.60	0.00	1.56	0.20	0.00	0.80	1.25	2.07	0.28	1.27	0.80
fLDP	2.94	2.74	1.22	4.20	0.83	3.10	0.28	1.42	0.42	5.69	2.41	0.40	1.70	0.66
fTGc	1.67	1.24	1.98	2.87	1.17	0.40	0.68	0.69	0.58	2.46	0.99	1.08	0.92	0.73
fMCc	2.05	1.11	0.63	2.42	0.00	0.48	0.07	0.18	0.97	0.16	0.41	0.09	0.19	0.98
fLCc	1.75	1.26	0.70	2.27	0.08	0.16	0.00	0.16	0.96	0.26	0.40	0.18	0.24	0.97
tMS	0.77	1.45	1.27	2.08	0.10	0.00	0.02	0.08	0.85	0.30	0.79	0.06	0.34	0.85
tLS	1.35	1.01	1.14	2.03	0.20	0.14	0.02	0.14	0.79	0.54	0.57	0.10	0.47	0.81
tSC	1.09	1.22	0.88	1.86	0.48	1.00	0.34	0.73	0.07	0.61	1.27	0.36	0.78	0.51
tMTP	2.88	2.30	1.00	3.83	0.36	0.60	1.28	0.64	0.88	0.38	2.69	1.26	0.65	0.94
tLTP	2.74	1.95	1.07	3.54	0.42	1.05	0.70	0.66	0.93	0.34	2.40	0.53	0.41	0.98
tMPP	3.56	2.02	1.06	4.23	0.69	1.09	1.31	0.84	0.75	2.37	0.68	0.89	1.42	0.81
tLPP	3.04	1.79	1.12	3.70	0.37	1.10	1.87	0.94	0.78	1.44	0.51	1.06	1.13	0.87
tAT	2.16	3.09	3.67	5.26	0.84	0.00	1.45	1.19	0.79	1.48	0.19	2.26	1.67	0.86
tMCRc	2.00	0.90	0.71	2.31	0.22	0.05	1.15	0.23	0.89	0.91	0.32	0.89	0.73	0.90
tLCRc	2.35	0.60	1.42	2.81	0.69	0.00	2.27	0.76	0.80	1.00	0.51	1.55	0.88	0.89
tMCc	2.10	1.28	0.63	2.54	0.76	0.54	0.15	0.75	0.42	0.87	1.24	0.21	0.91	0.65
tLCc	2.05	1.68	0.89	2.80	1.63	2.71	0.39	1.58	0.46	0.87	1.18	0.25	0.86	0.88

The computed landmarks of the tibia exhibit relatively low inter-observer deviation at less than 1.58 mm, though while the reliability of the cortical rim centers is greater or equal to 0.8, that of the condyle centers is 0.46 and less. Incidentally, the tLCc also has the greatest deviation along the AP axis, 2.71 mm. The pattern of agreement and reliability of the computed tibial landmarks repeats for intra-observer agreement and reliability, though in this case there are considerably more landmarks that have deviations of more than

2 mm. Finally, similar to the fINA, the most central landmark of the tibia, the tSC, has comparatively low deviation but poor reliability of both inter and intra-observer measurements.

3.4 Discussion

Variability in coordinate systems and the landmarks upon which they are based may have a detrimental effect on downstream measurements (Kedgley *et al.*, 2015; Osis *et al.*, 2015). Therefore, in order to investigate inter- and intra-observer reliability and agreement, we instead relied on GPA, a standard morphometric approach to align our measured coordinates to a mean reference. A potential drawback of GPA is that investigations of measurement error may be undermined as particularly large variations in local landmarks could spread to others through distance based least squares alignment (Fruciano, 2016). Resistant fit Procrustes could address this issue if most of the variation is found in less than half of the landmarks (Rohlf and Slice, 1990). However, there is evidence to suggest that the distribution of landmark errors of the knee are relatively equal (Victor *et al.*, 2009*a*), and so our approach might not benefit from this. Rather, we applied the same transformations obtained during inter-specimen alignment to a much larger dataset's mean, to the individual knees used for inter- and intra-observer analysis. The results we obtained thus is supported by the available literature.

Victor *et al.* (2009*a*) studied inter- and intra-observer agreement and reliability for a large set of landmarks defined on six CT knee reconstructions. They report mean intra-observer variability ranging from 0.4 to 1.4 mm, with their condyle centers also showing relatively low deviation at between 0.2 and 0.5 mm. Their inter-observer agreement ranges from 0.3 mm to 3.5 mm, with the joint centers' deviation again lower at between 0.3 and 0.6 mm. Intra-class ICC values were derived from the total variance of measurements by different observers and the variance between subjects only, ranging between 0.986 and 1. Similarly, Esfandiarpour *et al.* (2009) observed inter- and intra- observer ICCs above 0.97, with standard errors of measurement ranging between 1.03 and 4.74 mm for the femoral epicondyles identified on 16 MRI reconstructions. In comparison, while we obtain similar orders of magnitude and trends for agreement, our reliability measures contain fewer excellent correlations between measurements. We speculate that differences in results may be attributed to different methods, with ours perhaps more conservative in nature.

Many joint-related studies require an embedded coordinate system with clear definitions of the origin and various axes. In such cases we recommend the use of landmarks that deviate the least between specimens in order to avoid affecting the variance of downstream measurements. However, many landmarks exhibit the greatest variation in one or perhaps two principle di-

rections, and very few have good all round inter-specimen agreement. A compromise would therefore be to avoid having the selected landmarks' deviation occur in at least the most *important* directions. To illustrate, consider trying to fit a ML axis to the femur. The medial and lateral epicondyles (fME and fLE) are often used for this purpose, and from Figure 3.6 and Table 3.3 we see that they vary least along the directions orthogonal to the desired axis. These are our example's *important* directions as any variation in the ML direction would not affect rotational alignment of the axis, but deviation in the AP and CC directions would.

In fact, we suggest that the best candidates for ML axis definition are the fMCc and fLCc as well as the tMCRc and tLCRc for the femur and tibia respectively. Not only are these landmarks' inter-specimen variation concentrated along the ML direction, but they also have good inter and intra-observer agreement and reliability. We speculate that this may be due to the global 'smoothing' effect during least squares approximation of spheres and circles to otherwise locally complex geometries. As for coordinate systems' origins, the fINA and tSC are good candidates. Even though they exhibit poor agreement and reliability, both their local and global inter-specimen variation is small compared to the alternatives (perhaps except for the mean between the condyle centers, which we did not investigate). Therefore, their effect on downstream measurements' variation may not be so severe.

Once a suitable coordinate system which is robust against inter-specimen variation has been defined, subsequent measurements should prioritise observer agreement and reliability. By way of example, the femoral medial and lateral terminal sulci (fMTS and fLTS) are good candidates for defining the anterior boundaries of the condyles' articular surfaces. We *do* expect them to vary between targets, and therefore want to use them to study the variation in overall shape of the condyles as part of a downstream process. The question we should therefore concern ourselves with is whether or not they are repeatable and reliable enough should we or someone else wish to duplicate the work (they are).

3.5 Conclusions

We used Generalised Procrustes Analysis to evaluate the inter-specimen variation as well as inter- and intra-observer agreement and reliability of landmark coordinates defined on MRI models of the distal femur and proximal tibia. Our results show that landmarks computed from spheres or circles fitted to the joint centres are robust against both global and local inter-specimen variation, as well as repeatability and reproducibility. With regards to the remaining landmarks, we provide sufficient information for researchers to consider their appropriateness in future studies.

4. Population-based model of the knee

4.1 Introduction

Anthropometric studies are often used to guide implant design and selection as they provide valuable information with regards to the geometric variation of a population (Cheng *et al.*, 2009; Dargel *et al.*, 2011; Servien *et al.*, 2008; Vaidya *et al.*, 2000). Such information is of especial interest when considering Unicompartmental Knee Replacements (UKRs) based on an anatomic design approach (as in our case), since compatibility with the remaining structures is crucial when attempting to restore natural function during partial joint resurfacing. However, anatomic variation is usually described in terms of linear measurements such as width, length, angles and radii (Cho *et al.*, 2015; Cobb *et al.*, 2008; Puthumanapully *et al.*, 2014; Van Haver *et al.*, 2014; Victor *et al.*, 2009*b*), although some authors do make use of multi-dimensional parametrisations (Allaire *et al.*, 2007; Van den Heever *et al.*, 2011*b*; Walker, 1988). A disadvantage shared by such descriptions of anatomy is that they are discrete simplifications of complex, three dimensional shapes (Bredbenner *et al.*, 2010).

In contrast, Statistical Shape Models (SSMs) are deformable models based on the variation of entire geometries found within a population, with the defining characteristic that these models can only deform in ways captured by the training data (Albrecht *et al.*, 2013; Cootes *et al.*, 1995). This ability to represent the complete, three dimensional probability distributions of similar shapes have made SSMs useful tools with which to optimise conventional implant designs to best fit the largest percentage of a population, or to adapt such complex analyses to an individual's geometry (Bischoff *et al.*, 2014; Kozic *et al.*, 2010; Nicolella and Bredbenner, 2012). However, while there are a number of cases in literature where SSMs have been applied to both the bones and cartilage of the knee (Heimann and Meinzer, 2009; Sarkalkan *et al.*, 2014), not many focus on specific regions of these geometries that are of interest when considering UKRs. Furthermore, regardless of how well morphometric measurements are able to describe a shape's true variation or not, they nevertheless form the foundation of our understanding of anatomy and play a crucial role in conveying information in clinical settings, yet are mostly ignored during SSM

validation in literature (Schumann *et al.*, 2010).

The aim, therefore, of this study was to create SSMs that are capable of accurately describing the non-pathological shape variation of the tibiofemoral joint while addressing the aforementioned shortcomings. If successful, such models could provide valuable insight into the design of UKR implants. In particular, we used MRI scans of healthy knees to train gender based models that are representative of typical UKR patients' age, because that is what we hope to eventually restore their geometry to. These models are subdivided into the medial and lateral condyles, and the trochlear compartment too in the femur's case, which are the Regions of Interest (ROIs) for UKR development. Finally, we validate the models against the training data as well as unseen shapes in terms of both surface based metrics and discrete morphological measures.

4.2 Methods

4.2.1 Data

The data used in the preparation of this manuscript was obtained from the Osteoarthritis Initiative (OAI) database, which is available for public access at `http://www.oai.ucsf.edu/`. The specific dataset was the non-exposed control cohort, version number 0.F.1. The OAI is a public-private partnership comprised of five contracts (N01-AR-2-2258; N01-AR-2-2259; N01-AR-2-2260; N01-AR-2-2261; N01-AR-2-2262) funded by the National Institutes of Health (NIH), a branch of the Department of Health and Human Services, and conducted by the OAI Study Investigators. Private funding partners include: Merck Research Laboratories; Novartis Pharmaceuticals Corporation, GlaxoSmithKline; and Pfizer, Inc. Private sector funding for the OAI is managed by the Foundation for the National Institutes of Health. This manuscript was prepared using an OAI public use data set and does not necessarily reflect the opinions or views of the OAI investigators, the NIH, or the private funding partners.

The non-exposed control cohort contained data from 122 healthy participants. Inclusion criteria for the cohort were (The Osteoarthritis Initiative, 2006*b*):

- Absence of joint pain, aching or stiffness for a year prior to enrolment.
- Absence of radiographic indications of OA including osteophytes and joint space narrowing as per the Osteoarthritis Research Society International (OARSI) atlas grades (Altman *et al.*, 1995).
- Absence of OA risk factors, including:
  - Obesity
  - Previous injury to the knee

- Previous surgery to the knee
- Total knee replacement in a biological parent or sibling
- Osseous swellings (Herberden's nodes) in the most distal joints of the fingers in both hands
- Daily activities that require repetitive bending of the knee

We further only considered the cohort's right knee MRI scans, under the assumption that there are no major differences between two knees from a single healthy individual. The OAI used 3 Tesla MRI machines operating under a 3D Dual Echo Steady State (DESS) protocol to obtain sagittal images of the knee. Slice thickness was 0.7 mm with a pixel resolution of 0.365×0.365 mm (The Osteoarthritis Initiative, 2006*a*). Furthermore, since most volunteers were Caucasian with only eight that were Black and two Asian, these scans along with any that had obvious defects unrelated to OA were also excluded from our study. This left 40 male knees ranging in age from 45 to 78 with a mean of 57 years, and we selected a matching number of 40 female knees ranging in age from 46 to 69 with a mean of 55 years to train and evaluate gender based models. The tibiofemoral osseous and cartilaginous geometries were segmented from the scans in order to obtain face-vertes meshes. The method used was similar to that described in Chapter 3, with the exception that the wrapping operation was not performed on cartilage in order to avoid degrading thinner sections of the model.

4.2.2 Coordinate system

While the OAI scan protocol was very consistent, there were still differences in positioning of the knees during scanning (The Osteoarthritis Initiative, 2006*a*). The resulting meshes were therefore transformed spatially to a coordinate system similar to that of Grood and Suntay (1983) as discussed in Chapter 3. However, rather than placing the mesh origins at the femoral notch apex and tibial spine centres respectively, the means of the condyles' centres were used instead. This allowed automating the coordinate alignment of the individual meshes given their reasonable starting positions thanks to the scan protocol. As opposed to manually identifying the articular surfaces on the bones, because the cartilage was also segmented, vertices directly opposite it could be found by conducting a range-limited neighbourhood search. In the case of the proximal femur, the posterior condyles were further isolated during sphere fitting in an iterative manner by only considering the flexion-extension arc between zero and 115°.

After alignment, the distal femur and proximal tibia meshes were then cut off from the remaining geometry by performing plane cuts along their shafts, half of the root mean square sum of the Antero-Posterior (AP) and Medio-Lateral (ML) widths from their most distal and proximal points, respectively. Through experimentation it was found that this introduced less 'artificial'

shape variation than the fixed window-size used during scanning different sizes and shapes of knees. For example, a large knee might have a comparably shorter shaft within the same scan window than a smaller one if they were scale normalised.

4.2.3 Landmarks

Shape may be defined as the geometric information remaining after translation, rotation and scale effects are removed. A shape itself is represented by landmarks, a common descriptor in orthopaedic applications, and defined as points that correspond between similar objects (Dryden and Mardia, 1998). In our application we represented shapes by performing Poisson disk importance sampling across the bone meshes' surfaces as per Corsini *et al.* (2012). The absolute mean curvature of each surface was used to influence the minimum distance which pseudo-landmarks could be generated from their nearest neighbours. This guided the pseudo-landmarks' distribution to mirror the shape's local information density. Additionally, as per the characteristics of the Poisson disk sampling scheme, high frequency information was rendered into blue-noise. This aids the avoidance of false patterns such as may be caused by regular sampling techniques (Dippé and Wold, 1985). Examples of regular and Poisson disk sampling are shown in Figure 4.1.

Since they were 'cleaned' to a lesser extent than the bone during segmentation, the cartilage meshes were more irregular, potentially compromising surface-based importance functions. Therefore, we reproduced the sampling of each bone mesh on the articular surface of its associated cartilage mesh via ray tracing along the bone vertices' normals. Mesh connectivity for each bone shape was maintained during sampling and was carried over directly from successful projections to the cartilage. Refer to Appendix B for more details regarding Poisson disk sampling and other relevant mesh operations.

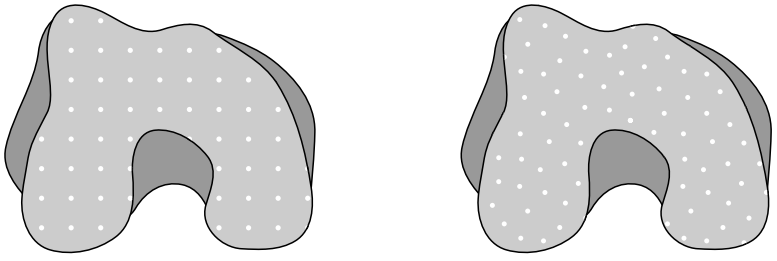

(a) Regular sampling (b) Poisson disk sampling

Figure 4.1: Sampling characteristics (Illustration: J. v.d. Merwe)

4.2.4 Correspondence

While anatomical landmarks are homologous by definition, establishing correspondence is rather more involved for pseudo-landmarks. In order to match points between some representative base and all other sets in the data, the non-rigid variant of the Coherent Point Drift (CPD) algorithm developed by Myronenko and Song (2010) was implemented. The CPD algorithm approaches registration of a reference point set $\mathbf{v}_r$ to some target $\mathbf{v}_t$ in d dimensional Cartesian space, centred about their respective barycentres and scaled to unity, as a probability density estimation problem. In our case we set the target to each sampled and coordinate aligned training shape in turn, while the reference point set was always the initially selected representative shape. The reference points are taken to represent Gaussian Mixture Model (GMM) centroids, and fitted to the target by maximising likelihood of correspondence using iterative Expectation Maximisation (EM). In order to preserve the reference's topology, the GMM centroids are constrained to move coherently by regularising the norm of a displacement function. The CPD algorithm does not result in a direct matching of points after convergence, but rather a best estimate, one-to-many probabilistic correspondence, described by the posterior probability of the transformed GMM centroids. We therefore employed the final, $n_r \times n_t$ posterior probability matrix P as a linear mapping such that:

$$\mathbf{v}_c = P(j|\mathbf{v}_{t_i})\mathbf{v}_t \qquad \text{where } i \in [1, 2, \ldots, n_t] \qquad \text{and } j \in [1, 2, \ldots, n_r] \tag{4.1}$$

Here $\mathbf{v}_c$ is the estimated n_r element correspondence of the transformed reference to the current n_t element target point set. The output of the CPD algorithm is affected by the values of the free parameters, f_n, f_d and f_k. The trade-off between motion smoothing and data-fitting is adjusted via f_d, with smaller values decreasing the smoothing effect and so favouring data-fitting. Parameter f_k controls the width of the smoothing kernel, the motion of discrete vertices being averaged over areas proportional to its value. And f_n, finally, represents the assumption of expected noise. Large values assume a more uniform distribution, decreasing the dependence of correspondence probability on Euclidean distance to mitigate the effect of outliers. Note that, in order to avoid nearby vertices from the bone influencing those on the cartilage and vice versa, we applied the CPD algorithm to each separately. We refer the interested reader to Appendix A.1 for more detail regarding the CPD algorithm, and Myronenko (2010) for the particular EM implementation as well as improvements in speed and reduced computational complexity.

4.2.5 Shape model construction

Generalised Procrustes Analysis (GPA) and Principle Component Analysis (PCA) are commonly used in statistical shape modelling applications to align

multiple corresponding point sets, thus removing variation due to pose, and to then model the residual shape variation within the population, respectively (Cootes *et al.*, 2004). We implemented a custom GPA algorithm based on that of Rohlf and Slice (1990) to iteratively solve the ordinary Procrustes problem. After pair-wise CPD, each individual corresponding model shape $\mathbf{v}_c$ was registered to the $n_r \times d$ Procrustes mean $\mathbf{v}_m$ by centring and scaling both to unity, and solving for the least squares orthogonal rotation matrix (Schönemann, 1966) while taking care to avoid reflections (Eggert *et al.*, 1997). After alignment, we elected to restore the mesh's original scaling in order to correctly represent cartilage thickness as part of our models' variation. The GPA algorithm is discussed in greater detail in Appendix A.2. The output of the GPA is a set of n_s aligned point sets $\mathbf{v}_a$, each concatenated along its d dimensions to form column vectors as shown here for the three dimensional case:

$$\mathbf{x} = \left[x_1, y_1, z_1, \ldots, x_{n_r}, y_{n_r}, z_{n_r}\right]^T \text{ where } \left[x_j, y_j, z_j\right] \in \mathbf{v}_a \tag{4.2}$$

As well as the $n_r d \times 1$ concatenated Procrustes mean $\bar{\mathbf{x}}$ from which we may construct the centred training matrix $\Delta\mathbf{X}$:

$$\Delta\mathbf{X} = \left[\mathbf{x}_1 - \bar{\mathbf{x}}, \ldots, \mathbf{x}_{n_s} - \bar{\mathbf{x}}\right] \qquad \text{where} \qquad \bar{\mathbf{x}} = \frac{1}{n_s}\sum_{l=1}^{n_s} \mathbf{x}_l \tag{4.3}$$

The aligned and corresponded pseudo-landmarks could then be segmented from the Procrustes mean shape into pre-defined ROIs which distinguish between the articular, osseous and cartilaginous surfaces of both the distal femur and proximal tibia, as shown in Figure 4.2. First, the resulting point sets prior to any ROI subdivision were defined as the femoral Full Shape (fFS) and the tibial Full Shape (tFS). The femoral Articular Surface (fAS) was then further subdivided into the femoral Lateral Condyle (fLC), femoral Medial Condyle (fMC) and femoral Anterior Condyle (fAC) by lines connecting the notch apex (fINA), the femoral Lateral Terminal Sulcus (fLTS), and the femoral Medial Terminal Sulcus (fMTS), respectively. Likewise, the tibial Lateral Condyle (tLC) and tibial Medial Condyle (tMC) were taken to be the tibial Articular Surface (tAS) separated to either side of the tibial Spine Center (tSC). The ROIs were stored separately for the bone and cartilage for later use.

We finally performed Singular Value Decomposition (SVD) based PCA in order to convert our datasets' n_r correlated and aligned landmarks into at most $n_s - 1$ non-degenerate, linearly uncorrelated orthogonal principle components of variation (Cootes *et al.*, 1995, 2004). These modes of variation are represented in direction by an $n_r d \times (n_s - 1)$ matrix $\mathbf{U}$, which contains the eigenvectors of the centred training data matrix along its columns, and in magnitude by $\mathbf{\Lambda}$, which is a diagonal matrix of the $n_s - 1$ respective eigenvalues λ_e. A shape instance $\tilde{\mathbf{x}}$ of the training set may then be approximated by a linear combination of the n_k most important modes of variation:

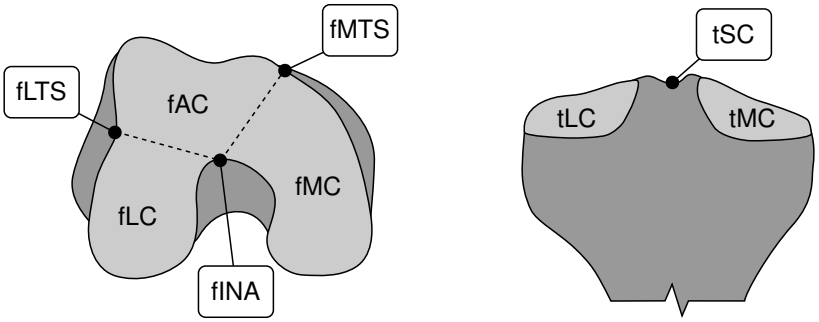

(a) Distal femur, axial view

(b) Proximal tibia, anterior view

Figure 4.2: Regions of interest (Illustration: J. v.d. Merwe)

$$\tilde{\mathbf{x}} = \bar{\mathbf{x}} + \mathbf{U}_k \mathbf{b} \tag{4.4}$$

where $\mathbf{b}$ is the $n_k \times 1$ parameter vector. Usually n_k is defined as the number of modes required to represent a cumulative variance $\sum_{e=1}^{n_k} \lambda_e$ of at least some pre-set minimum such as 95% or 98% in order to reduce noise and increase model compactness (Cootes *et al.*, 2004; Heimann and Meinzer, 2009). Refer to Appendix A.3 for more detail regarding PCA as applied to SSM. A pseudo representation of the algorithm used to construct the entire shape model is given in Figure 4.3.

4.2.6 Shape model fitting

A shape model is unable to exactly reproduce some given data $\mathbf{y}$ if it does not lie within the span defined by the training set (Albrecht *et al.*, 2013). In such cases, common practice dictates the introduction of a noise variable $\mathbf{N}_R$ to model the difference between the model result and input shape:

$$\mathbf{y} = \tilde{\mathbf{x}} + \mathbf{N}_R \tag{4.5}$$

Modelling the noise as $\mathbf{N}_R = \eta\mathbf{\Lambda}$, the least squares optimisation problem is then solved (Blanc *et al.*, 2009):

$$\begin{aligned} \mathbf{b} &= \arg\min_{\mathbf{b}}(||\mathbf{U}_k\mathbf{b} - \Delta\mathbf{y}|| + \eta\mathbf{b}^T\mathbf{\Lambda}^{-1}\mathbf{b}) \\ &= (\mathbf{U}_k^T\mathbf{U}_k + \eta\mathbf{\Lambda}^{-1})^{-1}\mathbf{U}_k^T\Delta\mathbf{y} \end{aligned} \tag{4.6}$$

to obtain the best fit parameter vector $\mathbf{b}$. Here $\Delta\mathbf{y}$ is the centred observation $\mathbf{y} - \bar{\mathbf{x}}$, and η is a regularisation term introduced to mitigate over-fitting and matrix inversion difficulties, often chosen proportional to the noise in the data. The eigenvalue matrix $\mathbf{\Lambda}$ weights the principle components according to their variance (Blanc and Székely, 2012). Figure 4.4 shows the pseudo-code for shape model fitting.

Function $[\bar{\mathbf{x}}, \mathbf{\Lambda}, \mathbf{U}, \mathbf{l}] =$ `ssmconstruct(v)`

Input:

$\mathbf{v}$	$? \times d(\times n_s)$	set of n_s training shapes

Output:

$\bar{\mathbf{x}}$	$n_r d \times 1$	Procrustes mean
$\mathbf{\Lambda}$	$n_k \times n_k$	eigenvalue matrix
$\mathbf{U}$	$n_r d \times n_k$	eigenvector matrix
$\mathbf{l}$	$n_r d \times 1$	RIO labels

```
/* initialisation                                              */
select v_{l_0} from v;     /* some initial representative shape */
v_{g_0} ← grood(v_0);       /* pre-align to coordinate system */
v_r ← pdisk(v_{g_0}, n_r);            /* poisson disk sampling */
for each training shape v do
    v_g ← grood(v);         /* pre-align to coordinate system */
    v_t ← pdisk(v_g, n_t);            /* poisson disk sampling */
    v_c ← cpd(v_t, v_r);            /* establish correspondence */
end
/* GPA                                                         */
v_m := v_r;                           /* initialise mean shape */
while mean shape v_m not converged do
    translate v_m to centroid and scale to unity;
    for each training shape v_c do
        v_a ← oprocrustes(v_m, v_c);          /* align to mean */
        x ← reshape(v_a);      /* reshape d dimensions to 1 */
    end
    compute x̄;                              /* Procrustes mean */
    v_m ← reshape(x̄);          /* reshape 1 dimension to d */
end
l ← roi(v_m);                  /* segment vertices into ROIs */
/* PCA                                                         */
compute ΔX;
compute Λ and U;                                        /* SVD */
retain n_k significant modes of variation;
end
```

Figure 4.3: Shape model construction

4.2.7 Shape model validation

The Root Mean Square Distance (RMSD) error was measured between the model approximations and input shapes in order to evaluate model performance. We used our gender based SSMs to approximate the data from which they were trained as well as previously unseen shapes. For both the training

Function $\tilde{\mathbf{v}} =$ `ssmfit`$(\mathbf{v}_y, \bar{\mathbf{x}}, \mathbf{\Lambda}, \mathbf{U})$

Input:

$\mathbf{v}_y$	$n_t \times d$	input shape point array
$\bar{\mathbf{x}}$	$n_r d \times 1$	Procrustes mean
$\mathbf{\Lambda}$	$n_k \times n_k$	eigenvalue matrix
$\mathbf{U}$	$n_d \times n_k$	eigenvector matrix

Output:

$\tilde{\mathbf{v}}$	$n_r \times d$	approximated point array

`/* initialisation */`
$\mathbf{b} := \mathbf{b}_0$;
$\tilde{\mathbf{x}} := \tilde{\mathbf{x}}_0$; `/* first approximation */`
$\tilde{\mathbf{v}} \leftarrow$ `reshape`$(\tilde{\mathbf{x}})$; `/* reshape 1 dimension to` d `*/`
$\mathbf{v}_c \leftarrow$ `cpd`$(\mathbf{v}_y, \tilde{\mathbf{v}})$; `/* establish correspondence */`
`/* estimation */`
while $\tilde{\mathbf{v}}$ *not converged* **do**
  $\mathbf{v}_a \leftarrow$ `oprocrustes`$(\tilde{\mathbf{v}}, \mathbf{v}_c)$; `/* align to estimate */`
  $\mathbf{y} \leftarrow$ `reshape`$(\mathbf{v}_a)$; `/* reshape` d `dimensions to 1 */`
  compute $\Delta\mathbf{y}$;
  $\mathbf{b} \leftarrow$ `solve`$(\mathbf{\Lambda}, \mathbf{U}, \eta, \Delta\mathbf{y})$;
  constrain $\mathbf{b}$;
  compute $\tilde{\mathbf{x}}$; `/* updated fit */`
  $\tilde{\mathbf{v}} \leftarrow$ `reshape`$(\tilde{\mathbf{x}})$; `/* reshape 1 dimension to` d `*/`
end
reverse $\tilde{\mathbf{v}}$'s pose; `/* align approximation to input shape */`
end

Figure 4.4: Shape model fitting

and unseen shapes, we measured the error of the bones, cartilage surface and cartilage thickness separately. The RMSD between two shapes was determined using a ray tracing method similar to that of Möller and Trumbore (2005). Cartilage thickness was also determined via ray tracing from bone vertices to the cartilage surface. Once correspondences were established, this allowed direct comparisons between the model approximations' and target shapes' cartilage thickness. The average thickness for the various ROIs and reconstructions were also tested for statistically significant differences via paired student's t-tests. We generally report the mean RMSD per ROI as well as the standard error of the mean σ_M for the sample.

Surface based metrics such as those discussed previously may not, however, provide a sufficient indication of local model behaviour. Schumann *et al.* (2010) therefore suggested using relevant morphological parameters in addition to error measures defined over the entire surface. Figures 4.5 and 4.6 show the morphological measures used in this study for the femur and tibia. Mea-

surements were automated with respect to the previously discussed coordinate system, and unless otherwise stated, all distances were defined along a single coordinate axis. Angles were measured within one of the primary planes, with positive defined in accordance with the right hand rule.

We defined the femoral Trans Epicondylar distance (fTEd) as the length on the x-axis between the epicondyles, or most medial and lateral points. The femoral Antero-Posterior Lateral distance (fAPLd) and femoral Antero-Posterior Medial distance (fAPMd) was measured between the most anterior and posterior points on the lateral and medial sides of the articular surface, respectively. The angles between the medial and lateral condyles were measured in the axial view as the femoral Medio-Lateral Anterior angle (fMLAa) and femoral Medio-Lateral Posterior angle (fMLPa). Similarly, the femoral Medio-Lateral Distal angle (fMLDa) was derived from the anterior view. We estimated the femoral Lateral radius (fLr) and femoral Medial radius (fMr) by fitting spheres to the posterior portions of each condyle. Finally, a plane orientable along all three axes was fitted to the deepest portion of the trochlear groove. A circle lying on this plane was then used to approximate the resulting section in order to obtain the femoral Anterior radius (fAr).

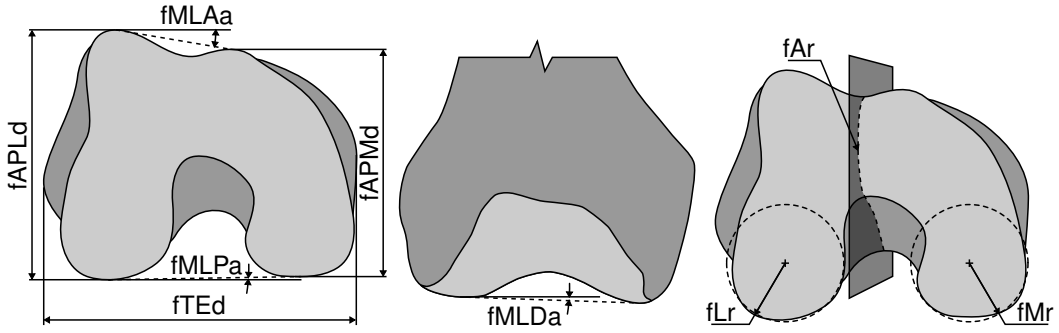

(a) Distances and angles, axial view (b) Distal angle, anterior view (c) Radii, axial view

Figure 4.5: Femoral morphological measurements (Illustration: J. v.d. Merwe)

The tibial Medio-Lateral distance (tMLd) and the tibial Antero-Posterior distance (tAPd) was measured between its most medial and lateral points, and most anterior and posterior points, respectively. Planar circles orientable in three dimensions were fitted to the cortical rim of the plateau's condyles in order to define the tibial Lateral radius (tLr) and the tibial Medial radius (tMr). The width between their centres was defined as the tibial Geometric Centre distance (tGCd). Furthermore, three dimensional planes were fitted to the medial and lateral articular surfaces. From their orientation in the sagittal plane the tibial Lateral Posterior angle (tLPa) and tibial Medial Posterior angle (tMPa) was derived, while the coronal plane was used to define the

tibial Lateral Varus angle (tLVa) and tibial Medial Varus angle (tMVa) as shown.

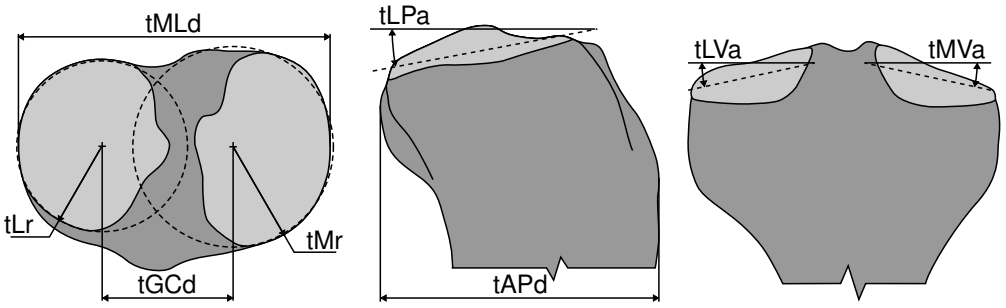

(a) Distances and radii, axial view

(b) Slope and length, lateral view

(c) VV angles, anterior view

Figure 4.6: Tibial morphological measurements (Illustration: J. v.d. Merwe)

Comparisons were made in Matlab, first testing for normality using a Lilliefors test. For normal distributions, Pearson's correlation coefficients were then calculated, and Spearman's otherwise. Since the model is intended to follow the sample population's variation, we consider correlation values of $0.9 < r_c \leq 1.0$ strong, $0.7 < r_c \leq 0.9$ moderate, and anything else as poor. Along with correlation results, we also report the standard error of the estimate σ_E of the sample.

4.3 Results

4.3.1 Model construction

For model construction, we selected 32 male and 32 female knees to form the gender based training sets, leaving eight knees each for a 80:20 distribution between seen and unseen data. The initial representative shapes were those training meshes whose normalised morphological measurements were closest to the median of the training dataset. The target number of samples n_r for the osseous geometries was set at 3000, but due to the nature of the Poisson disk sampling algorithm implemented, an exact number was difficult to obtain. The resulting mean male distal femur and proximal tibia therefore had 3007 and 3044 vertices in 3 dimensions, while the female mean shapes had 3023 and 3008 landmarks, respectively. After including the vertices traced to the cartilage surfaces, the total number of landmarks in the mean shapes went up to 4058 and 3582 for men and 4012 and 3529 for women, which was considered adequate. Furthermore, in an effort to promote good correspondence, each training shape's bone mesh was sampled to contain approximately $n_t = 4500$ landmarks prior to GPA. The CPD free parameters were set to $f_d = 2$, $f_k = 2$

and $f_n = 0.5$ based on values suggested in literature and determined from experimentation (Myronenko and Song, 2010; Rasoulian *et al.*, 2012). We defined $\eta = 0.5$ based on a series of leave one out tests using the training data, as per Albrecht *et al.* (2013). Finally, since model compactness was not an issue, we set k to the maximum number of modes for 100% cumulative variance as this generally gave best results. Note that, for the purposes of illustration and computing global surface metrics, mesh connectivity for each sampled shape was maintained by implementing a simplified version of the algorithm by Fu and Zhou (2008). This allows mapping a function, such as error or variation, onto a surface mesh in three dimensions. Refer to Appendix B for more detail.

4.3.2 Model analysis

Figures 4.7(a) and 4.8(a) show the standard deviation of the distances between the individual corresponding landmarks for all training sets and the Procrustes mean bone shapes. This serves as a first indication of the resulting shape variation after the training datasets have been made invariant to pose. In the case of the femur, it appears that the areas of largest variation include the epicondyles, while the trochlear groove and intercondylar notch exhibit the least variation. The average male femur also appears to be wider and less 'triangular' than the mean female femur. The tibias similarly have the most variation around the cortex. The variation of the cartilage illustrated by Figures 4.7(b) and 4.8(b) is greatest at the anterior portion of the femoral trochlear groove and the weight bearing regions of the condyles in the men's case. For women, the largest variation is found at the notch apex. Both men's and women's tibias have the greatest cartilage variation located centrally and towards the spine centres. Finally, the thickest cartilage regions shown in Figures 4.7(c) and 4.8(c) is found at the weight bearing regions of the femur and tibia, with male knees having the larger average thickness.

Alternatively, Figure 4.9 shows the percentage of variance described by the different modes for the men's and women's models. The first mode of the men's femur and tibia models was responsible for more than 41.4% and 49.6 % of the total variance, respectively. Thereafter the variances increased marginally, with the first 18 modes describing just over 95% cumulative variance. In the women's case, the first mode described just over 37% variance for both femur and tibia models, and reached a cumulative variance of slightly more than 95% at 18 and 20 modes, respectively.

Any further description of the actual effect that the principle modes of variation obtained from PCA has is abstract at best, although overall trends within the larger modes may be discerned from visual inspection. To that end, the first three components of the femur's and tibia's shape parameters were each set to $\pm 3\sqrt{\lambda_e}$ in order to illustrate the particular variation they encompass. This is shown in Figures 4.10 and 4.11, where variation is mapped

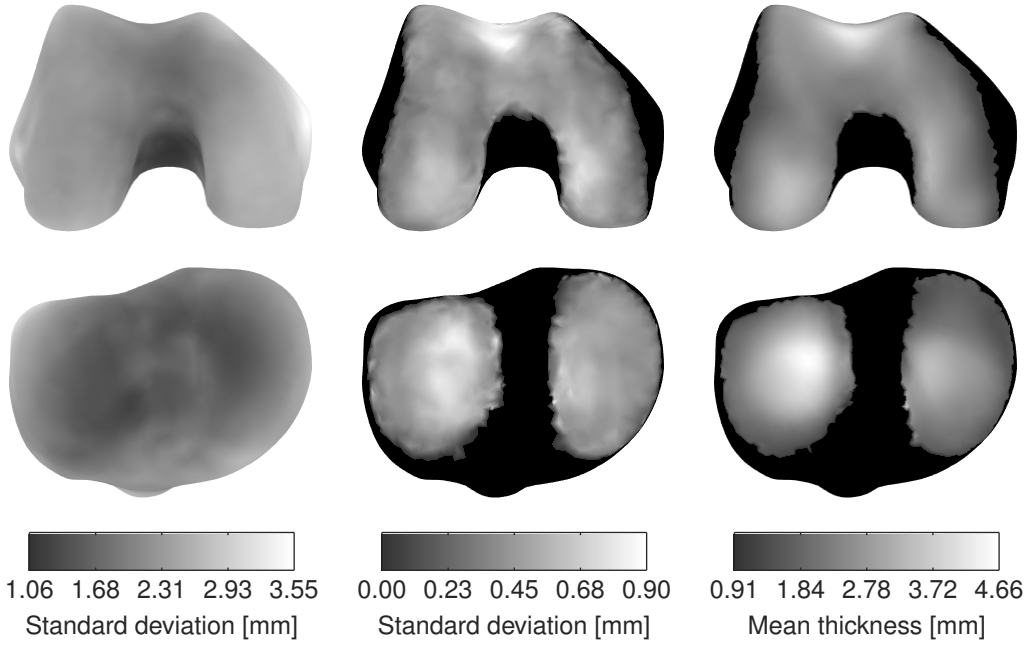

(a) Bone variation (b) Cartilage variation (c) Cartilage thickness

Figure 4.7: Male knee mean and variation (Illustration: J. v.d. Merwe)

based on the inter-landmark distance between the two adjusted shapes of each mode. During fitting procedures, it is of course the entire set of these n_k parameters that will be optimised to approximate a new shape.

In the case of both the distal femur and proximal tibia, the first and largest mode of variation generally describes a change in scale. The femur's second mode appears to affect the anterior shape of the trochlear region, while the third seems to adjust the medial and lateral condyles in particular. For both men and women, the tibia's second and third modes mainly seem to affect the shape of the cortical rim, plateaus and anterior tubercle. The effects that adjusting the modes of variation has on the tibiofemoral cartilage is also shown, and while certain areas exhibit greater changes than others, it is difficult to discern a clear pattern.

4.3.3 Model verification

When using the maximum number of n_k modes, it is possible to reconstruct training data exactly via Equation 4.4. Therefore, rather than performing fitting procedures to see how well the models are able to represent the training data, we instead investigate the errors between the original, sampled training set and the corresponding vertices from which the models were actually constructed. These are the mean RMSD errors per RIO given in Tables 4.1 and 4.2 for the bone surface, cartilage surface and cartilage thickness, ranging

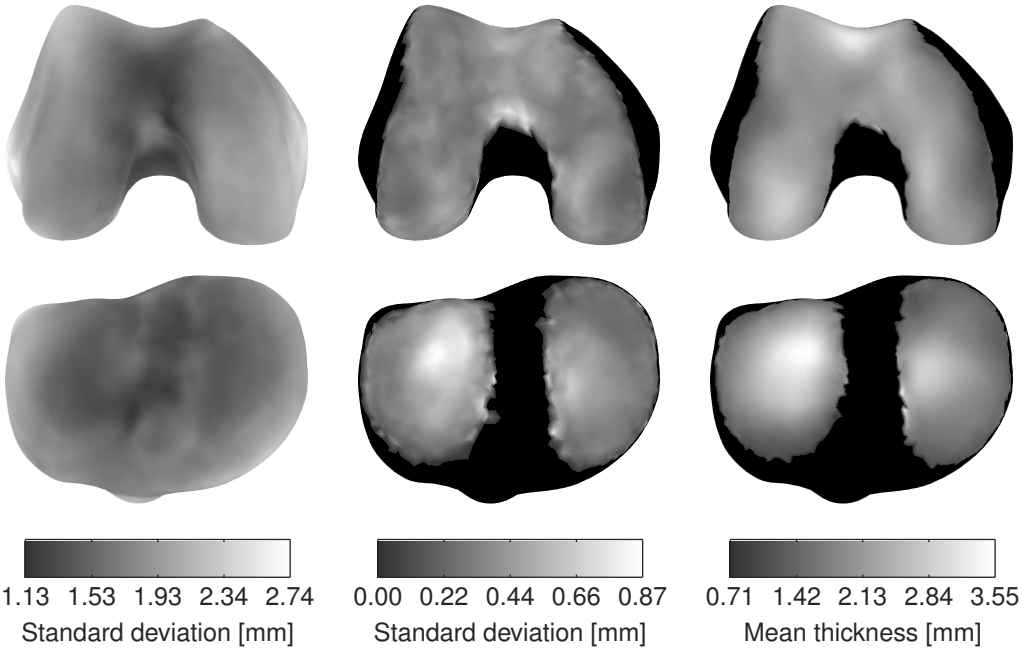

(a) Bone variation (b) Cartilage variation (c) Cartilage thickness

Figure 4.8: Female knee mean and variation (Illustration: J. v.d. Merwe)

between 0.08 and 0.17 mm. Tables 4.3 and 4.4 also list the mean cartilage measurements per ROI. Again, male knees have generally thicker cartilage than females, ranging between 2.11 and 2.63 mm and 1.85 and 2.09 mm respectively, depending on the ROI. Note that the corresponding meshes appear to overestimate the various ROI's cartilage thicknesses, though non-zero correlation at the 95% significance level was maintained. Finally, the point-wise standard errors of the estimate for the corresponding training sets are illustrated by Figures 4.12 and 4.13. Bony areas with high curvatures such as the periarticular regions and spines show the greatest deviation from the original sampled surfaces, while the cartilage surfaces and thicknesses exhibited more uniform error distributions.

In order to determine how well our SSMs are able to describe shapes other than the training data, we attempted to reconstruct a set of previously unseen knees. The mean RMSD errors for the ROIs of the bone, cartilage and cartilage thickness are also listed in Tables 4.1 and 4.2. Mean errors ranged between 0.41 to 0.84 mm and 0.38 to 0.69 mm for the male and female model reconstructions respectively, with the medial condyles of both the femur and tibia generally having the best results. Tables 4.3 and 4.4 list the mean cartilage measurements of the unseen data and their reconstructions per ROI. Again, the model appears to overestimate cartilage thickness, with all but the male fMC and fAC, and the tLC for both male and female knees exhibiting statisti-

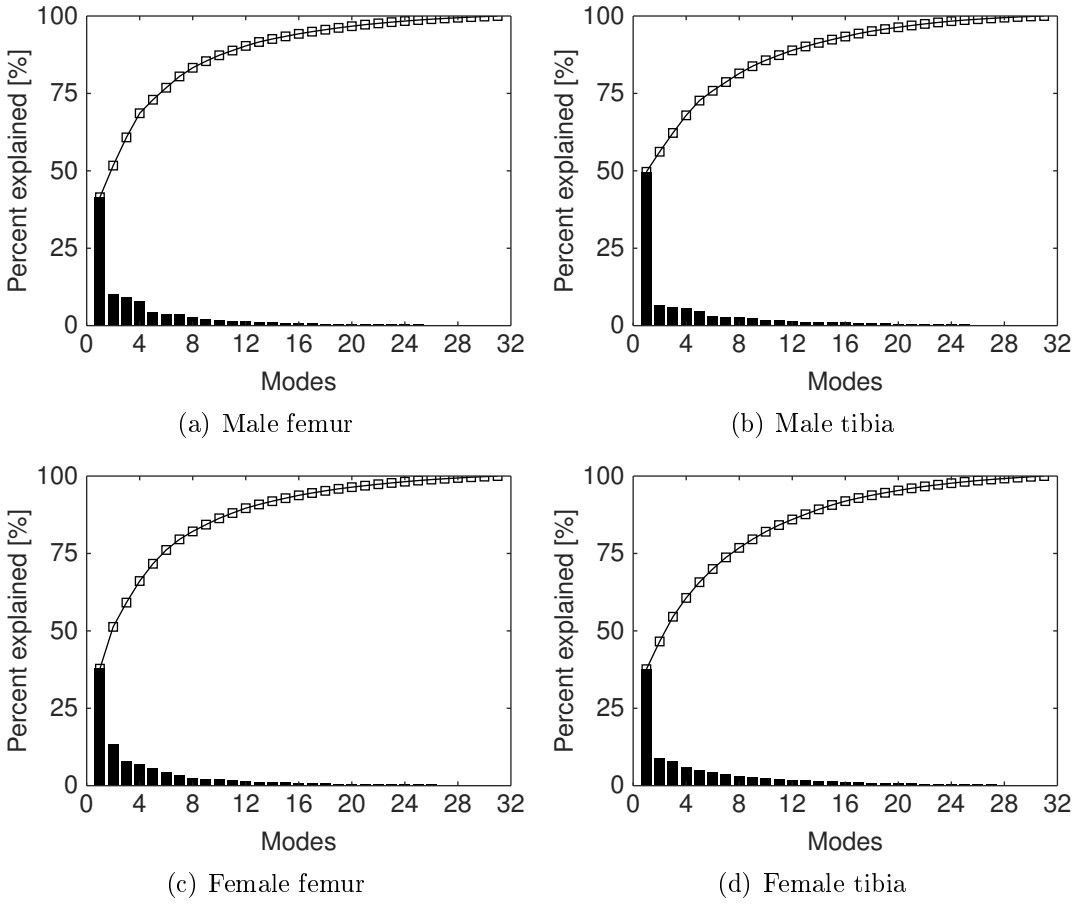

(a) Male femur (b) Male tibia

(c) Female femur (d) Female tibia

Figure 4.9: Male and female knee Pareto charts (Illustration: J. v.d. Merwe)

cally significant non-zero correlations with the targets. Figures 4.14 and 4.15 illustrate the point-wise standard errors of the estimate for the reconstructed shapes. Errors were larger for the male knees than the female knees, with the highest concentrations typically found on the bone shapes. The femurs' condylar tidemarks and the tibias' cortical rims also appeared to have larger errors than the remaining areas of the shape in most cases.

The first and third columns in Tables 4.5 and 4.6 list the mean and standard deviation for the various morphological measurements performed on the training and unseen knees. The remaining columns show the standard errors of the estimate σ_E of these same measurements obtained from the corresponding shapes and fitted models, as well as their correlation coefficients r with the targets. First, we consider the corresponding training meshes. All measurements showed moderate to strong correlations with the sampled training shapes, apart from the tLr in the men's case and the fAr, tGCd and tLr of the women that correlated poorly. All measurements except the female tLr exhibited non-zero correlation at the 95% significance level. The standard error of the distance measurements on the corresponding sets ranged between

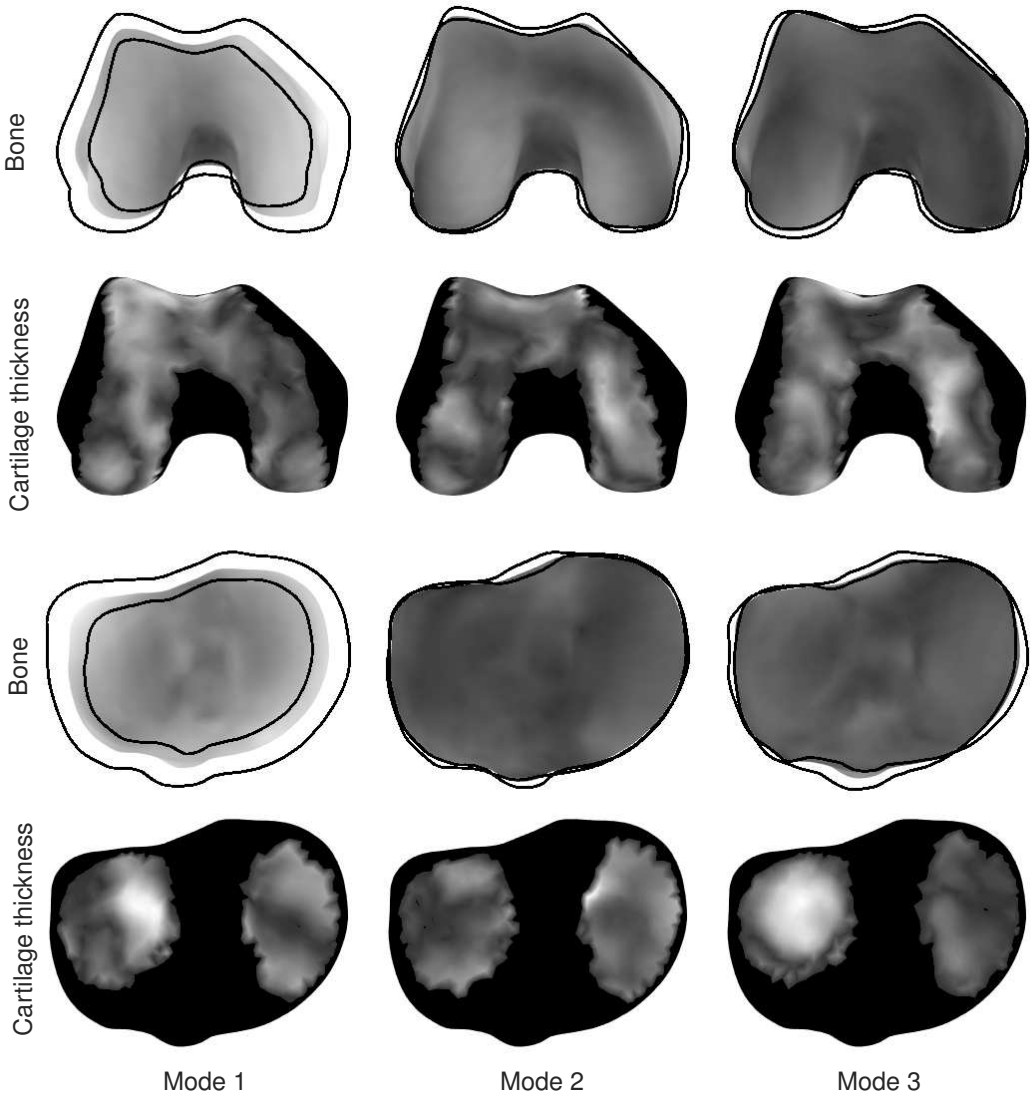

Figure 4.10: First three modes of the male knee (Illustration: J. v.d. Merwe)

0.37 and 0.82 mm, apart from the tGCd that exceeded 2.4 and 2.7 mm in both men and women respectively. The angular errors of the femurs ranged from 0.09 to 0.73° and between 0.32 and 2.13° for the tibias, with the tibial male medial condyle being least well reproduced. The anterior radii of the femurs had errors in excess of 2.4 and 3.3 mm for men and women respectively, while all remaining radii measurements had errors ranging between 0.32 and 1.92 mm. When reconstructing unseen shapes, the morphological results for the male femur showed moderate to strong correlations, apart from the fAr which had an error of 5.82 mm. The female femur model performed less well during reconstruction with all radii measurements as well as the fMLDa ex-

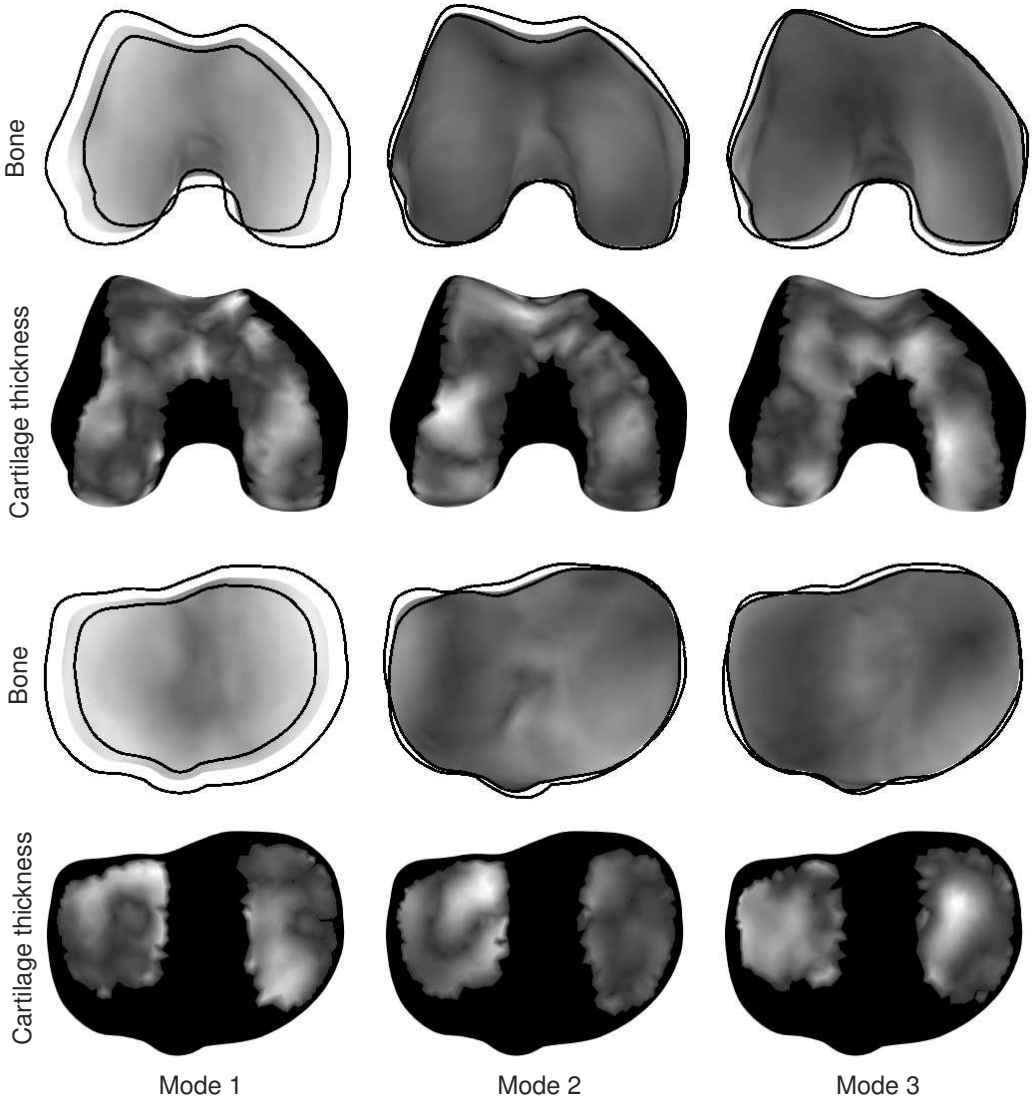

Figure 4.11: First three modes of the female knee (Illustration: J. v.d. Merwe)

hibiting poor correlation. Again, the fAr had a large error of 4.27 mm. For both male and female tibias, the tGCd had errors in excess of 3.6 mm, while the tLPa and varus angles' errors ranged from 3.56 to 5.19°. The womens' tibial condyle radii were also poorly correlated. In most of the aforementioned, unseen cases where large errors or poor correlations occur, significant non-zero correlation between the reconstruction and target measurements could not be observed. Nevertheless, the remaining reconstructed distance errors were all between 0.58 and 1.99 mm, angular errors were between 0.59 and 1.91°, and radii between 0.83 and 1.84 mm.

Table 4.1: Mean RMS surface errors, male knee

	Training data			Unseen data		
	Bone	Cartilage	Thickness	Bone	Cartilage	Thickness
ROI	mean RMS $\pm \sigma_M$					
fFS	0.17 ± 0.003			0.77 ± 0.032		
fAS	0.15 ± 0.003	0.12 ± 0.002	0.13 ± 0.002	0.58 ± 0.036	0.62 ± 0.048	0.50 ± 0.050
fMC	0.16 ± 0.003	0.11 ± 0.003	0.14 ± 0.002	0.53 ± 0.052	0.57 ± 0.049	0.41 ± 0.050
fLC	0.16 ± 0.003	0.12 ± 0.003	0.14 ± 0.002	0.64 ± 0.045	0.71 ± 0.086	0.58 ± 0.083
fAC	0.14 ± 0.004	0.12 ± 0.003	0.12 ± 0.002	0.56 ± 0.038	0.56 ± 0.057	0.46 ± 0.057
tFS	0.16 ± 0.002			0.84 ± 0.035		
tAS	0.15 ± 0.004	0.08 ± 0.002	0.09 ± 0.003	0.64 ± 0.037	0.69 ± 0.053	0.57 ± 0.048
tMC	0.16 ± 0.003	0.08 ± 0.003	0.09 ± 0.003	0.56 ± 0.042	0.65 ± 0.074	0.51 ± 0.056
tLC	0.14 ± 0.004	0.08 ± 0.003	0.10 ± 0.003	0.70 ± 0.054	0.71 ± 0.071	0.59 ± 0.074

Table 4.2: Mean RMS surface errors, female knee

	Training data			Unseen data		
	Bone	Cartilage	Thickness	Bone	Cartilage	Thickness
ROI	mean RMS $\pm \sigma_M$					
fFS	0.15 ± 0.003			0.64 ± 0.034		
fAS	0.14 ± 0.003	0.11 ± 0.002	0.13 ± 0.003	0.52 ± 0.031	0.51 ± 0.021	0.42 ± 0.019
fMC	0.12 ± 0.003	0.11 ± 0.003	0.14 ± 0.003	0.47 ± 0.033	0.49 ± 0.018	0.38 ± 0.016
fLC	0.15 ± 0.003	0.12 ± 0.003	0.13 ± 0.003	0.44 ± 0.046	0.49 ± 0.039	0.38 ± 0.028
fAC	0.12 ± 0.003	0.11 ± 0.003	0.13 ± 0.003	0.64 ± 0.055	0.55 ± 0.031	0.49 ± 0.034
tFS	0.15 ± 0.002			0.69 ± 0.041		
tAS	0.14 ± 0.002	0.08 ± 0.002	0.09 ± 0.002	0.54 ± 0.042	0.56 ± 0.054	0.41 ± 0.039
tMC	0.14 ± 0.003	0.08 ± 0.002	0.09 ± 0.004	0.45 ± 0.057	0.50 ± 0.068	0.39 ± 0.055
tLC	0.13 ± 0.003	0.08 ± 0.002	0.09 ± 0.003	0.60 ± 0.045	0.60 ± 0.050	0.42 ± 0.035

Table 4.3: Mean cartilage measurements, male knee

		Training data	Correspondence	Unseen data	Reconstruction
Measurement		mean $\pm\sigma$			
fAS	[mm]	2.32 ± 0.26	2.53 ± 0.27	2.31 ± 0.17	2.62 ± 0.16
fMC	[mm]	2.11 ± 0.23	2.34 ± 0.26	2.09 ± 0.16	$2.20 \pm 0.12^*$
fLC	[mm]	2.28 ± 0.28	2.47 ± 0.29	2.29 ± 0.21	2.71 ± 0.27
fAC	[mm]	2.63 ± 0.34	2.80 ± 0.36	2.61 ± 0.23	$2.98 \pm 0.22^*$
tAS	[mm]	2.33 ± 0.23	2.65 ± 0.29	2.31 ± 0.26	2.63 ± 0.37
tMC	[mm]	2.11 ± 0.26	2.34 ± 0.31	2.02 ± 0.21	2.26 ± 0.23
tLC	[mm]	2.59 ± 0.30	2.90 ± 0.34	2.61 ± 0.35	$2.94 \pm 0.51^*$

* $p \geq 0.05$

4.4 Discussion

The SSM yielded excellent reconstruction accuracy for all training data and good results for the unseen cases with mean surface errors ranging between 0.38 and 0.84 mm, with the medial condyles faring slightly better than the lateral. Furthermore, the morphological measurements relating to the medial and lateral femoral condyles in particular showed good results, with reconstruction errors for the unseen data ranging between 0.58 and 1.62 mm and 0.59 and 1.69° respectively. In contrast, local measurements that span the

Table 4.4: Mean cartilage measurements, female knee

Measurement		Training data	Correspondence	Unseen data	Reconstruction
		mean $\pm\sigma$			
fAS	[mm]	1.90 ± 0.16	2.10 ± 0.16	1.81 ± 0.22	2.10 ± 0.24
fMC	[mm]	1.85 ± 0.18	2.04 ± 0.20	1.76 ± 0.18	2.00 ± 0.27
fLC	[mm]	1.88 ± 0.17	2.04 ± 0.17	1.72 ± 0.25	1.85 ± 0.23
fAC	[mm]	2.09 ± 0.22	2.24 ± 0.23	1.99 ± 0.35	2.51 ± 0.39
tAS	[mm]	1.85 ± 0.20	2.03 ± 0.23	1.84 ± 0.26	1.87 ± 0.14
tMC	[mm]	1.71 ± 0.19	1.88 ± 0.21	1.70 ± 0.24	1.71 ± 0.26
tLC	[mm]	2.06 ± 0.26	2.19 ± 0.28	2.01 ± 0.35	$2.03 \pm 0.10^{*}$

* $p \geq 0.05$

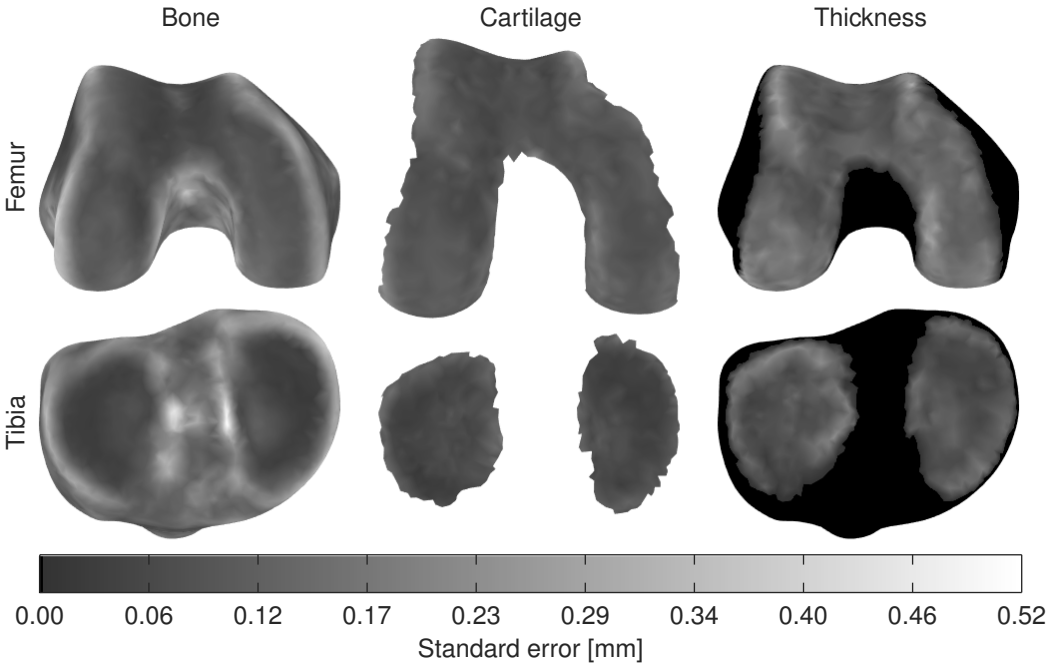

Figure 4.12: Male knee correspondence error (Illustration: J. v.d. Merwe)

femoral anterior condyle and tibial RIOs had poorer reconstruction accuracies. The method of statistical shape modelling as applied to the available data was therefore deemed sufficiently accurate to incorporate into the design of unicompartmental medial and lateral femoral components. In any case, anatomically relevant local morphological measurements in addition to the more common global surface metrics should invariably be used to validate SSMs intended for use in clinical applications. Towards that end and to the extent of our knowledge, this is the first study that investigates the ability of SSMs to represent specific ROIs of the distal femur and proximal tibia in terms of both surface metrics and local morphological measurements.

Our models are based on data from the freely available non-exposed control cohort of the OAI. While direct comparisons cannot be made due to differ-

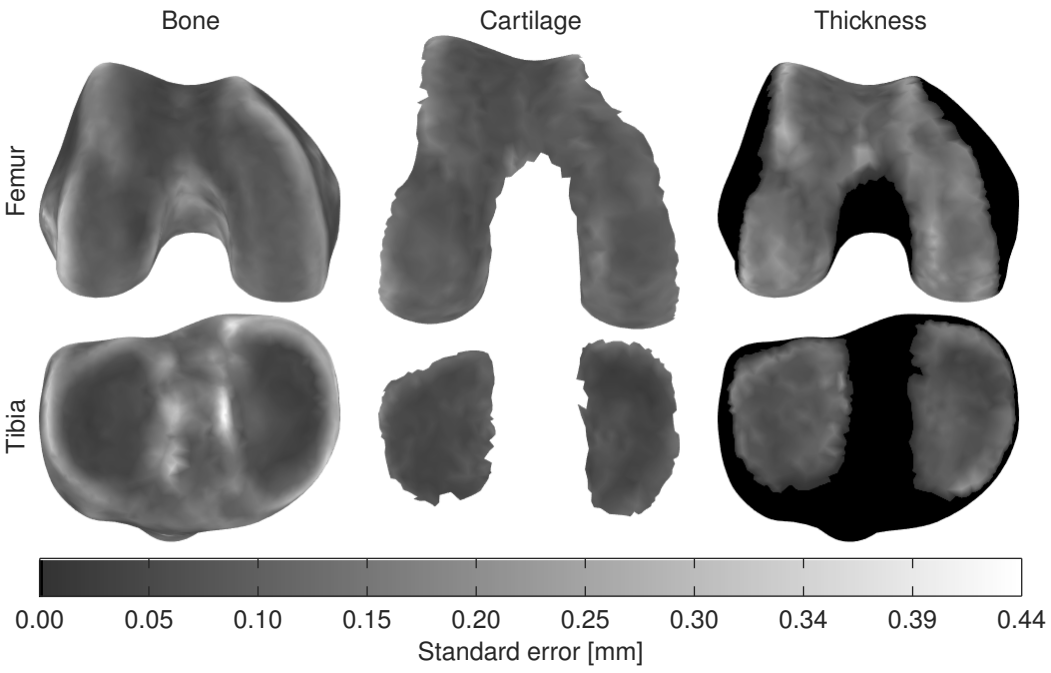

Figure 4.13: Female knee correspondence error (Illustration: J. v.d. Merwe)

ent methods, morphological measurements performed on the distal femur and proximal tibia were within the expected ranges observed in literature (Cobb *et al.*, 2008; Iranpour *et al.*, 2010; Mahfouz *et al.*, 2012). Similarly, the average cartilage thickness per region as well as the thickness distribution match well against the weight bearing regions found in other studies (Cohen *et al.*, 1999; Williams *et al.*, 2006). Furthermore, the variation exhibited by the first three modes of the distal femur and proximal tibia models appear similar to a study by Pedoia *et al.* (2015). They also found that, as is expected for non-scale normalised models, the first and largest mode of variation affects the size of the reconstruction. For the distal femur, the second and third modes adjusts the medial and lateral condyles' orientation and notch width, as well as the antero-posterior position of the trochlear region. In the tibia's case, the second and third modes affect the cortical rim and condyle orientation. Finally, a cursory inspection of the Procrustes mean shapes of the male and female distal femurs reveals that that of the women is smaller and narrower than the men's. Indeed, such gender-based differences in shape has previously been reported in literature, and is the reason for separate models in the first place (Mahfouz *et al.*, 2012). We therefore conclude that the data from which our models are constructed adequately represent the sample population.

Furthermore, other authors have also reported segmenting training shapes into anatomic regions of interest, though primarily with a focus towards establishing landmark correspondences or reference frames for cartilage measure-

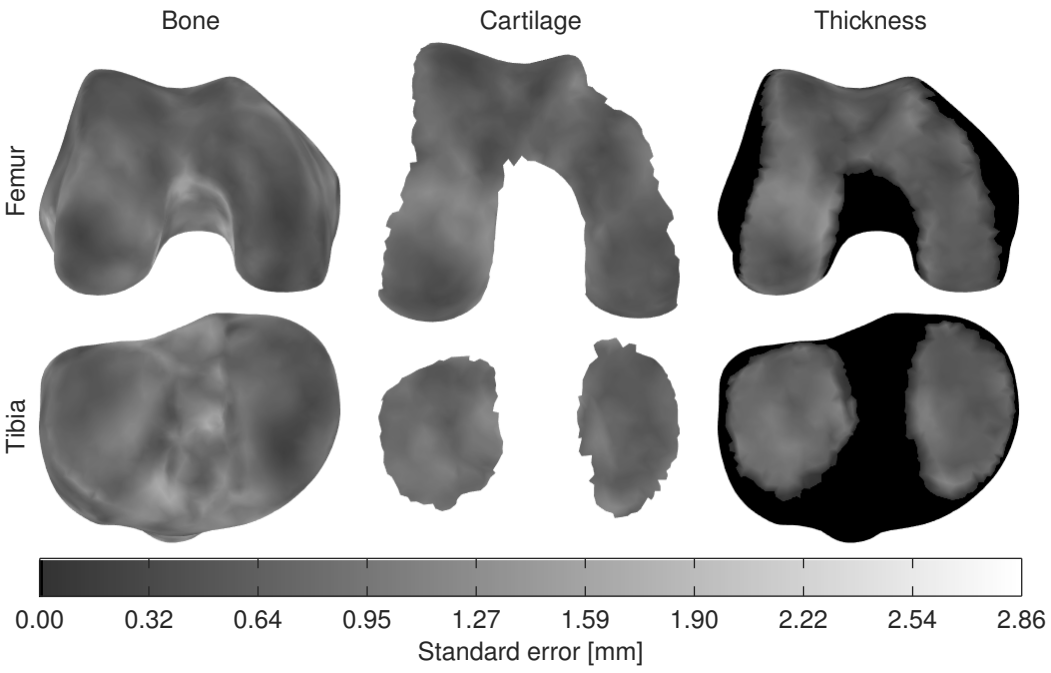

Figure 4.14: Male knee reconstruction error (Illustration: J. v.d. Merwe)

ment. For instance, Williams *et al.* (2006) reports using a SSM constructed from 20 manually segmented distal femurs and proximal tibias. Another example is that of Hunter *et al.* (2010), who first created an average image stack from 160 MRI scans from which the osseous and cartiligenous geometries of the knee were segmented afterwards. In both cases, the established correspondences were used to reliably transfer predefined ROIs to all knees within the training sets in order to investigate their cartilage. While the regions they define focus on the various functional compartments of the femur and tibia, making them similar to those we describe here, as per their scope these studies were limited to female knees and only reported variables relating to changes in cartilage due to OA. Therefore, as far as we may be certain we report here the first instance of a SSM study representing gender-based condylar ROI variation for the knee's bone and cartilage both.

The statistical shape model algorithms we implemented were loosely based on that of the Point Distribution Model (PDM) first introduced by Cootes *et al.* (1995, 2004), and well served to address each of the important aspects of shape model construction: correspondence, alignment, dimensionality reduction and reconstruction. We elected to use a probabilistic pair-wise non-rigid transformation procedure to estimate landmark correspondences rather than surface parametrisations or homeomorphic mappings, a method which has recently been garnering especial interest in literature (Rasoulian *et al.*, 2012; Mutsvangwa *et al.*, 2015; Pedoia *et al.*, 2015). As a result, our training data

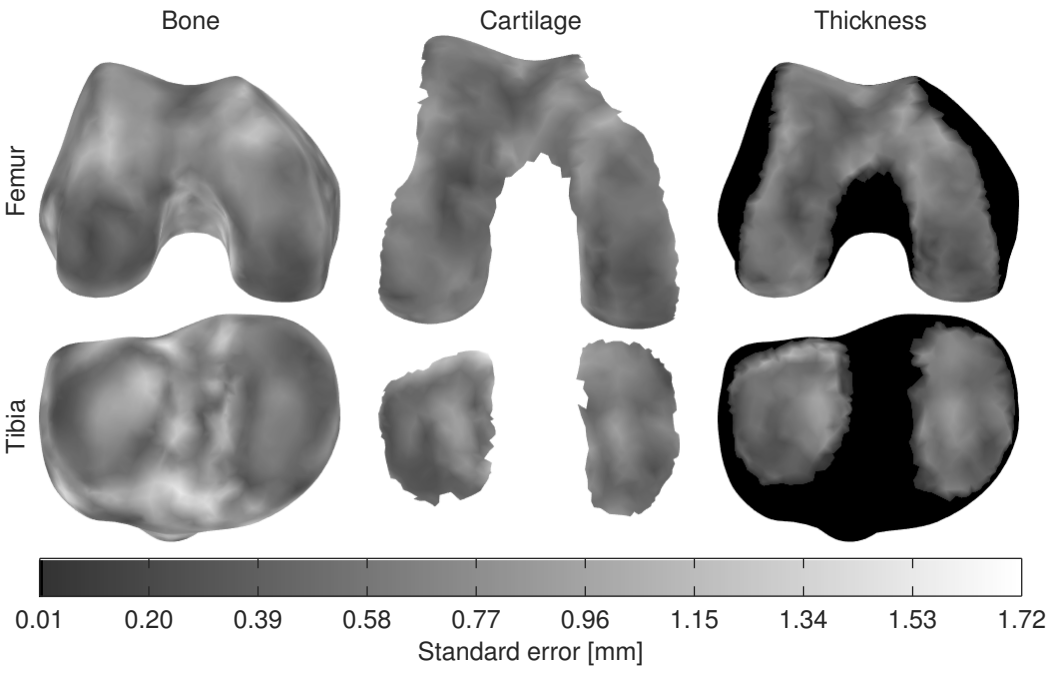

Figure 4.15: Female knee reconstruction error (Illustration: J. v.d. Merwe)

could be represented with surface errors considerably less than the voxel resolution of the MRI scans themselves. Still, it may be observed that correspondence errors were mainly concentrated on bone areas with high curvature, possibly as a result of motion smoothing. The same errors were uniformly distributed over the cartilage surface and thickness, although the latter was generally overestimated. In contrast, reconstruction errors for the unseen data where larger, with poorer fits in particular on the tidemarks of the femur's bone and cartilage, while the cartilage thickness was in general again over-estimated. Furthermore, a potential drawback of the approach is its susceptibility to bias introduced by the selection of an initial representative shape for pair-wise correspondence and shape alignment prior to PCA. However, we found through experimentation that the model's generalisation ability is sufficient such that choosing different starting meshes had little effect on global reconstruction accuracy. This might be due to dense oversampling, the probabilistic nature of CPD correspondence, the effect of the regularisation term, or any combination of the aforementioned. The success of the model is further supported by our reported average errors of less than 1 mm which comfortably falls within the range of similar studies from literature (Baek *et al.*, 2013; Mahfouz *et al.*, 2007; Van Haver *et al.*, 2014; Zhang *et al.*, 2014).

In contrast, while the importance of evaluating SSM performance at the hand of local morphological measurements has been highlighted before, detailed investigations of local model reconstruction errors in literature appear

Table 4.5: Morphological measurement errors, male knee

		Training data	Correspondence error	Unseen data	Reconstruction error
Measurement		mean $\pm\sigma$	σ_E, r_c	mean $\pm\sigma$	σ_E, r_c
fTEd	[mm]	87.99 $\pm$ 4.38	0.50, 1.00	87.78 $\pm$ 2.86	1.50, 0.92
fAPMd	[mm]	63.41 $\pm$ 3.55	0.56, 1.00	62.33 $\pm$ 4.16	0.58, 0.99
fAPLd	[mm]	66.52 $\pm$ 3.29	0.82, 1.00	66.06 $\pm$ 4.64	1.62, 0.99
fMLAa	[deg]	4.30 $\pm$ 2.97	0.73, 0.98	5.07 $\pm$ 2.90	1.69, 0.94
fMLPa	[deg]	-0.35 $\pm$ 1.46	0.09, 0.99†	-0.52 $\pm$ 1.57	1.05, 0.90
fMLDa	[deg]	0.91 $\pm$ 1.14	0.09, 1.00	0.97 $\pm$ 1.40	0.59, 0.98
fMr	[mm]	21.41 $\pm$ 1.75	0.60, 0.97	21.23 $\pm$ 1.81	0.83, 0.94
fLr	[mm]	21.71 $\pm$ 1.31	0.56, 0.92	21.83 $\pm$ 1.48	1.08, 0.74
fAr	[mm]	26.29 $\pm$ 3.53	2.43, 0.81	29.05 $\pm$ 3.86	5.82, 0.45*
tMLd	[mm]	81.39 $\pm$ 4.14	0.60, 1.00	82.39 $\pm$ 1.98	1.52, 0.62*†
tAPd	[mm]	62.33 $\pm$ 3.53	0.64, 1.00	62.83 $\pm$ 3.50	1.99, 0.97
tGCd	[mm]	30.86 $\pm$ 3.14	2.41, 0.77	33.78 $\pm$ 3.75	3.66, 0.91
tMPa	[deg]	2.51 $\pm$ 3.22	2.05, 0.85	2.21 $\pm$ 2.56	1.91, 0.76
tLPa	[deg]	2.44 $\pm$ 2.98	0.32, 0.99	1.66 $\pm$ 3.39	3.68, 0.84
tMVa	[deg]	8.69 $\pm$ 3.60	2.13, 0.82	9.56 $\pm$ 2.64	5.19, -0.02*
tLVa	[deg]	4.34 $\pm$ 4.42	0.91, 0.99	4.66 $\pm$ 3.81	4.06, 0.51*
tMr	[mm]	27.32 $\pm$ 2.47	1.92, 0.85	25.50 $\pm$ 2.43	1.93, 0.76†
tLr	[mm]	20.76 $\pm$ 1.63	1.58, 0.58	20.14 $\pm$ 1.25	1.53, 0.78

* $p \geq 0.05$, † Spearman's correlation

Table 4.6: Morphological measurement errors, female knee

		Training data	Correspondence error	Unseen data	Reconstruction error
Measurement		mean $\pm\sigma$	σ_E, r_c	mean $\pm\sigma$	σ_E, r_c
fTEd	[mm]	77.65 $\pm$ 3.68	0.37, 1.00	77.07 $\pm$ 3.11	1.18, 0.97
fAPMd	[mm]	58.36 $\pm$ 2.22	0.58, 0.99†	57.49 $\pm$ 1.89	0.87, 0.99
fAPLd	[mm]	60.78 $\pm$ 2.45	0.55, 1.00	59.65 $\pm$ 2.45	1.23, 0.97
fMLAa	[deg]	5.68 $\pm$ 2.33	0.58, 0.97	4.72 $\pm$ 2.85	0.82, 0.98
fMLPa	[deg]	1.02 $\pm$ 1.43	0.08, 1.00	0.63 $\pm$ 0.79	0.59, 0.79
fMLDa	[deg]	2.73 $\pm$ 1.51	0.22, 0.99	2.66 $\pm$ 0.55	0.77, 0.65*
fMr	[mm]	19.31 $\pm$ 1.24	0.32, 0.98	18.56 $\pm$ 0.61	0.70, 0.43*
fLr	[mm]	18.50 $\pm$ 1.22	0.59, 0.93	17.77 $\pm$ 0.65	1.01, 0.42*
fAr	[mm]	24.22 $\pm$ 3.60	3.32, 0.55	23.04 $\pm$ 3.04	4.27, -0.60*
tMLd	[mm]	72.10 $\pm$ 2.95	0.53, 1.00	71.30 $\pm$ 3.13	1.07, 0.98
tAPd	[mm]	54.95 $\pm$ 2.76	0.63, 1.00	53.87 $\pm$ 2.37	0.91, 0.95
tGCd	[mm]	26.22 $\pm$ 3.06	2.73, 0.69	27.00 $\pm$ 3.11	3.85, 0.88
tMPa	[deg]	-0.19 $\pm$ 3.30	1.04, 0.96	-1.39 $\pm$ 4.54	1.36, 0.97
tLPa	[deg]	0.10 $\pm$ 3.34	0.44, 0.99	1.69 $\pm$ 2.49	3.82, 0.33*
tMVa	[deg]	6.41 $\pm$ 2.57	1.25, 0.90	6.98 $\pm$ 2.25	3.56, 0.43*†
tLVa	[deg]	3.60 $\pm$ 4.70	1.27, 0.97	3.22 $\pm$ 4.29	3.88, 0.86
tMr	[mm]	25.52 $\pm$ 2.09	1.60, 0.79	24.85 $\pm$ 1.98	1.83, 0.61*
tLr	[mm]	18.68 $\pm$ 1.34	1.45, 0.35*	16.57 $\pm$ 1.44	1.84, 0.54*

* $p \geq 0.05$, † Spearman's correlation

to be scarce. Schumann *et al.* (2010) constructed a SSM of the proximal femur from 30 segmented CT scans using the Minimum Descriptive Length (MDL) method for correspondence, intended for 3D reconstructions of 2D X-ray radiographs. They validated the model by measuring a set of the seven most reproducible morphological parameters on normal and outlier ground truth shapes as well as the respective model reconstructions, and afterwards comparing the resulting variation between these two groups. While concluding that the SSM performed equally well for both the normal and outlier sets of test shapes, the error values themselves were not reported for a direct indication

of model accuracy. We computed the standard error and correlations between ground truths and model reconstructions for two sets of 9 morphological parameters. Though correlation could be demonstrated for most model fits, error values ranged between 0.58 and 5.82 mm and 0.59 and 5.19°. Measurements limited to the femoral medial and lateral condyles, however, exhibited errors of up to only 1.62 mm and 1.69° respectively. We speculate that the degradation in results are caused by smoothing inherent in our approach's correspondence and regression steps. Based on the results from Figures 4.12 to 4.15, this seems to especially affect the more prominent anatomical features which are generally used to perform measurements. The results reported in Tables 4.5 to 4.6 therefore serve to reiterate the importance of incorporating local error metrics into SSM validation for clinical applications.

By way of example, consider the measurement errors reported here against generally accepted surgical tolerances. Outliers in a knee implant's post operative angular alignment are often defined as those greater than 3° (Camarda *et al.*, 2015), while component overhang of more than 3 mm has been shown to be detrimental to clinical outcomes (Chau *et al.*, 2009; Mahoney and Kinsey, 2010). To ensure proper support at the bone-implant interface cortical bone is assumed to be 1.5 mm thick, so component undercoverage is recommended to not exceed this value (Fitzpatrick *et al.*, 2007). Allowable error in the AP dimensions during component selection has been prescribed as 3 to 4 mm (Vaidya *et al.*, 2000), while surgeons aim for between 1 and 2 mm planar accuracy during cutting (Lustig *et al.*, 2013; Scholes *et al.*, 2014). Therefore, in order for a model to be useful in a clinical setting, we recommend that its local errors should at least be below 3° and 2 mm to avoid increasing uncertainties related to downstream processes. In our case, both the fMC and fLC meet these conditions, while the remaining femoral and tibial ROIs don't. In future work, it may be beneficial to incorporate prior constraints in order to improve local model accuracy (Albrecht *et al.*, 2013).

4.5 Conclusions

While following best practices within SSM literature, our study is not only unique in its application but in the extended method of validation as well. We developed a PDM based on soft-correspondences between our datasets, and defined anatomic ROIs relating to the pathological geometry in order to investigate the model's estimation accuracy specifically within these features. We further performed a detailed investigation of local morphological landmark reconstruction accuracy to evaluate model performance beyond the global surface metrics most commonly used in literature. Based on our results, we may conclude that the model presented here is suitable for design of medial and lateral femoral components.

5. Estimating patient-specific condylar shapes of the knee

5.1 Introduction

The design of an anatomically correct patient-specific Unicompartmental Knee Replacement (UKR) has some unique challenges, one of which is the focus of this Chapter: what is 'normal' geometry given a pathological knee? A healthy contralateral knee from which to mirror the geometry is not always available, and duplicating scans increases cost as well. We speculate that this may have been a contributing factor to previous patient-specific implant designs being limited to cases where a generic implant would not work, such as revision surgery in the presence of severe bone erosion or abnormal patient geometries. In such cases, only the bone-implant interfaces were customised, with the articulating surfaces based on that of standard implants (Sathasivam *et al.*, 1999; Slamin and Parsley, 2012).

More recent literature, however, describe implants intended to compete with off-the-shelf designs, each with fully customised bearing surfaces in addition to the bone interface (Fitz, 2009; Harrysson *et al.*, 2007; Van den Heever *et al.*, 2012*b*). In most cases a technician must approximate the healthy geometry prior to implant design, but this is both time consuming and subject to observer interpretation. In order to overcome this problem, Van den Heever *et al.* (2011*b*) automated the estimation by training a self-organising map on healthy knee shapes. Their parametrisations, however, were limited to local planar sections and required subsequent manual alignment, while enquiry of a neural network is complicated by its 'black box' nature (Tickle *et al.*, 1998; Malone *et al.*, 2006). So while fully patient-specific implants have been investigated before, there remains a need to obtain a valid estimate of a patient's healthy 3D shape and pose to facilitate the design process.

Towards this end, we propose using the Statistical Shape Models (SSMs) from Chapter 4 to estimate unknown Regions of Interest (ROIs) from partially healthy knees. Such models are often used to extrapolate 3D anatomical structures from incomplete observations (Blanc and Székely, 2012). Applications in literature include reconstructions of 2D radiographs and fluoroscopic images, obscured ultrasound scans and locally digitized points (Heimann and Meinzer,

2009; Sarkalkan *et al.*, 2014), and notably pathological geometries (Krol *et al.*, 2013; Zachow *et al.*, 2005). The particular advantages of using an SSM as opposed to other deformable models are:

- *The model is only able to reproduce the variation found within the population of shapes from which it is trained* (Cootes *et al.*, 1995). In our case, since we trained our SSMs on knees from healthy, gender-divided population samples that had similar age ranges to candidates for UKR, any model reconstruction would reflect the normal, healthy shape one would expect considering the age and gender of such a patient.
- *Dimensionality reduction via Principle Component Analysis (PCA) essentially results in a set of 'global' parameters that affects the entire shape* (Heimann and Meinzer, 2009). Therefore, through the process of adjusting such parameters to best fit some partial input, we simultaneously obtain matching estimates of the omitted portions due to the inherent, global relationships between different parts of the shape. Since the inclusion criteria for UKR requires that there remain certain areas reasonably unaffected by Osteoarthritis (OA) on a given knee, we assume that there will be valid input for our model based on non-pathological data.

Therefore, in this Chapter we expand the previous SSM theory to accommodate the input of partial structures during shape reconstruction, as well as strengthening the model estimates by incorporating prior information in the form of manually identified landmarks. The reason for including prior constraints was because previous tests showed that, while the model yielded acceptable Root Mean Squared Distance (RMSD) errors during surface fitting, it didn't always perform well locally. We therefore developed a graphical user interface that allows a technician to guide the fitting process via manually placing a few such constraining landmarks. The process is iterative, and the user has the freedom to return to and repeat previous steps until they are satisfied with the result. We investigate the method's effectiveness by estimating the medial and lateral condyles of a set of previously unseen distal femurs. The tibia is not considered because matching tibial components will instead be made to fit the geometry of the resulting femoral components. This allows accommodating for the desired kinematics and conformance similar to Walker (1988, 2014), while joint alignment would ideally be pre-defined together with input from the attending surgeon. This will be discussed in a later Chapter. Implementation of the proposed SSM estimation Graphical User Interface (GUI) within a Computer Assisted Design (CAD) pipeline could potentially simplify and speed up the development of patient-specific implants, reducing lead time and improving repeatability.

5.2 Methods

5.2.1 Overview

Should a patient present with OA, we assume that both the bone and cartilage has degraded in the regions affected (Hernborg and Nilsson, 1973; Nagaosa *et al.*, 2002). Regardless of which Region of Interest (ROI) must be estimated, it is further also assumed that the cartilage surface as a whole will never be available as part of the input since it is generally more difficult to segment than bone. In addition, if properly validated, it might also be possible to use CT imaging instead of MRI as part of our implant design process in future. The current shape estimation process may be summarised as follows:

1. Segment the bone of the distal femur from a patient MRI scan.
2. Align the segmented mesh to the model coordinate system.
3. Define the ROI as the vertices of the model mesh on the pathological bone region, as well as the entire cartilage surface.
4. Identify homologous landmarks on both the patient and model meshes.
5. Perform sparse model fitting using the identified landmarks, excluding the ROI.
6. Construct posterior (constrained) shape model from the remaining variation.
7. Establish dense correspondences between the posterior model and patient mesh via Coherent Point Drift (CPD).
8. Perform posterior model fitting using CPD result, excluding the ROI.

While the pathological ROI is excluded during the fitting procedures, as mentioned the optimised model parameters affect the reconstruction as a whole. Therefore, once the model is fitted to the partial input, it naturally also includes the most likely shapes of the missing ROI on the bone and cartilage surfaces. The various shape estimation stages for the bone surface are illustrated in Figure 5.6 as part of the case study discussed later.

5.2.2 Shape estimation

In order to estimate an individual's pre-pathological geometry from some unaffected part, we follow a similar approach to the SSM fitting procedure described in Chapter 4 using Equations 4.4 and 4.6. However, $\mathbf{y}$ now represents a partial input observation along with $\mathbf{L}$, a linear mapping to the non-pathological training set (Blanz *et al.*, 2004). In our case, $\mathbf{L}$ defines the subset of landmarks that excludes pathological ROI's during shape estimation. In order to estimate a full shape $\tilde{\mathbf{x}}$ from partial input such that:

$$\mathbf{y} = \mathbf{L}\tilde{\mathbf{x}} + \mathbf{N}_R \tag{5.1}$$

We apply the mapping $\mathbf{L}$ to each of the eigenvector matrix's columns to obtain the predictor's component directions $\mathbf{U}_{k_y}$ as well as the centred partial observation $\Delta\mathbf{y} = \mathbf{y} - \mathbf{L}\bar{\mathbf{x}}$. The least squares optimisation problem may then be solved for $\mathbf{b}$ as before, substituting $\mathbf{U}_k$ and $\Delta\mathbf{y}$ respectively.

5.2.3 Posterior shape model

With an appropriate starting alignment between the Procrustes mean and target (or pathological shape in our case), the fitting and estimation procedures discussed generally yield good results. However, it is possible to use prior information to improve the initial estimate as well as constrain the result closer to the span of the model space that best approaches the target shape (Albrecht *et al.*, 2013).

Practically speaking, we manually identify a sparse set of homologous, typically anatomic landmarks contained in both $\bar{\mathbf{x}}$ and $\mathbf{y}$, and find the estimate by modifying $\mathbf{L}$ to map only between these few selected vertices. The result is the most likely shape given the sparse input. The remaining variation can be represented as another statistical shape model which already matches the prior information and has a reduced search space. This posterior shape model may be solved as usual, substituting the posterior mean $\bar{\mathbf{x}}_p$ and eigenvectors $\mathbf{U}_p$ in Equations 4.4 and 4.6. In order to extract the remaining model variation after sparse estimation, the posterior covariance of the data is required (Albrecht *et al.*, 2013):

$$\mathbf{C}_p = \mathbf{U}\eta\boldsymbol{\Sigma}\mathbf{M}^{-1}\boldsymbol{\Sigma}\mathbf{U}^T \text{ where } \mathbf{M} = \boldsymbol{\Sigma}^T(\mathbf{U}_{k_y}^T\mathbf{U}_{k_y} + \eta\boldsymbol{\Lambda}^{-1})\boldsymbol{\Sigma} \tag{5.2}$$

Where $\boldsymbol{\Sigma}$ contains the singular values of the centred training matrix, satisfying $\boldsymbol{\Lambda} = \frac{1}{n_s}\boldsymbol{\Sigma}^T\boldsymbol{\Sigma}$ (refer to Appendix A.3). $\mathbf{C}_p$ is a very large $n_r d \times n_r d$ matrix, so eigenvalue decomposition becomes computationally expensive. An alternative approach to solving the eigenvalue problem is to rewrite $\mathbf{C}_p$ in terms of its much smaller $n_k \times n_k$ inner matrix $\mathbf{C}_i$:

$$\mathbf{C}_p = \mathbf{U}\mathbf{C}_i\mathbf{U}^T \text{ where } \mathbf{C}_i = \eta\boldsymbol{\Sigma}\mathbf{M}^{-1}\boldsymbol{\Sigma} \tag{5.3}$$

The reduced eigenvalue decomposition is then:

$$\mathbf{C}_i = \mathbf{U}_i\boldsymbol{\Lambda}_i\mathbf{U}_i^T \tag{5.4}$$

The final posterior eigenvalues are given by $\boldsymbol{\Lambda}_i$, while the posterior eigenvectors are $\mathbf{U}_p = \mathbf{U}\mathbf{U}_i$. The posterior mean $\bar{\mathbf{x}}_p$ is simply the solution of the sparse fitting procedure from Equation 4.4, and in conjunction with $\mathbf{U}_p$ it defines a new shape model based on the remaining shape variation. This conditional model may then be used in subsequent fitting or estimation steps, for example by now including corresponding pseudo-landmarks on non-pathological ROIs

found via CPD. Figure 5.1 shows the pseudo-code for shape model estimation. Note that the posterior shape model is automatically computed after the estimation process, allowing subsequent calls to the algorithm to have the constrained model parameters as inputs.

Function $[\tilde{\mathbf{v}}, \bar{\mathbf{x}}_p, \mathbf{U}_p] =$ `ssmestimate`$(\mathbf{v}_y, \bar{\mathbf{x}}, \mathbf{\Lambda}, \mathbf{U}, \mathbf{L})$

Input:

$\mathbf{v}_y$	$? \times d$	partial shape point array
$\bar{\mathbf{x}}$	$n_r d \times 1$	Procrustes mean
$\mathbf{\Lambda}$	$n_k \times n_k$	eigenvalue matrix
$\mathbf{U}$	$n_r d \times n_k$	eigenvector matrix
$\mathbf{L}$	$n_r d \times 1$	map of ROIs

Output:

$\tilde{\mathbf{v}}$	$n_r \times d$	estimated complete point array
$\bar{\mathbf{x}}_p$	$n_r d \times 1$	posterior Procrustes mean
$\mathbf{U}_p$	$n_r d \times n_k$	posterior eigenvector matrix

`/* initialisation */`

$\mathbf{b} := \mathbf{b}_0$;

$\tilde{\mathbf{x}} := \tilde{\mathbf{x}}_0$; `/* first estimate */`

$\tilde{\mathbf{y}} := L\tilde{\mathbf{x}}$; `/* mapped partial estimate */`

$\tilde{\mathbf{v}}_y \leftarrow$ `reshape`$(\tilde{\mathbf{y}})$; `/* reshape 1 dimension to` d `*/`

$\mathbf{v}_c \leftarrow$ `cpd`$(\mathbf{v}_y, \tilde{\mathbf{v}}_y)$; `/* establish correspondence */`

`/* estimation */`

while *partial estimate* $\tilde{\mathbf{v}}_y$ *not converged* **do**

- $\mathbf{v}_a \leftarrow$ `oprocrustes`$(\tilde{\mathbf{v}}_y, \mathbf{v}_c)$; `/* align to estimate */`
- $\mathbf{y} \leftarrow$ `reshape`$(\mathbf{v}_a)$; `/* reshape` d `dimensions to 1 */`
- construct $\Delta\mathbf{y}$ and U_{k_y};
- $\mathbf{b}_y \leftarrow$ `solve`$(\mathbf{\Lambda}, \mathbf{U}, \eta, \Delta\mathbf{y})$;
- constrain $\mathbf{b}_y$;
- compute $\tilde{\mathbf{x}}$; `/* updated estimate */`
- $\tilde{\mathbf{y}} := \mathbf{L}\tilde{\mathbf{x}}$; `/* mapped partial estimate */`
- $\tilde{\mathbf{v}}_y \leftarrow$ `reshape`$(\tilde{\mathbf{y}})$; `/* reshape 1 dimension to` d `*/`

end

$\tilde{\mathbf{v}} \leftarrow$ `reshape`$(\tilde{\mathbf{x}})$; `/* reshape` $md \times 1$ `dimensions to` $m \times d$ `*/`

reverse $\tilde{\mathbf{v}}$'s pose; `/* align estimate to input shape */`

`/* Posterior model */`

$\bar{\mathbf{x}}_p := \tilde{\mathbf{x}}$; `/* posterior mean */`

compute $\mathbf{U}_p$; `/* posterior eigenvectors */`

end

Figure 5.1: Shape model estimation

5.2.4 Shape model evaluation

For the purposes of this study, we are interested only in estimating the femoral Medial Condyle (fMC), the femoral Lateral condyle (fLC) and in certain cases the femoral Cartilage Surface (fCS). The fMC and fLC are the same ROIs defined in Chapter 4, although we set up L so that we exclude both the particular region from the bone of the distal femur along with the entire cartilage surface during estimation. In the case of the fCS we use the entire bone surface to estimate just the missing cartilage. This is intended to serve as a more conservative result for comparison with the fMC and fLC, which has fewer landmarks to serve as input.

Davies (2002) described objective measures with which to evaluate comparisons between different models constructed from the same training set. These include generality and specificity, which are useful for benchmarking model performance against results from literature and for investigating the effects that leaving out different ROI's have. During these tests shape model estimation was performed directly from the coordinate aligned training data, without constrained prior information models. The generality of a model is an indication of how well it is able to match a new observation of the same class. It is constructed using a leave-one-out method based on the RMSD between two surfaces:

$$G(k) = \frac{1}{n_s} \sum_{l=1}^{n_s} \mathrm{RMSD}(\tilde{\mathbf{x}}_l, \mathbf{x}_l) \tag{5.5}$$

Here $\tilde{\mathbf{x}}_l$ is the model instance fitted to the left out member $\mathbf{x}_l$, generated using k principle modes. The standard error of the $G(k)$ mean with standard deviation σ is given by:

$$\sigma_G(k) = \frac{\sigma}{\sqrt{n_s - 1}} \tag{5.6}$$

Specificity, on the other hand, measures a model's ability to reproduce shape instances that are similar to those within the training set. It is defined by:

$$S(k) = \frac{1}{n_m} \sum_{l=1}^{n_s} \mathrm{RMSD}(\tilde{\mathbf{x}}_l, \acute{\mathbf{x}}_l) \tag{5.7}$$

where $\tilde{\mathbf{x}}_l$ represents each of the n_m randomly generated model instances with parameters $\mathrm{b}_e \in [-3\lambda_e, 3\lambda_e]$. The shape within the training set with the lowest RMS deviation from the generated instance is indicated by $\acute{\mathbf{x}}_l$. Results reported here are for $n_m = 100$ trials, with the standard error for specificity given by:

$$\sigma_S(k) = \frac{\sigma}{\sqrt{n_m - 1}} \tag{5.8}$$

Comparatively lower values of $G(k)$ and $S(k)$ indicate better generality or specificity for a particular model, respectively. We compared generality and specificity when omitting different ROI's during estimation procedures in order to investigate the shape model's reconstruction capabilities. For standard errors of the various model instances that overlap, we assume that there are no statistically significant differences between the data, while the converse holds for gaps between error bars that are greater than the average of the respective standard errors (Davies, 2002; Cumming *et al.*, 2007). During generality and specificity, each ROI for the left out shape was removed in turn prior to shape estimation. The surface error was then computed between the full original and reconstructed shapes. Registration for specificity was similar to the estimation algorithm used during generality, with the exception of $\mathbf{b}$ being randomly generated rather than initialised to zero and then iteratively solved.

The GUI shown in Figure 5.2 was created using Matlab in order to incorporate manually identified landmarks as prior information for constrained model fitting. It displays the pathological input bone mesh as well as the model result without cartilage, and allows the user to freely zoom, rotate, pan and toggle the visibility and opacity for each. The user is required to identify a predefined set of landmarks on both meshes, with the option to include more as required. Note that landmarks cannot be placed on the highlighted area of the model, which represents the pathological ROI. Once all the predefined landmarks have been located, a sparse estimation process may be performed based on them. This determines the initial alignment between the meshes and returns the initial fit as well as the posterior shape model. Afterwards, correspondence is manually initiated and the ROI is estimated by fitting the partial, constrained model to a dense point cloud containing only the healthy portions of the knee. The user may at any time return to and redo a previous step, with the display being updated accordingly.

Since this work is intended to form part of patient-specific implant design, apart from the accuracy of our results we were also interested in the method's repeatability given the user interaction as well as the effect of the number of landmarks used for the model prior. We therefore had a single user perform model fitting via the GUI for eight male and eight female, previously unseen, healthy distal femurs while excluding in turn the medial and lateral condyles. For every observation, we defined two sets of three and seven landmarks respectively, and repeated all observations three times. To avoid memorisation, the order of every unique combination of test variables were randomised during each repetition. The landmarks of each set and for the respective condyles are listed in Table 5.1 and shown in Figure 3.2.

For each observation, we computed the RMSD of the respective ROIs between the model reconstruction and healthy input shapes. Repeatability was evaluated by fitting a one way balanced ANOVA on the RMSD results from repeated observations for every unique combination of male and female knees, three and seven landmarks, and the different ROIs, assuming that the sample

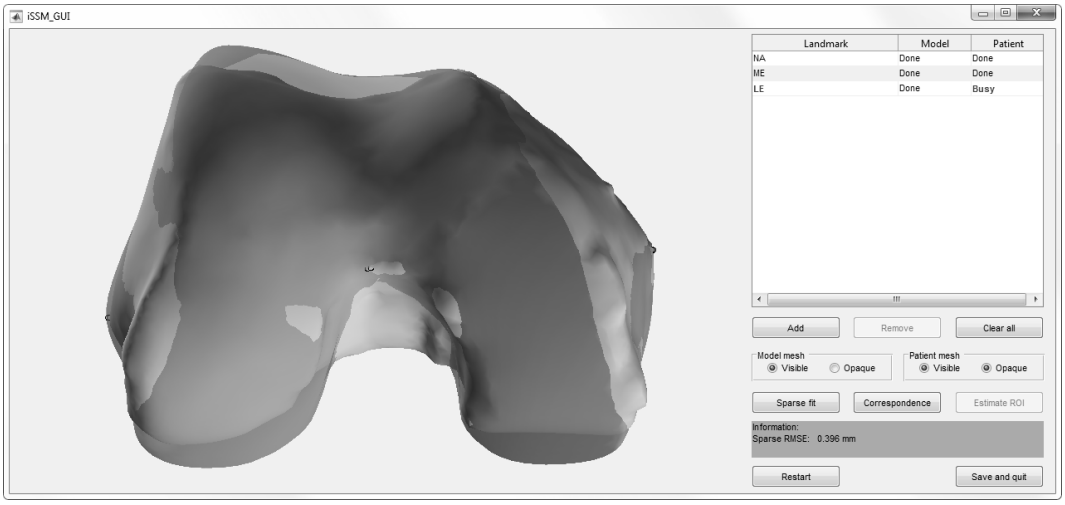

Figure 5.2: Statistical shape model GUI (Illustration: J. v.d. Merwe)

Table 5.1: Predefined landmarks

		Landmark set		ROI	
ID	**Landmark**	**Three**	**Seven**	**fMC**	**fLC**
fINA	Intercondylar notch apex	✓	✓	✓	✓
fME	Medial epicondyle	✓	✓	✓	✓
fLE	Lateral epicondyle	✓	✓	✓	✓
fMTP	Medial trochlea peak		✓	✓	✓
fLTP	Lateral trochlea peak		✓	✓	✓
fMDP	Medial distal point		✓		✓
fMPP	Medial posterior point		✓		✓
fLDP	Lateral distal point		✓	✓	
fLPP	Lateral posterior point		✓	✓	

of input knees were the only source of variance. Two way balanced ANOVA was performed to compare the two sets of three landmarks defined on the male and female knees for the various ROIs. The only sources of variance in this case were assumed to be due to the sample population and the two sets of landmarks. The level of significance was set at $p < 0.05$ for all cases and normality was confirmed via χ^2 tests. The investigation was performed in Matlab.

All tests discussed up to now merely removed the ROIs in question from otherwise healthy distal femurs so that model estimates could automatically be compared to the original target. Therefore, Autodesk Meshmixer (Autodesk, California, USA) was used to manually modify the medial condyle of a healthy male knee in order to simulate the pathology that might be encountered in a clinical situation. Four osteophytes were added by locally translating small regions on the periarticular boundary tangential to the articular surface (Hernborg and Nilsson, 1973; Nagaosa *et al.*, 2002; Neogi *et al.*, 2013). Following this, the entire medial condyle's articular area was selected and then

excessively smoothed in order to mimic flattening of the weight bearing areas that occur due to weakening of subchondral bone in OA (Buckland-Wright, 2004). The simulated pathological case was then supplied to the GUI in order to estimate the healthy shape of the affected ROI, which could again be compared to the original, unedited mesh. Figure 5.3 illustrates the original and edited meshes.

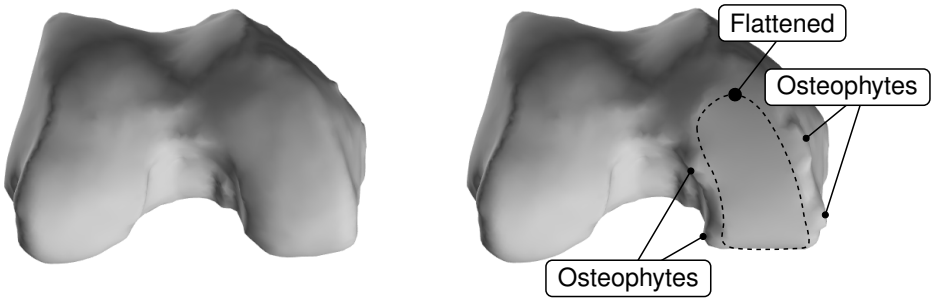

(a) Original (b) Edited

Figure 5.3: Simulated pathology (Illustration: J. v.d. Merwe)

5.3 Results

As mentioned, the shape models we used for estimating missing geometries were those described in Chapter 4. All variables were kept the same, except while fitting the model to a sparse set of landmarks when we modelled the noise variable as $\eta = 1$ based on the observer precision from Chapter 3 (Albrecht *et al.*, 2013). When fitting the posterior shape model to a dense set of pseudo-landmarks, we again set $\eta = 0.5$.

Figures 5.4(a) and 5.4(b) show the generality of the femurs' ROIs, which ranged from 0.67 to 1.09 mm and 0.55 to 0.87 mm for men and women respectively. The fCS yielded slightly better (lower) average errors than the fMC and fLC at higher modes of variation, though no statistically significant differences were observed. Specificity is shown in Figures 5.4(c) and 5.4(d), ranging from 0.92 to 1.75 mm and 0.71 to 1.38 mm for the male and female models. The fCS also performed best, though the differences were again not significant.

The standard deviations of RMSD errors from the repeated observations' geometries are listed in Tables 5.2 and 5.3. This ranged between $\pm$ 0.147 and 0.211 mm for the men, apart from the lateral condyle which exhibited variation in its cartilage and cartilage thickness estimates which was between $\pm$ 0.328 and 0.356 mm. This is supported by Figure 5.5 which illustrates the point-wise standard error of the estimate of the averaged repetitions using three landmarks. The male model's results generally had greater errors than

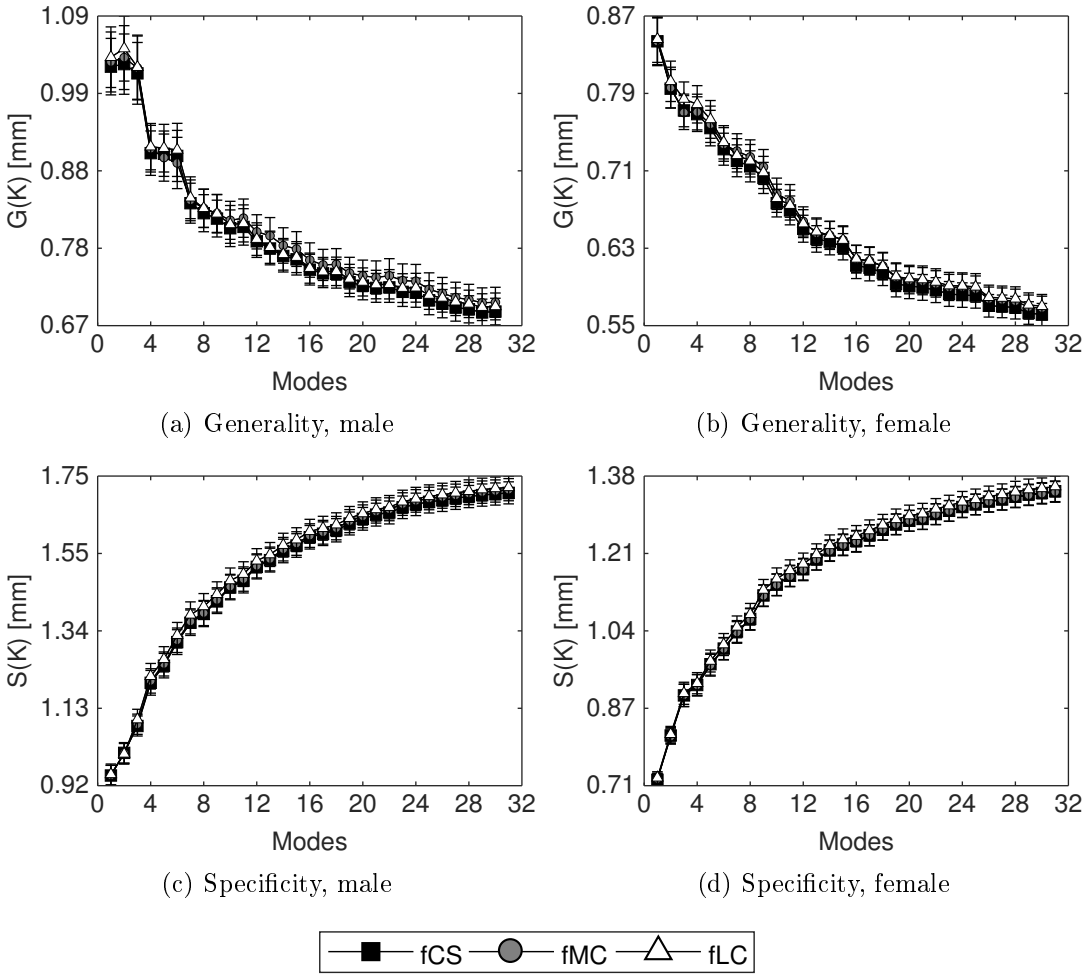

(a) Generality, male

(b) Generality, female

(c) Specificity, male

(d) Specificity, female

Figure 5.4: Generality and specificity of the femur (Illustration: J. v.d. Merwe)

that of the women, which again appear concentrated on the lateral condyle of the cartilage geometries. The standard deviations of the female models were between $\pm$ 0.134 and 0.162 mm, and no statistically significant differences were found between the repetitions' group means in either the men's or women's case.

Table 5.2: Standard deviation of repeated measurements, male knee

	Three landmarks			Seven landmarks		
	Bone	**Cartilage**	**Thickness**	**Bone**	**Cartilage**	**Thickness**
ROI	$\pm\ \sigma_w$ [mm]					
fMC	$\pm$ 0.180	$\pm$ 0.211	$\pm$ 0.149	$\pm$ 0.187	$\pm$ 0.207	$\pm$ 0.184
fLC	$\pm$ 0.147	$\pm$ 0.356	$\pm$ 0.349	$\pm$ 0.190	$\pm$ 0.344	$\pm$ 0.328

Table 5.3: Standard deviation of repeated measurements, female knee

	Three landmarks			Seven landmarks		
	Bone	Cartilage	Thickness	Bone	Cartilage	Thickness
ROI	$\pm\,\sigma_w$ [mm]					
fMC	± 0.144	± 0.141	± 0.144	± 0.139	± 0.133	± 0.134
fLC	± 0.134	± 0.141	± 0.135	± 0.160	± 0.162	± 0.147

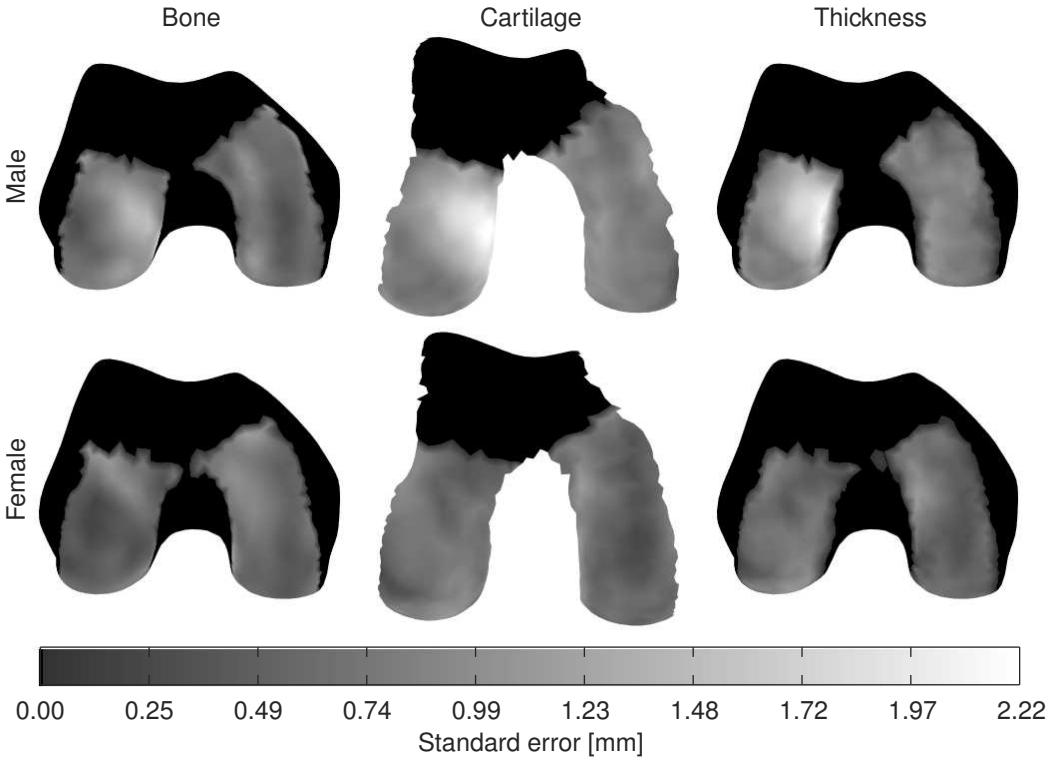

Figure 5.5: Averaged point-wise standard error of the estimate for three user landmarks (Illustration: J. v.d. Merwe)

Tables 5.4 and 5.5 show the mean RMSD surface estimation errors, which ranged between 0.58 and 1.05 mm for the male knees and 0.47 and 0.71 mm for the females. No evidence of significant differences between errors of the two sets of landmarks, three or seven, were found, except for the male lateral cartilage surface ($p = 0.018$). In this case, the mean error for seven landmarks was only slightly lower than for three as per Table 5.4.

The step-by-step results from the simulated pathological case study is illustrated in Figure 5.6. The top left image shows the same set of three landmarks identified on both the target mesh (shaded) and mean model (dots), prior to any estimation procedures. The result from the sparse fit using the three landmarks and from which the posterior model is created, is shown in the top right of the figure. Now the model is aligned to the target, and the landmarks

Table 5.4: Mean RMS surface estimation errors, male knee

	Three landmarks			Seven landmarks		
	Bone	Cartilage	Thickness	Bone	Cartilage	Thickness
ROI	mean RMS $\pm$ σ_M [mm]					
fMC	0.67 $\pm$ 0.065	0.81 $\pm$ 0.078	0.59 $\pm$ 0.055	0.67 $\pm$ 0.063	0.80 $\pm$ 0.072	0.58 $\pm$ 0.063
fLC	0.89 $\pm$ 0.054	1.05 $\pm$ 0.134	0.88 $\pm$ 0.131	0.85 $\pm$ 0.070	1.00 $\pm$ 0.128	0.84 $\pm$ 0.122

Table 5.5: Mean RMS surface estimation errors, female knee

	Three landmarks			Seven landmarks		
	Bone	Cartilage	Thickness	Bone	Cartilage	Thickness
ROI	mean RMS $\pm$ σ_M [mm]					
fMC	0.55 $\pm$ 0.053	0.58 $\pm$ 0.052	0.46 $\pm$ 0.054	0.54 $\pm$ 0.052	0.60 $\pm$ 0.049	0.47 $\pm$ 0.050
fLC	0.54 $\pm$ 0.049	0.70 $\pm$ 0.046	0.55 $\pm$ 0.045	0.55 $\pm$ 0.059	0.71 $\pm$ 0.057	0.56 $\pm$ 0.052

appear to constrain the model to the target quite well at the epicondyles and the notch apex. The anterior and condylar areas are unconstrained at this stage, but the sparse estimate is sufficient for finding CPD correspondences. Using the posterior model, the non-pathological shape of the ROI may then be estimated from the dense set of pseudo-landmarks on the 'healthy' part of the knee. This is shown in the bottom left of Figure 5.6, while the image at the bottom right displays the model result against the original, un-edited target knee. Note that the estimation result has a greater curvature than the flattened surface of the pathological region on the target knee, and that it also underestimates the osteophytes. This is as expected, as the flattened area was mostly excluded from the fitting procedure via the ROI map $\mathbf{L}$, while the model itself can only deform within the space defined by its training set which were healthy knees without osteophytes (Cootes *et al.*, 1995). Using the original as ground truth, the RMS errors of the estimated fMC were 0.58, 0.79 and 0.62 mm for the bone, cartilage surface and cartilage thickness, respectively. The cartilage surface is excluded from the image for the sake of clarity.

5.4 Discussion

The results we present here yielded generality and specificity values well comparable with other studies in literature. Furthermore, good estimation accuracy in the presence of sparse and partial inputs for the fMC and fLC was demonstrated, with mean RMSD values ranging between 0.47 and 1.05 mm depending on the ROI and gender. The user-guided method for incorporating prior information was shown to be repeatable, with few differences found between using different numbers of landmark constraints. Therefore we suggest that, during shape estimation for implant design, the technician adjust the model fit to prioritise the articular regions at the expense of the remaining

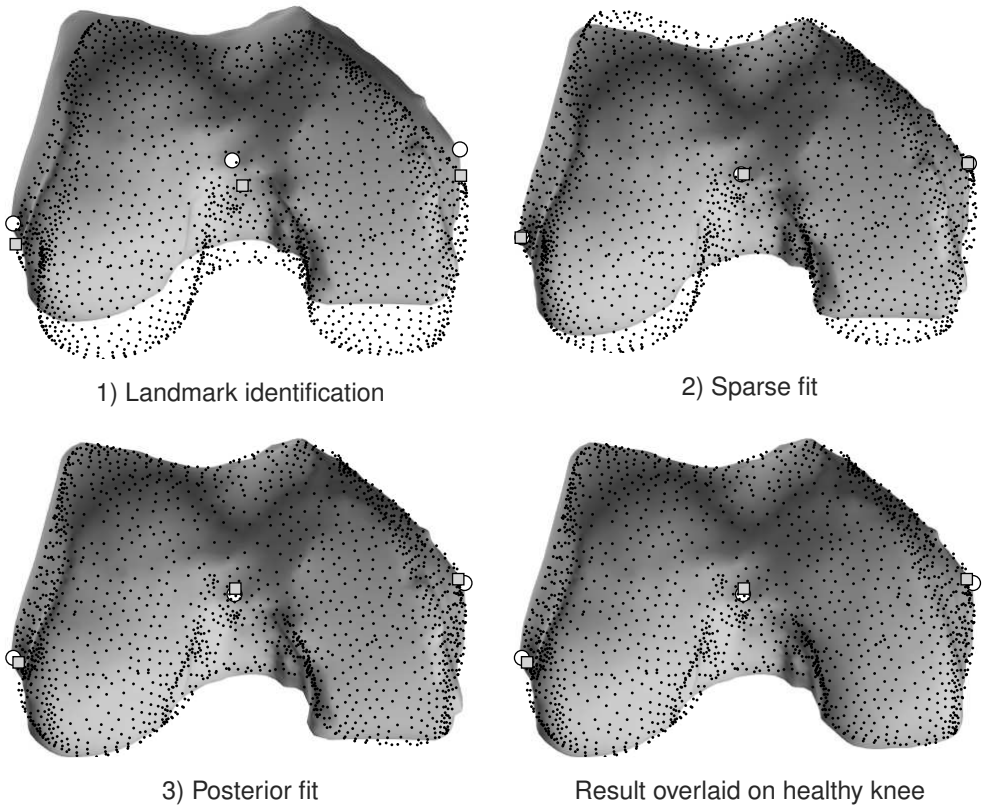

Figure 5.6: Case study (Illustration: J. v.d. Merwe)

bony areas, if necessary. Furthermore, good results may be achieved when starting with fewer prior constraints, and adding more landmarks as needed. Finally, to the best of our knowledge, this is the first study to focus on estimating ROIs of the distal femur's bone and cartilage that relate to UKR design.

Generality and specificity are often reported in literature for the purpose of model comparison, though not usually with sparse data as inputs. However, there are a number of cases in which soft-correspondences during model construction from osseous geometries is used, similar to our approach. For example, Rasoulian *et al.* (2012) developed a group-wise Gaussian Mixture Model (GMM) based registration method in order to establish correspondences between a set of shapes and to find a mean shape. Like Myronenko and Song (2010)'s CPD algorithm, they used an Expectation Maximisation (EM) algorithm to maximise the probability of correspondence between the targets and non-rigid transformations of locally constrained GMM centroids. The group mean was found via Quasi-Newton optimisation prior to a Procrustes analysis that removed pose variations, and the resulting SSM could be registered to

new shape instances by following a similar probabilistic approach to solve the model parameters. Based on their figures, Rasoulian *et al.* (2012) achieved generality values ranging roughly between 0.25 and 1.25 mm for SSMs constructed from 45 L2 vertebra and 42 hippocampi. The same models yielded approximately 0.42 and 2.25 mm for specificity. During another study, Mutsvangwa *et al.* (2015) applied an iterative median closest point algorithm on a dataset of 27 dry bone scapulae in order to generate an intrinsic consensus shape, followed by CPD to create a final, unbiased mean virtual shape and to establish correspondences. They reported generality values for non-normalised model approximations ranging between 1 and 1.9 mm, and specificity values between 1.4 and 1.6 mm. We are satisfied therefore that our results falling between 0.55 and 1.09 mm for generality and 0.71 and 1.75 mm for specificity are comparable to values obtained from similar shape modelling methods reported in literature. Furthermore, we suggest that the effect of excluding different predefined ROIs during model fitting may also be investigated via generality and specificity. In our case, we observed that the fCS performed slightly better than the fMC and fLC in most cases, though statistical significance was not shown.

There are also a number of studies reporting the use of SSMs to extrapolate sparse data inputs (Blanc and Székely, 2012; Heimann and Meinzer, 2009; Sarkalkan *et al.*, 2014). There are, however, relatively few examples of SSMs being employed to estimate geometries typically affected by pathology in literature, and as far as we may be certain, none of the femur and tibia's medial and lateral condyles ROIs. Zachow *et al.* (2005) described reconstructing mandibular dysplasia with a model based on 11 healthy subjects. Their training datasets were subdivided into regional patches each homeomorphic to a disk in order to establish correspondence, while estimation was achieved via Quasi-Newton optimisation of the transformation and model parameters based on the non-pathological portion of a patient's geometry. They reported mean distance errors of 1.2, 1.4 and 1.5 mm for the relevant parts of three case studies. Krol *et al.* (2013) used thin-plate spline transformations to generate correspondences between 50 male and 50 female pelvises, respectively. An evolutionary algorithm was then used in order to find anatomically viable bone shape estimates after tumour resection. Using the unaffected contralateral hemipelvises of eight pathological cases as ground truths, they report achieving a mean deviation distance of 1.76 ± 1.35 mm on the reconstructed equivalents of the defective areas. Albrecht *et al.* (2013) used probabilistic PCA to construct a Point Distribution Model (PDM) from 145 healthy distal femurs in order to estimate the non-pathological geometry of patients with trochlear dysplasia, given a healthy portion of the bone. Model parameters and correspondences were optimised via an implementation of the Iterative Closest Point (ICP) algorithm. Signed distance errors between their model's output and some case's healthy points ranged to within ± 2 mm, with the distribution centred around zero. In our study we employed mean RMSD and

point-wise standard error metrics to validate our model by excluding the fMC and fLC ROIs to simulate the partial input obtained from a pathological knee. The point-wise standard errors for three user landmarks ranged up to 2.22 mm while regional surface metrics fell between 0.47 and 1.05 mm. Although once again direct comparisons cannot be made, the reconstruction results presented here do appear to lie within the range of values one could expect based on our model's generality as well as the error metrics discussed. Furthermore, standard deviations for repeatability were low, with no significant differences between repetitions, and only one case where there was a clear difference between the number of landmarks used as model priori. The case study with simulated pathology also compared well with the original, healthy knee.

Based on the slightly better performance of the fCS as opposed to the fMC and fLC, we speculate that in order to obtain more accurate results, one should minimise the number of landmarks omitted during ROI estimation. We might therefore improve model performance by trimming the excluded articular areas' boundaries, as there is considerable variation at these non-weight bearing peri-articular regions (Williams *et al.*, 2006; Hunter *et al.*, 2010). The most notable effect might be a reduction of the large point-wise errors found on the males' medial cartilage surface seen in Figure 5.5. Furthermore, constrained SSM estimation via the GUI was shown to be repeatable, suggesting that model performance is not duly affected by intra-observer variability. Indeed, there is also the added benefit of being able to guide the model result to better fit (by way of example) the articular regions at the expense of the remainder of the bone shaft. This could potentially mitigate the situation where, even if a low global RMSD value is achieved, poor local fit at the ROI boundary undermines subsequent implant design. However, since the situations where the number of landmarks used as prior information made a difference in the results were limited, we suggest initially using three landmarks (the minimum needed for Procrustes alignment) and adding more constraints as needed, rather than using a larger set to begin with. We found that achieving a good model prior was difficult in some cases if too many landmarks were required before the first sparse fit, and that they should rather be considered individually. Finally, the characteristic behaviour of a successful SSM as discussed in the Introduction was demonstrated in the case study, where the effects of OA was effectively overturned to produce a normal, healthy shape even in the presence of bone deformation.

While we investigated model performance at the hand of standard generality and specificity metrics, in these cases model reconstructions did not make use of prior information as the observer study did. The reason for this was so that we could automate the large number of tests, as well as to more closely conform to the usual methodology reported in literature (Davies, 2002). We already deviated from the norm by incorporating regression based on the partial coordinate aligned meshes, as opposed to just approximating full normal shapes, since this allowed us to investigate the effect of omitting different ROIs.

Furthermore, in Chapter 4 we made the case for using local morphological measurements in addition to surface metrics to evaluate model performance. In fact, the RMSD errors degraded slightly from Tables 4.1 and 4.2 to Tables 5.4 and 5.5 when approximating ROIs from full shapes and reconstructing them from partial inputs. This suggests that the morphological measurements may suffer similarly. However, since most of these measurements span multiple condyles, we did not repeat them here as we focused solely on estimating one ROI at a time, though our work might benefit from comparing the fully approximated and partially reconstructed condyle radii. Finally, while the method we developed here could theoretically be applied to any pre-defined ROI or even combinations thereof, we only considered the case of OA isolated to either the medial or lateral femoral condyles. It may therefore be beneficial to consider estimating bi-unicompartmental geometries, the trochlear groove and even tibial geometries. Unfortunately, these last mentioned cases did not exhibit particularly promising results as per Chapter 4, suggesting even further degradation in model performance should ROIs be omitted. On the other hand, the fMC and fLC exhibited good results throughout and could therefore be used to derive the articular geometries of the tibial components instead. This has the added benefit of being able to match the desired joint mechanics, laxity and alignment, either natural or from surgeon preferences, when using engineering materials in the absence of soft cartilage and menisci (Walker, 1988, 2014).

5.5 Conclusions

We extended the previous SSM methodology to enable constrained shape estimation in the presence of missing regions of interest. Our method was shown to be repeatable, with results comparing well to the state of the art in literature. The findings suggest that our user-guided SSM estimation process is well suited to medial and lateral femoral component design.

6. Semi-automated patient-specific implant design

6.1 Introduction

Unicompartmental Knee Replacement (UKR) retains as much of the joint's natural geometry as possible by only resurfacing the pathological parts, which could result in more natural kinematics compared to total knee arthroplasty (Patil *et al.*, 2005; Newman *et al.*, 1998). Nevertheless, limitations inherent in off-the-shelf implants may cause a mismatch between their shape and the remaining, healthy parts of the knee. These include a predetermined range of sizes (Van den Heever *et al.*, 2012*b*), similar shapes for both medial and lateral condyles (Demange *et al.*, 2015) and poor implant fit (Fitz *et al.*, 2013). Such implants may therefore perform poorly within an individual, and much of the surgical procedure is devoted to fitting the patient to the implant, rather than the other way round.

Patient-specific implants aim to restore an individual's knee to its pre-pathological and corrected state, focusing on improved fit and more natural post-operative kinematics when compared to their off-the-shelf counterparts (Fitz, 2009; Van den Heever *et al.*, 2012*b*). In general, the design workflow of such implants is similar to that of commercially available patient-specific instrumentation, starting from scan-based planning, Computer Assisted Design (CAD) and eventually leading to product commissioning (Fitz, 2009). However, in contrast to mass produced products, this process must be repeated anew for each individual patient. This necessarily increases the product lead time, while differences due to observer interpretation of diseased geometry and inter-patient variation may have an adverse affect on repeatability.

There are relatively few examples of fully patient-specific UKR design processes in literature that attempt to address the aforementioned issues. Van den Heever (2011) used a neural network based estimation to generate curves that describe an individual's otherwise unknown healthy knee shape. This quickly creates a base from which to design an implant, reducing the uncertainty associated with trying to restore diseased joints to their original state. However, the subsequent positioning and design of the implant itself was performed manually, which could introduce differences between different iterations. Steines

and Zhuravlev (2012) foregoes trying to estimate the original geometry as part of their commercial product, the iUni®, and instead rely on the current state of the patient's knee being sufficiently healthy such that smooth parametrisations thereof would prove an adequate reconstruction. In contrast, their patient-specific implant generation process is automated to a much larger degree, though a trained technician is still responsible for delineating the region of interest. These two approaches combined probably represent the most feasible method to patient-specific UKR design:

- *A good prior* of the healthy shape ensures proper restoration of the natural state.
- *Standardisation* of the method facilitates automation and potentially reduces lead time during design.

We therefore developed a patient-specific UKR design concept that relies on the Statistical Shape Model (SSM) discussed in Chapters 4 and 5 in order to generate reliable estimates of non-pathological geometry. This has the additional benefits of making direct use of the face-vertex data structures obtained from scan segmentation, inherent support for automated Region of Interest (ROI) correspondence and alignment as well as full description of complex, three dimensional geometries. The prior serves as the foundation for a subsequent, semi-automated implant generation procedure. Here the user has the ability to intervene and adjust any of the default parameters, such as when accommodating the surgeon's preferences. In order to validate the approach, we investigate its ability to generate anatomically correct shapes as well as its repeatability, which appears to be lacking in literature.

6.2 Methods

The implant development process is illustrated in Figure 6.1. It proceeds sequentially from the left, starting with scan segmentation, estimation of the pathological regions of interest and joint alignment. The result is a set of anatomical models upon which the patient-specific implant may be designed. The implant concept itself consists of three components which, though patient-specific, are standardised to have similar features and construction regardless of patient geometry in order to standardize the design of the surgical instrumentation and to facilitate the automation process. The resulting CAD models may then be used to manufacture the actual implant, though this lies outside the scope of the current project. In this section we first provide a general overview of the implant design concept, followed by more detailed discussions on the individual processes for creating it.

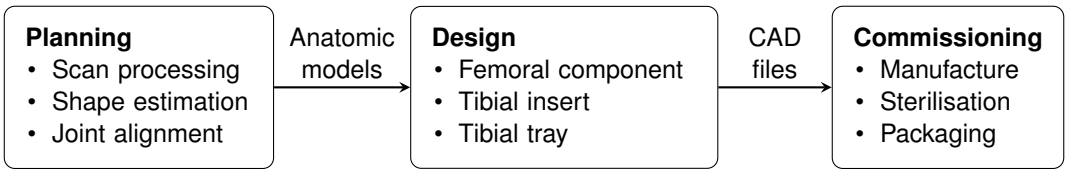

Figure 6.1: Patient-specific implant design process (Illustration: J. v.d. Merwe)

6.2.1 Design overview

Figure 6.2 shows the patient-specific UKR concept's primary design features. It consists of a Cobalt-Chrome (CoCr) femoral component, which attaches to the femur, an Ultra-High-Molecular-Weight Polyethylene (UHMWPE) insert that acts as a load bearing surface between the femur and tibia, and a tray which supports the insert and fixes it to the tibia. The tray may be manufactured from either titanium or CoCr. These materials are biomedically compatible, commonly used by commercial knee implants and deemed suitable as per the ISO 21534:2007 standard.

The femoral component's articulating surface is based on the estimated, pre-pathological geometry of the patient's condyle in order to facilitate more natural joint behaviour. The anterior and distal portions of the surface directly opposing the bone is based on the condyle's current state to minimise the amount of bone resected during surgery. Nevertheless, a single posterior cut is included in order to

- create additional space and a reference from which to perform any procedures on the tibia during Minimally Invasive Surgery (MIS),
- avoid situations where the femoral component may describe a closing arc and so not fit over the condyle,
- and finally to assist in constraining the component to the femur under transverse and rotational loads during normal gait.

The pins themselves further restrict unwanted motion, and are tapered to assist initial placement of the component. Pins are preferred by the consulting surgeon over webs or ribs due to the risk of the bone splitting while cutting the necessary grooves, especially in older patients. Finally, since the femoral component is based on the geometry of the patient, it follows the natural J-curve and conforms to the width of the condyle, as opposed to the fixed or simply straight designs from commercial implants. This is intended to maximise the articulating area.

The tibial tray and insert together create a fixed bearing as a mobile one would not be feasible due to the irregular geometry of the femoral component. A mobile bearing may result in local stress concentrations on the articular surfaces as well as snagging and subsequent dislocation of the bearing itself. Furthermore, rather than deriving the articular surface of the insert directly

from the patient's geometry as we did for the femoral component, we do so indirectly by performing a motion sweep of the estimated femoral surface. This enables us to create some congruence between the femoral and tibial components and so attempt to emulate the restraining effects of menisci, cartilage and ligaments in otherwise rigid materials, while potentially increasing contact between the components when compared to using a flat articular surface.

The outer edges of both the insert and tray are based on simulated cuts performed on the tibial plateau, and conform to the shape of each patient's cortical rim. This maximises coverage, facilitating load transfer via both the hard cortical and soft cancellous bone. Reducing unnecessary overhangs also serve to avoid soft tissue impingement. The pins of the tibial tray are slanted posteriorly to aid initial component placement diagonally and from an anterior direction, given the constraints imposed during MIS. Furthermore, the pins are located in a triangular arrangement to constrain unwanted rotation between the tray and the tibia, while walls around the proximal portion of the tray serve the same purpose for the insert. Finally, all edges and corners are rounded or filleted to reduce stress concentrations.

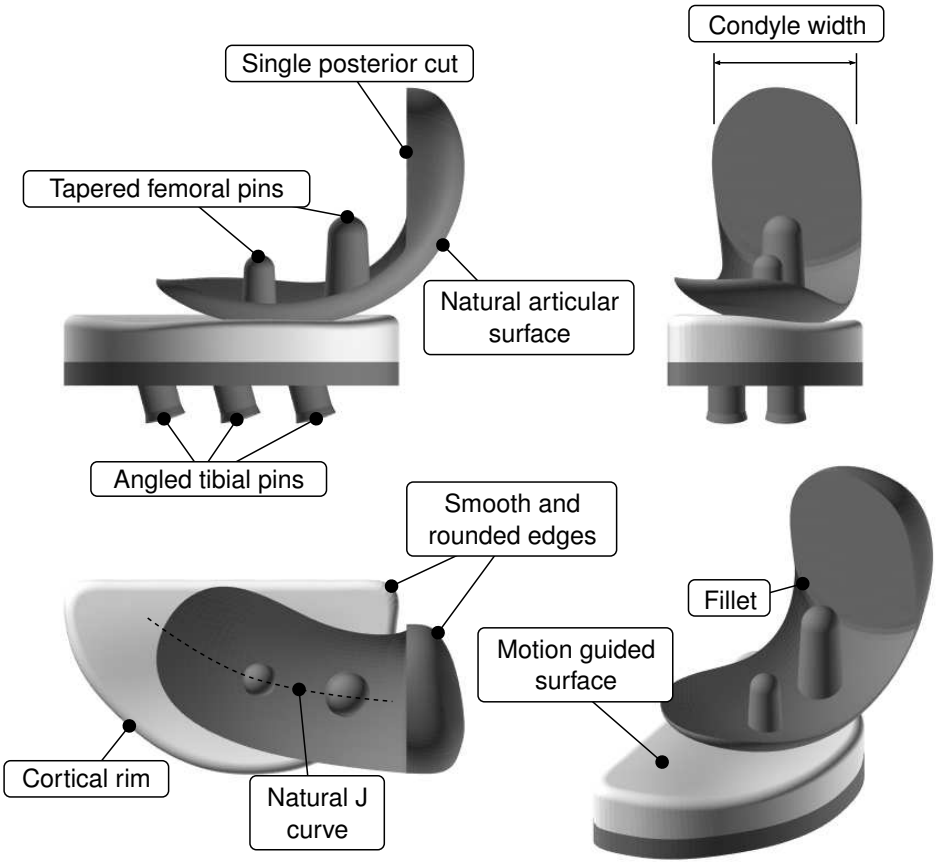

Figure 6.2: Implant features (Illustration: J. v.d. Merwe)

6.2.2 Planning phase

After consultation with a surgeon, a prospective patient will need to undergo an MRI scan of the affected joint. We recommend a 3D Dual Echo Steady State (DESS), sagittally imaged protocol with slice thicknesses of 0.7 mm and a pixel resolution of approximately 0.365×0.365 mm. This is the protocol used by the Osteoarthritis Initiative from which we obtained our model training data (The Osteoarthritis Initiative, 2006*a*). Scan segmentation is the same manual process described in Chapter 4, resulting in face-vertex models of the femur and tibia which, along with some basic patient information, serves as the input for the semi-automated design process. The required information includes the gender of the patient in order to select the appropriate SSM, the condylar ROI that is to be replaced (medial or lateral), as well as the side of the knee. The method accommodates left knees by mirroring them to right-sided knees across the sagittal plane before processing, with the final implant models transformed back afterwards. A simple Graphical User Interface (GUI) shown in Figure 6.3 was created to facilitate uploading of the meshes and collection of the basic patient information.

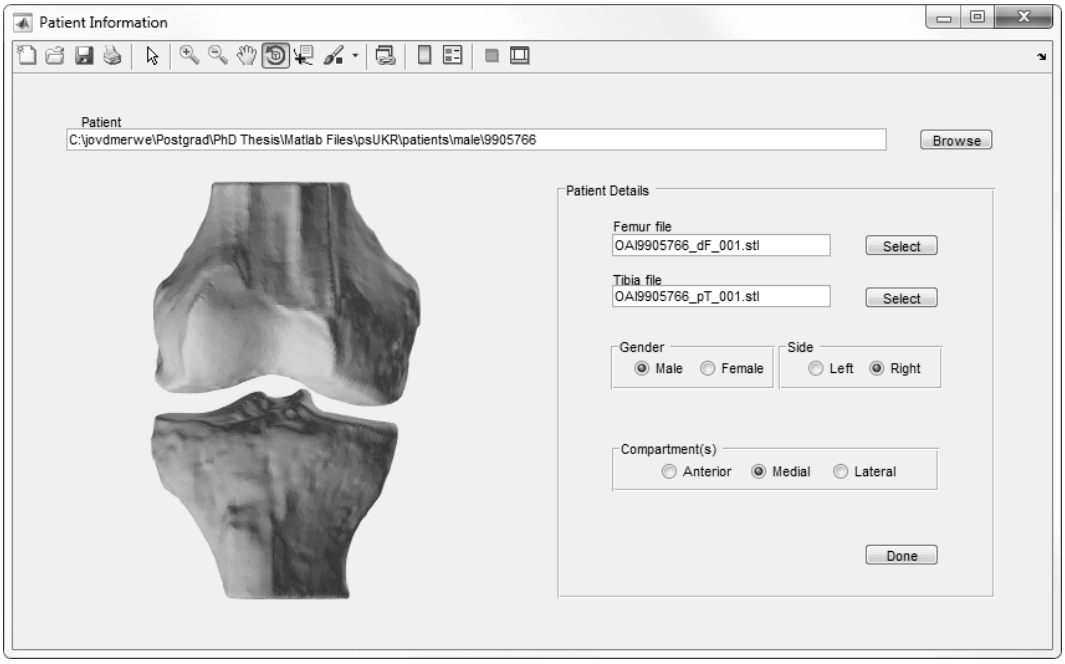

Figure 6.3: Patient information GUI (Illustration: J. v.d. Merwe)

Rough alignment of the joint is then performed based on three user landmarks defined on both the distal femur and proximal tibia. In the femur's case, we require the user to identify the Medial Epicondyle (fME), the Lateral Epicondyle (fLE) and the Intercondylar Notch Apex (fINA). For the tibia, the Spine Center (tSC) as well as best guesses of the Medial and Lateral Condyle

centers (tMCc and tLCc) are required. These landmarks are discussed in greater detail in Chapter 3, and all exhibit inter and intra-observer standard deviation of less than 2.7 mm. However, the main purpose of this step is to define the initial directions of the primary axes for subsequent automatic refinement, and the meshes are only transformed into a general coordinate system similar to that of Figure 3.5.

Cartilage is not included during the segmentation process in a bid to reduce the overall design time, the difficulty associated with delineating diseased geometries and in appreciation of possible future use of CT scans where only the bones would be visible. We therefore applied the Coherent Point Drift (CPD) algorithm as explained in Appendix A.1 in order to identify the articular regions of the femur and tibia directly from the Procrustes mean shapes explained in Chapters 4 and 5. This enables the automated update of the initial rough alignment to that which matches the SSM models from Section 4.2.2 based on the respective condyle centers of the femur and tibia. These centers are also among those which exhibit the least amount of inter-specimen variation as shown in Chapter 3.

Once the coordinate alignment has been finalised, the meshes are directly resampled via the Poisson disk method discussed in Chapter 4 and Appendix B, with a target of 4500 vertices each. This facilitates estimation of the non-pathological ROI of the distal femur which has been indicated during the initial information collection phase. The same method and GUI described in Chapter 5 is used, requiring a minimum of three landmarks to create the prior, though the user is free to add more. In the tibia's case, we instead directly fit the shape model developed in Chapter 4 to the mesh in order to estimate the missing ROI and cartilage surface, without any user constraints. The reason for this is that the tibial fit is secondary - the insert's articular surface will eventually be derived from that of the femoral component, and not an estimate of the tibia's healthy shape.

The final step is to establish joint alignment, as shown in Figure 6.4. The original orientation of the knee during the scanning process is not suitable because of variation in patient positioning as well as deviation from the intended, healthy state due to joint degradation. We therefore rely on information from Paley (2002) to define the default alignment of the bones relative to each other. The joint centers in the coronal plane are defined as the mean of the femoral Medial and Lateral Posterior Condyle centers (fMPCc and fLPCc) and the tMCc and tLCc, the femoral and tibial Geometric centers (fGc and tGc), respectively, and then aligned to each other. In the absence of the mechanical axis of the joint, we maintain the sagittal posture of the distal femur and proximal tibia based on their anatomical axes from the automated coordinate alignment step from before. Finally, we assume a default joint angle between the most distal points of the femoral condyles and the condyle centers of the proximal tibia in the sagittal plane, and transform the tibial mesh accordingly (Paley, 2002). The joint spacing is set to a minimum of four millimetres based

on the average cartilage thickness studied in Chapter 4, though this may be overridden if the average of the estimated, patient-specific cartilage is higher, or due to user preferences. Note that all joint space operations substitute the diseased ROI for the estimated non-pathological geometries prior to adjustment.

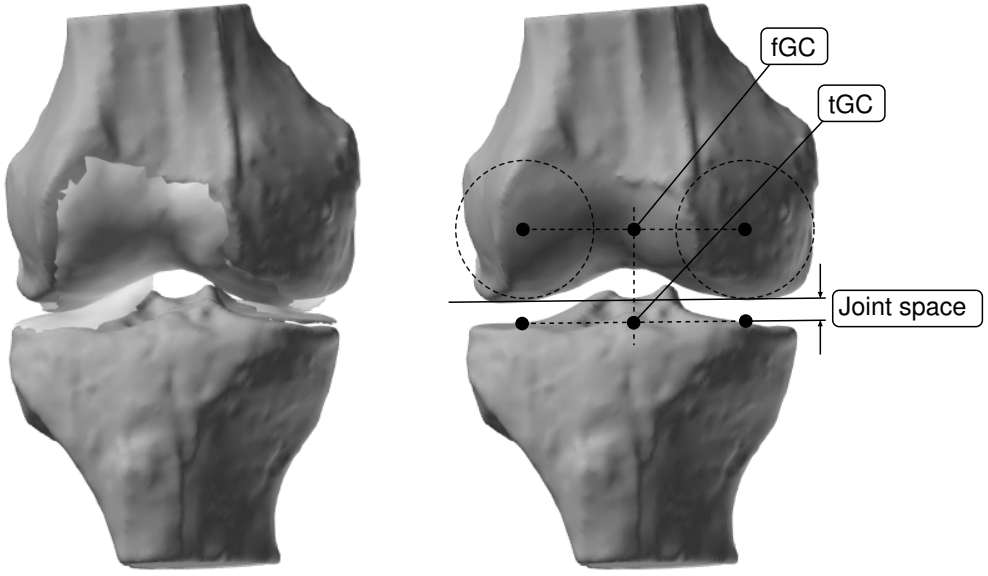

(a) Estimated cartilage (b) Joint alignment

Figure 6.4: Planning alignment and shape (Illustration: J. v.d. Merwe)

6.2.3 Parametrisation

The implants from Figure 6.2 are created using a series of Basis spline (B-spline) curves and surfaces fitted to the model meshes. The motivation for using B-splines are that (Piegl and Tiller, 1997):

- both *basic* and *complex* geometries can be represented,
- a *strong convex hull property* accommodates smooth, rounded surfaces where necessary,
- *local support* allows minor adjustments without affecting the overall geometry and
- B-splines are an *industry standard* method for transferring geometric data between CAD/Computer Assisted Manufacturing (CAM) applications.

A rational B-spline curve may be defined as

$$C(u) = \sum_{i=0}^{n_{Pu}} R_i(u)\mathbf{P}[i] \quad \text{where} \quad R_i(u) = \frac{N_{i,p_u}(u)\mathbf{W}[i]}{\sum_{j=0}^{n_{Pu}} N_{j,p_u}(u)\mathbf{W}[j]} \tag{6.1}$$

Here p_u is the degree of the curve while $\mathbf{P}$ is the control polygon or net, with $n_{Pu}+1$ points in Cartesian space. $N_{i,p_u}(u)$ are the normalised basis functions, while $R_i(u)$ are their rational equivalents. The weight matrix is indicated by $\mathbf{W}$, and a rational curve simplifies to its non-rational equivalent if all weights equal one. B-splines are defined over a knot vector $\mathbf{k}_u$ which may be uniform or not, enabling us to describe *open and clamped* or *closed and unclamped* curves, depending on the situation and with appropriate constraints on the control polygon. In a similar manner, $p_u \times p_v$ degree surfaces are defined by:

$$\begin{aligned} S(u,v) &= \sum_{i=0}^{n_{Pu}} \sum_{j=0}^{n_{Pv}} R_{i,j}(u,v)\mathbf{P}[i,j] \quad \text{where} \\ R_{i,j}(u,v) &= \frac{N_{i,p_u}(u)N_{j,p_v}(v)\mathbf{W}[i,j]}{\sum_{k=0}^{n_{Pu}} N_{k,p_u}(u) \sum_{l=0}^{n_{Pv}} N_{l,p_v}(v)\mathbf{W}[k,l]} \end{aligned} \tag{6.2}$$

In this case the $(n_{Pu}+1) \times (n_{Pv}+1)$ control net is bi-directional, and the surface is defined over two knot vectors $\mathbf{k}_u$ and $\mathbf{k}_v$. B-spline curves and surfaces may be fitted to input data $\mathbf{q}$ by solving the least squares minimisation problem:

$$||\mathbf{q} - f||^2 + \eta \int_a^b \left(f^{(2)}\right)^2 du \tag{6.3}$$

where f is either a B-spline curve or surface and $f^{(2)}$ denotes its second order derivative as part of a penalty on the bending energy. This reduces oscillation of the solution and further smooths the result in the presence of noisy or poorly conditioned data, depending on the value of the regularisation term η. Refer to Appendix C for a more detailed discussion on B-spline curves and surfaces as well as the approximation methods used in this study.

6.2.4 Femoral component

Figure 6.5 illustrates the first steps of building the femoral component, which requires fitting a B-spline surface to the vertices of the affected ROI on the bone. The process begins by creating a cylindrical coordinate system based on the axis defined by the original joint centres of the posterior condyles. From there the angle θ about the cylindrical axis for each vertex is obtained and used together with their original, normalised x or Medio-Lateral (ML) coordinates to obtain a flattened map of the vertices. A sufficiently dense grid is created to encompass the flattened coordinates, and then corresponding points are found

for each of the grid coordinates using a k-nearest neighbour search. The flattened vertex coordinates are subsequently replaced by their original, unsorted Cartesian counterparts in order to create a structured, bi-directional grid by maintaining the original vertex indices throughout the mapping process. The result serves as an input for penalised B-spline surface fitting in order to obtain a reasonable starting point for the following, iterative improvement of the fit to the unsorted vertices.

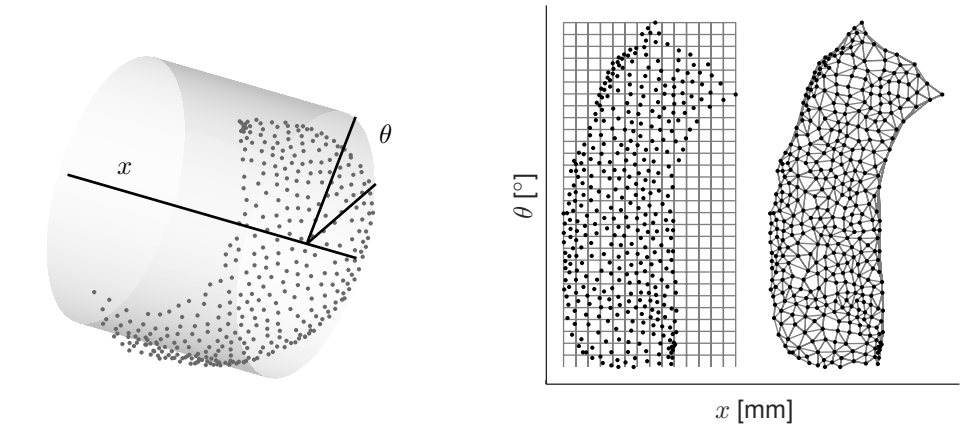

(a) Cylindrical coordinates

(b) 2D grid mapping

(c) Bone surface fit

(d) Boundary curve fit

Figure 6.5: Femoral bone surface fit (Illustration: J. v.d. Merwe)

The structured grid also enables us to extract the boundary of the ROI, which is then interpolated linearly in order to obtain a regular, ordered distribution of points. This is used as input to unsorted, closed and penalised B-spline curve fitting, the result of which describes the boundary of the femoral component. However, because the curve is a smooth approximation rather

than a direct interpolation of the boundary, overhangs may occur in certain situations. This is compensated for by first creating a regular grid of points on the parametrised bone surface, bounded by the curve. Then, surface normals are computed at these points, and used to find their intersections on the original bone mesh. If the distance between the parametrised points and their projections exceed a threshold, the control polygon of the boundary curve is locally adjusted inwards by a small increment, along the B-spline surface. The process is iterative, repeating until no further overhangs are present.

The articular surface of the femoral component is created by first generating a distance map between the parametrised bone surface and a mesh of the estimated, healthy cartilage shown in Figure 6.6. The bone surface is then simply offset along its sampled normal vectors as per the distance map, while a minimum thickness of two millimetres is enforced. This ensures that the implant has sufficient material to support the necessary loads and is based on the average thickness found in Chapter 4. The user may, however, override the default value. For example, while Van den Heever (2011) also uses a minimum thickness of two millimetres, Steklov *et al.* (2010) uses three and Fitz (2009) reports a maximum of 3.5 mm for each of their respective femoral components. The boundary curve is transferred to the final articular surface in a similar manner.

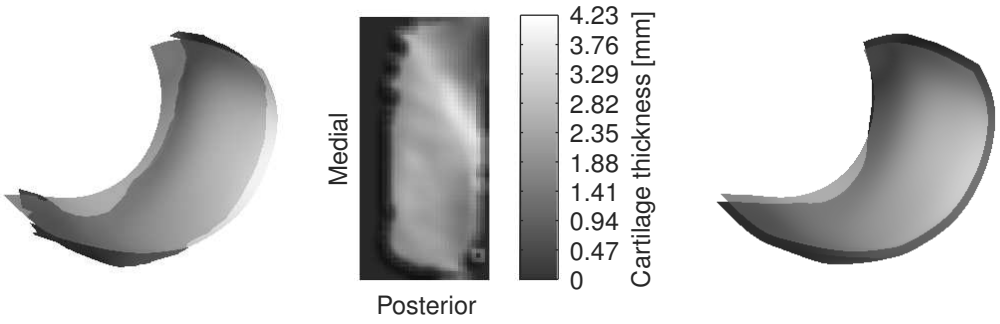

(a) Cartilage estimate (b) Thickness map (c) Articular surface offset

Figure 6.6: Femoral articular surface fit (Illustration: J. v.d. Merwe)

Once both the raw bone and cartilage surfaces have been obtained, together with their boundaries, the secondary features of the femoral component are generated as shown in Figure 6.7. First, a posterior cut plane with a normal vector along the anterior direction is defined. The plane itself is located at a predefined offset from the most anterior point of the anterior facing portion of the bone surface. The medial, lateral and posterior portions of the bone boundary located behind the plane is then projected onto it together with the intersection curve. A B-spline representation of a bilinear Coons patch is then created based on individual parametrisations of these four curves. The

anterior portion of the original bone surface is then split via knot insertion, and stitched together with the Coons patch with a fillet in between. This fillet is created by offsetting and parametrising the intersected edges of the bone surface and the Coons patch, and generating a smooth, tangential ruled surface between them. The most distal corners of the Coons surface's control polygon are also filleted by appropriately stitched curves in order to remove sharp edges. Both Coons patches and ruled surfaces are discussed in greater detail by Piegl and Tiller (1997) and may be represented by B-spline surfaces.

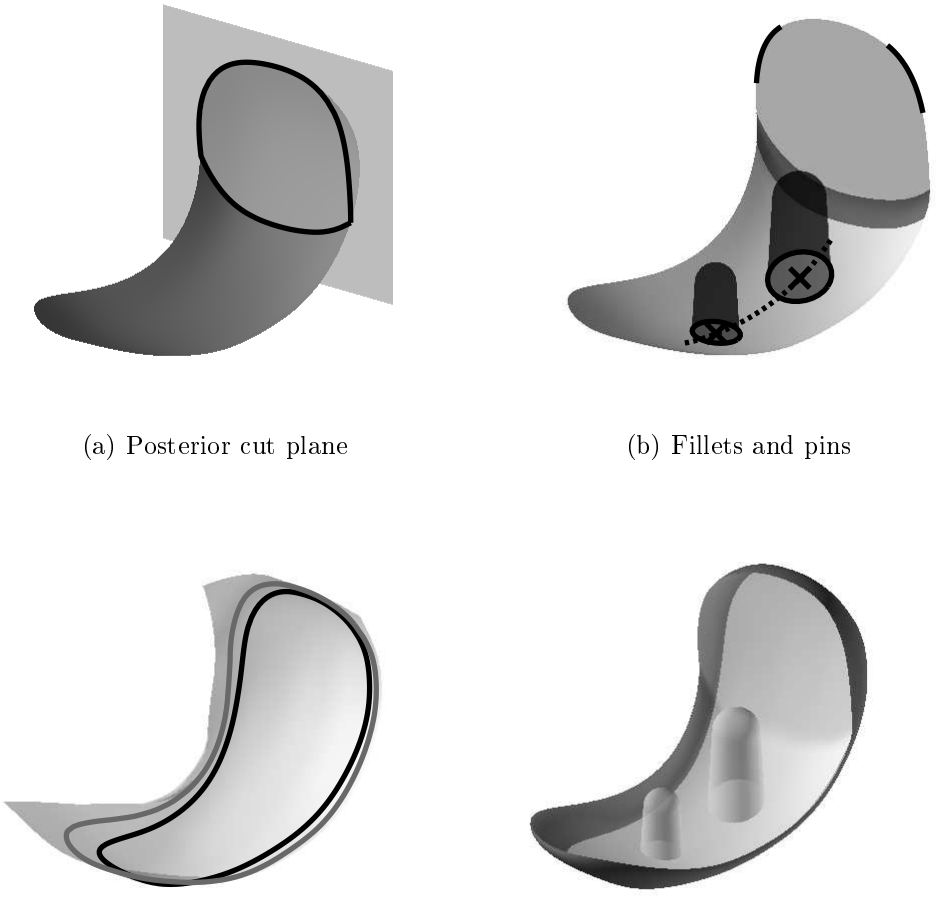

(a) Posterior cut plane

(b) Fillets and pins

(c) Articular boundary trim

(d) Boundary fillet

Figure 6.7: Femoral component construction (Illustration: J. v.d. Merwe)

Pins are constructed centrally on the anterior portion of the bone surface some distance from the posterior cut, adjusted to accommodate on the overall length of the implant. Their axes are aligned with the long axis of the knee, while the pins themselves consist of a stitched together dome and tapered

frustum that intersects with the bone surface. The diameter of the lower portion of the frustum, its taper angle and the overall pin length fully define each pin, which are represented by specially constructed, non-uniform and rational B-spline surfaces.

The final step in creating the femoral component is to combine the bone and articular surfaces with a fillet. However, in order to facilitate a smooth transition between the fillet and the articular surface, the boundary of the articular surface must first be trimmed inwards. The procedure is similar to that performed when reducing overhangs on the bone surface, with the exception that the iterative offset of the control polygon now proceeds a fixed distance in all directions from the original boundary. The fillet connecting the two surfaces is itself a ruled surface, respecting the tangential condition at the articular boundary but normal to the bone boundary. The bone boundary's normals are adjusted to exclude their ML components centrally, the Antero-Posterior (AP) components at the anterior edge and the Cranio-Caudal (CC) components at the distal edges in order to avoid overhangs.

6.2.5 Tibial tray

Construction of the tibial tray is illustrated in Figure 6.8. First, the plateau cut on the affected condyle is simulated by offsetting a transverse plane from the most distal point on the aligned femoral component in full extension. The distance by which the cut plane is offset is equal to the total height of the combined tibial tray and insert. The minimum required height for an UHMWPE insert is six millimetres as per the ISO 21536:2007 standard, while the default height of the metal backed tray is set as two millimetres. The sagittal boundary of the cut extends to the inner edge of the tibial ROI. The intersection between the cut plane and the cortical rim is parametrised by a B-spline curve, including appropriate fillets at the anterior and posterior edges. The bone surface is simply a B-spline plane bounded by the cortical rim.

Three pins are located on the distal side of the tibial tray, two of which are in-line, some pre-defined distance from the inner boundary as well as the most anterior and posterior edges of the component, respectively. These dimensions are automatically adjusted based on the overall length of the implant if the default values cause overhang or intersection with other features. The third pin is located midway between the centers of the anterior and posterior pins, with an additional transverse offset. The tibial pins are again constructed using non-uniform rational B-spline surfaces, this time as closed cylinders angled posteriorly. The pin angles, diameters and lengths are adjustable.

An inner, transverse surface against which the insert is to rest, is created two millimetres from the bone-tray interface. Its boundary is trimmed inwards by two millimetres as well in order to accommodate the outer wall of the component. The trimmed portion is reproduced at an additional offset, for a final component height of four millimetres, excluding the pins. Walls are

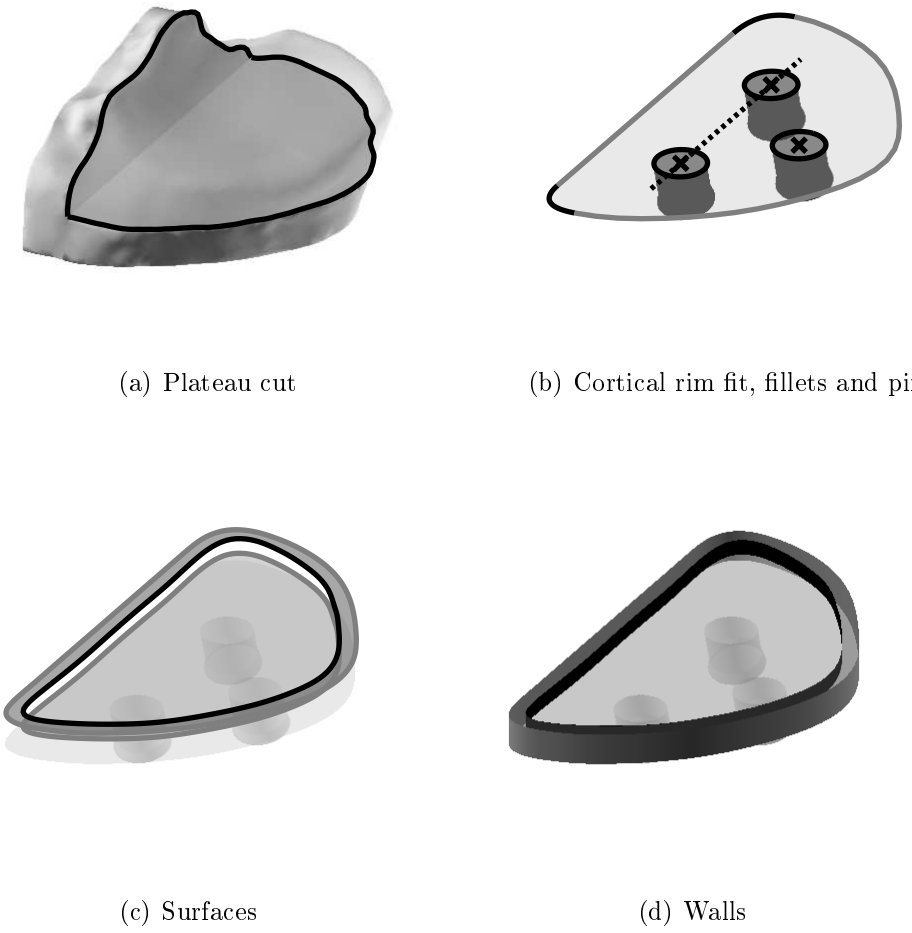

(a) Plateau cut

(b) Cortical rim fit, fillets and pins

(c) Surfaces

(d) Walls

Figure 6.8: Tibial tray construction (Illustration: J. v.d. Merwe)

made by constructing linear B-spline ruled surfaces between the respective boundaries of the flat surfaces.

6.2.6 Tibial insert

Creating a suitable articular surface for the tibial insert is made difficult by the complex shape of that of the femoral component. As seen from Chapter 4, the model's performance degrades when estimating tibial ROIs. Any inaccuracies introduced in this manner would create unnatural surface kinematics between the femoral and tibial components. The issue is potentially exacerbated by the rigid materials of the implants when compared to the soft tissue structures of the knee. Instead, we adapt the motion-guided Total Knee Replacement (TKR) design approach described by Walker (1988, 2014) to our application.

By subjecting the femoral components to simulated kinematic profiles, we create matching, patient-specific tibial surfaces by sweeping out a deformable grid. This has the advantage of creating a naturally conforming interface, thereby maximising contact area while mimicking the restraining effects of the menisci.

Table 6.1: Quasi-static knee kinematic studies

			AP			
Study	**Subjects**	**Method**	**Joint centre**	**Condyles**	**Contact**	**IE**
Asano *et al.* (2001)	6 male	Bi-planar imaging	-	~~Circles~~	~~Bone~~	GCA
Hill *et al.* (2000)	7 male	Open MRI	Mid-GCA†	FFCs	-	GCA†
Li *et al.* (2008)	6 male 2 female	Dual fluoroscopy	Mid-GCA	-	-	GCA
Johal *et al.* (2005)*	5 male	Open MRI	Mid-GCA†	FFCs	-	GCA†
Pinskerova *et al.* (2004)*	5 male	Open MRI	Mid-GCA†	FFCs	Cartilage	GCA†
Yamaguchi *et al.* (2009)	4 male 4 female	Lateral fluoroscopy	Mid-GCA	-	-	GCA

~~struck-through~~ data not considered due to differences in method of reporting
† estimated from reported values
* shared dataset

While the kinematics of the knee joint is a complex six Degree of Freedom (DOF) process, we limit our sweep to two primary motions, namely AP translation and Internal-External (IE) rotation as a function of FE. To determine what these motion profiles should be, we investigated a number of in vivo quasi-static studies wherein the participants performed squat or lunge-like activities due to the larger range of healthy knee flexion, and listed them in Table 6.1. It is important to note that there are differences between the studies which could complicate direct comparisons. These include the measurement methods, activities performed, coordinate system definitions and final variables reported. Some authors investigate kinematics based on the motion of Flexion Facet Centers (FFCs), which are the centres of arcs fitted to the posterior condyles in the sagittal plane. Others include the motion of the contact points between the bone and cartilage, while still others report only the motion of the joint center, which we define as the mid-point of the Geometric Center Axis (GCA), about which rotation occurs. We find this last mentioned most compatible with the coordinate system embedded in our femur models, and so attempt to convert all data from literature to motion of the fGc and about the GCA as shown in Figure 6.9. Note that there is a general posterior translation of the fGc relative to the tibia as flexion increases. The IE motion exhibits an initial large external rotation of the femur that slows down as flexion continues. We designed third degree polynomial curves to reproduce this behaviour:

$$f(x) = \sum_{i=0}^{3} \mathbf{a}[i]x^i \tag{6.4}$$

with coefficient vectors for the AP and IE curves respectively:

$$\mathbf{a}_{AP} = \begin{bmatrix} -2.59 \times 10^{-2} & -1.75 \times 10^{-1} & 2.23 \times 10^{-3} & -1.12 \times 10^{-5} \end{bmatrix}$$
$$\mathbf{a}_{IE} = \begin{bmatrix} 1.4 \times 10^{-1} & 5.09 \times 10^{-1} & -5.19 \times 10^{-3} & 1.9 \times 10^{-5} \end{bmatrix}$$

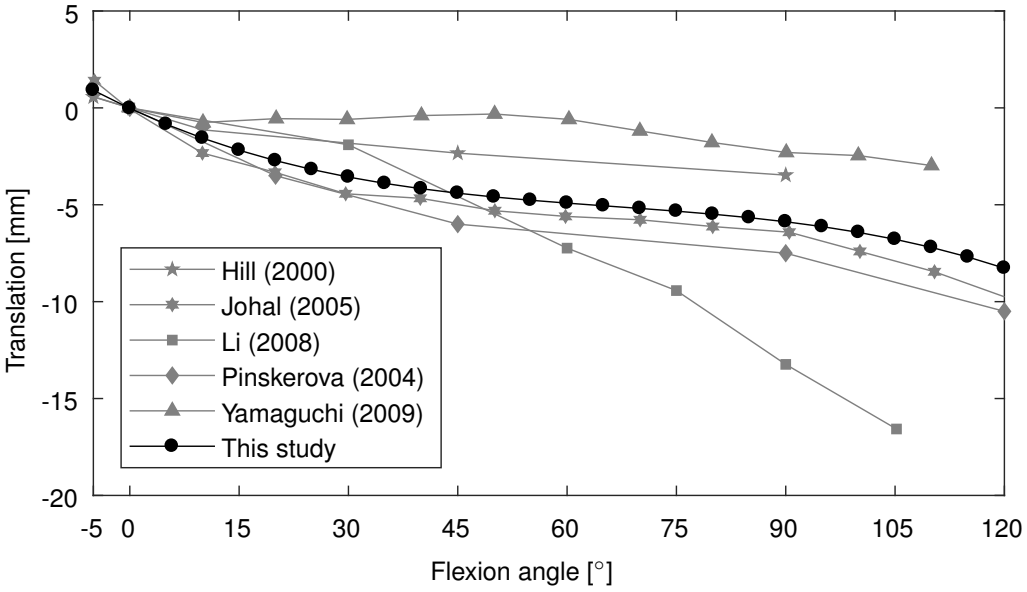

(a) Anterior translation of the femur relative to the tiba

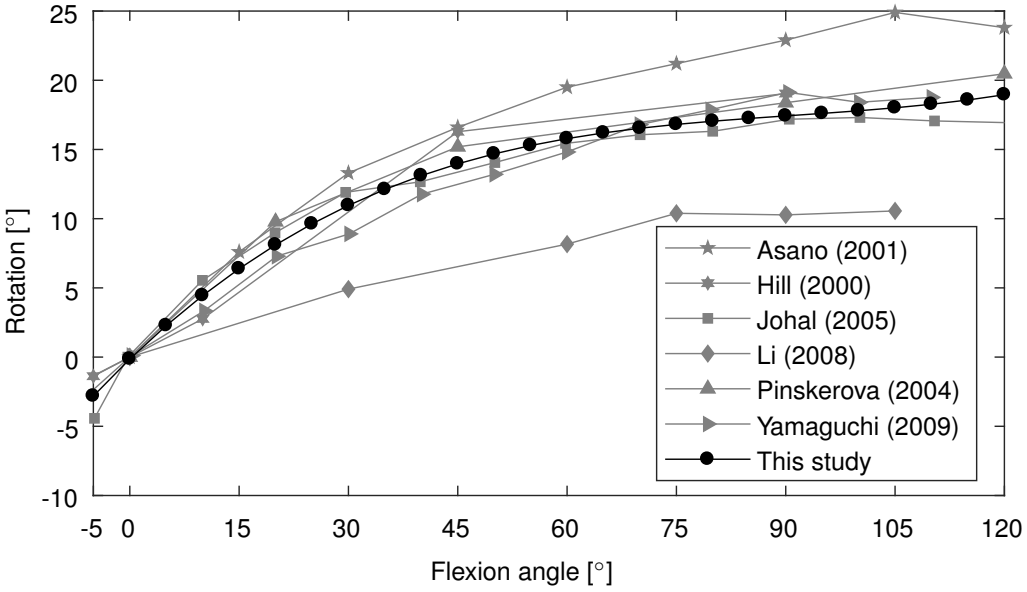

(b) External rotation of the femur relative the tibia

Figure 6.9: Kinematic sweep functions (Illustration: J. v.d. Merwe)

Simply gouging out an insert surface based on these motion profiles may create a highly conforming articular interface which could result in higher lo-

calised stresses, relative micro-motion between the tibial components and even dislocation, reducing the implant's life or leading to early failure. We therefore attempt to model the restraining effects of soft tissues on knee motion similar to the kinematic profiles from before. The results could be used to create an effective range of allowable motion about the different implant positions. Table 6.2 lists the studies considered and, while there are differences in the methods of measurement, the data is generally reported as a function of AP force, IE torque, FE motion or a combination thereof. Note that we considered only in-vitro studies in this case, as in-vivo data was scarcely available. The results are illustrated in Figure 6.10, and we create bivariate polynomial functions to model the behaviour:

$$f(x,y) = \sum_{i=0}^{3}\sum_{j=0}^{5} \mathbf{A}[i,j]x^i y^j \tag{6.5}$$

where the coefficient matrices are:

$$\mathbf{A}_{AP} = \begin{bmatrix} -1.49 & -3.29\times10^{-1} & -2.03\times10^{-1} & -3.32\times10^{-1} & 5.24\times10^{-2} & 2.65\times10^{-1} \\ 37.69 & 9.63 & 9.02\times10^{-2} & -6.81 & 1.66 & 0 \\ 1.95 & 8.98\times10^{-1} & 2.61\times10^{-1} & -5.93\times10^{-1} & 0 & 0 \\ 32.8 & -1.02 & 3.79 & 0 & 0 & 0 \end{bmatrix}$$

$$\mathbf{A}_{IE} = \begin{bmatrix} 3.3\times10^{-1} & -2.2\times10^{-1} & 7.81\times10^{-2} & 2.15\times10^{-1} & -2.58\times10^{-2} & -2.27\times10^{-2} \\ 1.01 & 7.92\times10^{-1} & -5.91\times10^{-1} & -5.59\times10^{-1} & 2.93\times10^{-1} & 0 \\ -3.77\times10^{-1} & 3.64\times10^{-2} & -6.74\times10^{-2} & -8.46\times10^{-2} & 0 & 0 \\ 3.49 & 3.47\times10^{-1} & 5.1\times10^{-1} & 0 & 0 & 0 \end{bmatrix}$$

Table 6.2: In vitro knee soft tissue restraint studies

			Load	
Study	**Subjects**	**Method**	**AP**	**IE**
Blankevoort *et al.* (1988)	4 cadavers	6 DOF rig	-	± 3 and -6 to 6 Nm
Fukubayashi *et al.* (1982)	9 cadavers	4 DOF rig	± 100 and -125 to 125 N	-
Lo *et al.* (2011)	14 cadavers	6 DOF robot	± 130 N	± 5 Nm
Ma *et al.* (2003)	10 cadavers	6 DOF robot	-134 N to 134 N	-
Markolf *et al.* (1976)	17 male 18 female	Force handle	-100 to 100 N	-8 to 8 Nm

Figure 6.11 shows how a motion swept insert surface is created. After the femoral component has been built, it is naturally located on the aligned joint. We consider this starting position as zero degrees flexion. As before, the origin of the femur is located at the mid-point between the fMPCc and the fLPCc, and the axis between these two centers is the GCA about which we assume flexion occurs. The AP and IE motion polynomials are sampled over the range of -5 to 120 degrees flexion, in 5 degree intervals. The resulting rotations and translations are then iteratively applied to the the femoral component. At each flexion interval, AP and IE laxity is also calculated from the bivariate parametrisations for a fixed force of $\pm$50 N and torque of $\pm$1.5 Nm, respectively, and applied to the transformed femoral component. These form the upper and

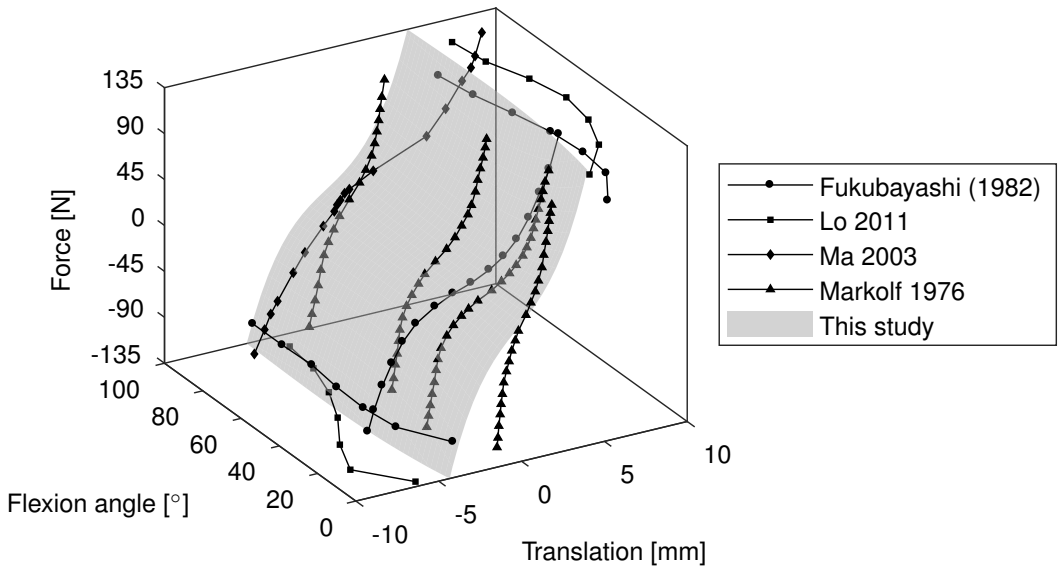

(a) Anterior translation

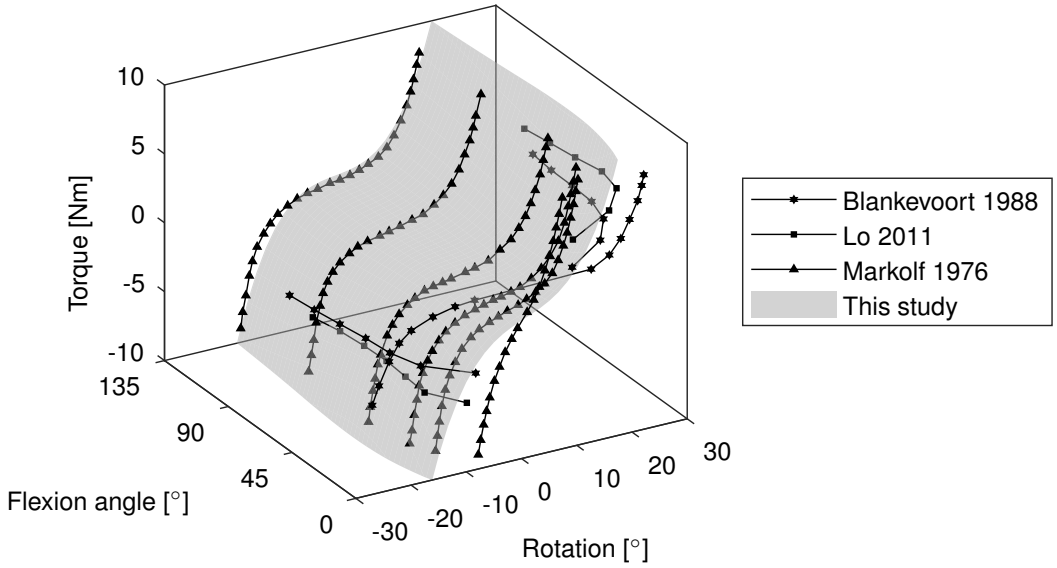

(b) External rotation

Figure 6.10: Soft tissue restraint functions (Illustration: J. v.d. Merwe)

lower boundaries of motion of the femoral component, and represent roughly 50% of the total laxity ranges studied in literature.

The insert's articular surface is initialised as a grid spanning the entire tibial ROI in the ML and AP directions. During the first iteration of the motion sweep, the most distal point of the transformed femoral component that falls within each grid cell's AP and ML boundaries are recorded as the CC coordinates for that portion of the grid. During subsequent motion sweep iterations, contact between the grid and the overall most distal point of the femoral com-

ponent is enforced. This process is repeated iteratively until no further changes in the grid occur. The remaining coordinates of the grid that have not been filled are simply offset some specified distance from its lowest point in order to create the boundaries of the insert. The final result is approximated by a B-spline for a smooth, partially congruent insert surface.

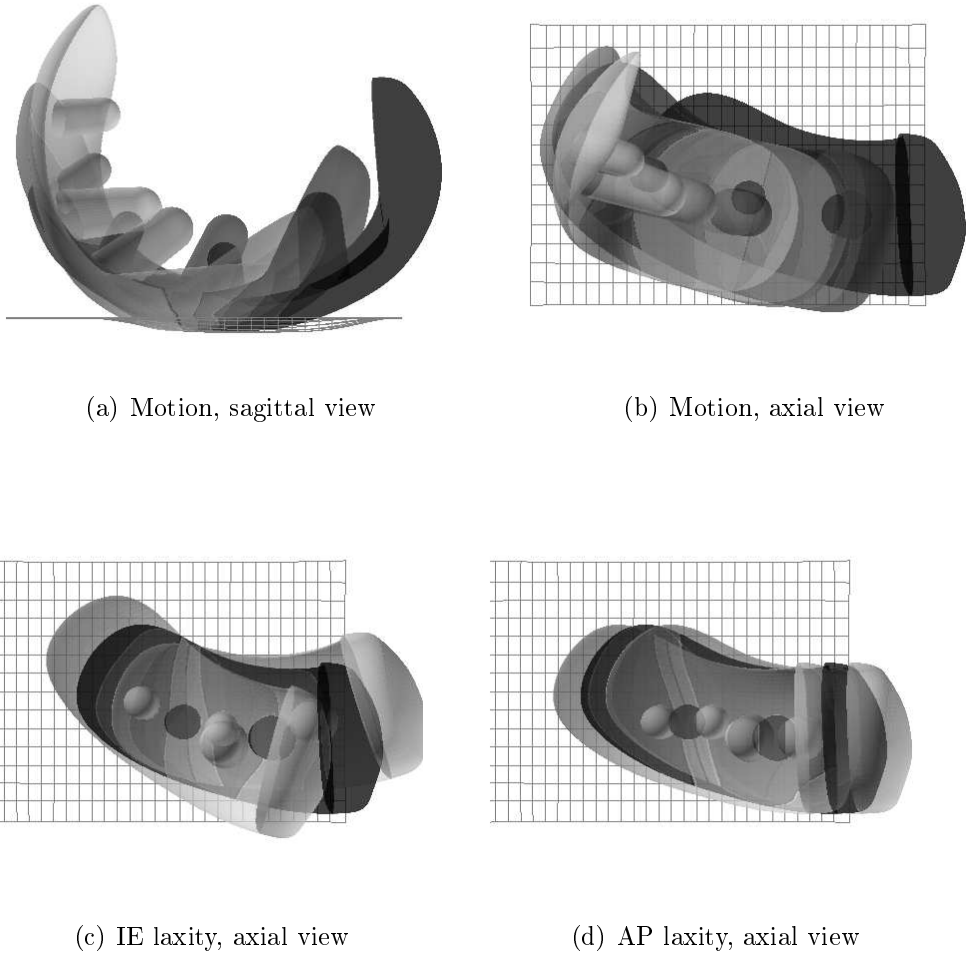

(a) Motion, sagittal view

(b) Motion, axial view

(c) IE laxity, axial view

(d) AP laxity, axial view

Figure 6.11: Motion sweep (Illustration: J. v.d. Merwe)

Once the kinematic sweep has been created, the insert itself is constructed as illustrated in Figure 6.12. The boundary on the articular surface is found by projecting the cortical rim curve obtained during the tray construction onto it. This boundary is then further trimmed inward in order to create space for an edge fillet between the outer wall of the insert and its articular surface. The outer wall itself is a ruled surface between the boundary of the tray's outer wall, and the original boundary of the articular surface offset proximally. The

edge fillet maintains the tangential conditions between both the outer wall and trimmed articular surface. Finally, the distal portions of the insert is created to match the inner walls and surfaces of the tibial tray.

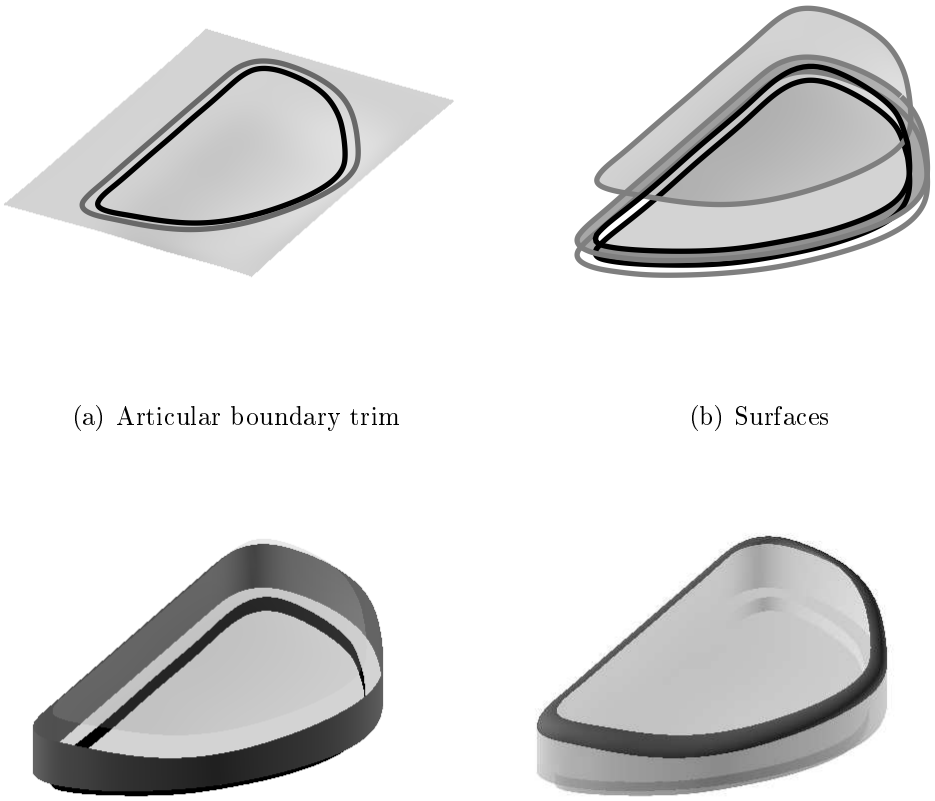

(a) Articular boundary trim

(b) Surfaces

(c) Walls

(d) Boundary fillet

Figure 6.12: Tibial insert construction (Illustration: J. v.d. Merwe)

6.2.7 Analyses

In order to validate the shapes created by our implant design method, we performed the semi-automated design process for eight male and eight female knees. Medial and lateral implants were created separately for each, and the default variables in Table 6.3 were strictly enforced.

Table 6.3: Default parameter values

			Affected components		
Variable	**Default**	**Description**	**Femoral**	**Insert**	**Tray**
η	0.5	B -spline regularisation term	✓	✓	✓
n_{Pu}	10	Number of B-spline basis functions in the u direction	✓	✓	✓
n_{Pv}	15	Number of B-spline basis functions in the v direction	✓	✓	✓
p_u	3	B-spline degree in the u direction	✓	✓	✓
p_v	3	B-spline degree in the v direction	✓	✓	✓
Anterior boundary offset	5 mm	Distance by which the anterior boundary of the femoral component's articular surface is trimmed	✓		
Anterior femoral pin diameter	6 mm	Lower diameter of the anterior femoral pin	✓		
Anterior femoral pin height	10 mm	Height of the anterior femoral pin	✓		
Anterior femoral pin offset	25 mm	Distance from the posterior cut to the anterior femoral pin	✓		
Anterior tibial pin offset	15 mm	Offset of the anterior pin from the anterior edge			✓
AP force	50 N	Force used to create motion bounds		✓	
Corner fillet radius	5 mm	Radii of corner fillets introduced on sharp boundary edges	✓	✓	✓
Femoral pin taper angle	3°	Taper angle of the pin body from its lower boundary	✓		
General boundary offset	2 mm	Distance by which surface boundaries are trimmed to accommodate ruled surface fillets	✓	✓	✓
IE torque	1.5 Nm	Torque used to create motion bounds		✓	
Insert minimum height	6 mm	Minimum height of the tibial insert		✓	✓
Insert maximum height	8 mm	Maximum height of the tibial insert		✓	
Inward step size	0.5 mm	Size of iterative step when curve boundaries are adjusted inwards along a surface	✓	✓	✓
Joint space	4 mm	Distance between distal femur and proximal tibia in the sagittal plane		✓	✓
Minimum femoral thickness	2 mm	Minimum allowable thickness of the femoral component	✓		
Overhang threshold	0.5 mm	Maximum allowable distance between femoral boundary curve and underlying bone	✓		
Posterior cut plane offset	1 mm	Posterior cut plane origin offset along its normal	✓		
Posterior cut plane rotation	0°	Rotation of the posterior cut plane norm about the Medio-Lateral axis	✓		
Posterior femoral pin diameter	8 mm	Lower diameter of the posterior femoral pin	✓		
Posterior femoral pin height	15 mm	Height of the posterior femoral pin	✓		
Posterior femoral pin offset	10 mm	Distance from the posterior cut to the posterior femoral pin	✓		
Posterior tibial pin offset	15 mm	Offset of the posterior pin from the posterior edge			✓
Tray base width	2 mm	Offset between the bone and inner surfaces of the tray		✓	✓
Tibial pin angle	15°	Posterior angle of the tibial pins			✓
Tibial pin diameter	7 mm	Diameter of the tibial pins			✓
Tibial pin length	6 mm	Length of the tibial pins			✓
Tibial pin transverse offset	10 mm	Transverse offset of the tibial pins			✓
Tray wall height	4 mm	Total height of the tibial tray		✓	✓

We compute the mean shapes of each component, with correspondences obtained from the implant parametrisations. This enables subsequent shape description via Generalised Procrustes Analysis (GPA) and Principle Component Analysis (PCA) as per Appendix A. Note that the pins were omitted as part of the shape analyses as they are located at artificially fixed positions and so may skew the results. Furthermore, the tibial tray was omitted from the analyses as its only source of inter-specimen variation is the cortical rim, which is sufficiently represented by the insert.

Repeatability of the method was investigated by having a single user repeat the design for each unseen knee three times. The order in which the knees were processed was randomised to avoid the effects of memorisation. Here the only assumed sources of variation were the inter-specimen differences as well as the observer variation during the rough alignment and shape estimation steps. For each component, we computed the Root Mean Squared Distance (RMSD) from the mean of the three repetitions as a measure of their similarity. Repeatability was investigated by fitting a one way balanced ANOVA on the RMSD results from the repeated observations. The level of significance was set at $p < 0.05$ and normality was confirmed via χ^2 tests. The semi-automated implant design process as well as the statistical analyses was performed in Matlab. Once again the pins and tray were omitted from the analyses.

6.3 Results

Figure 6.13 shows the mean shapes of the femoral components for the male and female, lateral and medial condyles. Note the pronounced transverse curvature of the medial femoral component as it follows the condyle's shape, while the lateral condyle is straighter and terminates more posteriorly. The male components are also generally wider than those of the females. Similarly, Figure 6.14 illustrates the mean insert shapes when viewed superiorly, with and without added laxity and where darker colors indicate greater depth of the articular surface. The medial inserts are generally larger, longer and narrower, with a contour akin to a logarithmic spiral (though we did not test for this). In contrast, the lateral condyle is wider, shorter and slightly more square in shape. The motion profile with added laxity has a more pronounced depth map than without it, with less material remaining towards its boundaries. Also note the localised 'dish' of the medial components' articular surfaces compared to the longer 'groove' of those of the lateral inserts.

Figure 6.15 illustrates the point-wise standard deviation from the Procrustes mean shape for the sixteen knees' implant components. In the case of the medial femoral components, the greatest deviation is found on the distal portion of the articular surfaces. Conversely, the female femoral components' variation is distributed around the edges. The female lateral tibial inserts exhibit greater variation that of the female medial, and both male inserts, while

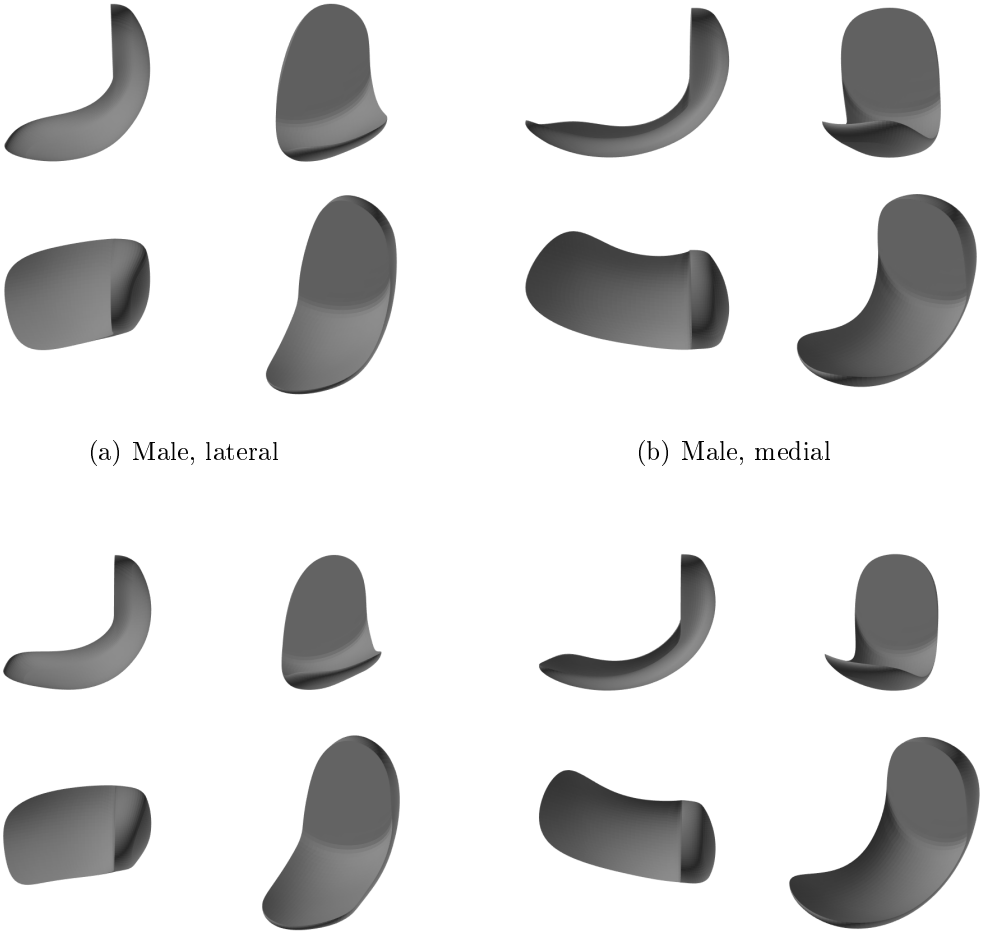

(a) Male, lateral

(b) Male, medial

(c) Female, lateral

(d) Female, medial

Figure 6.13: Mean femoral components (Illustration: J. v.d. Merwe)

deviation for all inserts is slightly higher around the implant walls than on the articular surfaces.

The percentages explained by each mode of variation are shown in Figures 6.16 and 6.17 for the male and female implants, respectively. In general, the first three modes account for between 85% and 92% of the total shape variation with the first mode contributing between 45% and 64%. To see which shape characteristics are described by the principle modes, we compute the $\pm 3\sigma$ offset from the mean. This is illustrated in Figures 6.18 and 6.19, with the variation calculated as the inter-landmark distance between the upper and lower shape boundaries. The first and largest mode accounts for scale regardless of component or gender, while the second mode of variation for the femoral component primarily appears to affect the transverse curvature or angle of the condyles. For the medial tibial component, the second mode represents vari-

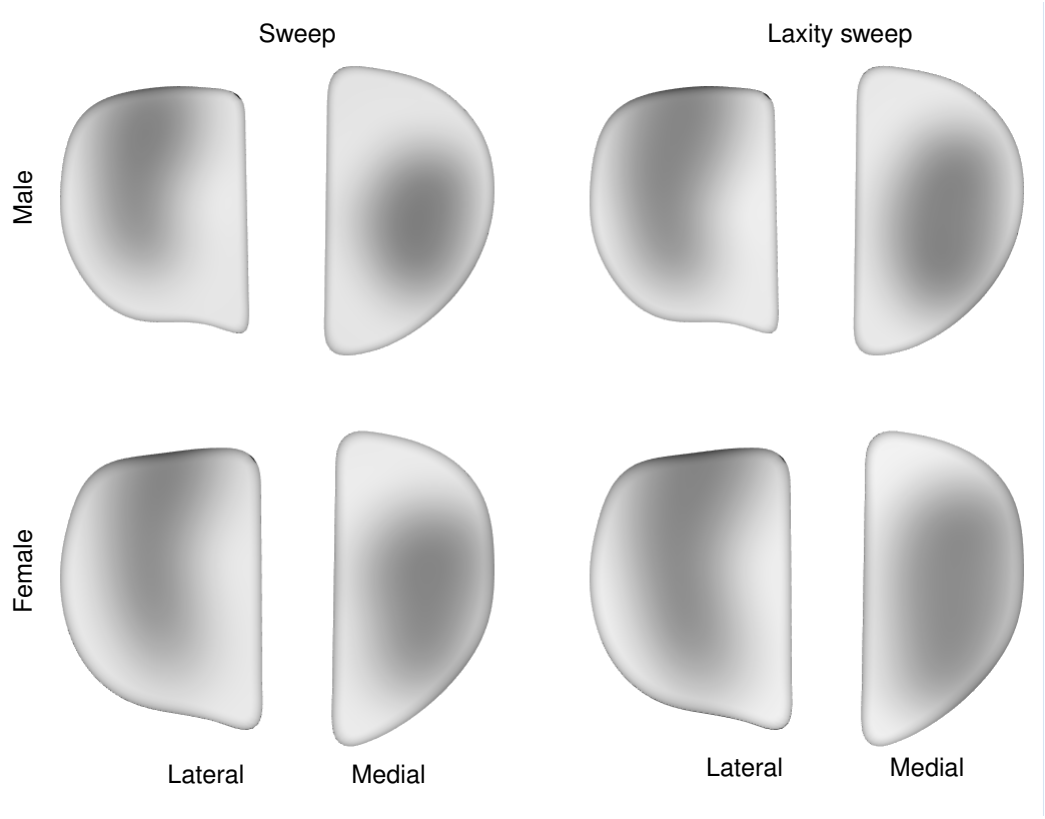

Figure 6.14: Mean tibial components (Illustration: J. v.d. Merwe)

ation in the cortical rim, making that of the male knees shorter and more rounded or longer with a sharper anterior corner. The differences for female knees are less pronounced, with the second mode mostly affecting just the length of the medial tibial component. The second mode affects the lateral condyle in a similar manner, though the anterior portion of the cortical rim ranges between concave and convex. Finally, the third mode appears to adjust the width of the femoral component's articular surface, and the various corners of the tibial component's cortical rim.

As validation of the kinematic profiles, we track the contact point between the femoral component and the articular surface of the insert, as well as the femoral center points, during the final motion sweep. The results are reported in Figure 6.20 as the distances from the ipsilateral posterior cortex of the implant, and compared to in-vivo data from (Pinskerova *et al.*, 2004). The medial contact point experiences an initial posterior translation during early flexion, after which it remains relatively constant. The fMPCc tracks anteriorly during early flexion, stabilises initially and then moves posteriorly in deeper flexion. Both the lateral contact point and fLPCc show greater posterior translation than their medial counterparts, which is initially quick but

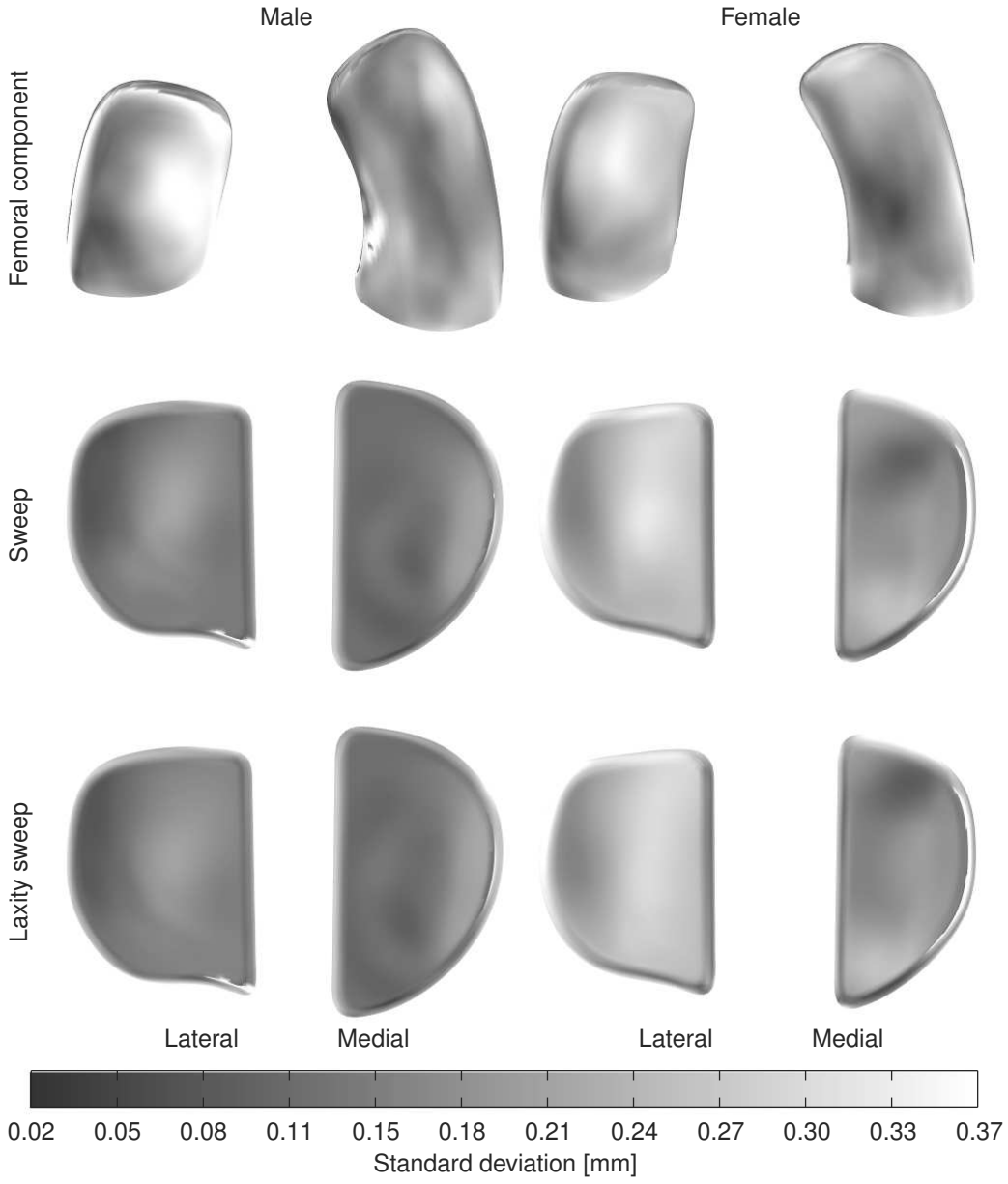

Figure 6.15: Point-wise standard deviation from the mean (Illustration: J. v.d. Merwe)

slows down at higher degrees of flexion. Male knees generally exhibit a larger offset than female knees for all cases.

Table 6.4 lists the RMS distances of the repeatedly generated implants from their average. This ranged between 0.59 and 0.67 mm for the femoral components and 0.49 and 0.56 mm for the tibial inserts. The standard deviations of the repeated RMS measurements shown in Table 6.5 range between ± 0.18 and ± 0.32 mm, with those of the women generally greater than the men's. No

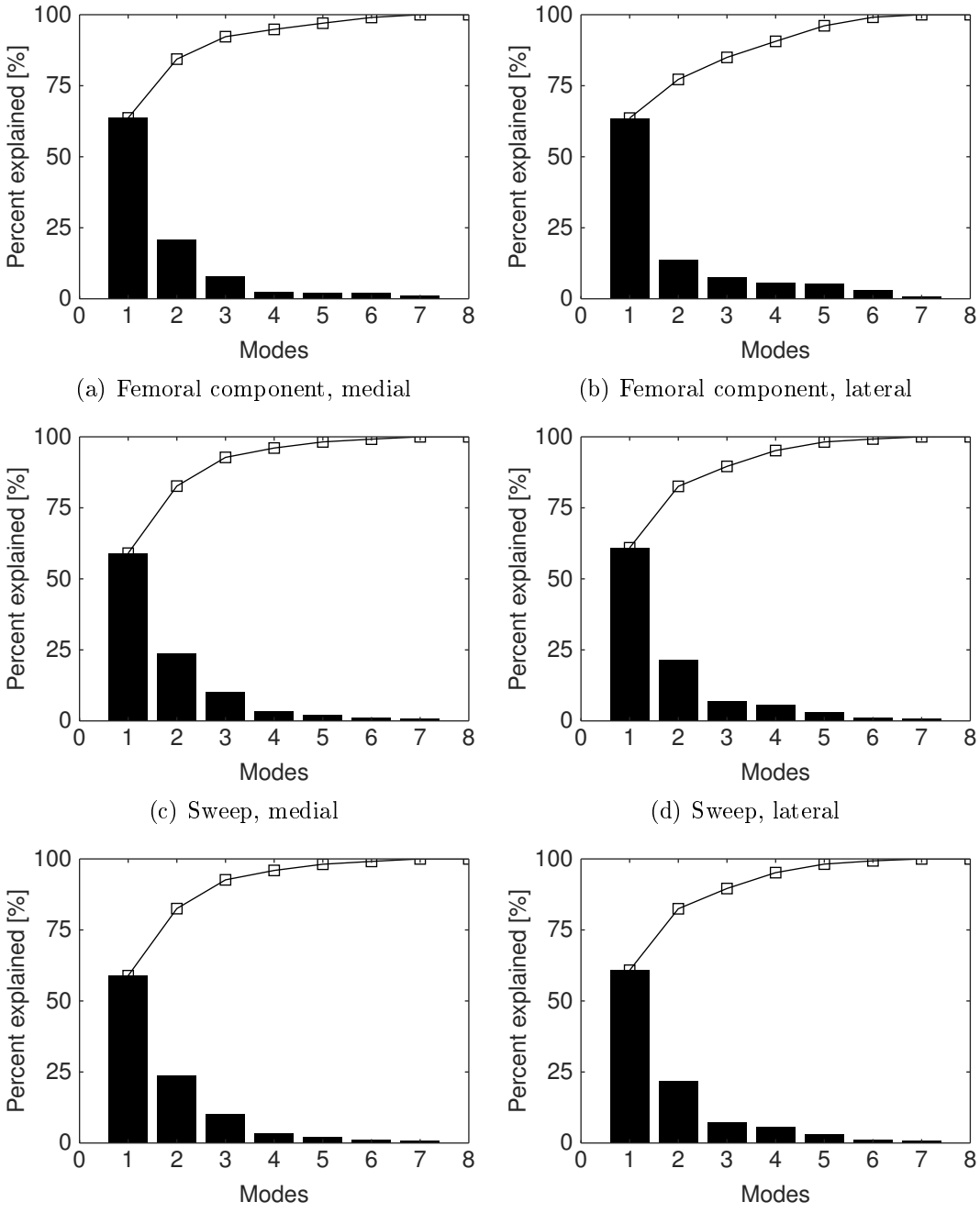

(a) Femoral component, medial

(b) Femoral component, lateral

(c) Sweep, medial

(d) Sweep, lateral

(e) Laxity sweep, medial

(f) Laxity sweep, lateral

Figure 6.16: Male UKR Pareto charts (Illustration: J. v.d. Merwe)

evidence of significant differences between the repeated implant components were found.

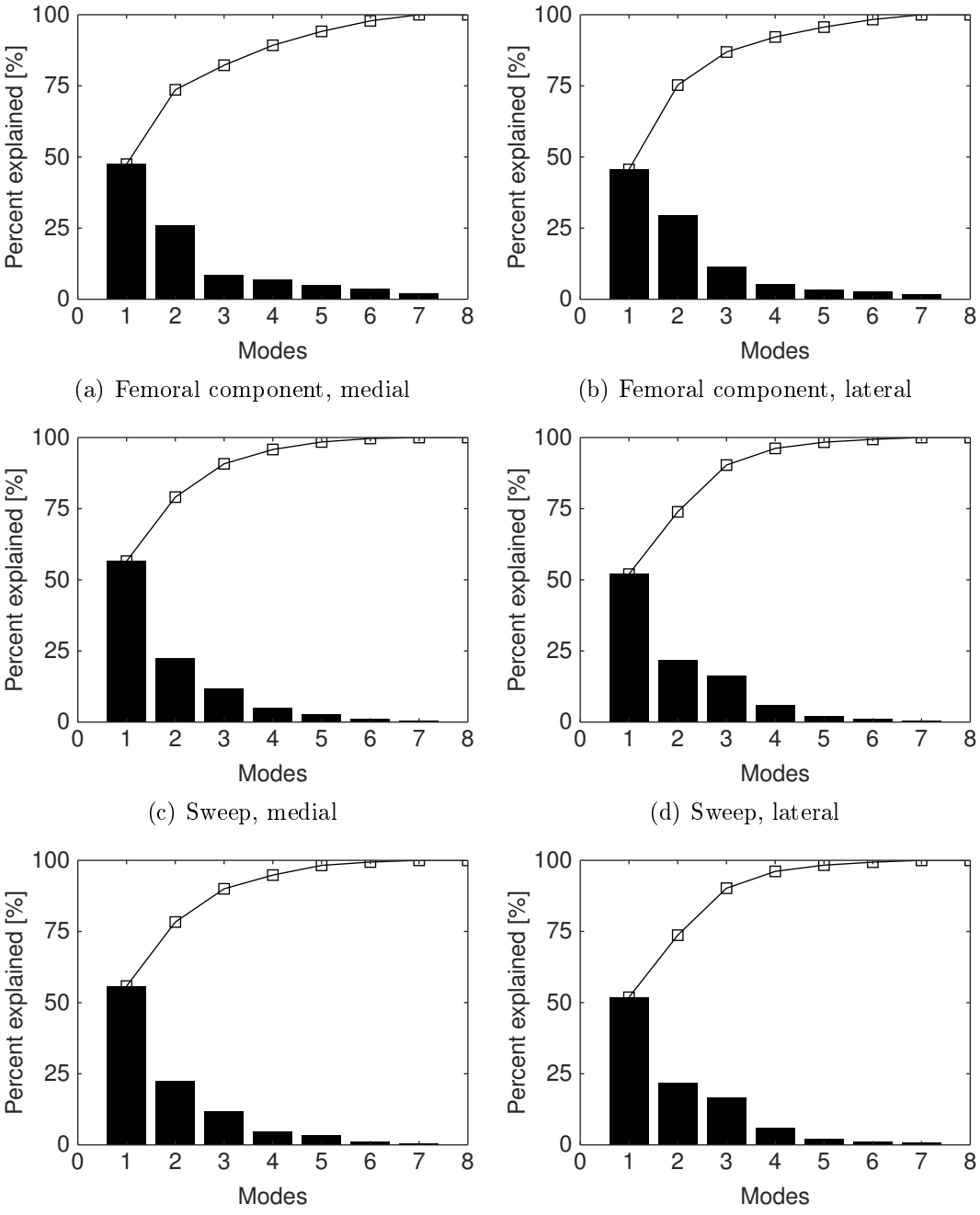

(a) Femoral component, medial

(b) Femoral component, lateral

(c) Sweep, medial

(d) Sweep, lateral

(e) Laxity sweep, medial

(f) Laxity sweep, lateral

Figure 6.17: Female UKR Pareto charts (Illustration: J. v.d. Merwe)

6.4 Discussion

Our semi-automated approach to designing patient-specific UKRs resulted in implants that compare favourably with normal knees. Additionally, the method was repeatable to within acceptable surgical tolerances, with the aver-

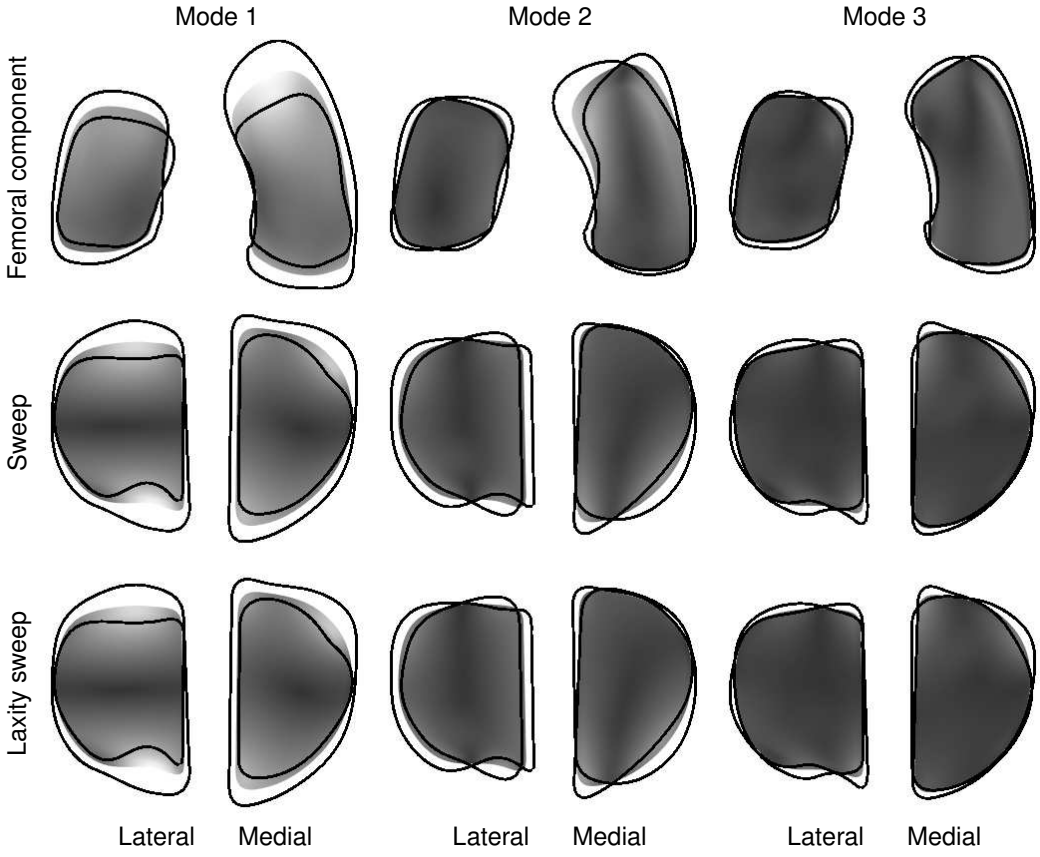

Figure 6.18: First three modes of the male UKRs (Illustration: J. v.d. Merwe)

Table 6.4: Mean RMS distance

	Male		Female	
	Medial	Lateral	Medial	Lateral
Component	mean RMSD $\pm$ σ_M [mm]			
Femoral component	0.59 $\pm$ 0.090	0.63 $\pm$ 0.081	0.60 $\pm$ 0.098	0.67 $\pm$ 0.095
Sweep	0.55 $\pm$ 0.109	0.49 $\pm$ 0.087	0.55 $\pm$ 0.111	0.55 $\pm$ 0.141
Laxity sweep	0.55 $\pm$ 0.109	0.49 $\pm$ 0.086	0.55 $\pm$ 0.109	0.56 $\pm$ 0.140

age RMS distances between the components' repetitions and their means being 0.67 mm or less and intra-observer standard deviations below $\pm$0.32 mm. The kinematic motion profiles resulted in movement of the femoral condyles' centers and approximated contact points that matches the trends observed in literature, and reproduces anatomically correct articular surfaces for the tibial components. The combination of a motion-guided, semi-automated, patient-specific UKR design approach based on non-pathological joint geometry rep-

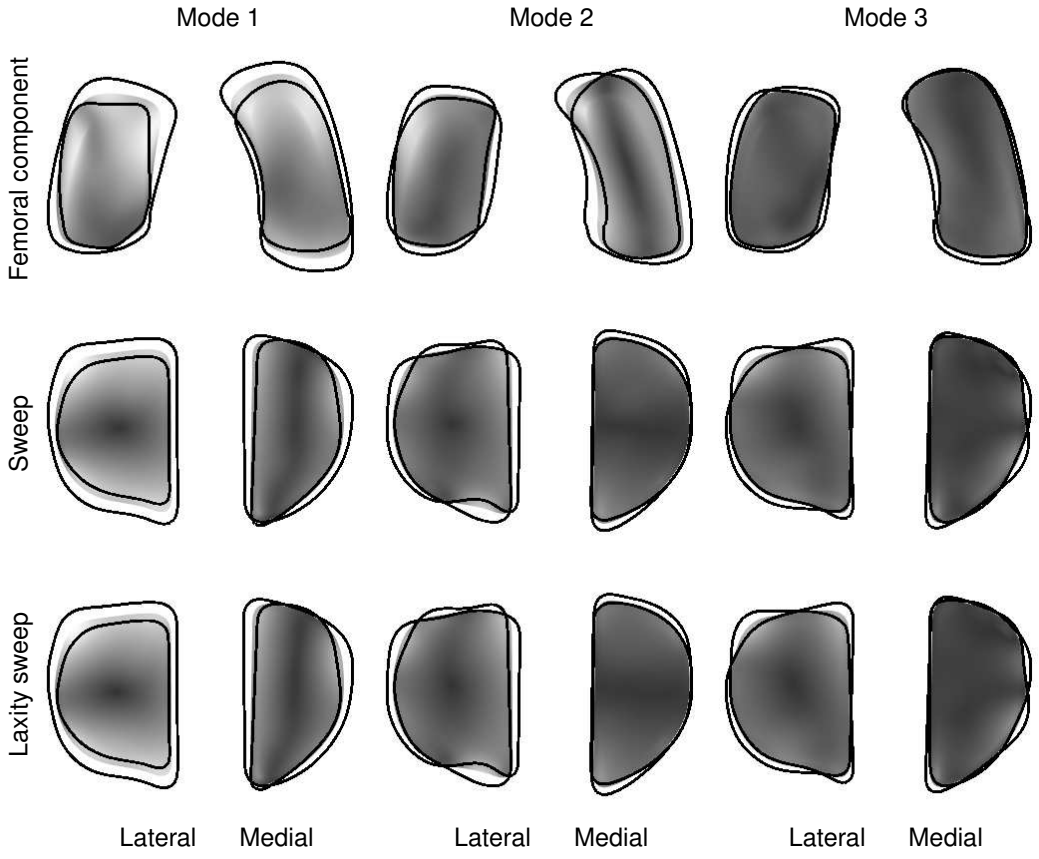

Figure 6.19: First three modes of the female UKRs (Illustration: J. v.d. Merwe)

Table 6.5: Standard deviation of repeated measurements

	Male		Female	
	Medial	**Lateral**	**Medial**	**Lateral**
Component	$\pm\,\sigma_w$ [mm]			
Femoral component	± 0.182	± 0.235	± 0.236	± 0.255
Sweep	± 0.227	± 0.212	± 0.245	± 0.321
Laxity sweep	± 0.227	± 0.211	± 0.241	± 0.322

resents a novel contribution to the field.

The shapes of the various implant components match the known geometries of the femur and tibia when compared to both literature and shape analyses from Chapters 3 and 4. Bonnin *et al.* (2016) observed the same inwardly angled medial femoral condyle, and Dai and Bischoff (2013) and Palastanga *et al.* (2006) the smaller, more square-ish shape of the lateral tibial component as we do in Figures 4.7 and 4.8. Palastanga *et al.* (2006) also describes the

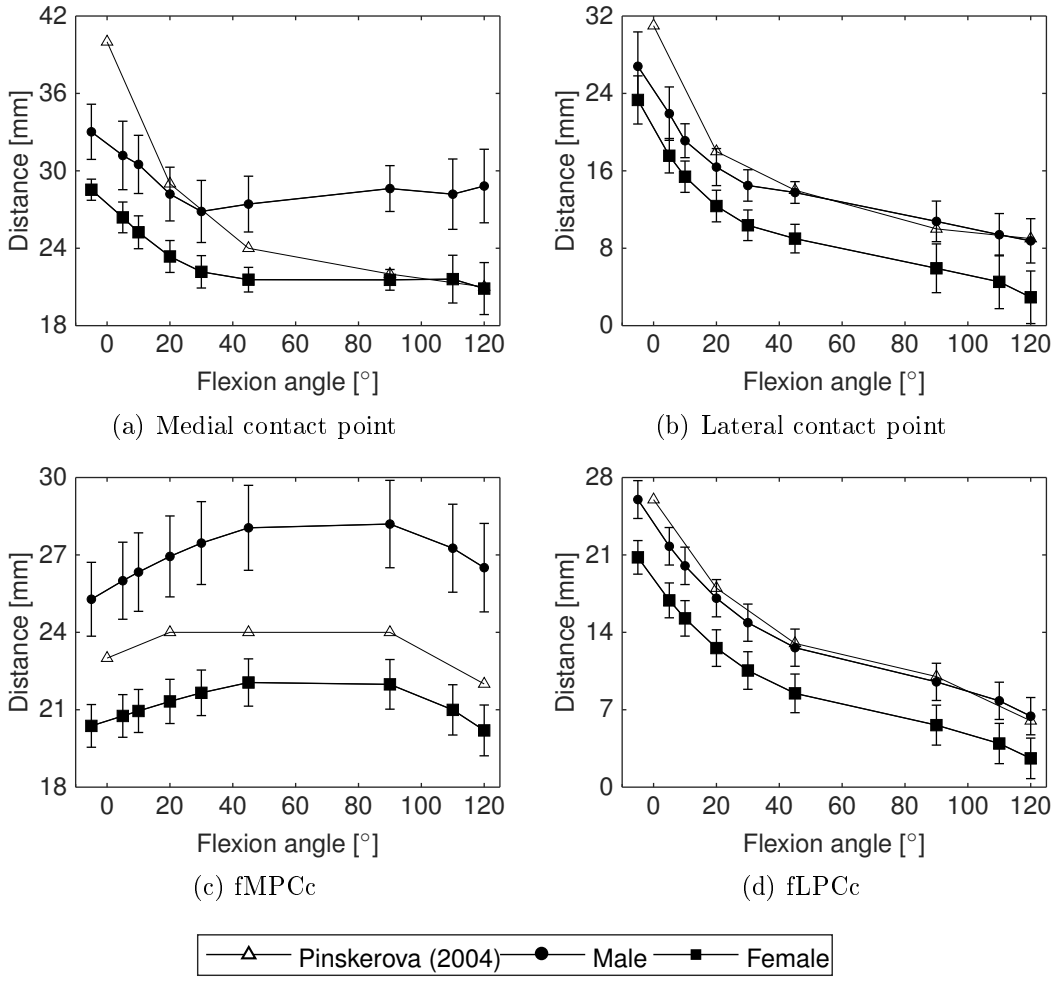

(a) Medial contact point

(b) Lateral contact point

(c) fMPCc

(d) fLPCc

Figure 6.20: Distance from the ipsilateral posterior cortex (Illustration: J. v.d. Merwe)

relatively posteriorly located femoral lateral suclus terminali which we expect from Figure 3.6. This results in shorter lateral femoral ROIs and components compared to the medial side. As for shape variation, we observe from Figures 4.10 and 4.11 that the largest mode again affects size and scale. Most of the remaining shape variation is also shared by the first few modes, which includes femoral condyle curvature and tibial cortical rim shape.

In contrast, the articular surfaces of the tibial components are predominantly influenced by the motion sweep. The natural femur translates posteriorly and rotates externally with flexion, relative to the tibia (Li *et al.*, 2008). However, due to the asymmetry of the femoral condyles, the medial condyle effectively remains immobile, with the lateral experiencing much larger posterior motion (Johal *et al.*, 2005; Pinskerova *et al.*, 2004) which coincides with a medially located center of rotation (Asano *et al.*, 2001; Yamaguchi *et al.*, 2009). This is further reflected in the estimated positions of the femoral contact points

and condyle centers, which matches the general trends from Pinskerova *et al.* (2004). We speculate that the differences between the ipsilateral distances for the male and female implants we observe in Figure 6.20 are due to the differences in size between the genders (Dai and Bischoff, 2013; Mahfouz *et al.*, 2012) which is not accounted for in the cited kinematic studies upon which we based our motion profiles. Regardless, Palastanga *et al.* (2006) describes the natural medial tibial condyle's surface as being concave, which matches the 'dished' articulating surfaces we obtain due to the medial femoral condyle remaining stable during flexion. That of the lateral condyle is said to be concave in the coronal plane, as is our 'grooved' components. In our case though, the lateral tibial components' articulating surfaces when viewed in the sagittal plane are flat posteriorly with raised anterior edges due to the pronounced posterior translation of the femoral condyle. This differs from the convex surface found in natural knees (Palastanga *et al.*, 2006) due to the fixed depth of the contact enforced after the initial kinematic sweep as well as the lack of a CC motion profile. However, given that the meniscus is sacrificed during UKA, we deem this a necessary measure to provide added joint stability and avoid dislocation.

The main sources of variation in the semi-automated design process are MRI segmentation, landmark identification for rough alignment and the user-guided shape estimation. Automated processes might improve segmentation repeatability and reproducibility at the cost of generalisability. Given the importance of obtaining an accurate representation of the patients' highly variable pathological bone surfaces (the issue is circumvented during shape estimation by excluding the affected regions) we opted instead for manual segmentation. This is still considered the 'gold standard' (Pedoia *et al.*, 2016), and to improve repeatability we relied instead on a single trained technician following an established protocol (Eckstein *et al.*, 2006). The inter and intra-observer variation of the landmarks used to establish rough alignment was recorded in Table 3.3, and were selected based on the recommendations in Chapter 3. Note that the initial rough alignment was updated during subsequent, automated ROI definition to base the coordinate systems instead on the more stable joint centres. This also mitigates variability due to differences between and within observers. Finally, the RMS distances of the repeated implant components from their means were within the same order of magnitude and generally slightly less than the overall mean RMS errors for repeated SSM estimations listed in Chapter 5. This also holds for the standard deviations between repeated estimations and implant components, suggesting that the semi-automated implant design process performs equally well than the estimations upon which it is based in terms of precision. Perhaps automating the estimation for the femoral ROIs as we do for those of the tibia could further improve repeatability. However, that would be at the cost of being able to constrain the model to appropriate local priors as per the user's discretion. The final results also lie well within achievable cutting accuracy and post op-

erative joint alignment tolerances (Camarda *et al.*, 2015; Lustig *et al.*, 2013), making the additional effort required to improve precision unnecessary.

The parameter values listed in Table 6.3 were selected and standardised such that they produced acceptable implant components for all sixteen unseen knees, although the user would normally be able to adjust them. This was done in order to accommodate the shape and repeatability analyses. Nevertheless, it would be prudent to investigate valid upper and lower limits for certain, crucial variables as part of a future study. These include the minimum component thicknesses, pin dimensions and even the laxity torque and force set-points. Quasi-static or even dynamic Finite Element Analyses (FEA) combined with biomechanical simulations to provide kinematic and kinetic inputs would be of great benefit in order to investigate stresses within the component as well as the resulting joint motions (Fitzpatrick *et al.*, 2012; Harrysson and Cormier, 2006; Hopkins *et al.*, 2010; Van den Heever *et al.*, 2012*a*). However, the matter is complicated by the one-of-a-kind nature of each implant and would require much effort in order to validate in a statistically significant manner. Regardless, the default values listed here do not deviate substantially from our observations of similar measurements from commercial implants, while the implant itself, though novel, is still unmistakeably a UKR. We therefore do not foresee significant alterations.

6.5 Conclusions

We presented a novel, semi-automated approach to patient-specific UKR design based on healthy approximation of otherwise pathological geometries. The method proved able to repeatedly generate anatomically and biomechanically compatible implant shapes. This suggests that the design would therefore facilitate the restoration of more normal post-operative joint function.

7. Conclusions

7.1 Introduction

Patient-specific Unicompartmental Knee Replacements (UKRs) have the potential to restore an individual's degraded knee closer to its natural state than off-the-shelf products. However, such designs ultimately rely on a technician's interpretation and skill in order to consistently reproduce healthy condyle shapes. Current state-of-the-art methods focus either on obtaining good estimates of pre-pathological geometries (Van den Heever, 2011), or automating the process (Steines and Zhuravlev, 2012), not both. The focus then of this work was to develop a repeatable, semi-automated method of generating patient-specific implant components.

7.2 Main findings and contributions

Little information was available on the most appropriate landmarks to use during measurement and Computer Assisted Design (CAD) activities based on knee (Victor *et al.*, 2009*a*). Specifically, we were interested in the inter-specimen variation as well as the inter- and intra-observer agreement and reliability of landmarks. This becomes especially relevant considering that the implant design process must be repeatable and reproducible. Therefore, a dense set of user-defined femoral and tibial landmarks were repeatedly identified by multiple observers and aligned to a mean reference via Generalised Procrustes Analysis (GPA). We concluded that some of the most reliable landmarks for coordinate axes definition were those derived from spheres and circles fitted to the joint condyles. Furthermore, despite the perceived difficulty in identifying the femoral terminalis sulci, both the medial and lateral coordinates were surprisingly repeatable and reproducible. They, along with the femoral notch apex, were used to define the condylar regions of interest (ROIs) in subsequent shape analyses of the joint.

In order to restore a joint to its pre-pathological state, an accurate representation of the shape of the knee was required. Osseous geometry variations are routinely studied via Statistical Shape Models (SSMs) and indeed, the knee is often represented (Heimann and Meinzer, 2009; Sarkalkan *et al.*, 2014).

Some few authors also segment the articular surfaces of their knee SSMs into ROIs relevant to UKR, though they focus mainly on establishing references for cartilage measurements (Hunter *et al.*, 2010; Williams *et al.*, 2006). We therefore extended this approach to consider the full shape variation of both the cartilaginous and osseous geometries. Furthermore, SSM performance is usually only evaluated at the hand of global error metrics rather than the more clinically relevant morphological measurements (Schumann *et al.*, 2010). Even our model, which yielded Root Mean Square Distance (RMSD) errors for the entire femur and tibia comparable with results in literature only achieved acceptable performance for the medial and lateral femoral condyles when considering discrete measurements.

Since SSMs vary according to the sample population from which they are trained (Cootes *et al.*, 1995) and yield a set of parameters that affect the shape globally (Heimann and Meinzer, 2009), they are often used to extrapolate missing geometries from sparse data (Blanc and Székely, 2012). In particular, we developed a Graphical User Interface (GUI) with which a user could identify specific landmarks on the *healthy* portions of a knee indicated for arthroplasty. With this we attempted to improve the local performance of the aforementioned SSM by creating a strong prior from which to estimate the *pathological* parts for UKR (Albrecht *et al.*, 2013). This user-guided approach to SSM estimation was shown to be repeatable and resulted in generality and specificity values that compared well with literature.

We finally developed a semi-automated, fixed bearing, metal-backed patient-specific UKR design. The femoral component's articular surface was based on healthy estimates obtained from the aforementioned SSM, while that of the tibial insert was motion-guided. A number of Total Knee Replacements (TKRs) designs that rely on kinematic profiles to create insert surfaces have been reported (Amiri, 2008; Koh *et al.*, 2017*b*; Pejhan *et al.*, 2016; Walker, 1988, 2014), though to the best of our knowledge this is the first application thereof to UKR design. Furthermore, the user is able to adjust most of the associated design parameters, though for the default values it was shown that the method is repeatable and reproduces normal, anatomically correct implant components. The motion sweep was also able to reproduce the expected translation of of the condyle centers and estimated contact points. We are confident therefore that the implant is ready for preliminary clinical testing.

7.3 Recommendations

The scope of the current study was limited to the design phase. Naturally, in order to validate and refine the concept, rigorous testing must be conducted. In particular, we recommend that in-vitro testing be done on cadaveric knees. Initial tests could be limited to unloaded kinematic flexion, similar to evaluation of ligament balancing during surgery. However, dynamically loaded tests

would give a more accurate indication of the extent to which the implant alters normal joint motion (Delport *et al.*, 2015; Varadarajan *et al.*, 2009; Victor *et al.*, 2010). This could serve as validation for accompanying biomechanical simulations which in turn could supply input and boundary conditions for Finite Element Analyses (FEA) (Fitzpatrick *et al.*, 2012; Harrysson and Cormier, 2006; Hopkins *et al.*, 2010; Van den Heever *et al.*, 2012*a*). Indeed, while the default parameters of the implant concept is based on equivalent features of contemporary implant designs, we suggest a detailed investigation into implant stress, fatigue and wear in order to establish a statistically 'safe' range of values. This of course, is not a trivial endeavour, and must also take into account eventual manufacturing processes and material constraints. Finally, in vitro wear testing according to the ISO 14243 series of standards is required to confirm long term performance of the implant, followed by clinical trials once reasonable evidence of success has been demonstrated.

List of references

Albrecht, T., Lüthi, M., Gerig, T. and Vetter, T. (2013). Posterior shape models. *Medical image analysis*, vol. 17, no. 8, pp. 959–973.

Allaire, S., Jacq, J.J., Burdin, V., Roux, C. and Couture, C. (2007). Type-constrained robust fitting of quadrics with application to the 3d morphological characterization of saddle-shaped articular surfaces. In: *Computer vision, 2007. ICCV 2007. IEEE 11th International conference on*, pp. 1–8. IEEE.

Altman, R.D., Hochberg, M., Murphy Jr, W., Wolfe, F. and Lequesne, M. (1995). Atlas of individual radiographic features in osteoarthritis. *Osteoarthritis & cartilage*, vol. 3, pp. 3–70.

American Academy of Orthopaedic Surgeons (1995). *Knee replacement implants*. [Online] (Reviewed September 2010) Available at: `http://orthoinfo.aaos.org` [Accessed 25 March 2011].

Amiri, S. (2008). *Conceptual design for a surface-guided total knee replacement with normal kinematics*. Ph.D. thesis, Queen's University.

Andrews, J. and Séquin, C.H. (2014). Type-constrained direct fitting of quadric surfaces. *Computer-aided design & applications*, vol. 11, no. 1, pp. 107–119.

Asano, T., Akagi, M., Tanaka, K., Tamura, J. and Nakamura, T. (2001). In vivo three-dimensional knee kinematics using a biplanar image-matching technique. *Clinical orthopaedics & related research*, vol. 388, pp. 157–166.

Ateshian, G., Rosenwasser, M. and Mow, V. (1992). Curvature characteristics and congruence of the thumb carpometacarpal joint: differences between female and male joints. *Journal of biomechanics*, vol. 25, no. 6, pp. 591–607.

Ateshian, G., Soslowsky, L. and Mow, V. (1991). Quantitation of articular surface topography and cartilage thickness in knee joints using stereophotogrammetry. *Journal of biomechanics*, vol. 24, no. 8, pp. 761–776.

Ateshian, G. *et al.* (1993). A b-spline least-squares surface-fitting method for articular surfaces of diarthrodial joints. *Transactions - American society of mechanical engineers journal of biomechanical engineering*, vol. 115, pp. 366–366.

Baek, S.Y., Wang, J.H., Song, I., Lee, K., Lee, J. and Koo, S. (2013). Automated bone landmarks prediction on the femur using anatomical deformation technique. *Computer-aided design*, vol. 45, no. 2, pp. 505–510.

Bartel, D., Burstein, A., Santavicca, E. and Insall, J. (1982). Performance of the tibial component in total knee replacement. *Journal of bone & joint surgery*, vol. 64, no. 7, pp. 1026–1033.

Bartlett, J. and Frost, C. (2008). Reliability, repeatability and reproducibility: analysis of measurement errors in continuous variables. *Ultrasound in obstetrics & gynecology*, vol. 31, no. 4, pp. 466–475.

Belyaev, A. (2006). Mesh smoothing and enhancing. Curvature estimation. *Saarbrucken*.

Biomet (2017). *The Oxford Partial Knee*. [Online] Available at: `http://www.biomet.com` [Accessed 21 November 2017].

Biščević, M., Hebibović, M. and Smrke, D. (2005). Variations of femoral condyle shape. *Collegium antropologicum*, vol. 29, no. 2, pp. 409–414.

Bischoff, J.E., Dai, Y., Goodlett, C., Davis, B. and Bandi, M. (2014). Incorporating population-level variability in orthopedic biomechanical analysis: A review. *Journal of biomechanical engineering*, vol. 136, no. 2, p. 021004.

Blanc, R., Syrkina, E. and Székely, G. (2009). Estimating the confidence of statistical model based shape prediction. In: *Information Processing in Medical Imaging*, pp. 602–613. Springer.

Blanc, R. and Székely, G. (2012). Confidence regions for statistical model based shape prediction from sparse observations. *Medical imaging, IEEE transactions on*, vol. 31, no. 6, pp. 1300–1310.

Blankevoort, L., Huiskes, R. and De Lange, A. (1988). The envelope of passive knee joint motion. *Journal of biomechanics*, vol. 21, no. 9, pp. 705–720.

Blanz, V., Mehl, A., Vetter, T. and Seidel, H.-P. (2004). A statistical method for robust 3D surface reconstruction from sparse data. In: *3D data processing, visualization and transmission, 2004. Proceedings. 2nd international symposium on*, pp. 293–300. IEEE.

Bonnin, M., Saffarini, M., Bossard, N., Dantony, E. and Victor, J. (2016). Morphometric analysis of the distal femur in total knee arthroplasty and native knees. *Bone & joint journal*, vol. 98, no. 1, pp. 49–57.

Bowes, M.A., Vincent, G.R., Wolstenholme, C.B. and Conaghan, P.G. (2015). A novel method for bone area measurement provides new insights into osteoarthritis and its progression. *Annals of the rheumatic diseases*, vol. 74, no. 3, pp. 519–525.

Braun, H.J. and Gold, G.E. (2012). Diagnosis of osteoarthritis: imaging. *Bone*, vol. 51, no. 2, pp. 278–288.

Bredbenner, T.L., Eliason, T.D., Potter, R.S., Mason, R.L., Havill, L.M. and Nicolella, D.P. (2010). Statistical shape modeling describes variation in tibia and femur surface geometry between control and incidence groups from the osteoarthritis initiative database. *Journal of biomechanics*, vol. 43, no. 9, pp. 1780–1786.

Buckland-Wright, C. (2004). Subchondral bone changes in hand and knee osteoarthritis detected by radiography. *Osteoarthritis & cartilage*, vol. 12, pp. 10–19.

Buckwalter, J. and Brown, T. (2004). Joint injury, repair, and remodeling: roles in post-traumatic osteoarthritis. *Clinical orthopaedics & related research*, vol. 423, pp. 7–16.

Buckwalter, J.A., Saltzman, C. and Brown, T. (2004). The impact of osteoarthritis: implications for research. *Clinical orthopaedics & related research*, vol. 427, pp. S6–S15.

Callaghan, J. (2003). *The adult knee*, vol. 1. Lippincott Williams & Wilkins.

Callahan, C., Drake, B., Heck, D. and Dittus, R. (1995). Patient outcomes following unicompartmental or bicompartmental knee arthroplasty. *Journal of arthroplasty*, vol. 10, no. 2, pp. 141–150.

Camarda, L., D'Arienzo, A., Morello, S., Peri, G., Valentino, B. and D'Arienzo, M. (2015). Patient-specific instrumentation for total knee arthroplasty: a literature review. *Musculoskeletal surgery*, vol. 99, no. 1, pp. 11–18.

Cavaignac, E., Savall, F., Faruch, M., Reina, N., Chiron, P. and Telmon, N. (2016). Geometric morphometric analysis reveals sexual dimorphism in the distal femur. *Forensic science international*, vol. 259, pp. 246–e1.

Chau, R., Gulati, A., Pandit, H., Beard, D., Price, A., Dodd, C., Gill, H. and Murray, D. (2009). Tibial component overhang following unicompartmental knee replacement - does it matter? *The knee*, vol. 16, no. 5, pp. 310–313.

Cheng, F.B., Ji, X.F., Lai, Y., Feng, J.C., Zheng, W.X., Sun, Y.F., Fu, Y.W. and Li, Y.Q. (2009). Three dimensional morphometry of the knee to design the total knee arthroplasty for chinese population. *The knee*, vol. 16, no. 5, pp. 341–347.

Cheng, T., Zhang, G. and Zhang, X. (2011). Metal-backed versus all-polyethylene tibial components in primary total knee arthroplasty: A meta-analysis and systematic review of randomized controlled trials. *Acta orthopaedica*, vol. 82, no. 5, pp. 589–595.

Cho, K., Müller, J. and Erasmus, P. (2015). Trochlear groove alignment measurement method for surgical applications. *Journal of mechanics in medicine & biology*, vol. 15, no. 02, pp. 15400331–15400337.

Choi, J.-A. and Gold, G.E. (2011). MR imaging of articular cartilage physiology. *Magnetic resonance imaging clinics of North America*, vol. 19, no. 2, pp. 249–282.

Cobb, J., Dixon, H., Dandachli, W. and Iranpour, F. (2008). The anatomical tibial axis. *Journal of bone & joint surgery, British volume*, vol. 90, no. 8, pp. 1032–1038.

Cohen, Z.A., Mccarthy, D.M., Kwak, S.D., Legrand, P., Fogarasi, F., Ciaccio, E.J. and Ateshian, G.A. (1999). Knee cartilage topography, thickness, and contact areas from MRI: in-vitro calibration and in-vivo measurements. *Osteoarthritis & cartilage*, vol. 7, no. 1, pp. 95–109.

Coons, S. (1967). Technical report ad-663 504. *Massachusetts Institute of Technology, Cambridge, MA*.

Cootes, T.F., Taylor, C.J., Cooper, D.H. and Graham, J. (1995). Active shape models-their training and application. *Computer vision & image understanding*, vol. 61, no. 1, pp. 38–59.

Cootes, T.F., Taylor, C.J. *et al.* (2004). Statistical models of appearance for computer vision.

Corsini, M., Cignoni, P. and Scopigno, R. (2012). Efficient and flexible sampling with blue noise properties of triangular meshes. *Visualization & computer graphics, IEEE transactions on*, vol. 18, no. 6, pp. 914–924.

Cross, M., Smith, E., Hoy, D., Nolte, S., Ackerman, I., Fransen, M., Bridgett, L., Williams, S., Guillemin, F., Hill, C.L. *et al.* (2014). The global burden of hip and knee osteoarthritis: estimates from the global burden of disease 2010 study. *Annals of the rheumatic diseases*, pp. annrheumdis–2013.

Cumming, G., Fidler, F. and Vaux, D.L. (2007). Error bars in experimental biology. *Journal of cell biology*, vol. 177, no. 1, pp. 7–11.

Dai, Y. and Bischoff, J.E. (2013). Comprehensive assessment of tibial plateau morphology in total knee arthroplasty: influence of shape and size on anthropometric variability. *Journal of orthopaedic research*, vol. 31, no. 10, pp. 1643–1652.

Dargel, J., Michael, J.W., Feiser, J., Ivo, R. and Koebke, J. (2011). Human knee joint anatomy revisited: morphometry in the light of sex-specific total knee arthroplasty. *Journal of arthroplasty*, vol. 26, no. 3, pp. 346–353.

Davies, R.H. (2002). *Learning shape: optimal models for analysing natural variability*. Ph.D. thesis, University of Manchester.

DeFrate, L.E., Sun, H., Gill, T.J., Rubash, H.E. and Li, G. (2004). In vivo tibiofemoral contact analysis using 3D MRI-based knee models. *Journal of biomechanics*, vol. 37, no. 10, pp. 1499–1504.

Della Croce, U., Cappozzo, A. and Kerrigan, D.C. (1999). Pelvis and lower limb anatomical landmark calibration precision and its propagation to bone geometry and joint angles. *Medical & biological engineering & computing*, vol. 37, no. 2, pp. 155–161.

Delport, H., Labey, L., Innocenti, B., De Corte, R., Vander Sloten, J. and Bellemans, J. (2015). Restoration of constitutional alignment in TKA leads to more physiological strains in the collateral ligaments. *Knee surgery, sports traumatology, arthroscopy*, vol. 23, no. 8, pp. 2159–2169.

Demange, M.K., Von Keudell, A., Probst, C., Yoshioka, H. and Gomoll, A.H. (2015). Patient-specific implants for lateral unicompartmental knee arthroplasty. *International orthopaedics*, vol. 39, no. 8, pp. 1519–1526.

Dettoni, F., Bonasia, D.E., Castoldi, F., Bruzzone, M., Blonna, D. and Rossi, R. (2010). High tibial osteotomy versus unicompartmental knee arthroplasty for medial compartment arthrosis of the knee: a review of the literature. *The Iowa orthopaedic journal*, vol. 30, p. 131.

Dippé, M.A.Z. and Wold, E.H. (1985). Antialiasing through stochastic sampling. *ACM siggraph computer graphics*, vol. 19, no. 3, pp. 69–78.

Dryden, I.L. and Mardia, K.V. (1998). *Statistical shape analysis*, vol. 4. Wiley Chichester.

Eckhoff, D., Bach, J., Spitzer, V., Reinig, K., Bagur, M., Baldini, T. and Flannery, N. (2005). Three-dimensional mechanics, kinematics, and morphology of the knee viewed in virtual reality. *Journal of bone & joint surgery*, vol. 87, no. suppl_2, pp. 71–80.

Eckstein, F., Cicuttini, F., Raynauld, J.-P., Waterton, J. and Peterfy, C. (2006). Magnetic resonance imaging (MRI) of articular cartilage in knee osteoarthritis (OA): morphological assessment. *Osteoarthritis & cartilage*, vol. 14, pp. 46–75.

Eckstein, F., Kwoh, C.K., Link, T.M. and OAI investigators (2014). Imaging research results from the osteoarthritis initiative (OAI): a review and lessons learned 10 years after start of enrolment. *Annals of the rheumatic diseases*, vol. 73, no. 7, pp. 1289–1300.

Eggert, D.W., Lorusso, A. and Fisher, R.B. (1997). Estimating 3D rigid body transformations: a comparison of four major algorithms. *Machine vision & applications*, vol. 9, no. 5-6, pp. 272–290.

Eilers, P.H. and Marx, B.D. (1996). Flexible smoothing with B-splines and penalties. *Statistical science*, pp. 89–102.

Esfandiarpour, F., Olyaei, G., Shakouri Rad, A., Farahmand, F., Talebian, S., Makhsous, M. and Parnianpour, M. (2009). Reliability of determination of bony landmarks of the distal femur on MR images and MRI based 3d models. *Iranian journal of radiology*, vol. 6, no. 4.

Fitz, W. (2009). Unicompartmental knee arthroplasty with use of novel patient-specific resurfacing implants and personalized jigs. *Journal of bone & joint surgery*, vol. 91, no. Supplement_1, pp. 69–76.

Fitz, W., Bliss, R. and Losina, E. (2013). Current fit of medial and lateral unicompartmental knee arthroplasty. *Acta orthopaedica Belgica*, vol. 79, no. 2, p. 191.

Fitzpatrick, C., FitzPatrick, D. and Auger, D. (2008). Size and shape of the resection surface geometry of the osteoarthritic knee in relation to total knee replacement design. *Proceedings of the Institution of Mechanical Engineers, Part H: Journal of Engineering in Medicine*, vol. 222, no. 6, pp. 923–932.

Fitzpatrick, C., FitzPatrick, D., Lee, J. and Auger, D. (2007). Statistical design of unicompartmental tibial implants and comparison with current devices. *The knee*, vol. 14, no. 2, pp. 138–144.

Fitzpatrick, C.K., Clary, C.W. and Rullkoetter, P.J. (2012). The role of patient, surgical, and implant design variation in total knee replacement performance. *Journal of biomechanics*, vol. 45, no. 12, pp. 2092–2102.

Freeman, M. (2001). How the knee moves. *Current Orthopaedics*, vol. 15, no. 6, pp. 444–450.

Freeman, M., Pinskerova, V. *et al.* (2005). The movement of the normal tibio-femoral joint. *Journal of biomechanics*, vol. 38, no. 2, p. 197.

Fruciano, C. (2016). Measurement error in geometric morphometrics. *Development genes & evolution*, vol. 226, no. 3, pp. 139–158.

Frye, B.M., Najim, A.A., Adams, J.B., Berend, K.R. and Lombardi, A.V. (2015). MRI is more accurate than CT for patient-specific total knee arthroplasty. *The knee*, vol. 22, no. 6, pp. 609–612.

Fu, Y. and Zhou, B. (2008). Direct sampling on surfaces for high quality remeshing. In: *Proceedings of the 2008 ACM symposium on solid and physical modeling*, pp. 115–124. ACM.

Fukubayashi, T., Torzilli, P., Sherman, M. and Warren, R. (1982). An in vitro biomechanical evaluation of anterior-posterior motion of the knee. tibial displacement, rotation, and torque. *Journal of bone & joint surgery*, vol. 64, no. 2, pp. 258–264.

Garstang, S.V. and Stitik, T.P. (2006). Osteoarthritis: epidemiology, risk factors, and pathophysiology. *American journal of physical medicine & rehabilitation*, vol. 85, no. 11, pp. S2–S11.

Grood, E.S. and Suntay, W.J. (1983). A joint coordinate system for the clinical description of three-dimensional motions: application to the knee. *Journal of biomechanical engineering*, vol. 105, no. 2, pp. 136–144.

Gudnason, A., Hailer, N.P., Annette, W., Sundberg, M., Robertsson, O. *et al.* (2014). All-polyethylene versus metal-backed tibial components - an analysis of 27,733 cruciate-retaining total knee replacements from the swedish knee arthroplasty register. *Journal of bone & joint surgery*, vol. 96, no. 12, pp. 994–999.

Guéziec, A. (1999). Locally toleranced surface simplification. *Visualization & computer graphics, IEEE transactions on*, vol. 5, no. 2, pp. 168–189.

Hamilton, T.W., Pandit, H.G., Jenkins, C., Mellon, S.J., Dodd, C.A. and Murray, D.W. (2017). Evidence-based indications for mobile-bearing unicompartmental knee arthroplasty in a consecutive cohort of thousand knees. *Journal of arthroplasty*, vol. 32, no. 6, pp. 1779–1785.

Harmon, E.H. (2007). The shape of the hominoid proximal femur: a geometric morphometric analysis. *Journal of anatomy*, vol. 210, no. 2, pp. 170–185.

Harrysson, O., Hosni, Y. and Nayfeh, J. (2007). Custom-designed orthopedic implants evaluated using finite element analysis of patient-specific computed tomography data: femoral-component case study. *BMC musculoskeletal disorders*, vol. 8, no. 1, p. 91.

Harrysson, O.L. and Cormier, D.R. (2006). Direct fabrication of custom orthopedic implants using electron beam melting technology. *Advanced manufacturing technology for medical applications*, pp. 191–206.

Hefzy, M. and Yang, H. (1993). A three-dimensional anatomical model of the human patello-femoral joint, for the determination of patello-femoral motions and contact characteristics. *Journal of biomedical engineering*, vol. 15, no. 4, pp. 289–302.

Heimann, T. and Meinzer, H.-P. (2009). Statistical shape models for 3D medical image segmentation: a review. *Medical image analysis*, vol. 13, no. 4, pp. 543–563.

Hernborg, J. and Nilsson, B.E. (1973). The relationship between osteophytes in the knee joint, osteoarthritis and aging. *Acta orthopaedica Scandinavica*, vol. 44, no. 1, pp. 69–74.

Hill, P.F., Vedi, V., Williams, A., Iwaki, H., Pinskerova, V. and Freeman, M. (2000). Tibiofemoral movement 2: the loaded and unloaded living knee studied by MRI. *Bone & Joint Journal*, vol. 82, no. 8, pp. 1196–1198.

Hirokawa, S., Ueki, T. and Ohtsuki, A. (2004). A new approach for surface fitting method of articular joint surfaces. *Journal of biomechanics*, vol. 37, no. 10, pp. 1551–1559.

Hollister, A., Jatana, S., Singh, A., Sullivan, W. and Lupichuk, A. (1993). The axes of rotation of the knee. *Clinical orthopaedics & related research*, pp. 259–259.

Hopkins, A.R., New, A.M., Rodriguez-y Baena, F. and Taylor, M. (2010). Finite element analysis of unicompartmental knee arthroplasty. *Medical engineering & physics*, vol. 32, no. 1, pp. 14–21.

Howell, S.M., Kuznik, K., Hull, M.L. and Siston, R.A. (2008). Results of an initial experience with custom-fit positioning total knee arthroplasty in a series of 48 patients. *Orthopedics*, vol. 31, no. 9.

Hunter, D., Bowes, M., Eaton, C., Holmes, A., Mann, H., Kwoh, C., Maciewicz, R., Samuels, J. and Waterton, J. (2010). Can cartilage loss be detected in knee osteoarthritis (Oa) patients with 3–6 months' observation using advanced image analysis of 3T MRI? *Osteoarthritis & cartilage*, vol. 18, no. 5, pp. 677–683.

Hutt, J., Farhadnia, P., Massé, V., LaVigne, M. and Vendittoli, P. (2015). A randomised trial of all-polyethylene and metal-backed tibial components in unicompartmental arthroplasty of the knee. *Bone & joint journal*, vol. 97, no. 6, pp. 786–792.

Iranpour, F., Merican, A., Dandachli, W., Amis, A. and Cobb, J. (2010). The geometry of the trochlear groove. *Clinical Orthopaedics and Related Research*, vol. 468, no. 3, pp. 782–788.

Iwaki, H., Pinskerova, V., Freeman, M. *et al.* (2000). Tibiofemoral movement 1: the shapes and relative movements of the femur and tibia in the unloaded cadaver knee. *Journal of bone & joint surgery, British volume*, vol. 82, no. 8, pp. 1189–1195.

Jemmett, P. and Roy, S. (2016). The iDuo bi-compartmental knee replacement: our early experience. *Reconstructive review*, vol. 6, no. 4.

Johal, P., Williams, A., Wragg, P., Hunt, D. and Gedroyc, W. (2005). Tibio-femoral movement in the living knee. A study of weight bearing and non-weight bearing knee kinematics using 'interventional' MRI. *Journal of biomechanics*, vol. 38, no. 2, pp. 269–276.

Jones, L.D., Palmer, J. and Jackson, W.F. (2017). Unicompartmental knee arthroplasty. *Orthopaedics & trauma*, vol. 31, no. 1, pp. 8–15.

Kedgley, A.E., McWalter, E.J. and Wilson, D.R. (2015). The effect of coordinate system variation on in vivo patellofemoral kinematic measures. *The knee*, vol. 22, no. 2, pp. 88–94.

Ko, Y.B., Gujarathi, M.R. and Oh, K.J. (2015). Outcome of unicompartmental knee arthroplasty: a systematic review of comparative studies between fixed and mobile bearings focusing on complications. *Knee surgery & related research*, vol. 27, no. 3, p. 141.

Koh, I.J., Suhl, K.H., Kim, M.W., Kim, M.S., Choi, K.Y. and In, Y. (2017*a*). Use of all-polyethylene tibial components in unicompartmental knee arthroplasty increases the risk of early failure. *Journal of knee surgery*.

Koh, Y., Son, J., Kwon, S., Kim, H., Kwon, O. and Kang, K. (2017*b*). Preservation of kinematics with posterior cruciate-, bicruciate-and patient-specific bicruciate-retaining prostheses in total knee arthroplasty by using computational simulation with normal knee model. *Bone & joint research*, vol. 6, no. 9, pp. 557–565.

Koo, S., Gold, G. and Andriacchi, T. (2005). Considerations in measuring cartilage thickness using MRI: factors influencing reproducibility and accuracy. *Osteoarthritis & cartilage*, vol. 13, no. 9, pp. 782–789.

Kosel, J., Giouroudi, L., Scheffer, C., Dillon, E. and Erasmus, P. (2010). Anatomical study of the radius and center of curvature of the distal femoral condyle. *Journal of biomechanical engineering*, vol. 132, no. 9.

Kozic, N., Weber, S., Büchler, P., Lutz, C., Reimers, N., Ballester, M.Á.G. and Reyes, M. (2010). Optimisation of orthopaedic implant design using statistical shape space analysis based on level sets. *Medical image analysis*, vol. 14, no. 3, pp. 265–275.

Kozinn, S. and Scott, R. (1989). Unicondylar knee arthroplasty. *Journal of bone & joint surgery, American volume*, vol. 71, no. 1, p. 145.

Krames, C. (2001). *Knee anatomy - patella reflected to show knee anatomy.* [Image Online] Available at: `http://www.kramestudios.com` [Accessed 24 January 2011].

Krevolin, J. (2003). Specimen-specific, three dimensional knee joint mechanics: Normal and reconstructed.

Krol, Z., Skadlubowicz, P., Hefti, F. and Krieg, A.H. (2013). Virtual reconstruction of pelvic tumor defects based on a gender-specific statistical shape model. *Computer aided surgery*, vol. 18, no. 5-6, pp. 142–153.

Kurosawa, H., Walker, P., Abe, S., Garg, A. and Hunter, T. (1985). Geometry and motion of the knee for implant and orthotic design. *Journal of biomechanics*, vol. 18, no. 7, pp. 487–499.

Kurtz, S., Ong, K., Lau, E., Mowat, F. and Halpern, M. (2007). Projections of primary and revision hip and knee arthroplasty in the United States from 2005 to 2030. *Journal of bone & joint surgery*, vol. 89, no. 4, pp. 780–785.

Lagae, A. and Dutré, P. (2005). A procedural object distribution function. *ACM transactions on graphics (TOG)*, vol. 24, no. 4, pp. 1442–1461.

Laskin, R. (2001). Unicompartmental knee replacement: some unanswered questions. *Clinical orthopaedics & related research*, vol. 392, p. 267.

Lewis, J., Askew, M. and Jaycox, D. (1982). A comparative evaluation of tibial component designs of total knee prostheses. *Journal of bone & joint surgery*, vol. 64, no. 1, pp. 129–135.

Li, G., Papannagari, R., Li, M., Bingham, J., Nha, K.W., Allred, D. and Gill, T. (2008). Effect of posterior cruciate ligament deficiency on in vivo translation and rotation of the knee during weightbearing flexion. *American journal of sports medicine*, vol. 36, no. 3, pp. 474–479.

Lim, J., Chong, H., Pang, H., Tay, K., Chia, S., Lo, N. and Yeo, S. (2017). Revision total knee arthroplasty for failed high tibial osteotomy and unicompartmental knee arthroplasty have similar patient-reported outcome measures in a two-year follow-up study. *Bone & joint journal*, vol. 99, no. 10, pp. 1329–1334.

Lin, Y., Wang, C. and Dai, K. (2005). Reverse engineering in CAD model reconstruction of customized artificial joint. *Medical engineering & physics*, vol. 27, no. 2, pp. 189–193.

Lo, J., Müller, O., Dilger, T., Wülker, N. and Wünschel, M. (2011). Translational and rotational knee joint stability in anterior and posterior cruciate-retaining knee arthroplasty. *The knee*, vol. 18, no. 6, pp. 491–495.

Lu, K. (2010). Least squares approximation.

Lustig, S., Scholes, C.J., Oussedik, S.I., Kinzel, V., Coolican, M.R. and Parker, D.A. (2013). Unsatisfactory accuracy as determined by computer navigation of visionaire patient-specific instrumentation for total knee arthroplasty. *Journal of arthroplasty*, vol. 28, no. 3, pp. 469–473.

Ma, C.B., Kanamori, A., Vogrin, T.M., Woo, S.L. and Harner, C.D. (2003). Measurement of posterior tibial translation in the posterior cruciate ligament-reconstructed knee. *American journal of sports medicine*, vol. 31, no. 6, pp. 843–848.

Mahfouz, M., Fatah, E.E.A., Bowers, L.S. and Scuderi, G. (2012). Three-dimensional morphology of the knee reveals ethnic differences. *Clinical orthopaedics & related research*, vol. 470, no. 1, pp. 172–185.

Mahfouz, M., Merkl, B., Abdel Fatah, E., Booth Jr, R. and Argenson, J. (2007). Automatic methods for characterization of sexual dimorphism of adult femora: distal femur. *Computer methods in biomechanics & biomedical engineering*, vol. 10, no. 6, pp. 447–456.

Mahoney, O.M. and Kinsey, T. (2010). Overhang of the femoral component in total knee arthroplasty: risk factors and clinical consequences. *Journal of bone & joint surgery*, vol. 92, no. 5, pp. 1115–1121.

Malone, J., McGarry, K., Wermter, S. and Bowerman, C. (2006). Data mining using rule extraction from kohonen self-organising maps. *Neural computing & applications*, vol. 15, no. 1, pp. 9–17.

Mancuso, C., Ranawat, C., Esdaile, J., Johanson, N. and Charlson, M. (1996). Indications for total hip and total knee arthroplasties: results of orthopaedic surveys. *Journal of arthroplasty*, vol. 11, no. 1, pp. 34–46.

March, L.M. and Bachmeier, C.J. (1997). 10 economics of osteoarthritis: a global perspective. *Baillière's clinical rheumatology*, vol. 11, no. 4, pp. 817–834.

Markolf, K.L., Mensch, J. and Amstutz, H.C. (1976). Stiffness and laxity of the knee–the contributions of the supporting structures. A quantitative in vitro study. *Journal of bone & joint surgery*, vol. 58, no. 5, pp. 583–594.

Martelli, S. and Pinskerova, V. (2002). The shapes of the tibial and femoral articular surfaces in relation to tibiofemoral movement. *Journal of bone & joint surgery, British volume*, vol. 84, no. 4, pp. 607–613.

Martin, J. and Buckwalter, J. (2002). Aging, articular cartilage chondrocyte senescence and osteoarthritis. *Biogerontology*, vol. 3, no. 5, pp. 257–264.

Max, N. (1999). Weights for computing vertex normals from facet normals. *Journal of graphics tools*, vol. 4, no. 2, pp. 1–6.

Miranda, D., Rainbow, M., Leventhal, E., Crisco, J. and Fleming, B. (2010). Automatic determination of anatomical coordinate systems for three-dimensional bone models of the isolated human knee. *Journal of biomechanics*, vol. 43, no. 8, pp. 1623–1626.

Möller, T. and Trumbore, B. (2005). Fast, minimum storage ray/triangle intersection. In: *ACM siggraph 2005 courses*, p. 7. ACM.

Murase, K., Crowninshield, R.D., Pedersen, D.R. and Chang, T.-S. (1983). An analysis of tibial component design in total knee arthroplasty. *Journal of biomechanics*, vol. 16, no. 1, pp. 13–22.

Murphy, R., Fraser, T. and Mihalko, W. (2015). Mobile versus fixed bearing medial unicompartmental knee arthroplasty: a series of 375 patients. *Reconstructive review*, vol. 5, no. 1.

Mutsvangwa, T., Burdin, V., Schwartz, C. and Roux, C. (2015). An automated statistical shape model developmental pipeline: application to the human scapula and humerus. *Biomedical engineering, IEEE transactions on*, vol. 62, no. 4, pp. 1098–1107.

Myronenko, A. (2010). *Non-rigid image registration regularization, algorithms and applications*. Ph.D. thesis, Oregon Health and Science University.

Myronenko, A. and Song, X. (2010). Point set registration: Coherent point drift. *Pattern analysis and machine intelligence, IEEE transactions on*, vol. 32, no. 12, pp. 2262–2275.

Nagaosa, Y., Lanyon, P. and Doherty, M. (2002). Characterisation of size and direction of osteophyte in knee osteoarthritis: a radiographic study. *Annals of the rheumatic diseases*, vol. 61, no. 4, pp. 319–324.

Nakagawa, S., Kadoya, Y., Todo, S., Kobayashi, A., Sakamoto, H., Freeman, M. and Yamano, Y. (2000). Tibiofemoral movement 3: full flexion in the living knee studied by MRI. *Journal of bone & joint surgery, British volume*, vol. 82, no. 8, pp. 1199–1200.

Neogi, T., Bowes, M.A., Niu, J., Souza, K.M., Vincent, G.R., Goggins, J., Zhang, Y. and Felson, D.T. (2013). Magnetic resonance imaging–based three-dimensional bone shape of the knee predicts onset of knee osteoarthritis: data from the osteoarthritis initiative. *Arthritis & rheumatology*, vol. 65, no. 8, pp. 2048–2058.

Newman, J., Ackroyd, C. and Shah, N. (1998). Unicompartmental or total knee replacement? Five-year results of a prospective, randomised trial of 102 osteoarthritic knees with unicompartmental arthritis. *Journal of bone & joint surgery, British volume*, vol. 80, no. 5, pp. 862–865.

Nicholson, E. and Harvati, K. (2006). Quantitative analysis of human mandibular shape using three-dimensional geometric morphometrics. *American journal of physical anthropology*, vol. 131, no. 3, pp. 368–383.

Nicolella, D.P. and Bredbenner, T.L. (2012). Development of a parametric finite element model of the proximal femur using statistical shape and density modelling. *Computer methods in biomechanics & biomedical engineering*, vol. 15, no. 2, pp. 101–110.

Nuno, N., Ahmed, A. *et al.* (2001). Sagittal profile of the femoral condyles and its application to femorotibial contact analysis. *Journal of biomechanical engineering*, vol. 123, no. 1, p. 18.

Osis, S.T., Hettinga, B.A., Macdonald, S.L. and Ferber, R. (2015). A novel method to evaluate error in anatomical marker placement using a modified generalized procrustes analysis. *Computer methods in biomechanics & biomedical engineering*, vol. 18, no. 10, pp. 1108–1116.

Palastanga, N., Field, D. and Soames, R. (2006). *Anatomy and human movement: structure and function*, vol. 20056. Butterworth-Heinemann.

Paley, D. (2002). Normal lower limb alignment and joint orientation. In: *Principles of deformity correction*, pp. 1–18. Springer.

Palumbo, B.T. and Scott, R.D. (2014). Diagnosis and indications for treatment of unicompartmental arthritis. *Clinics in sports medicine*, vol. 33, no. 1, pp. 11–21.

Pandit, H., Jenkins, C., Beard, D., Price, A., Gill, H., Dodd, C. and Murray, D. (2010). Mobile bearing dislocation in lateral unicompartmental knee replacement. *The knee*, vol. 17, no. 6, pp. 392–397.

Patil, S., Colwell, C.W., Ezzet, K.A. and D'lima, D.D. (2005). Can normal knee kinematics be restored with unicompartmental knee replacement? *Journal of bone & joint surgery, American volume*, vol. 87, no. 2, pp. 332–338.

Pedoia, V., Lansdown, D.A., Zaid, M., McCulloch, C.E., Souza, R., Ma, C.B. and Li, X. (2015). Three-dimensional MRI-based statistical shape model and application to a cohort of knees with acute ACL injury. *Osteoarthritis & cartilage*, vol. 23, no. 10, pp. 1695–1703.

Pedoia, V., Majumdar, S. and Link, T.M. (2016). Segmentation of joint and musculoskeletal tissue in the study of arthritis. *Magnetic resonance materials in physics, biology & medicine*, vol. 29, no. 2, pp. 207–221.

Peersman, G., Stuyts, B., Vandenlangenbergh, T., Cartier, P. and Fennema, P. (2015). Fixed-versus mobile-bearing UKA: a systematic review and meta-analysis. *Knee surgery, sports traumatology, arthroscopy*, vol. 23, no. 11, pp. 3296–3305.

Pejhan, S., Bohm, E., Brandt, J.-M. and Wyss, U. (2016). Design and virtual evaluation of a customized surface-guided knee implant. *Proceedings of the Institution of Mechanical Engineers, part H: Journal of engineering in medicine*, vol. 230, no. 10, pp. 949–961.

Pena, E., Calvo, B., Martinez, M. and Doblare, M. (2006). A three-dimensional finite element analysis of the combined behavior of ligaments and menisci in the healthy human knee joint. *Journal of biomechanics*, vol. 39, no. 9, pp. 1686–1701.

Peterfy, C., Schneider, E. and Nevitt, M. (2008). The osteoarthritis initiative: report on the design rationale for the magnetic resonance imaging protocol for the knee. *Osteoarthritis & cartilage*, vol. 16, no. 12, pp. 1433–1441.

Piegl, L. and Tiller, W. (1997). *The NURBS book*. Springer Verlag.

Pinskerova, V., Johal, P., Nakagawa, S., Sosna, A., Williams, A., Gedroyc, W. and Freeman, M. (2004). Does the femur roll-back with flexion? *Bone & joint journal*, vol. 86, no. 6, pp. 925–931.

Price, A., Webb, J., Topf, H., Dodd, C., Goodfellow, J., Murray, D. *et al.* (2001). Rapid recovery after oxford unicompartmental arthroplasty through a short incision. *Journal of arthroplasty*, vol. 16, no. 8, pp. 970–976.

Puthumanapully, P.K., Harris, S.J., Leong, A., Cobb, J.P., Amis, A.A. and Jeffers, J. (2014). A morphometric study of normal and varus knees. *Knee surgery, sports traumatology, arthroscopy*, vol. 22, no. 12, pp. 2891–2899.

Rasoulian, A., Rohling, R. and Abolmaesumi, P. (2012). Group-wise registration of point sets for statistical shape models. *Medical imaging, IEEE transactions on*, vol. 31, no. 11, pp. 2025–2034.

Rehder, U. (1983). Morphometrical studies on the symmetry of the human knee joint: femoral condyles. *Journal of biomechanics*, vol. 16, no. 5, pp. 351–361.

Riddle, D., Jiranek, W. and McGlynn, F. (2008). Yearly incidence of unicompartmental knee arthroplasty in the United States. *Journal of arthroplasty*, vol. 23, no. 3, pp. 408–412.

Rohlf, F.J. and Slice, D. (1990). Extensions of the Procrustes method for the optimal superimposition of landmarks. *Systematic biology*, vol. 39, no. 1, pp. 40–59.

Rossignac, J. (2001). 3D compression made simple: edgebreaker on a corner-table. In: *Shape modeling and applications, SMI 2001 international conference on.*, pp. 278–283. IEEE.

Sabatini, L., Giachino, M., Risitano, S. and Atzori, F. (2016). Bicompartmental knee arthroplasty. *Annals of translational medicine*, vol. 4, no. 1.

Saldanha, K., Keys, G., Svard, U., White, S. and Rao, C. (2007). Revision of Oxford medial unicompartmental knee arthroplasty to total knee arthroplasty-results of a multicentre study. *The knee*, vol. 14, no. 4, p. 275.

Santoso, M.B. and Wu, L. (2017). Unicompartmental knee arthroplasty, is it superior to high tibial osteotomy in treating unicompartmental osteoarthritis? a meta-analysis and systemic review. *Journal of orthopaedic surgery & research*, vol. 12, no. 1, p. 50.

Sarkalkan, N., Weinans, H. and Zadpoor, A.A. (2014). Statistical shape and appearance models of bones. *Bone*, vol. 60, pp. 129–140.

Sathasivam, S., Walker, P., Pinder, I., Cannon, S. and Briggs, T. (1999). Custom constrained condylar total knees using CAD-CAM. *The knee*, vol. 6, no. 1, pp. 49–53.

Scheffer, C., van den Heever, D., Erasmus, P. and Dillon, E. (2010 December 10). A method of designing a knee prosthesis. WO Patent 2,010,140,036.

Scherrer, P. and Hillberry, B. (1979). Piecewise mathematical representation of articular surfaces. *Journal of biomechanics*, vol. 12, no. 4, pp. 301–311.

Scholes, C., Sahni, V., Lustig, S., Parker, D.A. and Coolican, M.R. (2014). Patient-specific instrumentation for total knee arthroplasty does not match the pre-operative plan as assessed by intra-operative computer-assisted navigation. *Knee surgery, sports traumatology, arthroscopy*, vol. 22, no. 3, pp. 660–665.

Schönemann, P.H. (1966). A generalized solution of the orthogonal procrustes problem. *Psychometrika*, vol. 31, no. 1, pp. 1–10.

Schroeder, W.J., Zarge, J.A. and Lorensen, W.E. (1992). Decimation of triangle meshes. In: *ACM siggraph computer graphics*, vol. 26, pp. 65–70. ACM.

Schumann, S., Tannast, M., Nolte, L.-P. and Zheng, G. (2010). Validation of statistical shape model based reconstruction of the proximal femur - a morphology study. *Medical engineering & physics*, vol. 32, no. 6, pp. 638–644.

Scuderi, G.R. and Tria, A.J. (2009). *Minimally invasive surgery in orthopedics*. Springer Science & Business Media.

Servien, E., Saffarini, M., Lustig, S., Chomel, S. and Neyret, P. (2008). Lateral versus medial tibial plateau: morphometric analysis and adaptability with current tibial component design. *Knee surgery, sports traumatology, arthroscopy*, vol. 16, no. 12, pp. 1141–1145.

Shakespeare, D. and Jeffcote, B. (2003). Unicondylar arthroplasty of the knee - cheap at half the price? *The knee*, vol. 10, no. 4, pp. 357–361.

Slamin, J. and Parsley, B. (2012). Evolution of customization design for total knee arthroplasty. *Current reviews in muscoskeletal medicine*, pp. 1–6.

Smith, J. (1956). Observations on the postural mechanism of the human knee joint. *Journal of anatomy*, vol. 90, no. 2, p. 236.

Smith, P.N., Refshauge, K.M. and Scarvell, J.M. (2003). Development of the concepts of knee kinematics. *Archives of physical medicine & rehabilitation*, vol. 84, no. 12, pp. 1895–1902.

Steines, D. and Zhuravlev, A. (2012 July 31). Automated systems for manufacturing patient-specific orthopedic implants and instrumentation. US Patent 8,234,097.

Steklov, N., Slamin, J., Srivastav, S. and D'Lima, D. (2010). Unicompartmental knee resurfacing: enlarged tibio-femoral contact area and reduced contact stress using novel patient-derived geometries. *The open biomedical engineering journal*, vol. 4, p. 85.

Stern, S., Becker, M., Insall, J. *et al.* (1993). Unicondylar knee arthroplasty. An evaluation of selection criteria. *Clinical orthopaedics & related research*, , no. 286, p. 143.

Taubin, G. (1995). A signal processing approach to fair surface design. In: *Proceedings of the 22nd annual conference on computer graphics and interactive techniques*, pp. 351–358. ACM.

The Osteoarthritis Initiative (2006*a*). *MRI procedure manual for examinations of the knee and thigh. The Osteoarthritis Initiative: a knee health study.* [Online] (Reviewed October 2006) Available at: `http://www.oai.ucsf.edu/` [Accessed 11 January 2017].

The Osteoarthritis Initiative (2006*b*). *Protocol for the cohort study.* [Online] (Reviewed June 2006) Available at: `http://www.oai.ucsf.edu/` [Accessed 11 January 2017].

Tickle, A.B., Andrews, R., Golea, M. and Diederich, J. (1998). The truth will come to light: directions and challenges in extracting the knowledge embedded within trained artificial neural networks. *Neural networks, IEEE transactions on*, vol. 9, no. 6, pp. 1057–1068.

Vaidya, S.V., Ranawat, C.S., Aroojis, A. and Laud, N. (2000). Anthropometric measurements to design total knee prostheses for the indian population. *Journal of arthroplasty*, vol. 15, no. 1, pp. 79–85.

Van den Broeck, J., Vereecke, E., Wirix-Speetjens, R. and Vander Sloten, J. (2014). Segmentation accuracy of long bones. *Medical engineering & physics*, vol. 36, no. 7, pp. 949–953.

Van den Heever, D. (2011). *Development of patient-specific knee joint prostheses for unicompartmental knee replacement (UKR).* Ph.D. thesis, Stellenbosch University.

Van den Heever, D., Scheffer, C., Erasmus, P. and Dillon, E. (2011*a*). Method for selection of femoral component in total knee arthroplasty (TKA). *Australasian physical & engineering science in medicine*, vol. 34, no. 1, pp. 23–30.

Van den Heever, D., Scheffer, C., Erasmus, P. and Dillon, E. (2012*a*). Classification of gender and race in the distal femur using self organising maps. *The knee*, vol. 19, no. 4, pp. 488–492.

Van den Heever, D., Scheffer, C., Erasmus, P. and Dillon, E. (2012*b*). Development and testing of patient-specific knee replacements. In: *Engineering in medicine and biology society (EMBC), 2012 annual international conference of the IEEE*, pp. 4875–4878. IEEE.

Van den Heever, D.J., Scheffer, C., Erasmus, P. and Dillon, E. (2011*b*). Mathematical reconstruction of human femoral condyles. *Journal of biomechanical engineering*, vol. 133, no. 6, p. 064504.

Van der Merwe, J., Scheffer, C., Van den Heever, D. and Erasmus, P. (2013). Reverse engineering the human knee. In: *COMA'13*.

Van Haver, A., De Roo, K., De Beule, M., Van Cauter, S., Audenaert, E., Claessens, T. and Verdonk, P. (2014). Semi-automated landmark-based 3D analysis reveals new morphometric characteristics in the trochlear dysplastic femur. *Knee surgery, sports traumatology, arthroscopy*, vol. 22, no. 11, pp. 2698–2708.

Van Ruijven, L., Beek, M. and Van Eijden, T. (1999). Fitting parametrized polynomials with scattered surface data. *Journal of biomechanics*, vol. 32, no. 7, pp. 715–720.

Van Schalkwyk, E. (2010). *Determining femoral component goodness-of-fit using computer segmentation and numerical simulation*. Ph.D. thesis, Stellenbosch: University of Stellenbosch.

Varadarajan, K.M., Harry, R.E., Johnson, T. and Li, G. (2009). Can in vitro systems capture the characteristic differences between the flexion–extension kinematics of the healthy and TKA knee? *Medical engineering & physics*, vol. 31, no. 8, pp. 899–906.

Victor, J. (2009). Rotational alignment of the distal femur: a literature review. *Orthopaedics & traumatology: surgery & research*, vol. 95, no. 5, pp. 365–372.

Victor, J., Labey, L., Wong, P., Innocenti, B. and Bellemans, J. (2010). The influence of muscle load on tibiofemoral knee kinematics. *Journal of orthopaedic research*, vol. 28, no. 4, pp. 419–428.

Victor, J., Van Doninck, D., Labey, L., Innocenti, B., Parizel, P. and Bellemans, J. (2009*a*). How precise can bony landmarks be determined on a ct scan of the knee? *The knee*, vol. 16, no. 5, pp. 358–365.

Victor, J., Van Doninck, D., Labey, L., Van Glabbeek, F., Parizel, P. and Bellemans, J. (2009*b*). A common reference frame for describing rotation of the distal femur: A CT-based kinematic study using cadavers. *Journal of bone & joint surgery, British volume*, vol. 91, no. 5, pp. 683–690.

Vieira, A.W., Velho, L., Lopes, H., Tavares, G. and Lewiner, T. (2003). Fast stellar mesh simplification. In: *Computer graphics and image processing, 2003. SIBGRAPI 2003. XVI Brazilian symposium on*, pp. 27–34. IEEE.

Voss, B., El-Othmani, M.M., Schnur, A.K., Botchway, A., Mihalko, W.M. and Saleh, K.J. (2016). A meta-analysis comparing all-polyethylene tibial component to metal-backed tibial component in total knee arthroplasty: assessing survivorship and functional outcomes. *Journal of arthroplasty*, vol. 31, no. 11, pp. 2628–2636.

Walker, P. (1988). Bearing surface design in total knee replacement. *Engineering in medicine*, vol. 17, no. 4, pp. 149–156.

Walker, P., Sussman-Fort, J., Yildirim, G. and Boyer, J. (2009). Design features of total knees for achieving normal knee motion characteristics. *Journal of arthroplasty*, vol. 24, no. 3, pp. 475–483.

Walker, P.S. (2014). Application of a novel design method for knee replacements to achieve normal mechanics. *The knee*, vol. 21, no. 2, pp. 353–358.

Weale, A., Halabi, O., Jones, P. and White, S. (2001). Perceptions of outcomes after unicompartmental and total knee replacements. *Clinical orthopaedics & related research*, vol. 382, p. 143.

Williams, T.G., Holmes, A.P., Waterton, J.C., Maciewicz, R.A., Nash, A.F. and Taylor, C.J. (2006). Regional quantitative analysis of knee cartilage in a population study using MRI and model based correspondences. In: *Biomedical imaging: nano to macro, 2006. 3rd IEEE international symposium on*, pp. 311–314. IEEE.

Wismans, J., Veldpaus, F., Janssen, J., Huson, A. and Struben, P. (1980). A three-dimensional mathematical model of the knee-joint. *Journal of biomechanics*, vol. 13, no. 8, pp. 677–685.

Yamaguchi, S., Gamada, K., Sasho, T., Kato, H., Sonoda, M. and Banks, S.A. (2009). In vivo kinematics of anterior cruciate ligament deficient knees during pivot and squat activities. *Clinical biomechanics*, vol. 24, no. 1, pp. 71–76.

Yue, B., Varadarajan, K.M., Moynihan, A.L., Liu, F., Rubash, H.E. and Li, G. (2011). Kinematics of medial osteoarthritic knees before and after posterior cruciate ligament retaining total knee arthroplasty. *Journal of orthopaedic research*, vol. 29, no. 1, pp. 40–46.

Zachow, S., Lamecker, H., Elsholtz, B. and Stiller, M. (2005). Reconstruction of mandibular dysplasia using a statistical 3D shape model. In: *International congress series*, vol. 1281, pp. 1238–1243. Elsevier.

Zhang, J., Malcolm, D., Hislop-Jambrich, J., Thomas, C.D.L. and Nielsen, P.M. (2014). An anatomical region-based statistical shape model of the human femur. *Computer methods in biomechanics & biomedical engineering: imaging & visualization*, vol. 2, no. 3, pp. 176–185.

ZhenWu Cao, M., XiuJun Mai, M., Jun Wang, M., EnHui Feng, M. and Huang, Y. (2017). Unicompartmental knee arthroplasty vs high tibial osteotomy for knee osteoarthritis: A systematic review and meta-analysis. *Journal of arthroplasty*, vol. 30, p. 1e8.

Zimmer, Inc (2014). *Knee Solutions*. [Online] Available at: `http://www.zimmer.com` [Accessed 23 November 2017].

Zoghi, M., Hefzy, M., Fu, K. and Jackson, W. (1992). A three-dimensional morphometrical study of the distal human femur. *Proceedings of the Institution of Mechanical Engineers, part H: journal of engineering in medicine*, vol. 206, no. 3, pp. 147–157.

Appendices

A. Statistical shape analysis

Statistical Shape Analysis (SSA) enables the investigation of geometric properties of a set of complex yet similar shapes via statistical methods, and have seen considerable use in the orthopaedic field (Heimann and Meinzer, 2009; Sarkalkan *et al.*, 2014). The method we discuss here starts with the establishment of corresponding landmarks, then removal of rotation, scale and translational differences between the obtained landmarks, and finally dimensionality reduction.

A.1 Pseudo-landmark correspondence

While anatomical landmarks are homologous by definition, establishing correspondence is rather more involved for pseudo-landmarks. We found the non-rigid variant of the Coherent Point Drift (CPD) algorithm developed by Myronenko and Song (2010) to be effective in matching such points between a representative base and all other sets in the data. The CPD algorithm performs registration of a reference point set $\mathbf{v}_r$ to some target $\mathbf{v}_t$ in d dimensional Cartesian space via probability density estimation. Each point set is first centred about their respective barycenters and scaled to unity, with the reference points subsequently taken to represent Gaussian Mixture Model (GMM) centroids. The likelihood of correspondence is estimated via iterative Expectation Maximisation, with the GMM centroids being constrained to move coherently by regularising the norm of the displacement function ψ. The transformed reference $\tilde{\mathbf{v}}_r$ for a particular instance is defined as:

$$\tilde{\mathbf{v}}_r = \mathbf{v}_r + \psi(\mathbf{v}_r) \tag{A.1}$$

with ψ and σ^2 found by iteratively minimising the energy function E:

$$E(\psi, \sigma^2) = -\sum_{i=1}^{n_t} log(p(\mathbf{v}_t[i])) + \frac{f_d}{2}\phi(\psi) \tag{A.2}$$

given that we have n_t target points and σ denotes the Gaussian components' width. The contribution of the regularisation term that smooths the displacement function is controlled by f_d, and is given in terms of the frequency domain variable s by:

$$\phi(\psi) = \int_{\mathbb{R}^d} \frac{|\hat{\psi}(s)|^2}{\hat{\mathbf{G}}(s)} ds \tag{A.3}$$

with $\hat{\psi}$ and $\hat{\mathbf{G}}$ being the Fourier transforms of the displacement function and a Gaussian kernel with a user supplied standard deviation f_k, respectively. The kernel's elements are given by:

$$\mathbf{G}[\mathbf{v}_r[k], \mathbf{v}_r[l]] = e^{-\frac{||\mathbf{v}_r[k]-\mathbf{v}_r[l]||^2}{2{f_k}^2}} \text{ where } k, l \in [1, 2, \ldots, n_r] \tag{A.4}$$

The GMM probability density function, on the other hand, is:

$$p(\mathbf{v}_t[i]) = \sum_{j=1}^{n_r} P(j) p(\mathbf{v}_t[i]|j) + \frac{1}{n_t} \tag{A.5}$$

defined for n_r reference points plus an additional uniform distribution term to account for noise and outliers. The Gaussian distribution centred about the reference is defined as:

$$p(\mathbf{v}_t[i]|j) = \frac{1}{(2\pi\sigma^2)^{d/2}} e^{-\frac{||\mathbf{v}_t[i]-\mathbf{v}_r[j]||^2}{2\sigma^2}} \tag{A.6}$$

If we weight the uniform distribution's contribution with $f_n \in [0, 1]$, assume equal membership probability $P(j) = \frac{1}{n_r}$ and isotropic covariances σ^2 for all GMM components, substituting we can re-write Equation A.5 as:

$$p(\mathbf{v}_t[i]) = \frac{1 - f_n}{n_r (2\pi\sigma^2)^{d/2}} \sum_{j=1}^{n_r} e^{-\frac{||\mathbf{v}_t[i]-\mathbf{v}_r[j]||^2}{2\sigma^2}} + \frac{f_n}{n_t} \tag{A.7}$$

Finally, point correspondence is defined as the posterior probability of the GMM centroids, given the current estimate of the transformed reference:

$$P(j|\mathbf{v}_t[i]) = \frac{P(j) p(\mathbf{v}_t[i]|j)}{p(\mathbf{v}_t[i])} = \frac{e^{-\frac{||\mathbf{v}_t[i]-\tilde{\mathbf{v}}_r[j]||^2}{2\sigma^2}}}{\sum_{j=1}^{n_r} e^{-\frac{||\mathbf{v}_t[i]-\tilde{\mathbf{v}}_r[j]||^2}{2\sigma^2}} + (2\pi\sigma^2)^{d/2} \frac{f_n}{1-f_n} \frac{n_r}{n_t}} \tag{A.8}$$

The output is affected by the values of the free parameters, f_n, f_d and f_k. The trade-off between motion smoothing and data-fitting is adjusted via f_d, with smaller values decreasing the smoothing effect and so favouring data-fitting. Parameter f_k controls the width of the smoothing kernel, the motion of discrete vertices being averaged over areas proportional to its value. And f_n, finally, represents the assumption of expected noise. Large values assume a more uniform distribution, decreasing the dependence of correspondence probability on Euclidean distance to mitigate the effect of outliers. The convergence condition as per Rasoulian *et al.* (2012) is the value of σ being less than an additional user specified threshold. They suggest using a value derived from

the data, such as an average distance between points. It may be noted that the CPD algorithm does not result in a direct matching of points after convergence, but rather a best estimate, one-to-many probabilistic correspondence. We therefore employ the final, $n_r \times n_t$ posterior probability matrix as a linear mapping such that:

$$\mathbf{v}_c = P(j|\mathbf{v}_t[i])\mathbf{v}_t \tag{A.9}$$

Here $\mathbf{v}_c$ is the estimated n_r element correspondence of the transformed reference to the current target point set. Also, the initial pre-alignment may be reversed for $\tilde{\mathbf{v}}_r$ and $\mathbf{v}_c$ after termination in like manner to Equation A.16. We refer the interested reader to Myronenko (2010) for more detail regarding the CPD algorithm illustrated in Figure A.1, the particular EM implementation as well as improvements in speed and reduced computational complexity.

Function $[\tilde{\mathbf{v}}_r, \mathbf{v}_c]$ = `cpd(`$\mathbf{v}_t$, $\mathbf{v}_r$`)`

Input:

$\mathbf{v}_t$	$n_t \times d$	target point array
$\mathbf{v}_r$	$n_r \times d$	reference point array

Output:

$\tilde{\mathbf{v}}_r$	$n_r \times d$	transformed reference point array
$\mathbf{v}_c$	$n_r \times d$	corresponding point array

`/* initialisation */`

translate $\mathbf{v}_t$ and $\mathbf{v}_r$ to centroid;

scale $\mathbf{v}_t$ and $\mathbf{v}_r$ to unity;

$f_k > 0$, $f_d > 0$, $f_n \in [0, 1]$;

$\psi := \psi_0$;

$\sigma := \sigma_0$;

construct $\mathbf{G}$;

$\tilde{\mathbf{v}}_r := \mathbf{v}_r$;

`/* optimisation */`

while σ *not converged* **do**

- compute P; `/* E-step */`
- $\psi, \sigma^2 \leftarrow$ `solve(`$\mathbf{v}_t$, $\tilde{\mathbf{v}}_r$, P`)`; `/* M-step */`
- update $\tilde{\mathbf{v}}_r$; `/* transformation */`

end

calculate $\mathbf{v}_c$; `/* correspondence */`

reverse $\tilde{\mathbf{v}}_r$ and $\mathbf{v}_c$ pre-alignment;

end

Figure A.1: Coherent point drift (Algorithm: adapted from Myronenko and Song (2010))

A.2 Procrustes Analysis

A.2.1 Least squares ordinary Procrustes

Procrustes superimposition is the process whereby a d dimensional model point set $\mathbf{v}_c$ is scaled, rotated and translated to a target $\mathbf{v}_t$ with an equal number of corresponding vertices n_r. First, both $\mathbf{v}_c$ and $\mathbf{v}_t$ must be centred and scaled to unity, which is achieved by subtracting their respective arithmetic means $\bar{\mathbf{v}}_{c,t}$, and dividing the results with their root mean squared distances from the origin $f_{c,t}$ as shown here for the three dimensional case:

$$\begin{aligned} \bar{\mathbf{v}}_{c,t} &= \frac{1}{n_r}\sum_{j=1}^{n_r}\left[x_j, y_j, z_j\right], \\ f_{c,t} &= \sqrt{\frac{\sum_{j=1}^{n_r}(x_j^2+y_j^2+z_j^2)}{n_r}} \quad \text{where} \quad \left[x_j, y_j, z_j\right] \in \mathbf{v}_{c,t}[j] \end{aligned} \tag{A.10}$$

We are now left with finding an orthogonal rotation matrix $\mathbf{R}$ for the model point set such that:

$$\mathbf{v}_t = \mathbf{v}_c\mathbf{R} + \mathbf{N}_R \tag{A.11}$$

where $\mathbf{N}_R$ is the residual or noise matrix. Known as the orthogonal Procrustes problem, Schönemann (1966) presented the solution to the following least squares optimisation, minimising the residual:

$$\begin{aligned} \mathbf{R} &= \arg\min_{\mathbf{R}}\left(\sum_{j=1}^{n_r}||\mathbf{v}_c\mathbf{R} - \mathbf{v}_t||\right) \\ &= \mathbf{V}\mathbf{U}^T \end{aligned} \tag{A.12}$$

Here $\mathbf{U}$ and $\mathbf{V}$ are the unitary matrices of the Singular Value Decomposition (SVD):

$$\mathbf{v}_c^T\mathbf{v}_t = \mathbf{U}\mathbf{\Sigma}\mathbf{V} \tag{A.13}$$

Eggert *et al.* (1997) constrains the problem further by modifying the solution in order to prevent reflection:

$$\mathbf{R} = \mathbf{U}\begin{bmatrix} 1 & & \\ & 1 & \\ & & det(\mathbf{U}\mathbf{V}^T) \end{bmatrix}\mathbf{V}^T \tag{A.14}$$

From Equation A.11, we can transform the particular model point set to obtain its best fit of the scaled and centred target:

$$\mathbf{v}_a = \mathbf{v}_c\mathbf{R} \tag{A.15}$$

or, as is important in our case, the original target:

$$\mathbf{v}_a = f_s\mathbf{v}_c\mathbf{R} + \mathbf{t} \quad \text{where} \quad f_s = \frac{f_t}{f_c} \quad \text{and} \quad \mathbf{t} = \bar{\mathbf{v}}_t - f\bar{\mathbf{v}}_c\mathbf{R} \tag{A.16}$$

Here the scale factor f_s is composed of the root mean square distances from the origin of the centred model and target vertices, respectively. The target is aligned to the rotated and scaled centroid of the model points via $\mathbf{t}$. An algorithm for ordinary Procrustes alignment is presented in Figure A.2.

Function $\mathbf{v}_a$ = `oprocrustes(`$\mathbf{v}_t$, $\mathbf{v}_c$`)`

Input:

$\mathbf{v}_t$	$n_r \times d$	target point array
$\mathbf{v}_c$	$n_r \times d$	model point array

Output:

$\mathbf{v}_a$	$n_r \times d$	aligned point array

`/* initialisation */`
translate $\mathbf{v}_t$ and $\mathbf{v}_c$ to centroid;
scale $\mathbf{v}_t$ and $\mathbf{v}_c$ to unity;
`/* optimisation */`
$\mathbf{R} \leftarrow$ `solve(`$\mathbf{v}_c$, $\mathbf{v}_t$`);` `/* SVD */`
constrain reflection;
`/* alignment */`
calculate $\mathbf{v}_a$;

end

Figure A.2: Ordinary Procrustes alignment (Algorithm: adapted from Schönemann (1966))

A.2.2 Generalised Procrustes

Generalised Procrustes Analysis (GPA) iteratively solves the ordinary Procrustes problem, registering a set of n_s model shapes $\mathbf{v}_c$ with corresponding landmarks to the procrustes mean shape $\mathbf{v}_m$. After we've obtained n_s point sets $\mathbf{v}_a$ aligned with some initially selected representative base, each is concatenated along its d dimensions to form a column vector as shown here for the three dimensional case:

$$\mathbf{x} = \left[x_1, y_1, z_1, \ldots, x_{n_r}, y_{n_r}, z_{n_r}\right]^T \quad \text{where} \quad \left[x_j, y_j, z_j\right] \in \mathbf{v}_a[j] \tag{A.17}$$

The Procrustes mean may then be computed as:

$$\bar{\mathbf{x}} = \frac{1}{n_s} \sum_{l=1}^{n_s} \mathbf{x}_l \tag{A.18}$$

The result is shaped back to an $n_r \times d$ point set, and the process is repeated iteratively until the mean shape converges to within a specified tolerance. The algorithm for GPA is illustrated by Figure A.3.

Function $[\bar{\mathbf{x}}, \mathbf{v}_a] = \texttt{gpa}(\mathbf{v}_c)$
- **Input:**
- $\mathbf{v}_c$ $n_r \times d(\times n_s)$ set of n_s training shapes
- **Output:**
- $\bar{\mathbf{x}}$ $n_r d \times 1$ Procrustes mean
- $\mathbf{v}_a$ $n_r \times d(\times n_s)$ set of n_s aligned shapes
- `/* GPA */`
- $\mathbf{v}_m := \mathbf{v}_r$; `/* initialise mean shape */`
- **while** *mean shape* $\mathbf{v}_m$ *not converged* **do**
  - translate $\mathbf{v}_m$ to centroid and scale to unity;
  - **for** *each model shape* $\mathbf{v}_c$ **do**
    - $\mathbf{v}_a \leftarrow$ `oprocrustes(`$\mathbf{v}_m$, $\mathbf{v}_c$`);` `/* align to mean */`
    - $\mathbf{x} \leftarrow$ `reshape(`$\mathbf{v}_a$`);` `/* reshape` d `dimensions to 1 */`
  - **end**
  - compute $\bar{\mathbf{x}}$; `/* Procrustes mean */`
  - $\mathbf{v}_m \leftarrow$ `reshape(`$\bar{\mathbf{x}}$`);` `/* reshape 1 dimension to` d `*/`
- **end**

end

Figure A.3: Generalised procrustes analysis

A.3 Principle component analysis

Principle component analysis (PCA) is a statistical technique that attempts to convert a datasets' n_r correlated landmarks into at most $n_s - 1$ non-degenerate, linearly uncorrelated orthogonal principle components of variation. From this we construct a more densely represented deformable model with which to approximate new shape instances. Given a set of n_s corresponding point sets $\mathbf{v}_a$ aligned with the same representative base and concatenated to their one dimensional forms together with the Procrustes mean (see Appendix A.2, Equations A.17 and A.18) we compute the centred training matrix:

$$\Delta\mathbf{X} = \left[\mathbf{x}_1 - \bar{\mathbf{x}}, \ldots, \mathbf{x}_{n_s} - \bar{\mathbf{x}}\right] \tag{A.19}$$

The covariance of the data is then:

$$\mathbf{C} = \frac{1}{n_s}\Delta\mathbf{X}\Delta\mathbf{X}^T \tag{A.20}$$

with its eigenvalue decomposition:

$$\mathbf{C} = \mathbf{U}\mathbf{\Lambda}\mathbf{U}^T \tag{A.21}$$

The $min(n_s - 1, n_r d)$ non-degenerate principle modes of variation are represented in magnitude by $\mathbf{\Lambda}$, which is a diagonal matrix of the eigenvalues, and in direction by $\mathbf{U}$, which contains the eigenvectors along its columns. The individual eigenvalues λ_e and the corresponding eigenvectors $\mathbf{u}_e$ are sorted in decreasing order of magnitude. However, due to higher numerical stability the preferred method for computing the modes of variation is an SVD of the centred training data (Heimann and Meinzer, 2009):

$$\Delta\mathbf{X} = \mathbf{U}\mathbf{\Sigma}\mathbf{V}^T \tag{A.22}$$

Here $\mathbf{\Sigma}$ is a diagonal matrix that contains the singular values of $\Delta\mathbf{X}$, and relates to $\mathbf{\Lambda}$ as:

$$\mathbf{\Lambda} = \frac{1}{n_s}\mathbf{\Sigma}^T\mathbf{\Sigma} \tag{A.23}$$

A shape instance may then be approximated by a linear combination of the n_k most important modes of variation:

$$\tilde{\mathbf{x}} = \bar{\mathbf{x}} + \mathbf{U}_k\mathbf{b} \tag{A.24}$$

where $\mathbf{U}_k$ is a $n_r d \times n_k$ matrix containing the n_k retained eigenvectors and $\mathbf{b}$ is a n_k dimensional vector of parameters that describes the model's deformation along the respective principle directions. For a particular entry $\mathbf{x}_l$ in the training set its parameter vector $\mathbf{b}_l$ can be determined from:

$$\mathbf{b}_l = \mathbf{U}_k^T(\mathbf{x}_l - \bar{\mathbf{x}}) \tag{A.25}$$

The number of retained eigenvectors are often chosen so that their cumulative variance $\sum_{e=1}^{n_k}\lambda_e$ is between 90% to 98% of the total (Heimann and Meinzer, 2009). In this way, $n_k \leq n_s - 1$, which potentially increases model compactness and reduces the assumed noise associated with modes that have small eigenvalues (Cootes *et al.*, 2004). Refer to Figure A.4 for a pseudo-code representation of PCA.

Function $[\mathbf{\Lambda}, \mathbf{U}] = \texttt{pca}(\bar{\mathbf{x}}, \mathbf{x})$

Input:

$\bar{\mathbf{x}}$	$n_r d \times 1$	Procrustes mean
$\mathbf{x}$	$n_r d \times 1 (\times n_s)$	set of n_s concatenated shapes

Output:

$\mathbf{\Lambda}$	$n_k \times n_k$	eigenvalue matrix
$\mathbf{U}$	$n_r d \times n_k$	eigenvector matrix

`/* PCA */`

compute $\Delta\mathbf{X}$;

compute $\mathbf{\Lambda}$ and $\mathbf{U}$; `/* SVD */`

retain n_k significant modes of variation;

end

Figure A.4: Principle component analysis

B. Surface mesh operations

This Chapter discusses a number of mesh operations that we implemented throughout the course of this project. Note that, while each algorithm is useful in its own right, the work presented here is generally intended to build up to direct mesh re-sampling, discussed in Section B.11.

B.1 Corner-table structure

In many of our mesh handling algorithms we made use of the corner-table data structure proposed by Rossignac (2001) in order to simplify access to and navigation within a uniformly oriented, closed triangulated mesh. For our purposes, assume that such a mesh describes a three-dimensional surface represented by a $n_v \times d$ array of vertices $\mathbf{v}$ and a $n_f \times d$ face connectivity array $\mathbf{f}$. The corner-table structure is represented by the $n_f d \times 1$ tables $\mathbf{w}$ and $\mathbf{o}$ which contain all triangle corners' geometric vertex indices and opposing corner indices, respectively. Following the description from Vieira *et al.* (2003), each triangle has three consecutive corners based on its orientation. So the first triangle may be represented by corners 0, 1 and 2, the second by corners 3, 4 and 5, and so forth. Given a corner c, we may then determine its associated triangle index $c.t$ as follows:

$$c.t = \text{floor}\left(\frac{c}{3}\right) \tag{B.1}$$

Here $\mathbf{w}[c]$ returns the index of the geometric vertex associated with corner c. Furthermore, given that the original mesh is uniformly clock-wise oriented, we can compute the next corner $c.n$ and previous corner $c.p$ of any triangle by:

$$c.n = 3c.t + (c+1)(\text{mod}3) \quad \text{and} \quad c.p = 3c.t + (c+2)(\text{mod}3) \tag{B.2}$$

The table operation $\mathbf{o}[c]$ returns $c.o$, the index into $\mathbf{w}$ of the corner opposite c, which is has the properties $\mathbf{w}[c.n] = \mathbf{w}[c.o.p]$ and $\mathbf{w}[c.p] = \mathbf{w}[c.o.n]$. The notation we employed here proceeds from left to right, so that for example $c.o.p$ refers to the previous corner of that opposite c (Rossignac, 2001). Refer to Figure B.1 for a representation of the corner-table structure and Figure B.2 for the algorithm we used to construct $\mathbf{w}$ and $\mathbf{o}$.

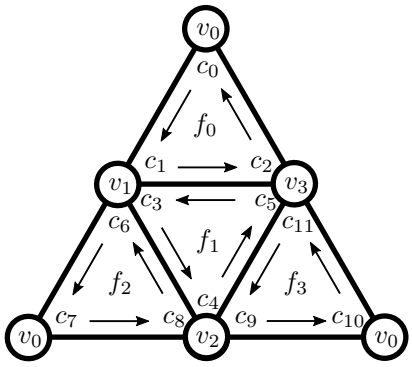

Corner	w	o	Face
0	0	4	0
1	1	9	0
2	3	8	0
3	1	10	1
4	2	0	1
5	3	7	1
6	1	11	2
7	0	5	2
8	2	2	2
9	2	1	3
10	0	3	3
11	3	6	3

Figure B.1: Corner table structure for a tetrahedron (Adapted from: Vieira *et al.* (2003))

Function $[\mathbf{w}, \mathbf{o}] =$ `cornertable(v, f)`

Input:

v	$n_v \times d$	vertex array
f	$n_f \times d$	face array

Output:

w	$n_f d \times 1$	vertex indices
o	$n_f d \times 1$	opposing corner indices

```
/* construct w                                              */
w ← reshape(f);            /* reshape d dimensions to 1 */
/* construct o                                              */
o := [ ];              /* initialise to full size empty array */
flag :=ones(n_f d, 1);              /* flag array of n_f d ones */
```

for *each successive corner* c **do**

  if $\mathbf{flag}[c]$ **then**

    $\mathbf{o}[c] \leftarrow$ `find`$(c_a : \mathbf{w}[c_a.n] = \mathbf{w}[c.p], \mathbf{w}[c_a.p] = \mathbf{w}[c.n], \mathbf{flag}[c_a])$;

    $\mathbf{o}[c_a] \leftarrow c$;

    $\mathbf{flag}[c], \mathbf{flag}[c_a] \leftarrow 0$;

  end

end

end

Figure B.2: Corner table construction

B.2 Basic corner-table mesh operations

Here we briefly present some useful mesh functions based on the corner-table structure. While we employ them throughout the sections that follow, we do not necessarily specify the exact details with regards to their use in favour of brevity. One may, after all, in many cases achieve the same or similar

ends with different means, and we trust that the following sections, without referring hereafter directly to the corner-table structure, will be clear enough in any case.

B.2.1 One-ring neighbours

The `ring` algorithm shown in Figure B.3 relies on the uniform counter-clockwise ordering (outward facing normals) of mesh vertices to return the 1-ring neighbours of a vertex indicated by corner c_0. Multiple calls to said algorithm also allow us to find the set of n-ring neighbours.

Function $[\mathbf{c}_n, \mathbf{w}_n] =$ `ring`$(\mathbf{w}, \mathbf{o}, c_0)$
  Input:
  $\mathbf{w}$ $n_f d \times 1$ vertex indices
  $\mathbf{o}$ $n_f d \times 1$ opposing corner indices
  c_0 1×1 starting corner
  Output:
  $\mathbf{c}_n$ $? \times 1$ 1-ring corners
  $\mathbf{w}_n$ $? \times 1$ 1-ring vertex indices
  `/* initialise */`
  $c_a \leftarrow c_0.n$; `/* first neighbour */`
  $\mathbf{c}_n := [c_a]$;
  $\mathbf{w}_n := [\mathbf{w}[c_a]]$;
  `/* traverse neighbours */`
  $c_a \leftarrow c_a.o.p$; `/* next ccw neighbour */`
  while $a \neq \mathbf{c}_r[1]$ **do**
    $\mathbf{c}_n \leftarrow [\mathbf{c}_n; c_a]$; `/* append to output */`
    $\mathbf{w}_n \leftarrow [\mathbf{w}_n; \mathbf{w}[c_a]]$;
    $c_a \leftarrow c_a.o.p$; `/* next ccw neighbour */`
  end
end

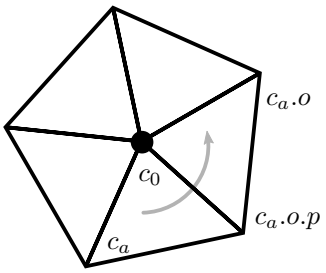

Figure B.3: One-ring neighbours (Algorithm: J. v.d. Merwe)

B.2.2 Edge flip

The `edgeflip` algorithm shown in Figure B.4 flips the common edge between two faces and opposite c_0 to form two different faces.

Function $[\mathbf{w}, \mathbf{o}] =$ `edgeflip`$(\mathbf{w}, \mathbf{o}, c_0)$

Input:

$\mathbf{w}$	$n_f d \times 1$	vertex indices
$\mathbf{o}$	$n_f d \times 1$	opposing corner indices
c_0	1×1	starting corner

Output:

$\mathbf{w}$	$n_f d \times 1$	vertex indices
$\mathbf{o}$	$n_f d \times 1$	opposing corner indices

`/* label incident corners */`

$c_2 \leftarrow c_0.p$; $c_1 \leftarrow c_0.n$;

$c_3 \leftarrow c_0.o$; $c_4 \leftarrow c_3.n$; $c_5 \leftarrow c_3.p$;

$c_a \leftarrow c_5.o$; $c_b \leftarrow c_1.o$; $c_c \leftarrow c_4.o$; $c_d \leftarrow c_2.o$;

`/* label incident vertices */`

$v_0 \leftarrow \mathbf{w}[c_3]$; $v_1 \leftarrow \mathbf{w}[c_0]$;

$v_2 \leftarrow \mathbf{w}[c_2]$; $v_3 \leftarrow \mathbf{w}[c_1]$;

`/* perform flip */`

$\mathbf{w}[c_1] \leftarrow v_0$; $\mathbf{w}[c_3] \leftarrow v_3$;

$\mathbf{w}[c_4] \leftarrow v_0$; $\mathbf{w}[c_5] \leftarrow v_1$;

`/* reset opposite corners */`

$\mathbf{o}[c_2] \leftarrow c_3$; $\mathbf{o}[c_0] \leftarrow c_a$;

$\mathbf{o}[c_3] \leftarrow c_2$; $\mathbf{o}[c_4] \leftarrow c_d$;

$\mathbf{o}[c_5] \leftarrow c_c$; $\mathbf{o}[c_a] \leftarrow c_0$;

$\mathbf{o}[c_c] \leftarrow c_5$; $\mathbf{o}[c_d] \leftarrow c_4$;

end

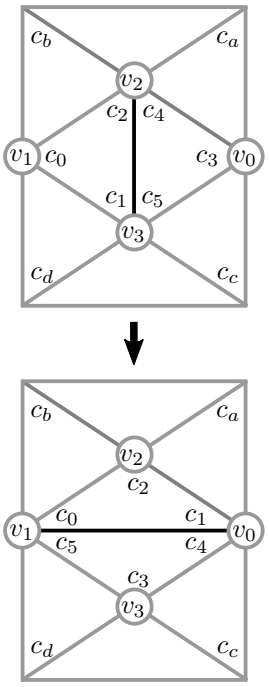

Figure B.4: Edge flip (Adapted from: Vieira *et al.* (2003))

B.2.3 Edge split

The algorithm `edgesplit` in Figure B.5 splits the faces incident to the edge opposite c_0 with a vertex that has been appended to the vertex list.

B.2.4 Face split

A face with corner c_0 may be split by a vertex that has been appended to the vertex list via `facesplit` shown in Figure B.6.

B.3 Normal vectors

As per Max (1999), in our applications we approximate a vertex normal as a weighted sum of the incident faces' normals:

Function $[\mathbf{w}, \mathbf{o}] =$ `edgesplit(`$\mathbf{w}, \mathbf{o}, c_0$`)`

Input:

$\mathbf{w}$	$n_f d \times 1$	vertex indices
$\mathbf{o}$	$n_f d \times 1$	opposing corners
c_0	1×1	starting corner

Output:

$\mathbf{w}$	$(n_f d + 6) \times 1$	vertex indices
$\mathbf{o}$	$(n_f d + 6) \times 1$	opposing corners

`/* label incident corners */`

$c_1 \leftarrow c_0.n$; $c_2 \leftarrow c_0.p$;

$c_3 \leftarrow c_0.o$; $c_4 \leftarrow c_3.n$; $c_5 \leftarrow c_3.p$;

$c_a \leftarrow c_1.o$; $c_d \leftarrow c_5.o$;

`/* label incident vertices */`

$v_1 \leftarrow \mathbf{w}[c_2]$; $v_2 \leftarrow \mathbf{w}[c_0]$; $v_3 \leftarrow \mathbf{w}[c_3]$;

$v_n \leftarrow$ `max(`$\mathbf{w}$`)+1;` `/* new vertex index */`

`/* create new corners */`

$c_6 \leftarrow n_f d + 1$; $c_7 \leftarrow n_f d + 2$; $c_8 \leftarrow n_f d + 3$;

$c_9 \leftarrow n_f d + 4$; $c_{10} \leftarrow n_f d + 5$; $c_{11} \leftarrow n_f d + 6$;

`/* append new faces */`

$\mathbf{w} \leftarrow [\mathbf{w}; v_1; v_n; v_3; v_1; v_2; v_n]$;

$\mathbf{o} \leftarrow [\mathbf{o}; c_5; c_d; c_{10}; c_1; c_8; c_a]$;

`/* update existing faces */`

$\mathbf{w}[c_2] \leftarrow v_n$; $\mathbf{w}[c_4] \leftarrow v_n$;

$\mathbf{o}[c_1] \leftarrow c_9$; $\mathbf{o}[c_5] \leftarrow c_6$;

$\mathbf{o}[c_a] \leftarrow c_{11}$; $\mathbf{o}[c_d] \leftarrow c_7$;

end

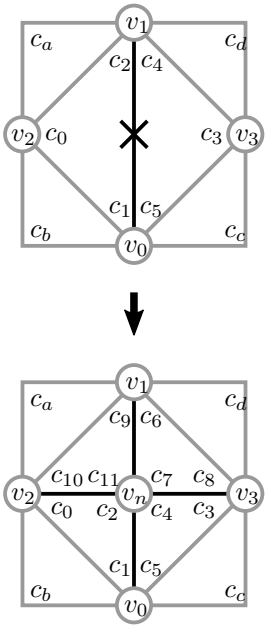

Figure B.5: Edge split (Algorithm: J. v.d. Merwe)

$$\mathbf{n}[i] = \sum_{l=1}^{n_{f_i}} \frac{\mathbf{e}[l] \times \mathbf{e}[l+1]}{||\mathbf{e}[l]||^2 ||\mathbf{e}[l+1]||^2} \tag{B.3}$$

Here $\mathbf{e}[l]$ and $\mathbf{e}[l+1]$ are edge vectors of the l^{th} of n_{f_i} faces that each share the vertex $\mathbf{v}[i]$. They may be obtained through the `ring` algorithm.

B.4 Curvature

Many applications benefit from the curvature information of a surface. In particular, we are interested in the principal curvatures or minimum and maximum curves k_1 and k_2 within a surface orthogonal to the normal at a specific point. Their signs are positive if these curvatures twist in the same direction

Function $[\mathbf{w}, \mathbf{o}] =$ `facesplit(`$\mathbf{w}, \mathbf{o}, c_0$`)`

Input:

$\mathbf{w}$	$n_f d \times 1$	vertex indices
$\mathbf{o}$	$n_f d \times 1$	opposing corners
c_0	1×1	starting corner

Output:

$\mathbf{w}$	$(n_f d + 6) \times 1$	vertex indices
$\mathbf{o}$	$(n_f d + 6) \times 1$	opposing corners

`/* label incident corners */`

$c_1 \leftarrow c_0.n$; $c_2 \leftarrow c_0.p$;

$c_a \leftarrow c_0.o$; $c_b \leftarrow c_1.o$;

`/* label incident vertices */`

$v_0 \leftarrow \mathbf{w}[c_1]$; $v_1 \leftarrow \mathbf{w}[c_2]$; $v_2 \leftarrow \mathbf{w}[c_0]$;

$v_n \leftarrow$ `max(w)`$+1$; `/* new vertex index */`

`/* create new corners */`

$c_3 \leftarrow n_f d + 1$; $c_4 \leftarrow n_f d + 2$; $c_5 \leftarrow n_f d + 3$;

$c_6 \leftarrow n_f d + 4$; $c_7 \leftarrow n_f d + 5$; $c_8 \leftarrow n_f d + 6$;

`/* append new faces */`

$\mathbf{w} \leftarrow [\mathbf{w}; v_2; v_n; v_1; v_0; v_1; v_n]$;

$\mathbf{o} \leftarrow [\mathbf{o}; c_6; c_b; c_1; c_3; c_0; c_a]$;

`/* update existing faces */`

$\mathbf{w}[c_2] \leftarrow v_n$;

$\mathbf{o}[c_0] \leftarrow c_7$; $\mathbf{o}[c_1] \leftarrow c_5$;

$\mathbf{o}[c_b] \leftarrow c_4$; $\mathbf{o}[c_a] \leftarrow c_8$;

end

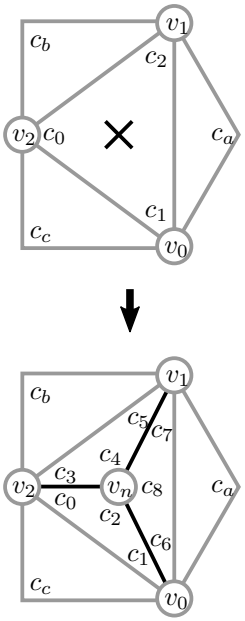

Figure B.6: Face split (Algorithm: J. v.d. Merwe)

as the normal, and negative otherwise. From this the Gaussian and Mean curvatures, K and H respectively, may be computed. The Gaussian curvature is a useful metric with which to describe a surface at a point as per Table B.1, while the Mean curvature is often used in the analysis of minimal surfaces.

Table B.1: Surface characterisation

K	Interpretation	Example
positive	elliptical	dome
negative	hyperbolic	saddle
zero	parabolic	trough

Following Belyaev (2006), we first estimate the normal of each vertex before using the inverse as the z-axes in an orthonormal base centred at the vertex of interest. A biquadratic surface may subsequently be fitted to the local neighbouring vertices via least squares approximation:

$$z = \gamma(x, y) = a_1x^2 + a_2y^2 + a_3xy + a_4x + a_5y + a_6 \tag{B.4}$$

The Hessian matrix of second derivatives is then:

$$\mathbf{H} = \begin{bmatrix} 2a_1 & a_3 \\ a_3 & 2a_2 \end{bmatrix} \tag{B.5}$$

of which eigenvalue decomposition yields the principle curvatures k_1 and k_2 as eigenvalues. We then compute the Gaussian and Mean curvatures:

$$K = k_1k_2 \tag{B.6}$$

$$H = \frac{k_1 + k_2}{2} \tag{B.7}$$

Figure B.7 shows pseudo-code for estimating per-vertex surface curvature.

```
Function [k, h] = curvature(v, f)
    Input:
    v          n_v × d   vertex array
    f          n_f × d   face array
    Output:
    k          n_v × 1   Gaussian curvature array
    h          n_v × 1   Mean curvature array
    /* estimate Gaussian and Mean curvatures                    */
    for each vertex v[i] do
        /* transform local neighbours to base coordinates      */
        nrm[i] ← normal(v, f, i);      /* estimate vertex normal */
        T ← base(−nrm[i]);             /* transformation matrix */
        neigh ← neighbours(v, f, i);   /* get local vertices    */
        neigh_b ← transform(neigh, T) ;          /* transform    */
        /* fit biquadratic surface                              */
        a ← solve(neigh_b, γ) ;          /* LSQ approximation   */
        /* estimate curvatures                                  */
        construct H ;                        /* Hessian matrix */
        compute k_1 and k_2 ;        /* eigenvalue decomposition */
        compute k[i] and h[i] ;                  /* curvatures */
    end
end
```

Figure B.7: Surface mesh curvature

B.5 Smoothing

Taubin (1995) removes noise from a mesh by projecting its coordinates onto an approximation of the low frequency subspace, similar to the application of a low pass filter. This has the advantage of reducing computational complexity when compared to Fourier decomposition, while the low pass kernel avoids mesh shrinkage inherent with Gaussian kernel smoothing. To start, the $n_v \times n_v$ circulant matrix $\mathbf{O}$ may be determined:

$$\mathbf{O} = \mathbf{I} - \mathbf{W} \tag{B.8}$$

Function $\mathbf{v}_f$ = `fair`$(\mathbf{v}, \mathbf{f}, n_F)$
  Input:
  $\mathbf{v}$ $n_v \times d$ vertex array
  $\mathbf{f}$ $n_v \times d$ face array
  N $\#$ number of faring iterations
  Output:
  $\mathbf{v}_f$ $n_v \times d$ faired vertex array
  `/* construct weight matrix */`
  $\mathbf{W}$:= `zeros`(n_v, n_v); `/* initialise weights to zero */`
  for *each vertex* $\mathbf{v}[i]$ **do**
    neigh ← `neighbours`$(\mathbf{v}, \mathbf{f}, i)$; `/* get local vertices */`
    n_{v_j} ←`numel(neigh)`; `/* number of neighbours */`
    for *each neighbour* **neigh**$[j]$ **do**
      $\mathbf{W}[i, j] \leftarrow {}^1/_{n_{v_j}}$; `/* assign weight */`
    end
  end
  `/* construct transfer function */`
  compute $\mathbf{O}$; `/* circulant matrix */`
  compute $\mathbf{F}^{n_F}$; `/* transfer function, power */`
  `/* apply low pass filtering */`
  compute $\mathbf{v}_f$; `/* smoothing */`
end

Figure B.8: Mesh fairing

where $\mathbf{I}$ is an appropriately sized identity matrix and $\mathbf{W}$ is a $n_v \times n_v$ square matrix of vertex weights. To construct $\mathbf{W}$, for all n_{v_j} vertices $\mathbf{v}[j]$ that belong to the neighbourhood of $\mathbf{v}[i]$ we set the j rows of the i^{th} column to ${}^1/_{n_{v_j}}$, and zero otherwise. Other weighting schemes may be used, as long as the values are positive and scaled to sum to one along the columns of $\mathbf{W}$. The transfer function $\mathbf{F}$ of the low pass filter may then be constructed:

$$\mathbf{F} = (\mathbf{I} - f_p\mathbf{O})(\mathbf{I} - f_n\mathbf{O}) \tag{B.9}$$

Here the variables $f_p > 0$ and $f_n < -f_p$ are scale factors such that the pass band frequency $k_{pb} = {}^1/_{f_p} + {}^1/_{f_n} > 0$. Setting k_{pb} between 0.01 and 0.1, with $f_p = 0.5$ and f_n subsequently solved generally produces good results. Iterating the smoothing step n_F times, the faired mesh $\mathbf{v}_f$ is then simply:

$$\mathbf{v}_f = \mathbf{F}^{n_F}\mathbf{v} \tag{B.10}$$

Note that the vertices $\mathbf{v}$ may be substituted with any n_v-row discrete input that also has connectivity $\mathbf{f}$, such as for example to obtain a valid fairing of the surface's $n_v \times 1$ Gaussian curvature array $\mathbf{k}$. The algorithm for mesh fairing, or smoothing as we apply it, is shown in Figure B.8. For more detail regarding fair surface design and extensions to include smooth and hierarchical constraints, we refer the interested reader to Taubin (1995).

B.6 Sampling

In order to sample directly on a mesh, we implemented the methods described by Corsini *et al.* (2012).

B.6.1 Monte Carlo sampling

The streaming Monte Carlo algorithm generates a uniformly distributed set of points on a mesh by first bijectively mapping all the triangle areas onto a real line, which is then randomly sampled and indexed back to the appropriate face for subsequent coordinate sampling. In this manner larger triangles are likely to be sampled more often than smaller ones.

The algorithm, shown in Figure B.9, starts by computing the $n_f \times 1$ array of triangle areas $\mathbf{a}$, and afterwards generating an array of $\mathbf{a}$'s cumulative sum. By including zero, the cumulative sum array serves as the set of intervals for a binning operation performed on n_{mc} randomly generated samples ranging between 0 and $\mathbf{a}[n_f]$. The resulting bin indices are used to select the appropriate mesh faces which are then sampled by again randomly generating values between 0 and 1 as barycentric coordinates, u and v. Note that care should be taken to avoid generating points that lie outside the triangles, i.e. both u and v should lie on the interval $[0, 1]$ and add up to one. The barycentric coordinates are finally mapped back to Cartesian space by computing the weighted sum of the faces' vertices:

$$\mathbf{v}_{mc}(u, v) = (1 - u - v)\mathbf{v}_1 + u\mathbf{v}_2 + v\mathbf{v}_3 \tag{B.11}$$

Here $\mathbf{v}_{mc}(u, v)$ is the resulting Cartesian sample point, while $\mathbf{v}_1$, $\mathbf{v}_2$ and $\mathbf{v}_3$ are the vertices that make up the triangle's corners.

Function $[\mathbf{v}_{mc}, \mathbf{bary}, \mathbf{ind}] =$ `montecarlo(`$\mathbf{v}, \mathbf{f}, n_{mc}$`)`

Input:

$\mathbf{v}$	$n_v \times d$	vertex array
$\mathbf{f}$	$n_f \times d$	face array
n_{mc}	$\#$	number of samples

Output:

$\mathbf{v}_{mc}$	$n_{mc} \times d$	samples, Cartesian coordinates
bary	$n_{mc} \times 2$	samples, Barycentric coordinates u, v
ind	$n_{mc} \times 1$	sampled face indices

```
/* map triangles to line                                    */
a ← triareas(v, f);              /* compute triangle areas */
intervals ← cumsum([0; a]);              /* cumulative sum */
/* sample line                                              */
urd ← rand([0, a[n_f]], n_mc);   /* uniform random distribution
 */
ind ← bin(urd, intervals);             /* bin line samples */
/* sample faces                                             */
```

for *each sample* i **do**

- **bary**$[i] \leftarrow$ `rand(`$[0, 1], 2$`);` `/* uniform random distribution */`
- check that **bary**$[i]$ is valid;
- $\mathbf{v}_{mc}[i] \leftarrow$ `barytocart(`**bary**$[i]$, **ind**$[i]$, $\mathbf{v}, \mathbf{f}$`);` `/* weighted sum */`

end

end

Figure B.9: Streaming Monte Carlo sampling (Adapted from: Corsini *et al.* (2012))

B.6.2 Poisson disk sampling

The Poisson disk sampling algorithm described by Corsini *et al.* (2012) works by first oversampling a mesh using the streaming Monte Carlo algorithm, and then for each available sample paring away all other points in the pool that lie within a sphere of radius r millimetres. The result is a uniformly random distributed point cloud where each sample is at least r millimetres away from its neighbours.

One difficulty with this method is finding an appropriate radius to ensure that the number of remaining samples are close to the desired number of samples n_{pd}. In order to estimate the disk radius, we use the method prescribed by Lagae and Dutré (2005), i.e. given that the densest packing of n_{pd} disks on a plane with area A is a hexagonal lattice, the diameter of the inscribed circle would then be the maximum Poisson radius, r_{max}:

Function $\mathbf{v}_{pd} =$ `poisson`$(\mathbf{v}, \mathbf{f}, \mathbf{h}_v, n_{pd})$

Input:

$\mathbf{v}$	$n_v \times d$	vertex array
$\mathbf{f}$	$n_f \times d$	face array
$\mathbf{h}_v$	$n_v \times 1$	importance function
n_{pd}	$\#$	target number of samples

Output:

$\mathbf{v}_{pd}$	$? \times d$	Poisson disk samples

`/* initialisation */`

$f_{pd} = 0.6$, $f_r = 0.5$, $n_{mc} = 20 \times n_{pd}$;

$\mathbf{v}_{pd} := [\,]$; `/* empty array */`

$[\mathbf{v}_{mc}, \mathbf{bary}, \mathbf{ind}] \leftarrow$ `montecarlo`$(\mathbf{v}, \mathbf{f}, n_{mc})$; `/* over sampling */`

$A \leftarrow$ `mesharea`$(\mathbf{v}, \mathbf{f})$; `/* mesh surface area */`

estimate r; `/* Poisson disk radius */`

`/* importance-based radii */`

for *each pool sample* i **do**

  $\mathbf{h}_{mc}[i] \leftarrow$ `barytocart`$(\mathbf{bary}[i], \mathbf{ind}[i], \mathbf{h}_v, \mathbf{f})$; `/* weighted sum */`

end

store $h_{min}, h_{max}, rf_r, {}^{r}/_{f_r}$;

for *each pool sample* i **do**

  compute $\mathbf{r}[i]$;

end

`/* Poisson disk sampling */`

while $\mathbf{v}_{mc}$ *is not empty* **do**

  $j \leftarrow$ `min`$(\mathbf{r})$; `/* prioritise sampling */`

  $\mathbf{v}_{pd} \leftarrow [\mathbf{v}_{pd}; \mathbf{v}_{mc}[j]]$; `/* append sample */`

  $\mathbf{pare} \leftarrow$ `find`$(||\mathbf{v}_{mc} - \mathbf{v}_{mc}[j]|| < \mathbf{r}[j])$; `/* trim condition */`

  $\mathbf{v}_{mc} \leftarrow$ `remove`$(\mathbf{v}_{mc}, \mathbf{pare})$; `/* trim samples from pool */`

  $\mathbf{r} \leftarrow$ `remove`$(\mathbf{r}, \mathbf{pare})$; `/* update available radii */`

end

end

Figure B.10: Poisson disk sampling (Adapted from: Corsini *et al.* (2012))

$$r_{max} = \sqrt{\frac{A}{2\sqrt{3}n_{pd}}} \tag{B.12}$$

The maximum Poisson disk radius is then multiplied by f_{pd} to obtain r, where f_{pd} is some factor with a value between 0.6 and 0.9 necessary to avoid overly regular arrangements. Note that the concept does not carry over directly to a 3D surface mesh which, in conjunction with use of the f_{pd} factor, adversely

affects the accurate approximation of exactly n_{pd} samples.

Furthermore, rather than using a fixed r, it may be advantageous to inversely correlate the individual disk radii $\mathbf{r}[i]$ for each of the n_{mc} oversampled points in the starting pool to the values of some importance function $\mathbf{h}_v$ defined on the mesh vertices. The resulting samples therefore end up being distributed more densely in regions with high importance, and vice versa. This is achieved via Equation B.13, where $\mathbf{h}_{mc}$ denotes the importance function mapped to the initial sample pool and f_r controls the density factors associated with the minimum and maximum importance values. Since we know the face indices and barycentric coordinates of the Monte Carlo samples, $\mathbf{h}_{mc}$ may be computed as a weighted sum by replacing the vertices from Equation B.11 with the triangles' per-vertex importance values $\mathbf{h}_v$.

$$\mathbf{r}[i] = \frac{r f_r - {}^{r}/_{f_r}}{h_{max} - h_{min}} \left(\mathbf{h}_{mc}[i] - h_{min}\right) + \frac{r}{f_r} \tag{B.13}$$

While useful, importance sampling makes obtaining an exact number of target samples even more difficult. We have found, however, that by iteratively adjusting some artificial target with a factor derived from the actual number of attained samples until the result is within an acceptable tolerance of n_{pd} generally works well. Finally, oversampling the starting pool by a factor of 20 and using values for $f_{pd} = 0.7$ and $f_r = 0.5$ gives good results. An implementation of the algorithm is shown in Figure B.10.

B.7 Ray tracing

Ray tracing allows us to project points onto a triangulated mesh in order to estimate surface errors or find face split locations during re-sampling operations. We adapt the approach by Möller and Trumbore (2005) to perform efficient one-point-to-many-face intersections, afterwards keeping only the projection with the shortest ray distance from all valid possibilities. We start by defining the intersection point $\mathbf{v}_p(u, v)$ of some ray with a triangle similar to Equation B.11, and equate that to:

$$\mathbf{v}_p(t) = \mathbf{v}_o + t\mathbf{n}_d \tag{B.14}$$

where $\mathbf{v}_o$ is the ray origin, $\mathbf{n}_d$ is the direction vector and t a variable denoting the projection distance. The problem is then to find u, v and t such that $\mathbf{v}_p(u, v) = \mathbf{v}_p(t)$. The resulting set of linear equations may be solved by:

$$\begin{bmatrix} u \\ v \\ t \end{bmatrix} = \frac{1}{\mathbf{u}_u \cdot \mathbf{e}_{12}} \begin{bmatrix} \mathbf{u}_u \cdot \mathbf{e}_{o1} \\ \mathbf{u}_v \cdot \mathbf{n}_d \\ \mathbf{u}_v \cdot \mathbf{e}_{13} \end{bmatrix}, \quad \text{where} \quad \mathbf{u}_u = \mathbf{n}_d \times \mathbf{e}_{13} \quad \text{and} \quad \mathbf{u}_v = \mathbf{e}_{o1} \times \mathbf{e}_{12} \tag{B.15}$$

```
Function [v_p, bary] = raytrace(v, f, v_o, n_d)
    Input:
    v        n_v × d   vertex array
    f        n_f × d   face array
    v_o      n_p × d   set of ray origins
    n_d      n_p × d   set of ray directions
    Output:
    v_p      n_p × d   ray-mesh intersections
    bary     n_p × 2   barycentric coordinates
    /* initialisation                                          */
    v_p := nan(n_p, d);                          /* array of NaN's */
    bary := nan(n_p, 2);
    for each face f[j] do
        pre-compute e_12, e_13;
    end
    /* calculate intersections                                 */
    for each ray n_r[i] do
        t_cur =Inf;          /* define current distance as large */
        for each face f[j] do
            compute u_u, m;
            if m ≠ 0 then
                /* ray is not parallel to face                 */
                compute e_o1;              /* vector to ray origin */
                compute u;      /* first barycentric coordinate */
                if 0 ≤ u ≤ 1 then
                    compute u_v;
                    compute v; /* second barycentric coordinate */
                    if 0 ≤ v ≤ 1 then
                        /* intersection lies inside face       */
                        compute t;    /* distance from ray origin */
                        if t < t_cur then
                            store bary[i];  /* barycentric coordinates
                             */
                            compute v_p[i]; /* current intersection */
                            t_cur ← t;    /* update current distance */
                        end
                    end
                end
            end
        end
    end
end
```

Figure B.11: Ray tracing (Adapted from: Möller and Trumbore (2005))

Here $\mathbf{e}_{o1}$ denotes the pseudo-edge vector between the ray origin and the triangle's first vertex $\mathbf{v}[v_1]$, and $\mathbf{e}_{12}$ and $\mathbf{e}_{13}$ are the edge vectors between the first vertex and vertices $\mathbf{v}[v_2]$ and $\mathbf{v}[v_3]$, respectively. For convenience, we also denote the determinant $\mathbf{m} = {}^{1}/_{\mathbf{u}_u \cdot \mathbf{e}_{12}}$. Furthermore, Möller and Trumbore (2005)'s algorithm works by postponing calculations until they are required, i.e. pending tests to see if the ray is parallel to the triangle or that the barycentric coordinates lie within the face's bounds. We implement these tests to avoid unnecessary computations in our one-to-many intersection algorithm shown in Figure B.11.

B.8 Mesh triangle splitting

Triangle splitting is performed in order to include samples that lie on or near some mesh, into it. This may be accomplished by projecting each individual sample onto the mesh in order to obtain its barycentric coordinates. If samples lie directly on the mesh, projection directions may be taken from the mesh faces on which the additional points were placed. Otherwise, ray directions may be estimated either from some parametric surface fitted to the nearest mesh vertices, or by considering the target mesh normals themselves.

The table operations `facesplit` or `edgesplit` are subsequently performed, depending on whether or not the barycentric coordinates lie close to the limits $[0, 1]$ to within some tolerance. An edge split is performed if only one coordinate lies within the tolerance band, the sample is considered as a pre-existing mesh vertex if all three coordinates lie within the tolerances (in which case nothing is done), and a face split is performed otherwise. Refer to Figure B.12 for the pseudo-algorithm.

B.9 Mesh quality

Since mesh face splitting generally results in poor mesh connectivity which could inhibit simplification, Fu and Zhou (2008) suggests performing a series of edge flips in order to improve a local measure of the mesh faces' quality. If we let $\mathbf{a}[j]$ be an individual face's area and l_1, l_2, and l_3 denote the triangle side lengths, we can define its aspect ratio as (Guéziec, 1999):

$$\mathbf{c}[j] = \frac{4\sqrt{3}\mathbf{a}[j]}{l_1^2 + l_2^2 + l_3^2} \tag{B.16}$$

Triangle aspect ratio and edge flipping is illustrated in Figure B.13. Edges are considered candidates for flipping via `edgeflip` if it would increase the sum of the involved triangles' aspect ratios without degrading either beyond some minimum value τ_c. Topology is further preserved by enforcing limits on the minimum allowable vertex incidence and the largest change in dihedral

```
Function [v_u, f_u] = meshsplit(v, f, v_o)
    Input:
    v       n_v × d   vertex array
    f       n_f × d   face array
    v_o     ? × d     sample origin array
    Output:
    v_u     ? × d     updated vertex array
    f_u     ? × d     updated face array
    /* initialisation                                   */
    tol ≈ 0; v_u := v; f_u := f;
    estimate n_d;                              /* ray directions */
    /* triangle splitting                               */
    for each sample v_o[i] do
        bary ← raytrace(v_u, f_u, v_o[i], n_d[i]);   /* find intersection
         */
        loc ← threshold(bary, tol);        /* location threshold */
        if loc on edge then
            [v_u, f_u] ← edgesplit(v_u, f_u, v_o[i]);
        else if loc on vertex then
            do nothing;
        else
            [v_u, f_u] ← facesplit(v_u, f_u, v_o[i]);
    end
end
```

Figure B.12: Mesh triangle splitting

angle (angle between two planes) τ_d for all involved triangle neighbours. Figure B.14 shows the algorithm. We found that values of $\tau_c = 0.5$ and $\tau_d = 45°$ work well, while fewer than four incident edges per vertex sometimes caused invalid topologies.

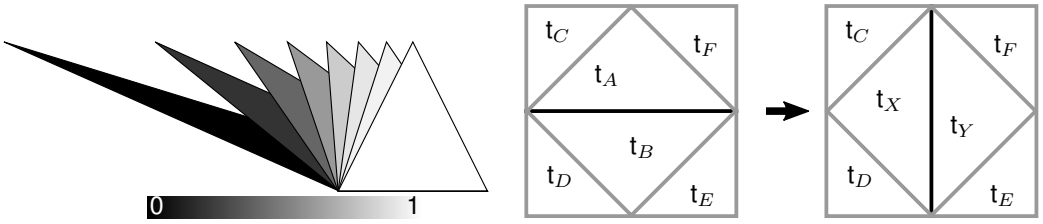

(a) Triangle aspect ratio (b) Incident faces

Figure B.13: Improving mesh connectivity (Illustration: J. v.d. Merwe)

```
Function [f_u] = meshflip(v, f)
    Input:
    v          n_v × d   vertex array
    f          n_f × d   face array
    Output:
    f_u        n_f × d   improved face array
    /* precompute                                                    */
    f_u = f;
    nrms ← normals(v, f);                          /* face normals */
    dihs ← dihedrals(nrms);                    /* dihedral angles */
    compute c;                              /* triangle compactness */
    /* improve mesh connectivity                                    */
    while edge flips occur do
        for each unique edge i do
            if incidence is valid then
                find incident triangle indices t_A to t_F;
                simulate edge flip to get triangles t_X and t_Y;
                nrm_X ← normals(v, f_X);
                nrm_Y ← normals(v, f_Y);
                /* determine dihedral angle changes                 */
                Δ_XY ← dihs[t_AB]−dihedrals([nrm_X; nrm_Y]);
                Δ_XC ← dihs[t_AC]−dihedrals([nrm_X; nrms[t_C]]);
                Δ_XD ← dihs[t_BD]−dihedrals([nrm_X; nrms[t_D]]);
                Δ_YE ← dihs[t_BE]−dihedrals([nrm_Y; nrms[t_E]]);
                Δ_YF ← dihs[t_AF]−dihedrals([nrm_Y; nrms[t_F]]);
                if max(|Δ_XY|, |Δ_XC|, |Δ_XD|, |Δ_YE|, |Δ_YF|) < τ_d then
                    compute c_X, c_Y;   /* simulated aspect ratios */
                    if c_X, c_Y ≥ τ_c then              /* degradation */
                        if c[t_A] + c[t_B] < c_X + c_Y then /* local test */
                            f_u ← edgeflip(f_u, i);       /* edge flip */
                            update nrms and dihs;
                            update c;
                        end
                    end
                end
            end
        end
    end
end
```

Figure B.14: Mesh connectivity improvement

B.10 Vertex removal

Given a set of unwanted vertices on a mesh, we apply a simplified version of the method described by Fu and Zhou (2008) in order to remove them and restore mesh connectivity. Here the 1-ring neighbours $\mathbf{v}[v_i], i = 1, \ldots, n_{v_i}$ of a vertex $\mathbf{v}[v]$ marked for removal are first mapped to their two-dimensional counterparts, $\grave{\mathbf{v}}$ as shown in Figure B.15(a) by solving:

$$\begin{aligned} &\grave{\mathbf{v}}[v] = 0, \\ &||\grave{\mathbf{v}}[v_i] - \grave{\mathbf{v}}[v]|| = ||\mathbf{v}[v_i] - \mathbf{v}[v]||, \text{and} \\ &\angle(\grave{\mathbf{v}}[v_i], \grave{\mathbf{v}}[v], \grave{\mathbf{v}}[v_1]) = 2\pi \frac{\sum_{j=1}^{v_i - 1} \angle(\mathbf{v}[v_j], \mathbf{v}[v], \mathbf{v}[v_j + 1])}{\sum_{j=1}^{n_{v_i}} \angle(\mathbf{v}[v_j], \mathbf{v}[v], \mathbf{v}[v_j + 1])} \end{aligned} \tag{B.17}$$

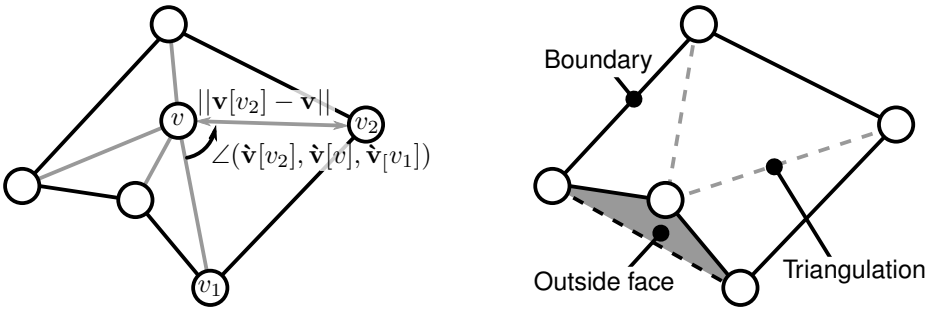

(a) 2D vertex mapping (b) Constrained triangulation

Figure B.15: Vertex removal (Illustration: J. v.d. Merwe)

Constrained Delaunay triangulation is then performed without $\grave{\mathbf{v}}[v]$ in order to generate a parametrised sub-mesh, taking care to maintain the ring's boundary connectivity whilst disallowing edge generation outside of it as shown in Figure B.15(b). The resulting sub-mesh is then mapped back to the original mesh (which now excludes $\grave{\mathbf{v}}[v]$) unless it already contains one of the new non-boundary edges (Fu and Zhou, 2008). We have also implemented a priority queue based on the vertex removal error of Schroeder *et al.* (1992) in an attempt to guide the decimation process (Vieira *et al.*, 2003). Said error is merely the projection distance of a vertex onto a plane fitted to its neighbours, with vertices masked from removal assigned Inf values. Once a vertex has been considered, its error is set to Inf as well, regardless of whether or not it is actually removed. It is only reintroduced into the algorithm if its error is updated as a neighbour to a successfully removed vertex, i.e. if the local topology changed, thus making it a possible candidate again. The pseudo-code is shown in Figure B.16.

Function $\mathbf{f}_u = \texttt{meshreduce}(\mathbf{v}, \mathbf{f}, \mathbf{mask})$
Input:
$\mathbf{v}$ $n_v \times d$ vertex array
$\mathbf{f}$ $n_f \times d$ face array
$\mathbf{mask}$ $n_v \times 1$ vertex removal mask
Output:
$\mathbf{f}_u$ $n_f \times d$ reduced face array
`/* initialisation */`
$\mathbf{f}_u := \mathbf{f}$;
$\mathbf{e} \leftarrow \texttt{edges}(\mathbf{v}, \mathbf{f})$; `/* all face edges */`
$\mathbf{E}_r \leftarrow \texttt{error}(\mathbf{v}, \mathbf{f}, \mathbf{mask})$; `/* vertex removal error */`
`/* reduce mesh */`
while *removals occur* **do**
  while $\texttt{any}(\mathbf{E}_r) \neq$ Inf **do**
    $v \leftarrow \texttt{min}(\mathbf{E}_r)$; `/* vertex with smallest error */`
    $\mathbf{E}_r[v] \leftarrow$ Inf; `/* remove from consideration */`
    $\mathbf{neigh} \leftarrow \texttt{neighbours}(\mathbf{v}, \mathbf{f}, v)$; `/* 1-ring neighbours */`
    $\grave{\mathbf{v}} \leftarrow \texttt{anglemap}(\mathbf{v}[\mathbf{neigh}])$; `/* 2D parametrisation */`
    $\mathbf{f}_p \leftarrow \texttt{delaunaytri}(\grave{\mathbf{v}})$; `/* re-triangulate boundary */`
    $\mathbf{e}_p \leftarrow \texttt{edges}(\mathbf{v}, \mathbf{f}_p)$; `/* new patch edges */`
    if $\texttt{all}(\mathbf{e} \neq \mathbf{e}_p)$ **then**
      substitute $\mathbf{f}_p$ into $\mathbf{f}_u$ and $\mathbf{e}_p$ into $\mathbf{e}$;
      $\mathbf{E}_r[\mathbf{neigh}] \leftarrow \texttt{error}(\mathbf{v}[\mathbf{neigh}], \mathbf{f}, \mathbf{mask})$; `/* update */`
    end
  end
end
end

Figure B.16: Vertex removal

B.11 Re-sampling

We discuss here a method for re-meshing a triangulated surface via direct sampling as per Fu and Zhou (2008). It works by first computing Poisson disk samples using the mean absolute surface curvature as an importance function, and then including said samples in the mesh via splitting operations. Iterative edge flipping and mesh reduction steps are then performed until no further changes occur. Note that Fu and Zhou (2008) also included a vertex smoothing operation which we elected to forego since we did not wish to alter the point coordinates. However, we get good results when fairing the mesh curvature prior to importance sampling. Figure B.17 illustrates the pseudo-code for our method which uses the previously discussed algorithms, while Figure B.18 shows the various stages of a Stanford Bunny model being re-meshed.

Function $[\mathbf{v}_u, \mathbf{f}_u] =$ `resample`$(\mathbf{v}, \mathbf{f}, n_{pd})$

Input:

$\mathbf{v}$	$n_v \times d$	vertex array
$\mathbf{f}$	$n_f \times d$	face array
n_{pd}	$\#$	target number of samples

Output:

$\mathbf{v}_s$	$? \times d$	re-sampled vertex array
$\mathbf{f}_s$	$? \times d$	re-sampled face array

```
/* sampling                                                    */
h = curvature(v, f);                  /* importance function */
h_a ← |h|;                                 /* absolute value */
h_f = fair(h_a, f, N);                          /* smoothing */
v_pd = poisson(v, f, h_f, n_pd);          /* direct sampling */
/* re-meshing                                                 */
[v_u, f_u] = meshsplit(v, f, v_pd);       /* include samples */
mask ← find(v_u = v);          /* mask samples from removal */
while changes occur do
    f_u = meshflip(v_u, f_u);      /* improve mesh connectivity */
    f_u = meshreduce(v_u, f_u, mask);          /* remove original
     vertices */
end
/* clean up                                                   */
[v_u, f_u] = unref(v_u, f_u);    /* remove unreferenced vertices */
```

Figure B.17: Mesh re-sampling

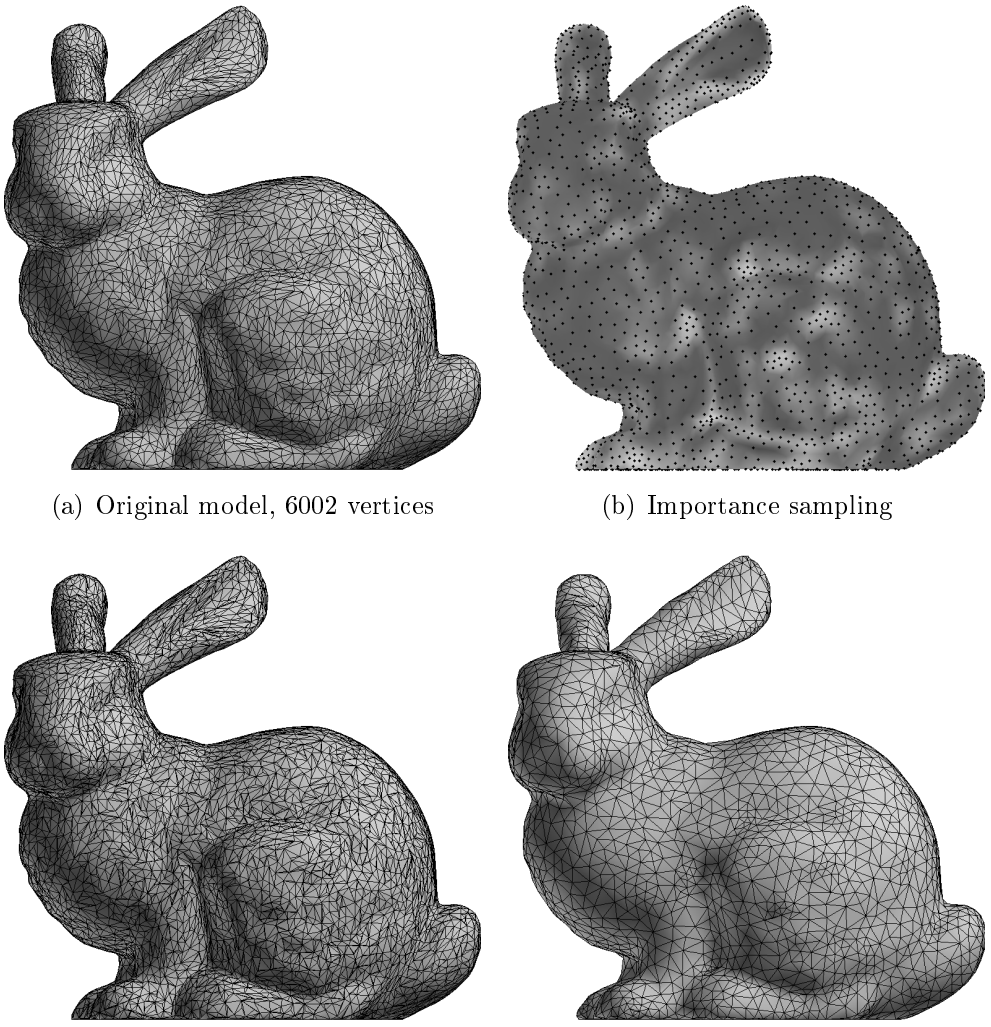

(a) Original model, 6002 vertices

(b) Importance sampling

(c) Mesh after triangle splitting

(d) Re-meshed model, 3008 vertices

Figure B.18: Re-meshing example (Illustration: J. v.d. Merwe)

C. B-splines

Basis or B-splines are powerful free-form parametrisations able to accurately represent a wide variety of curves and surfaces, which has led to their use in many Computer Assisted Design and Computer Graphics (CG) applications. It is perhaps only natural therefore to see them employed in the study of diathrodal joints (Ateshian *et al.*, 1993; DeFrate *et al.*, 2004; Kosel *et al.*, 2010; Van den Heever *et al.*, 2011*b*) and even implant design as we do here (Van den Heever *et al.*, 2012*b*; Walker, 2014). In this Chapter we present a basic introduction to B-spline theory and application.

C.1 Curves

A B-spline curve is defined as

$$C(u) = \sum_{i=0}^{n_{Pu}} N_{i,p_u}(u)\mathbf{P}[i] \tag{C.1}$$

Here p_u is the degree of the curve, $\mathbf{P}$ describes the $n_{Pu}+1$ point control polygon in 2D or 3D Cartesian space and $N_{i,p_u}(u)$ denotes the p_u^{th} degree normalised basis functions. For *open* and *clamped* curves we define the non-uniform, $n_{ku}+1$ element knot vector as:

$$\mathbf{k}_u = \{ \underbrace{0,\ldots,0}_{p_u+1}, \; u_{p_u+1},\ldots,u_{n_u-p_u-1}, \; \underbrace{1,\ldots,1}_{p_u+1} \; \} \tag{C.2}$$

where $n_{ku} = n_{Pu} + p_u + 1$. Multiplicity of 0 and 1 at the ends of the knot vector ensures that the ends of the curve are *clamped*, i.e. coincidental with those of the control polygon. Alternatively, we use a uniform knot sequence to represent an *unclamped* and *closed* knot curve:

$$\mathbf{k}_u = \{0, u_1, \ldots, u_{n_{ku}-1}, 1\} \tag{C.3}$$

Note that in the latter case, the curve is limited to the domain $[\mathbf{k}_u[p_u],\ldots,\mathbf{k}_u[n_{ku}-p_u]]$ while the first and last p_u control points are wrapped:

$$\mathbf{P}[n_{Pu}+2-p_u+j] = \mathbf{P}[j] \quad \text{where} \quad j \in [0,\ldots,p_u-1] \tag{C.4}$$

B-splines may also be adapted to rational functions that allow the representation of important types of curves and surfaces including circles, spheres, cones etc. which is not possible otherwise. A rational basis spline curve is defined as:

$$C(u) = \sum_{i=0}^{n_{Pu}} R_i(u)\mathbf{P}[i] \quad \text{where} \quad R_i(u) = \frac{N_{i,p_u}(u)\mathbf{W}[i]}{\sum_{j=0}^{n_{Pu}} N_{j,p_u}(u)\mathbf{W}[j]} \tag{C.5}$$

where $R_i(u)$ are the rational basis functions. For the special case of all weights $\mathbf{W}[i] = 1$, $R_{i,p_u}(u) = N_{i,p_u}(u)$ and Equation C.5 therefore reduces to its non-rational equivalent. Furthermore, basis splines are piecewise functions, which offer the additional benefit of requiring lower degrees for reasonable fits to complex shapes. The basis functions on which B-splines rely are also known as *blending* functions, and are defined here according to the recurrence formula:

$$\begin{aligned} N_{i,0}(u) &= \begin{cases} 1 & \text{if } \mathbf{k}_u[i] \leq u < \mathbf{k}_u[i+1] \\ 0 & \text{otherwise} \end{cases} \\ N_{i,p_u}(u) &= \frac{u-\mathbf{k}_u[i]}{\mathbf{k}_u[i+p_u]-\mathbf{k}_u[i]} N_{i,p_u-1}(u) + \frac{\mathbf{k}_u[i+p_u+1]-u}{\mathbf{k}_u[i+p_u+1]-\mathbf{k}_u[i+1]} N_{i+1,p_u-1}(u) \end{aligned} \tag{C.6}$$

An important property of the basis functions is that $N_{i,p_u}(u) = 0$ if u lies outside the interval $[\mathbf{k}_u[i], \mathbf{k}_u[i+p_u+1])$. In other words, B-splines are capable of *local support*, meaning that if the control point associated with an interval is moved, the curve is only affected in a local region. Furthermore, for a given knot span $[\mathbf{k}_u[i], \mathbf{k}_u[i+1])$, there are a maximum of only $p_u + 1$ basis functions $N_{i-p_u,p}, \ldots, N_{i,p_u}$ which are non-zero. This represents an opportunity for efficient computation of a point on a curve via the following procedure:

1. Find which knot span $[\mathbf{k}_u[i], \mathbf{k}_u[i+1])$ which u belongs to.
2. Determine all non-zero basis functions $N_{i-p_u,p_u}, \ldots, N_{i,p_u}$ in that span.
3. Multiply the resulting basis functions' values with the matching control points.

Refer to Figure C.1 for an example of B-spline curves that show the effect of different weights. For a degree of $p_u = 3$ the knot vector is defined as $\mathbf{k}_u = [0\ 0\ 0\ 0\ 0.25\ 0.5\ 0.75\ 1\ 1\ 1\ 1]$, while the weights are $\mathbf{W} = [1\ 1\ 1\ w\ 1\ 1\ 1]$ The local support property is also illustrated via dashed lines that denote the span between two knots. It is also important to mention that B-splines are invariant to affine transformations of $\mathbf{P}$; translating, scaling or rotating the control polygon does not affect the B-spline itself (not illustrated here). Figure C.2 also shows examples of clamped open and unclamped closed curves, respectively.

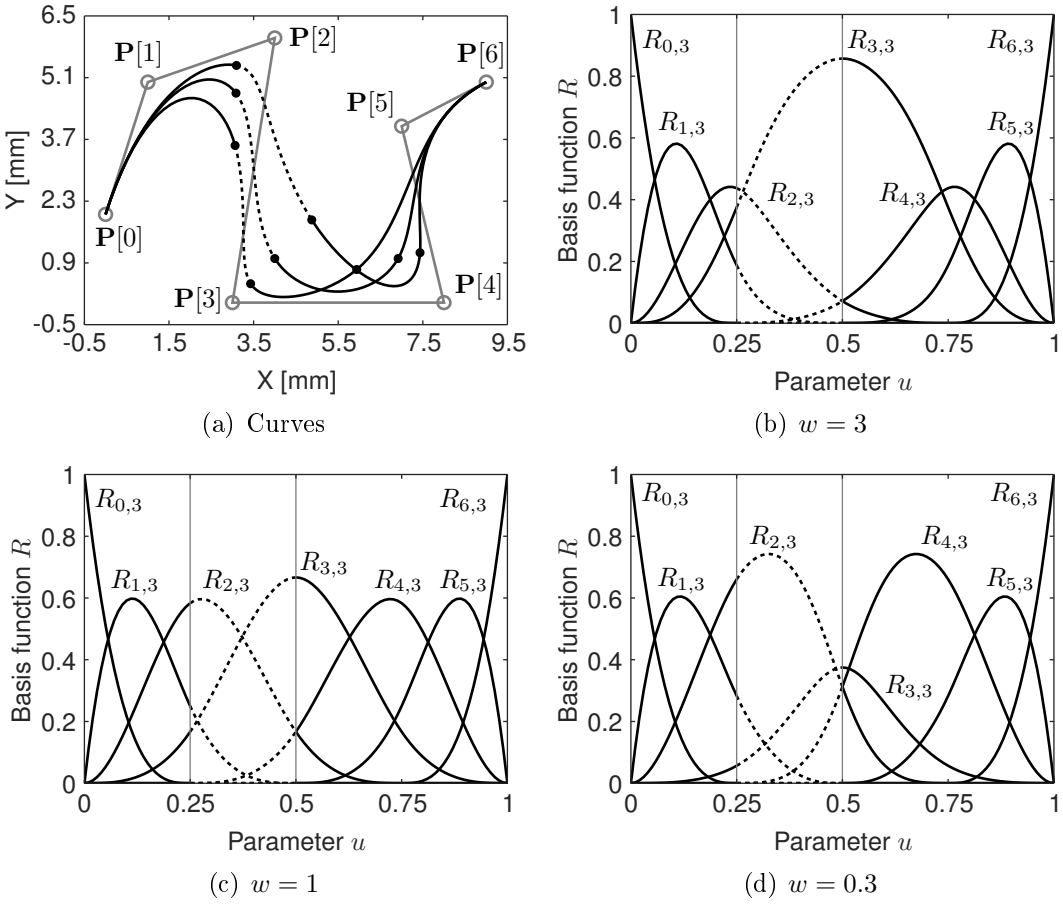

(a) Curves (b) $w = 3$

(c) $w = 1$ (d) $w = 0.3$

Figure C.1: B-spline curve examples (Adapted from: Piegl and Tiller (1997))

C.2 Curve approximation

While there are a number of approaches to B-spline curve fitting, we start here with the simplest linear least squares approach as discussed by Piegl and Tiller (1997), adapted for our purposes. For curves, the objective is to determine an unknown control polygon $\mathbf{P}$ so that our B-spline approximates an ordered set of $n_q + 1$ data points $\mathbf{q}$, minimising:

$$\sum_{k=0}^{n_q+1} ||\mathbf{q}[k] - C(\mathbf{u}_u[k])||^2 \tag{C.7}$$

We assume knowledge of the desired number of control points n_{Pu} such that they are $\leq n_q$, as well as the degree of the curve $p_u \geq 1$. In order to generate a linear set of equations, we must first choose appropriate curve parameters $\mathbf{u}_u[k]$ as well as a knot vector $\mathbf{k}_u$. In the absence of prior knowledge of the intended curve, the chord length method solves the problem for the curve parameters

by mapping the Euclidean distances between the respective data points to a normalised one dimensional axis according to:

$$\mathbf{u}_u[k] = \mathbf{u}_u[k-1] + \frac{||\mathbf{q}[k] - \mathbf{q}[k-1]||}{\sum_{k=1}^{n_q} ||\mathbf{q}[k] - \mathbf{q}[k-1]||} \quad \text{where} \quad k \in [1, \ldots, n_q - 1] \tag{C.8}$$

Here the parameters for the end points are simply set to $\mathbf{u}_u[0] = 0$ and $\mathbf{u}_u[n_q] = 1$ respectively. It is important to mention in this case that $C(\mathbf{u}_u[k])$ is not necessarily the closest point $C(u)$ to $\mathbf{q}[k]$. However, given some initial B-spline, we may use Newton's iterative approach as an alternative to find parameter values $\mathbf{u}_u[k]$ that denote curve positions closest to the data points. Continuing, we then require a total of $n_{ku} + 1$ knots in the knot vector. In the case of clamped B-splines, this equates to a set of $n_{Pu} - p_u$ unique internal knots, the 'external' knots being the $p_u + 1$ zeros and $p_u + 1$ ones at each end of the knot vector. The following equation ensures that there is at least one $\mathbf{u}_u[k]$ in each knot span of the resulting knot vector:

$$\begin{gathered} \alpha = \frac{j^2(n_{ku}+1)}{n_{Pu}-p_u+1} - 1, \quad i = int(\alpha + 1), \\ \mathbf{k}_u[p_u + j] = (1-\alpha)\mathbf{u}_u[i-1] + \alpha \mathbf{u}_u[i] \quad \text{where} \quad j \in [1, \ldots, n_{Pu} - p_u] \end{gathered} \tag{C.9}$$

Closed curves merely require a uniform knot sequence $\mathbf{k}_u[j] = {}^{j}/_{n_{ku}}$ for all $j \in [0, \ldots, n_{ku}]$. In general, the $n_{Pu} + 1$ set of unknown control points $\mathbf{P}$ may then be solved:

$$\mathbf{AP} = \mathbf{N}^T\mathbf{q} \text{ where } \mathbf{N} = \begin{bmatrix} N_{0,p_u}(\mathbf{u}_u[0]) & \cdots & N_{n_{Pu},p_u}(\mathbf{u}_u[0]) \\ \vdots & \ddots & \vdots \\ N_{0,p_u}(\mathbf{u}_u[n_q]) & \cdots & N_{Pu,p_u}(\mathbf{u}_u[n_q]) \end{bmatrix} \text{ and } \mathbf{A} = \mathbf{N}^T\mathbf{N} \tag{C.10}$$

C.3 Curve constraints

For clamped curves we desire that the end-points of the curve $C(0)$ and $C(1)$ be constrained to $\mathbf{q}[0]$ and $\mathbf{q}[n_q]$ respectively. Only the remaining $\mathbf{q}[k]$ must then be approximated such that $C(\mathbf{u}_u[k]) \approx \mathbf{q}[k]$. Since the end points are constrained to $\mathbf{q}[0]$ and $\mathbf{q}[n_q]$, we adjust the remaining data points to exclude their effect (Piegl and Tiller, 1997; Lu, 2010):

$$\hat{\mathbf{q}} = \begin{bmatrix} \mathbf{q}[1] - N_{0,p_u}\mathbf{q}[0] - N_{n_{Pu},p_u}\mathbf{q}[n_q] \\ \vdots \\ \mathbf{q}[k] - N_{0,p_u}\mathbf{q}[0] - N_{n_{Pu},p_u}\mathbf{q}[n_q] \end{bmatrix} \quad \text{where} \quad k \in [1, \ldots, n_q - 1] \tag{C.11}$$

Equation C.24 then becomes:

$$\mathbf{AP} = \mathbf{N}^T\hat{\mathbf{q}}$$
$$\text{where } \mathbf{N} = \begin{bmatrix} N_{1,p_u}(\mathbf{u}_u[1]) & \cdots & N_{n_{Pu}-1,p_u}(\mathbf{u}_u[1]) \\ \vdots & \ddots & \vdots \\ N_{1,p_u}(\mathbf{u}_u[n_q-1]) & \cdots & N_{n_q-1,p_u}(\mathbf{u}_u[n_q-1]) \end{bmatrix} \text{ and } \mathbf{A} = \mathbf{N}^T\mathbf{N} \tag{C.12}$$

We subsequently append $\mathbf{q}[0]$ and $\mathbf{q}[n_q]$ on either end of $\mathbf{P}$ in order to obtain the full set of control points with the appropriate end conditions. For closed curves we follow a slightly different approach, requiring instead that the first and last p_u control points be wrapped. We define $\mathbf{N}$ and $\mathbf{A}$ as in Equation C.24 in order to obtain the $(n_{Pu}+1) \times (n_{Pu}-p_u+2)$ matrix:

$$\mathbf{B}[i,j] = \begin{cases} \mathbf{A}[i,j] + \mathbf{A}[i, n_q+2-p_u+j] & \text{for} \quad j \in [0,\ldots,p_u) \\ \mathbf{A}[i,j] & \text{for} \quad j \in [p_u,\ldots,n_q-p_u+1] \end{cases} \tag{C.13}$$

for all $i \in [0,\ldots,n_{Pu}]$. The constrained solution is obtained by solving for $\mathbf{P}$:

$$\mathbf{BP} = \mathbf{N}^T\mathbf{Q}_k \tag{C.14}$$

The first p_u elements of the solution are then also appended to the end of $\mathbf{P}$ in order to obtain a full $n_{Pu}+1$ control polygon. Figure C.2(a) illustrates clamped, open curves while Figure C.2(b) shows an unclamped, closed curve.

C.4 Penalised curves

B-spline approximation often results in undesirable oscillation in the presence of poorly conditioned data or larger knot vectors than that warranted by the variability in the data. Such effects are usually mitigated by minimising the objective function from Equation C.23 with an added penalty based on the bending energy of the curve (Lu, 2010):

$$\sum_{k=0}^{n_q+1} ||\mathbf{q} - C(\mathbf{u}_u[k])||^2 + \eta \int_a^b \left(\sum_{i=0}^{n_{Pu}} N^{(2)}_{i,p_u}(u)\mathbf{P}[i] \right)^2 du \tag{C.15}$$

Here η is an appropriately selected regularisation term. The least squares solution is then found from Equations C.24, C.12 or C.14 as before, but with:

$$\mathbf{A} = \mathbf{N}^T\mathbf{N} + \eta\mathbf{E} \quad \text{where} \quad \mathbf{E}[i,j] = \int_a^b N^{(2)}_{i,p_u}(u)N^{(2)}_{j,p_u}(u)dt \tag{C.16}$$

Instead of using the squared integral of the second order derivatives, Eilers and Marx (1996) suggest using the much simpler difference penalty as a discrete approximation thereof. The penalty matrix therefore becomes $\mathbf{E} = \mathbf{D}^{(2)T}\mathbf{D}^{(2)}$ where $\mathbf{D}$ is initialised as the $(n_{Pu}+1)\times(n_{Pu}+1)$ identity matrix and the d^{th} derivative's elements are recursively computed:

$$\begin{aligned} \mathbf{D}[i,j]^{(d)} &= \mathbf{D}[i,j+1]^{(d-1)} - \mathbf{D}[i,j]^{(d-1)} \\ \text{for} \quad i \in [0, n_{Pu}+1] \quad &\text{and} \quad j \in [0, n_{Pu}+1-d] \end{aligned} \tag{C.17}$$

Only in the case of clamped curves constrained to the end-points of the data does $\hat{\mathbf{q}}$ require additional modification before solving:

$$\tilde{\mathbf{q}} = \begin{bmatrix} \hat{\mathbf{q}}[1] - \mathbf{E}[1,0]\mathbf{v}[0] - \mathbf{E}[1,n_{Pu}+1]\mathbf{q}[n_q] \\ \vdots \\ \hat{\mathbf{q}}[k] - \mathbf{E}[k,0]\mathbf{q}[0] - \mathbf{E}[k,n_{Pu}+1]\mathbf{q}[n_q] \end{bmatrix} \quad \text{where} \quad k \in [1,\ldots,n_q-1] \tag{C.18}$$

Likewise $\mathbf{E}$ must be altered to contain only the internal $(n_{Pu}-1)\times(n_{Pu}-1)$ elements after its initial computation and before approximation via C.12. Figure C.2(a) shows a clamped curve fitted to some data versus its penalised counterpart. Incidentally, the closed curve in Figure C.2(b) is also penalised.

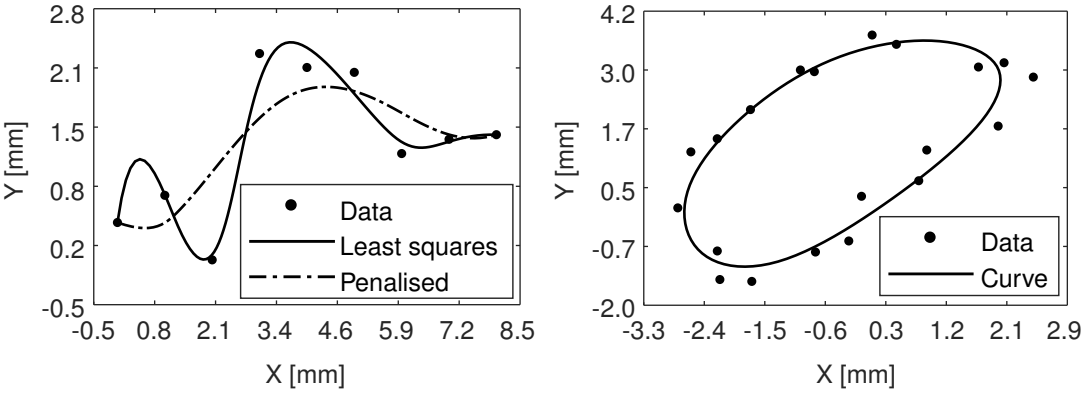

(a) Penalised curve

(b) Closed curve

Figure C.2: B-spline curve approximation (Illustration: J van der Merwe)

C.5 Un-ordered curve approximation

The curve fitting methods discussed up to here require a sorted set of data points to fit. Depending on the application, this may require careful pre-processing of the data, such as for instance in the case of unsorted point

clouds from Stereolithography (STL) files. Alternatively, for a set of randomly sampled $\mathbf{q}[k]$ points, we may use Newton's iterative approach to find their associated parameters $\mathbf{u}_u$, as the chord length method is no longer valid. The unknown control polygon is computed as before, and we only require some initial B-spline sufficiently close to the data for this method to work. The result is then iteratively updated until convergence occurs.

C.6 Surfaces

B-spline surfaces are for the most part an extension of the normal curve theory. By making the control polygon a bi-directional net and incorporating an additional knot vector we can make use of the product of separate univariate basis functions to define a surface:

$$S(u,v) = \sum_{i=0}^{n_{Pu}} \sum_{j=0}^{n_{Pv}} N_{i,p_u}(u) N_{j,p_v}(v) \mathbf{P}[i,j] \tag{C.19}$$

For surfaces, the degree in the u direction is indicated by p_u, while that of the v direction is p_v. Apart from the knot vector $\mathbf{k}_u$ as before, there is also an additional $n_{kv}+1$ knot vector:

$$\mathbf{k}_v = \{ \underbrace{0,\ldots,0}_{p_v+1}, \; v_{p_v+1},\ldots,v_{n_{kv}-p_v-1}, \; \underbrace{1,\ldots,1}_{p_v+1} \; \} \tag{C.20}$$

where $n_{kv} = n_{Pv} + p_v + 1$. Naturally, we can also unclamp and close a surface in one or both the u and v directions, though we don't require that functionality in our work so we limit our discussion to clamped and closed surfaces. Again similar to B-spline curves, rational surfaces are defined as:

$$\begin{aligned} S(u,v) &= \sum_{i=0}^{n_{Pu}} \sum_{j=0}^{n_{Pv}} R_{i,j}(u,v) \mathbf{P}[i,j] \quad \text{where} \\ R_{i,j}(u,v) &= \frac{N_{i,p_u}(u) N_{j,p_v}(v) \mathbf{W}[i,j]}{\sum_{k=0}^{n_{Pu}} N_{k,p_u}(u) \sum_{l=0}^{n_{Pv}} N_{l,p_v}(v) \mathbf{W}[k,l]} \end{aligned} \tag{C.21}$$

Figure C.3 illustrates a B-spline surface, while the procedure for computing a point on a surface is as follows:

1. Find which knot span $[\mathbf{k}_u[i], \mathbf{k}_u[i+1])$ which u belongs to.
2. Determine all non-zero basis functions $N_{i-p_u,p_u},\ldots,N_{i,p_u}$ in that span.
3. Find which knot span $[\mathbf{k}_v[j], \mathbf{k}_v[j+1])$ which v belongs to.
4. Determine all non-zero basis functions $N_{j-p_v,p_v},\ldots,N_{j,p_v}$ in that span.
5. Multiply the resulting basis functions' values with the matching control points.

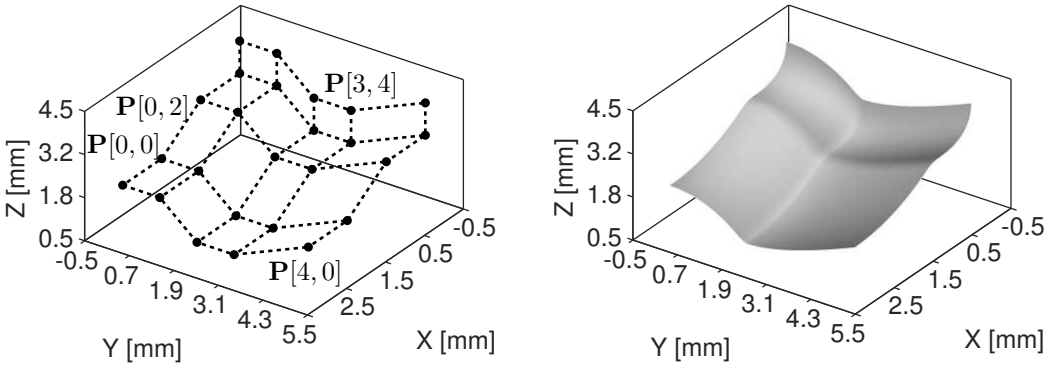

(a) Control net

(b) Surface

Figure C.3: B-spline surface example (Adapted from: Piegl and Tiller (1997))

C.7 Surface approximation

Piegl and Tiller (1997) describes a simple method of surface approximation that relies on multiple curve fits. Assume that an ordered grid of $(n_{Qu}+1) \times (n_{Qv}+1)$ points $\mathbf{Q}[k,l]$, as well as the desired degrees p_u and p_v in the u and v directions, and the size of the control grid $(n_{Pu}+1) \times (n_{Pv}+1)$ are all given. First, the parameters $\mathbf{u}_u$ and $\mathbf{u}_v$ are estimated based on the row and column means of the input grid, respectively. This allows the knot vectors $\mathbf{k}_u$ and $\mathbf{k}_v$ to be computed. Curve fitting is then repeatedly performed over the $n_{Qv}+1$ columns of the data matrix, with the resulting control polygons stored in a $(n_{Pu}+1) \times (n_{Qv}+1)$ temporary matrix. The process is then repeated over the $n_{Pu}+1$ rows of control points from the temporary matrix in order to create the final control net. The corners $\mathbf{Q}[0,0]$, $\mathbf{Q}[n_{Qu},0]$, $\mathbf{Q}[0,n_{Qv}]$ and $\mathbf{Q}[n_{Qu},n_{Qv}]$ will naturally be interpolated using successive clamped fits, while the remaining $\mathbf{Q}[k,l]$ are all approximated. It is important to note that the $n_{Qv}+1$ rows could be fitted first just as easily, though this yields a different result from the first approaches with the same input data. However, in practice we have found that either option performs well regardless, and that the general method of Piegl and Tiller (1997) is suitable for obtaining initial fits to gridded points for subsequent iterative parameter correction or re-parametrising previous fits.

In contrast, the method discussed by Lu (2010) enables us to solve a linear least squares problem to directly obtain the unknown control net. The advantages of this is that we can include a global penalty function and accommodate random and unsorted input data. We start again with known degrees p_u, p_v and intended control net size $(n_{Pu}+1) \times (n_{Pv}+1)$, however rather than a grid, our input data is an array of n_q+1 coordinates. Additionally writing our control net as an $n_P+1 = (n_{Pu}+1) \times (n_{Pv}+1)$ array, our B-spline surface equation becomes similar to that of curves:

$$S(u,v) = \sum_{l=0}^{n_P} M_l(u,v)\mathbf{P}[l] \quad \text{where} \quad M_{j(n_{Pu}+1)+i}(u,v) = N_{i,p_u}(u)N_{j,p_v}(v) \tag{C.22}$$

We then need to minimise the function:

$$\sum_{k=0}^{n_q+1} ||\mathbf{q}[k] - S(\mathbf{u}_u[k], \mathbf{u}_v[k])||^2 \tag{C.23}$$

By solving for the unknown control net $\mathbf{P}$:

$$\mathbf{AP} = \mathbf{M}^T\mathbf{q}[k]$$
$$\text{where } \mathbf{M} = \begin{bmatrix} M_0(\mathbf{u}_u[0], \mathbf{u}_v[0]) & \cdots & M_{n_P}(\mathbf{u}_u[0], \mathbf{u}_v[0]) \\ \vdots & \ddots & \vdots \\ M_0(\mathbf{u}_u[n_q], \mathbf{u}_v[n_q]) & \cdots & M_{n_P}(\mathbf{u}_u[n_q], \mathbf{u}_v[n_q]) \end{bmatrix} \text{ and } \mathbf{A} = \mathbf{M}^T\mathbf{M} \tag{C.24}$$

If the input data originated as a grid of points, we can determine the associated parameter values $\mathbf{u}_u$ and $\mathbf{u}_v$ via the chord length method in a similar manner to that previously mentioned. Alternatively, should we have a good enough starting estimate of the B-spline fit, we can use Newton's iterative method. Clamped $\mathbf{k}_u$ and $\mathbf{k}_v$ are determined as before. Note that we do not enforce interpolation of the corners as we fit separate boundaries to our parametrisations as discussed in Chapter 6.

C.8 Penalised surfaces

The penalty function is again based on the bending energy of the B-spline. For surfaces this becomes:

$$\sum_{k=0}^{n_q+1} ||\mathbf{q}[k] - S(\mathbf{u}_u[k], \mathbf{u}_v[k])||^2$$
$$+\eta \int_a^b \int_c^d \left(||S_{uu}^{(2)}(u,v)||^2 + 2||S_{uv}^{(2)}(u,v)||^2 + ||S_{vv}^{(2)}(u,v)||^2 \right) dudv \tag{C.25}$$

where

$$S^{(2)}_{uu}(u,v) = \sum_{l=0}^{n_P} \frac{\delta^2 M_l(u,v)}{\delta u^2}\mathbf{P}[l], \quad S^{(2)}_{uv}(u,v) = \sum_{l=0}^{n_P} \frac{\delta^2 M_l(u,v)}{\delta uv}\mathbf{P}[l],$$
$$S^{(2)}_{vv}(u,v) = \sum_{l=0}^{n_P} \frac{\delta^2 M_l(u,v)}{\delta v^2}\mathbf{P}[l] \tag{C.26}$$

Note that the input data is an array of coordinates, rather than a grid. The least squared problem is the same as in Equation C.24, except for the blended penalty matrix:

$$\mathbf{A} = \mathbf{M}^T\mathbf{M} + \eta\tilde{\mathbf{E}} \tag{C.27}$$

Here the $n_P + 1 = (n_{Pu} + 1) \times (n_{Pv} + 1)$ elements for $\tilde{\mathbf{E}}$ are computed via:

$$\begin{aligned}\tilde{\mathbf{E}}[j(n_{Pu}+1)+i, k(n_{Pv}+1)+l] = \mathbf{E}[i,l]^{(2)}\mathbf{E}[j,k]^{(0)} \\ +2\mathbf{E}[i,l]^{(1)}\mathbf{N}[j,k]^{(1)} + \mathbf{E}[i,l]^{(0)}\mathbf{E}[j,k]^{(1)}\end{aligned} \tag{C.28}$$

where $\mathbf{E}^{(d)} = \mathbf{E}^{(d)T}\mathbf{D}^{(d)}$ are the discrete sum of the difference matrices' elements.

C.9 Un-ordered surface approximation

As for curves, given an appropriate starting guess as to our surface fit, we can use Newton's method to estimate the closest parameters $\mathbf{u}_u$ and $\mathbf{u}_v$ for an array of unorganised input points $\mathbf{q}[k]$. The unknown control polygon may then be iteratively computed via the aforementioned method. The only problem is finding appropriate knot vectors $\mathbf{k}_u$ and $\mathbf{k}_v$. Earlier iterations could merely use those carried over from the starting surface, while error adaptive knot insertion could improve subsequent approximations (Lu, 2010; Piegl and Tiller, 1997). In contrast, we take care to make the starting fit as good as possible by mapping the unordered vertices to a grid as discussed in Chapter 6, and only perform an iterative fit to the original set of unordered points as a final post-processing step. Therefore, simply using the knot vectors from the starting fit suffices.

C.10 Algorithms

B-spline curves and surfaces share many of their important properties, a discussion which, apart from those mentioned here, lies outside the scope of this work. Most of the theory however is discussed in detail by Piegl and Tiller

(1997), who also provide a large number of useful algorithms as well as curve and surface constructions for advanced CAD applications. For reference, we list those most applicable to our work in Tables C.1 and C.2. Finally, we present our more general approach to curve and surface fitting in Algorithm C.4.

Table C.1: Relevant B-spline algorithms from Piegl and Tiller (1997)

	Algorithm	Description
A2.1	`FindSpan`	Returns the knot span index of u
A2.2	`BasisFuns`	Computes all $N_{i-p_u,p_u}(u), \ldots, N_{i,p_u}(u)$
A2.3	`DersBasisFuns`	Computes all $N^{(d)}_{i-p_u,p_u}(u), \ldots, N^{(d)}_{i,p_u}(u)$ for all $0 \leq d \leq p_u$
A2.4	`OneBasisFun`	Computes a single basis function $N_{i,p_u}(u)$
A2.5	`DersOneBasisFun`	Computes a single basis function's derivative $N^{(d)}_{i,p_u}(u)$ where $0 \leq d \leq p_u$
A3.1	`CurvePoint`	Calculates a point on a curve
A3.2	`CurveDerivsAlg1`	Calculates a point on a curve and all its derivatives up to d where $0 \leq d \leq p_u$
A3.5	`SurfacePoint`	Calculates a point on a surface
A3.6	`SurfaceDerivsAlg1`	Calculates a point on a surface and all its derivatives up to d where $0 \leq d \leq p_u, p_v$
A4.1	`CurvePoint`	Calculates a point on a rational curve
A4.3	`SurfacePoint`	Calculates a point on a rational surface
A5.1	`CurveKnotIns`	Inserts a new knot u_{new} into a curve multiple times
A5.3	`SurfaceKnotIns`	Inserts new knots u_{new} and v_{new} into a surface
A5.9	`DegreeElevateCurve`	Raises the degree of a curve without changing its shape
A5.10	`DegreeElevateSurface`	Raises the degree of a surface without changing its shape
A7.1	`MakeNurbsCircle`	Creates a circular arc
A8.1	`MakeRevolvedSurf`	Creates a surface of revolution
A9.1	`GlobalCurveInterp`	Interpolates a curve to points given the degree p_u and control polygon length n_{Pu}
A9.7	`GlobalSurfApproxFixednm`	Fits a surface to points given degrees p_u, p_v and net size n_{Pu}, n_{Pv}

Table C.2: Relevant B-spline theory sections from Piegl and Tiller (1997)

	Section	Description
§5.2	B-spline subdivision	Splits curves and surfaces at specified locations without changing their shape
§6.1	Newton iteration	Minimises the distance between $\mathbf{q}[k]$ and given $C(u)$ or $S(u,v)$
§8.4	Ruled surfaces	Linearly interpolates a surface between two curves
§10.6	Coons surfaces	Creates a blended patch surface between four curves

Function $[\mathbf{u}, \mathbf{P}] =$ `fitbspline(`$\mathbf{q}, \eta$`)`

Input:

$\mathbf{q}$	$n_q \times d$	input point array
η		regularisation term

Output:

$\mathbf{u}$	$n_k + 1$	knot vector(s)
$\mathbf{P}$	$n_P + 1$	Control polygon (net)

`/* initialisation */`

$p > 0, n_P \leq n_q$;

$n_k := n_P + p + 1$;

estimate $\mathbf{u}$; `/* chord length or Newton iteration */`

calculate $\mathbf{k}$;

`/* estimation */`

if $\eta \neq 0$ **then**

  compute $\mathbf{E}$; `/* discrete penalty matrix */`

end

while $\mathbf{P}$ *not converged* **do**

  compute $\mathbf{A}$;

  apply constraints ; `/* clamped or closed functions */`

  $\mathbf{P} \leftarrow$ `solve(`$\mathbf{A}, \mathbf{q}, \eta$`)` ; `/* linear least squares */`

  update $\mathbf{u}$;

end

end

Figure C.4: General B-spline approximation